The synthesis, structures and physical properties of fluoride and oxalate based magnetic coordination polymers

Teng Li

A thesis submitted for the degree of PhD
at the
University of St Andrews

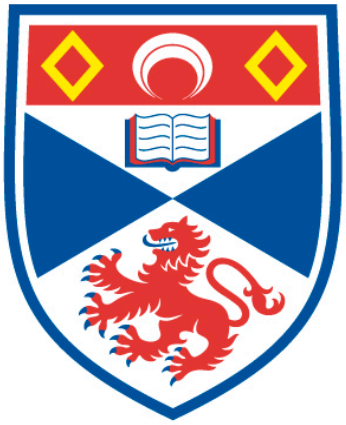

2020

Identifiers to use to cite or link to this thesis:

DOI: https://doi.org/10.17630/10023-24312

Candidate's declaration

I, Teng Li, do hereby certify that this thesis, submitted for the degree of PhD, which is approximately 40,000 words in length, has been written by me, and that it is the record of work carried out by me, or principally by myself in collaboration with others as acknowledged, and that it has not been submitted in any previous application for any degree.

I was admitted as a research student at the University of St Andrews in August 2016.

I, Teng Li, received assistance in the writing of this thesis in respect of language, grammar and spelling, which was provided by Dr Jason McNulty.

I received funding from an organisation or institution and have acknowledged the funder(s) in the full text of my thesis.

Date 14/11/2020 Signature of candidate

Supervisor's declaration

I hereby certify that the candidate has fulfilled the conditions of the Resolution and Regulations appropriate for the degree of PhD in the University of St Andrews and that the candidate is qualified to submit this thesis in application for that degree.

Date 14/11/2020 Signature of supervisor

Permission for publication

In submitting this thesis to the University of St Andrews we understand that we are giving permission for it to be made available for use in accordance with the regulations of the University Library for the time being in force, subject to any copyright vested in the work not being affected thereby. We also understand, unless exempt by an award of an embargo as requested below, that the title and the abstract will be published, and that a copy of the work may be made and supplied to any bona fide library or research worker, that this thesis will be electronically accessible for personal or research use and that the library has the right to migrate this thesis into new electronic forms as required to ensure continued access to the thesis.

I, Teng Li, confirm that my thesis does not contain any third-party material that requires copyright clearance.

The following is an agreed request by candidate and supervisor regarding the publication of this thesis:

Printed copy

Embargo on all of print copy for a period of 1 year on the following ground(s):

- Publication would preclude future publication

Supporting statement for printed embargo request

Some compounds described in this thesis are not published, we need time to organise the data and publish papers.

Electronic copy

Embargo on all of electronic copy for a period of 1 year on the following ground(s):

- Publication would preclude future publication

Supporting statement for electronic embargo request

Same reason as the previous one.

Title and Abstract

- I require an embargo on the abstract only.

Date 14/11/2020 Signature of candidate

Date 14/11/2020 Signature of supervisor

Underpinning Research Data or Digital Outputs

Candidate's declaration

I, Teng Li, understand that by declaring that I have original research data or digital outputs, I should make every effort in meeting the University's and research funders' requirements on the deposit and sharing of research data or research digital outputs.

Date 14/11/2020 Signature of candidate

Permission for publication of underpinning research data or digital outputs

We understand that for any original research data or digital outputs which are deposited, we are giving permission for them to be made available for use in accordance with the requirements of the University and research funders, for the time being in force.

We also understand that the title and the description will be published, and that the underpinning research data or digital outputs will be electronically accessible for use in accordance with the license specified at the point of deposit, unless exempt by award of an embargo as requested below.

The following is an agreed request by candidate and supervisor regarding the publication of underpinning research data or digital outputs:

Embargo on all of electronic files for a period of 1 year on the following ground(s):

- Publication would preclude future publication

Supporting statement for embargo request

The data need to be secured for further paper publication.

Title and Description

- I require an embargo on the title and description

Date 14/11/2020 Signature of candidate

Date 14/11/2020 Signature of supervisor

Abstract

This thesis describes the crystal structures and physical properties of three types of organic-inorganic hybrid coordination polymers (CPs): organic-inorganic hybrid fluoride layered perovskites, oxalate fluoride CPs and metal(III)-fluoride compounds. Most of the compounds presented here were synthesised through hydrothermal and solvothermal reactions, except two metal(III)-fluoride compounds which were synthesised by a layered solution method.

For the organic-inorganic hybrid layered perovskites, seven compounds are reported. The crystal structures are revealed by single crystal X-ray diffraction. The magnetic properties of some have also been characterised by SQUID magnetometry, and the results show the metal centres in all the compounds display antiferromagnetic interactions at high temperature. For the compounds (*en*H_2)MnF_4 (**1**) and (*en*H_2)CoF_4 (**2**), variable temperature crystal structure analysis has been carried by the powder synchrotron X-ray diffraction and powder neutron diffraction. The results of Rietveld refinements show no phase transition was observed for both compounds. The magnetic structure of **2** has also been determined from the neutron data, in which the interactions of Co remain antiferromagnetic, with the magnetic moment (Mx0, My0, Mz0) = (3.53, 0, 0.53) at 20 K. In addition, the crystal structures of two derived compounds are also presented in this section.

For the oxalate fluoride compounds, nine crystal structures are also characterised by single crystal X-ray diffraction. The compounds are in the form of 1D or 2D magnetic structures which are constructed by the metal centres and versatile coordination modes of the oxalate ligands. Magnetic characterisations show nearly all the compounds display antiferromagnetic interactions at high temperature, which are all well fitted by the 1D Heisenberg model.

The majority of the seven metal(III)-fluoride compounds contain monomeric units. However, two unusual layered structures, which may form part of a homologous series, have been discovered, and there are some relationships between the syntheses and structures which can be applied in more targeted work in the future.

Acknowledgement

Firstly, I would express my sincere gratitude for my supervisor, Prof. Philip Lightfoot for all his support during my entire PhD study, including the guidance and ideas in research and also the help and advice for my four-year life living in this country. I also want to thank the other group members, especially, Dr Jason McNulty, Dr Wenjiao Yao, Dr Lucy Clark, Dr Rebecca Clulow, Mr Alasdair Bradford and Miss Yuanyuan Guo, for their help in research, in life and even in English thesis writing. Besides, I would thank all the group members for making the PL group a warm family, surrounded by whom my PhD is more enjoyable.

I would also thank the people who helped me with accomplishing this thesis, Prof. Alexandra Slawin and Dr David Cordes for their help in collecting and analysing single crystal data; Dr Yuri Andreev and Dr Julia Payne for their help on powder X-ray diffraction; Prof. Stephen Lee for his help on magnetic data measurement and analysis; Mr. Stephen Boyer for CHN elemental analysis; Dr Alexandra Gibbs, Dr Ivan da Silva (ISIS) and Prof Chiu Tang (Diamond) for the assistants in neutron and synchrotron data collecting and analysing.

I also thank my friends in St Andrews, especially my roommates, Mr Xuan Feng, Miss Jianyi Mai and Mr Weihao Sun, who make me not feel lonely during the COVID-19 pandemic.

I thank CSC, the University of St Andrews and RSC for the funding.

Finally, I really appreciate my fiancée, Dr Yiqing Zhao, for supporting me both spiritually and in general life during my entire university stage. Last but not least, I also appreciate my parents and grandma, for their continued love and support.

Table of Contents

Chapter 1 Introduction and Background

1-1 Hydrothermal and Solvothermal Reactions

1-1-1 Background

Hydrothermal and solvothermal syntheses refer to reactions in aqueous and non-aqueous solutions under high temperature and/or high-pressure environments. These reaction methods have been known for more than 100 years. The term "hydrothermal" first appeared in the mid 19th century, and was used to describe the process of mineral formation from cooling magma in hot water solution by the British geologist Sir Roderick Murchison (1792-1871).[1] Since then, hydrothermal and solvothermal reactions have been widely used to synthesise functional materials, such as zeolites, Metal-Organic Frameworks (MOFs), ionic and electronic conductors, and nanomaterials, etc. Today, both reactions commonly refer to a chemical reaction in which the reactants are mixed and placed in aqueous or organic solvent and sealed in a container, then reacted under different temperatures (100-1000 °C) and pressures (1-100 MPa). The containers used in hydrothermal and solvothermal reactions in this thesis are high-pressure autoclaves (Fig. 1-1). An autoclave is composed of two parts: a stainless steel can (for maintaining pressure) and a Teflon liner (for the chemical reaction). When the reaction is being conducted on a micro-scale level, glass tubes may also be used as the reactor, but these are not appropriate in the case of corrosive environments, such as fluoridic media. Additionally, the glass tubes are not suitable for high temperature and high pressure reactions.

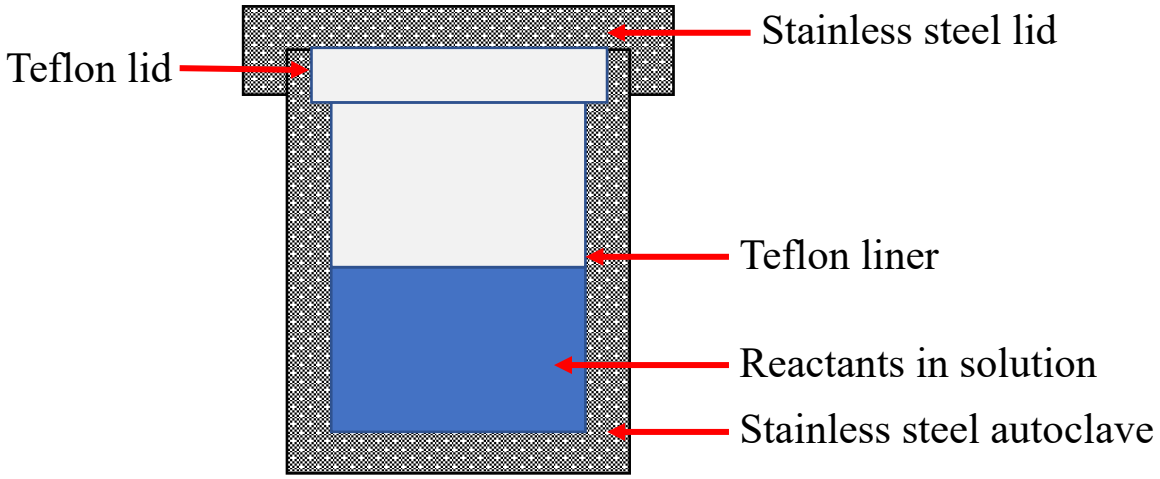

Fig. 1-1 Schematic diagram of autoclave

Compared with traditional solid state reactions, the mechanisms of hydrothermal and solvothermal reactions are quite different. Solid state reactions process on the interface of the solid reagents, but the hydro/solvothermal reactions occur in solution. These different mechanisms will occasionally result in different products, even though the starting materials may be the same. In some cases, hydro/solvothermal reactions are regarded as an alternative method to solid state reactions because of their milder synthetic method and lower reaction temperature. Furthermore, as the temperatures for hydro/solvothermal reactions are normally lower than solid state reactions, this makes them more suitable to construct organic related products. Thus, the hydro/solvothermal reactions are normally used to synthesise compounds through a solution route which cannot be prepared from solid state reactions.

In general, the hydro/solvothermal reactions can be classified into two types: supercritical and subcritical, according to the reaction temperature. For supercritical synthesis, the reaction temperature may reach up to 1000 °C and the pressure up to 0.3 GPa. Supercritical synthesis can be used to produce interesting crystalline materials with special structures. Since 1980, supercritical reactions have mostly been used in synthesis of inorganic, large single crystal materials, e.g. $LiNbO_3$ crystals for laser materials, $AlPO_4$ for optical materials and other inorganic ferroelectric, magnetoelectric or superconducting materials.[2-4] Subcritical synthesis

is more commonly used in industrial and laboratory work with reaction temperatures in the range of 100-240 °C. Solvents used for subcritical solvothermal reactions can boil at lower or higher temperatures and this leads to a lower or higher temperature range at which the reactions become solvothermal. For example, methanol (MeOH, b.p. 64.7 °C) and ethanol (EtOH, b.p. 78 °C) are in lower temperature range, but *N, N'*-dimethylformamide (DMF, b.p. ~153 °C) and ethylene glycol (EG, b.p. 197.3 °C) are in higher temperature range. This subcritical synthesis method makes up the majority of hydro/solvothermal reactions today and is the method used to synthesise the compounds in this thesis.

While we are using subcritical hydro/solvothermal reactions to do synthesis there are many factors to consider that may influence the products formed. Some of these include: percentage of solution filling; reaction time; solvent used; concentration and acidity. Variations in the filling percentage of the autoclave influences the pressure generated throughout the reaction. In general, higher filling percentages lead to higher pressures, which in turn may build more complex compounds. Longer reaction times can also lead to more complex compound formation. Longer reaction times also are more likely to yield larger, high quality crystals for structural determination. Shape and quality of crystals can be influenced by the solvent used and the concentration. Generally, dilute solutions contribute to larger pure single crystal products and while this can be helped with different solvents this may also lead to different product formation. The acidity of the reaction mixture is an important factor in the synthesis of organic-inorganic hybrid products especially for the 3*d* metal based compounds. In some instances, products formed are different in acidic and basic conditions even when all other variables remain unchanged.

1-1-2 Organic-Inorganic Hybrid Compounds

In recent years, research into organic-inorganic hybrid compounds has developed rapidly. These materials have a wide variety of crystal structures and consequently have a lot of potential applications in many chemical, physical or even medical fields.[5-8] As crystallised products are needed for structure determination and the inability of organic compounds to withstand high temperature, many solution reaction methods are ideal synthetic routes for crystal growth, such as solvent extraction, slow intermixing solutions and hydro/solvothermal reactions, etc. However, in some instances, the compatibility between reactants and solutions is not very good under ambient conditions, which can cause the diffusion problems to interrupt crystal growth. The situation in hydro/solvothermal reactions is different, as the viscosity of the solution is much lower in hydro/solvothermal environment than in ambient conditions, the slow diffusion problem observed in the normal solution method does not occur in hydro/solvothermal reactions. In addition, the hydro/solvothermal method can increase the solubility of reactants, through which some new phases (compared to traditional solution reactions) can be prepared. For example, under mild hydrothermal conditions, the dielectric constant of water (sub-supercritical H_2O) is decreased, which enable both polar and non-polar reagents can be dissolved due to the greater degree of ionisation and disrupted hydrogen bonding networks.

So far, many organic ligands have been tested in the synthesis of organic-inorganic hybrid materials. One common principle for ligand selection is that organic ligands with N- or O- donors are ideal as these act as coordination sites to link the organic and inorganic parts. However, there are significant differences in the selection of organic ligands for different types of organic-inorganic hybrid materials. For coordination polymers (CPs) or MOF constructions, the selected organic ligands normally have two or more coordination sites, for example, pyrimidine, pyrazine, piperazine (*pipz*), 4,4’-bipyridine (4,4’-*bpy*), ethylenediamine (*en*),

oxalic acid, etc[9-11] but for organic-inorganic hybrid clusters, there must be some organic ligands that have a terminal coordination site, for example, amino acids, pyridonates and Schiff-base etc (Fig. 1-2).[12-14]

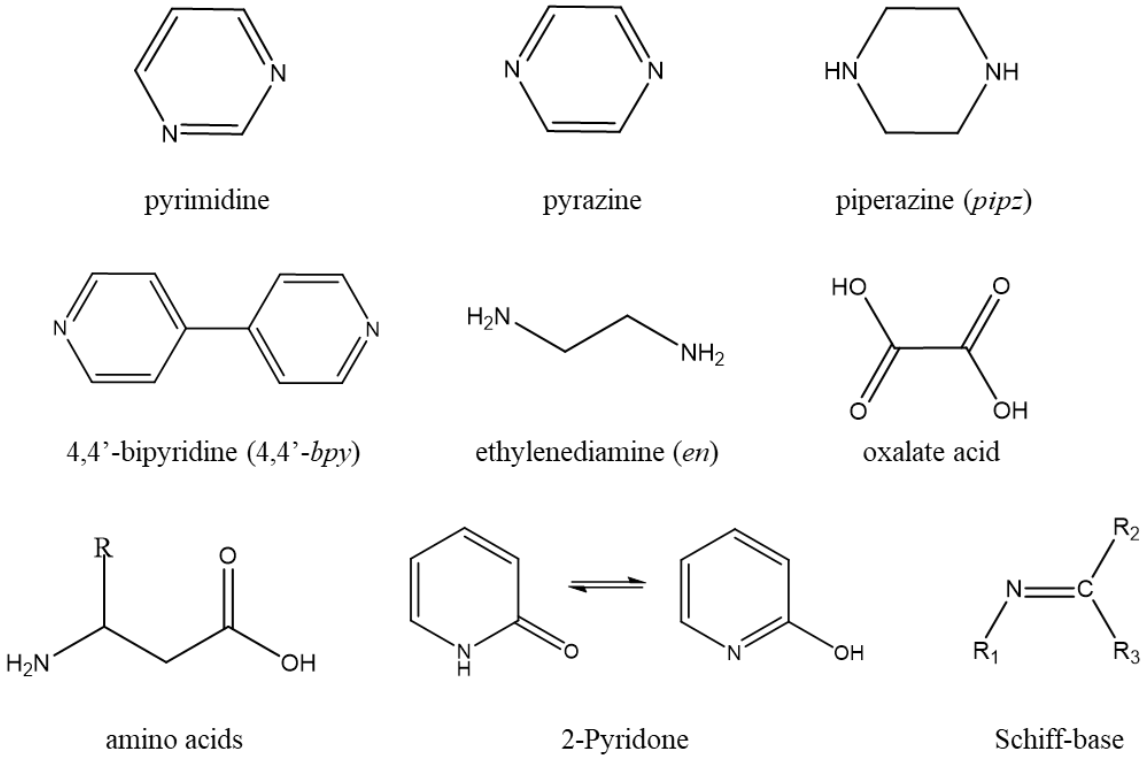

Fig. 1-2 Example of organic ligands in organic-inorganic hybrid materials.

1-1-3 Coordination Polymers (CPs) and Metal-Organic Frameworks (MOFs)

CPs refer to coordination compounds with repeating coordination entities extending into one, two or three dimensions. MOFs are a type of CP with potential voids and are also known as porous coordination polymers.[15] Like CPs, there are also coordination bonds in MOFs, which help to build two or three dimensional extended structures, or the cross-link one-dimensional chains. The term CP first appeared in the early 1960s, then in 1964, this area was reviewed for the first time.[16] Over the last few decades, the research of CPs has made significant progress into the design and synthesis of new materials with optical, catalytic, electronic, and magnetic properties.[17-19] The term MOF was first used in the 1990s,[15] but the progress in this field has been very rapid; more so than CPs. So far, because of their special void structures,

MOFs have been used as good candidates for gas storage separation[20-24], catalytic materials[25-27], optical materials[28-35], and molecular magnets[36-38].

Other than hydro/solvothermal reactions, many other reaction types have been used in CP and MOF synthesis, such as the evaporation method, microwave reaction, ultrasonic method, or even diffusion method.[39] Compared to these other methods, the hydro/solvothermal reaction is the most widely applied in synthesis. This is likely due to its many advantages, such as easy operation, short preparation time, highly crystallised products, and sometimes even unexpected new MOF structures (the autogenous pressure can cause the *in-situ* metal/ligand reactions).[40-43]

However, there are also some disadvantages of hydro/solvothermal reactions. The disadvantages of hydro/solvothermal reactions can include the formation of impure, mixed phase products, which can lead to waste of starting materials when preparing sufficient pure single-phase materials for analysis. In addition, based on the quality of the autoclaves, sometimes the repeatability of hydro/solvothermal reactions can be poor.

1-2 Hybrid Layered Perovskites

1-2-1 Introduction

Perovskite was discovered and named after a Russian mineralogist Perovski in 1839.[44] The first discovered perovskite structure was calcium titanate $CaTiO_3$ (Fig. 1-3).[44] The general formula of perovskite is ABX_3, where A is a large cation (such as group 1 or group 2 cations), B is a relative smaller cation (such as a 3*d* transition metal) and X is usually an oxide or halide anion. Fig. 1-3 shows the crystal structure of 3D $CaTiO_3$ perovskite. The diagram shows each titanium atom (B) coordinates with 6 oxygen atoms (X) to form an octahedron. All the octahedra are corner sharing, thus expanding the structure in three dimensions. The calcium is positioned between the octahedra and is 12-coordinated by the surrounding oxygens.

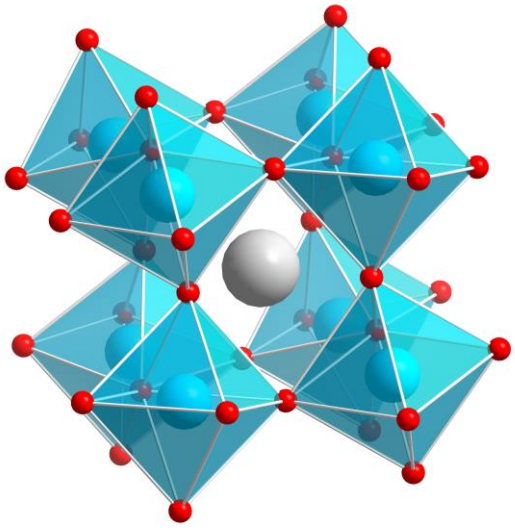

Fig. 1-3 Crystal structure of $CaTiO_3$ perovskite structure.

(colour code: white for Ca, blue for Ti, and red for O)

While there are many combinations possible for A, B and X, the selection of these is not random. Firstly, the total electronic charge should be balanced. Secondly, the Goldschmidt tolerance factor, *t*, normally should be in the range 0.825 to 1.059.[45] The Goldschmidt tolerance factor was firstly described by Victor Moritz Goldschmidt in 1926.[46] It is calculated from the ratio of the A, B and X ionic radius:

$$t = \frac{r_A + r_X}{\sqrt{2}(r_B + r_X)} \qquad (1-1)$$

Where r_A is the radius of A cation, r_B is the radius of B cation and r_X is the radius of X anion.

Due to the range of compositions available, perovskite materials have a lot of interesting physical properties, such as ferromagnetism[47-49], ferroelectricity[50-52], low exciton-binding energy, and high dielectric constant[53-57], etc. These make the materials good candidates for multiferroic, optoelectronic and photovoltaic applications. Based on the anion used for X, perovskites can be classified into two main types: oxide (ABO_3) and halide (ABX_3) perovskites.

In general, oxide perovskites are synthesised by solid state chemistry methods at high temperature, while halide perovskites are synthesised by solution methods at low temperature. While oxide perovskites are known for their considerable ferroelectric and superconductive properties, halide perovskite materials are more commonly known as potential materials for use in optoelectronic and photovoltaic devices.[58]

1-2-2 Layered Perovskites

The structures of 2D perovskites, while related to those of conventional 3D perovskites, can be considered as built from octahedra separated into 2D layers by some special "A cations". In general, there are three different layered perovskite types, Dion-Jacobson (DJ), Ruddlesden-Popper (RP) and Aurivillius (Fig. 1-4). [59-61]

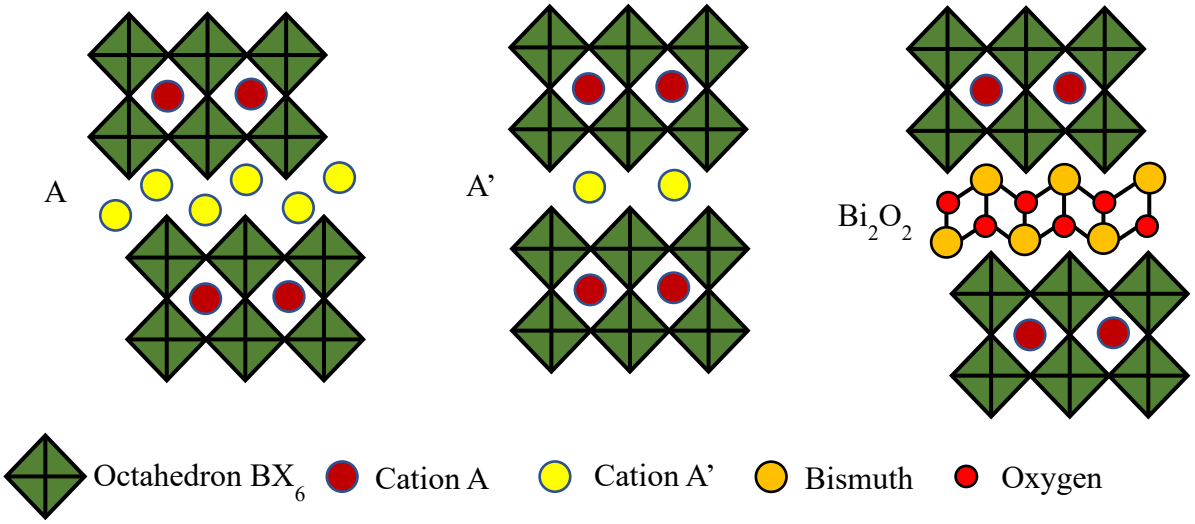

Fig. 1-4 The structure of RP phase (left), DJ phase (middle) and Aurivillius phase (right).[61]

The general formula for RP phase is $A_{n+1}B_nX_{3n+1}$, for DJ phase is $A'A_{n-1}B_nX_{3n+1}$ and for Aurivillius phase is $(Bi_2O_2)A_{n-1}B_nO_{3n+1}$. Here, *n* represents the thickness of the octahedral layers and is determined by the number of octahedra positioned between neighbouring sheets.

Based on different *n* we can get mono-layered, double-layered, triple-layered… structures. If $n = \infty$, we will get the aristotype perovskite structure (Fig. 1-5).[60,61]

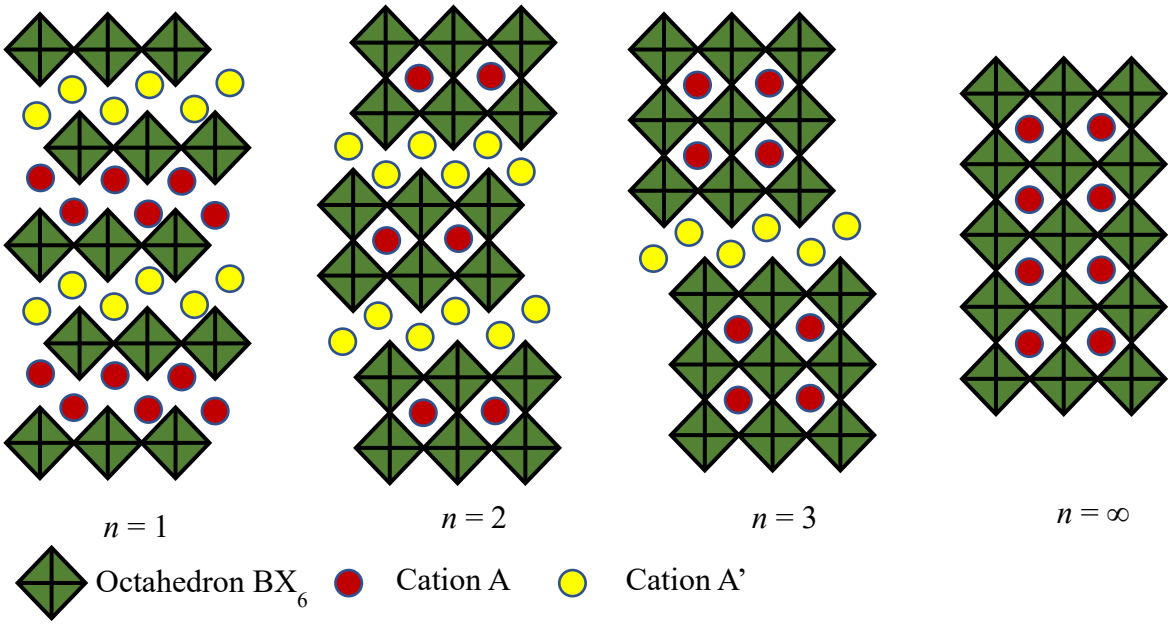

Fig. 1-5 Layered perovskites with different sheet thicknesses, *n*.[61]

The RP phase was named after S. N. Ruddlesden and P. Popper in 1957 who published the first examples of the RP phase compounds Sr_2TiO_4, Ca_2MnO_4 and $SrLaAlO_4$.[62,63] Rather than, $A_{n+1}B_nX_{3n+1}$, the general RP formula can also be represented as $A_{n-1}A'_2B_nX_{3n+1}$. For oxide RP structures, the A and A' cations can be alkali, alkaline earth or rare earth metal, while B cations are normally transition metals. For A and A' cation, if $n = 1$, then only A' exists, which adopts a nine-coordinate position; if $n \neq 1$, then the A cation is in the square perovskite channel surrounded by octahedra and is 12-coordinated with surrounding oxygen atoms.

The DJ phase was first discovered in 1981 by Dion and then further studied under the supervision of Jacobson.[64-66] In contrast to the oxide RP phase, A' in an oxide DJ phase is normally an alkali metal, and A could be alkaline earth or rare earth metal, which consequently limits B to a pentavalent metal (mostly tantalum or niobium). The A' cation in the middle of the layers is normally eight-coordinated.

The Aurivillius phase was first described in 1949 by B. Aurivillius.[67] In the Aurivillius structure, the A' is substituted by $[Bi_2O_2]$. The Aurivillius structures are famous for their ferroelectric properties.[68]

1-2-3 Organic-inorganic Hybrid Layered Halide Perovskites.

As we have mentioned before, the halide perovskites can be synthesised using relatively milder conditions than those used in synthesis of oxide perovskites (lower temperature, solution synthesis). The mild synthesis method allows the incorporation of organic cations in halide perovskites. The first organic-inorganic hybrid perovskite $(CH_3NH_3)PbI_3$ was reported in 1978 by Weber[69] but did not garner much interest until 2009 when the Miyasaka group presented work on nano-crystallised $(CH_3NH_3)PbI_3$ self-assembled on TiO_2 films exhibiting strong bandgap absorption as a semiconductor and subsequently started the trend of research into organic-inorganic hybrid perovskites for photovoltaic applications.[70]

For organic-inorganic hybrid layered halide perovskites, various organic ligands have been selected as A or A' cations, for instance, organoamines[71,72], diamines[73], halo(pseudohalo)-amines[74,75], hydroxyl-amines[76], carboxyl-amines[77], heterocycles[78], etc (Fig. 1-6). Most A or A' cations in organic-inorganic hybrid layered halide perovskites contain protonated amine groups. The hydrogen bonds of the protonated amine groups link the organic and inorganic parts of the perovskites. In early research, the main purpose of trying different organic ligands is to build different perovskite structures, while in recent years, the main purpose has been to introduce different functional groups into the perovskites.

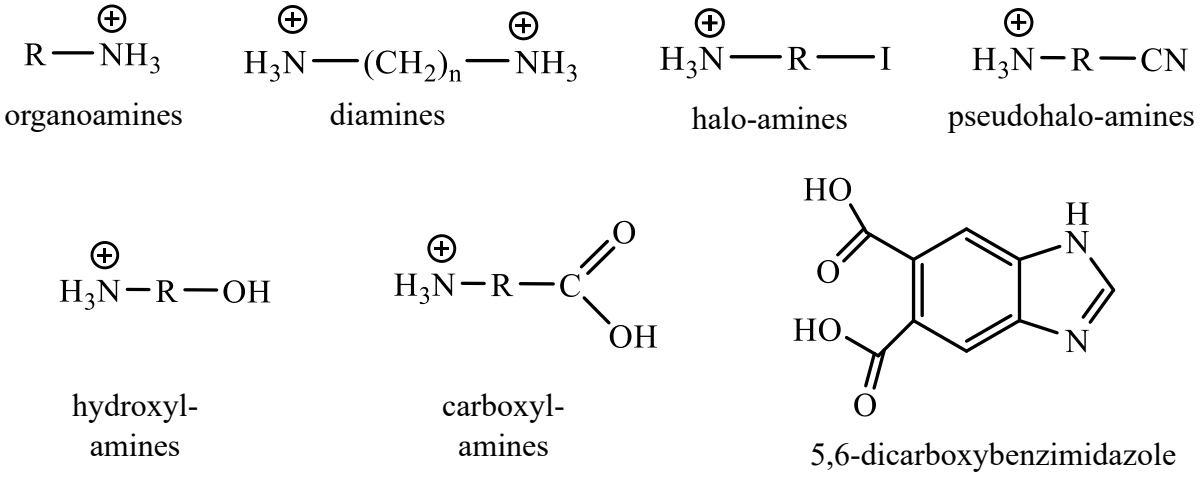

Fig. 1-6 Examples of organic cations in layered halide perovskites.

Based on different B cations, halide perovskites can be classified into two types; the transition metal perovskites and the group 14 perovskites. While research on transition metal perovskites focuses on magnetic and ferroelectric properties[79,80], research on group 14 perovskites more focuses on their photocurrent, electroluminescence and semiconducting properties[58,81,82]. There are also some examples of trivalent cations Bi^{3+} and Sb^{3+} used in the B position but these are much less common.[83-85] In these compounds, one-third of the trivalent cations are replaced by a vacancy to balance the charge.[86]

Considering the X anions, beyond for the traditional halogens (Cl^-, Br^- and I^-), some pseudohalides (N_3^-, SCN^-, and I_3^-) can also be incorporated[87-89] (N_3^- was only reported in 3D perovskite $((CH_3)_4N)Mn(N_3)_3$)[87], although there are no previous examples of F^- based hybrid layered perovskites. We reported the first example of a hybrid fluoride layered perovskite in 2019.[90] The details of this work will be presented in chapter 3.

1-2-3-1 Group 14 Perovskites

In 1986, Maruyama reported the first organic-inorganic hybrid layered lead-halide perovskite $(C_9H_{19}NH_3)_2PbI_4$.[91] Since then, the research into this kind of layered perovskites has risen rapidly because of their potential applications in luminescence and optoelectronic facilities.[92-95] The organic components make layered perovskites more flexible and stable but have weaker optoelectronic properties, compared with the 3D perovskites. For example, in the RP phase layered perovskite $(CH_3(CH_2)_3NH_3)_2(CH_3NH_3)_{n-1}Pb_nI_{3n+1}$ series, the bandgap is 1.50 eV for $n = \infty$, 1.91 eV for $n = 4$, 2.03 eV for $n = 3$, 2.17 eV for $n = 2$, and 2.43 eV for $n = 1$.[96] From the data, we can conclude that the optical bandgap of layered perovskites approach to the 3D perovskite with the increasing layer thickness, if other parameters are unchanged. A similar trend was also found in another RP phase layered perovskite $(NH_3C_mH_{2m}NH_3)(CH_3NH_3)_{n-1}Pb_nI_{3n+1}$ (m = 4−9; n = 1−4) series.[97] However, further work on group 14 perovskites is needed to find the optimal point between the properties and the applications.

1-2-3-2 Transition Metal Perovskites

Research into transition metal layered perovskites was even earlier than the group 14 perovskites and started in the 1960s.[98-100] The study on d^9 Cu^{2+} perovskites showed strong Jahn-Teller (JT) distortion around the metal. The elongated axes of these octahedra are in the inorganic plane, connecting adjacent octahedra by corner sharing with the shorter axes.[99,101] The overall magnetic behaviour in these materials arises mainly from interactions within the 2D inorganic layers, with the organic ligands causing very weak inter-layer magnetic connections.

In the 1970s, the $(C_nH_{2n+1}NH_3)_2MCl_4$ and $(NH_3(CH_2)_nNH_3)MCl_4$ (M = Cu, Mn, Fe, Cd) layered perovskite series attracted a lot of attention because of their interesting magnetic properties and structural phase transitions.[73,102-104] The research suggested that for the Mn

compounds, in the n = 2-5 range, only n = 2 has no phase transition versus temperature. One interesting thing is that even though the phase transition factors are different based on different n, the magnetic susceptibilities are very similar.

1-3 Oxalate Coordination Polymers

1-3-1 Carboxylate Ligand

The carboxylate ligand is a common element in CP synthesis. Based on different geometry characteristics of the carboxylate ligands and the metal ions, the carboxylates can adopt different bridging modes (Fig. 1-7) such as *syn-syn*, *anti-anti*, *syn-anti*, and monatomic, and they can normally mediate ferro- or antiferromagnetic coupling between metal ions under different situations.[36]

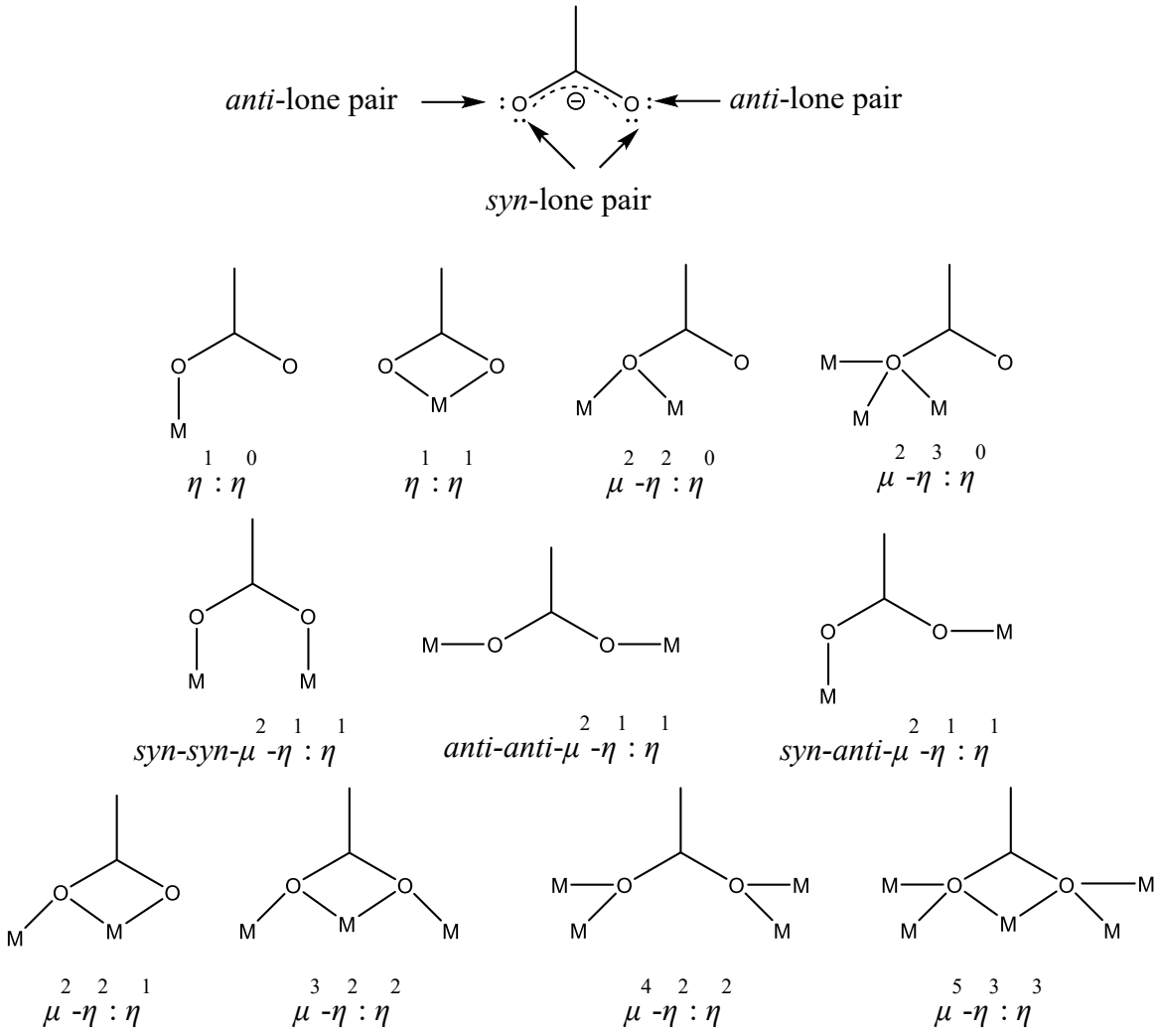

Fig. 1-7 The coordination modes of mono-carboxylate. The symbol μ^n-η^u:η^v means *n* metal centres are bridged by the carboxylate, in which one oxygen coordinates *u* and the other oxygen coordinates *v* metal centres.[36]

1-3-1-1 Formate Ligand Based Compounds

The simplest organic compound with a carboxylate ligand is formic acid. One famous example of formate ligand-based MOFs is $[Mn_3(HCOO)_6]\cdot$(guest), which displays the magnetoelectric (ME) effect or potential ME effect.[105] $[Mn_3(HCOO)_6]\cdot C_2H_5OH$ could be obtained when the compound is kept in ethanol vapour (Fig. 1-8). The ethanol molecules reside in the 1D channels along the *b* axis. The compound undergoes a ferromagnetic transition at 8.5

K, which confirms the magnetic interactions between neighbouring Mn^{2+} cations. Apart from the ferromagnetic transition, some ferroelectric behaviours can also be observed in this compound. The dielectric constant exhibits a very strong sharp peak at 165 K along the *a* axis, while only small peaks appear along *b* and *c* axes. The *P*-*E* hysteresis loop was recorded in a narrow temperature range from 145 to 166 K. It is suggested that the interaction between the host lattice and C_2H_5OH molecules is the main reason for the ferroelectric phase transition. This speculation is further confirmed by the sharp peak in dielectric constant at 164 K of the deuterated $[Mn_3(HCOO)_6]\cdot C_2H_5OD$. The coexistence of ferromagnetism and ferroelectricity in one compound offers us a clue to design new structures which may possibly contain the both properties.

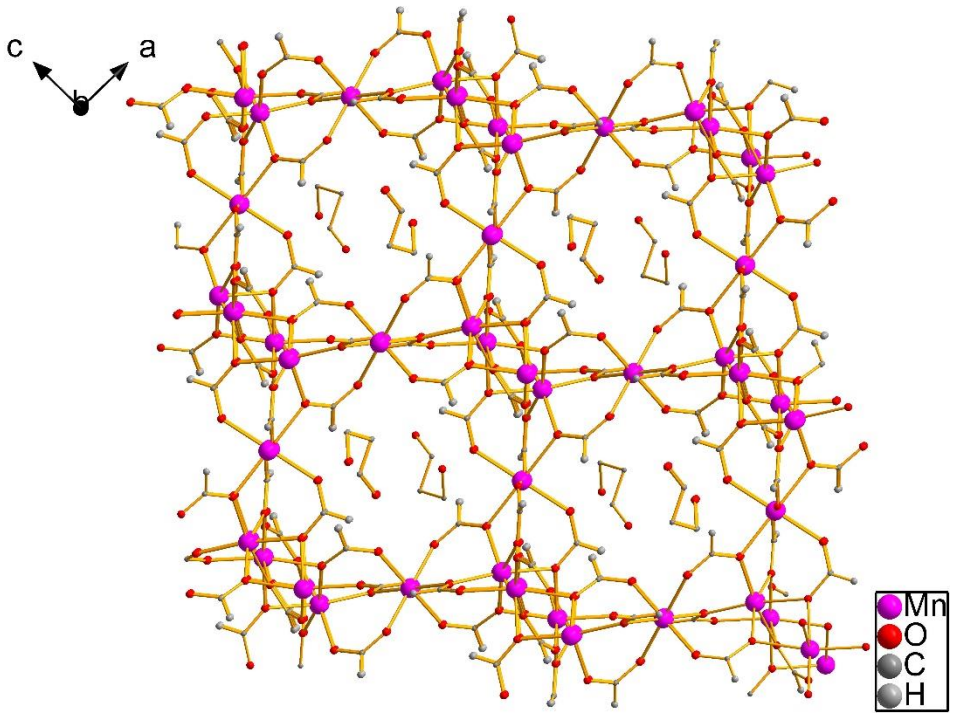

Fig. 1-8 The crystal structure of $[Mn_3(HCOO)_6]\cdot C_2H_5OH$. Figure drawn using data from the Cambridge Crystallographic Database (CSD), structure 685237.

1-3-1-2 Oxalate Ligand Based Compounds

Compared with the formate ligand, the oxalate ligand is more common in magnetic CP synthesis. We can control the magnetic properties of oxalate-based CPs as well by adjusting the bridging modes during the synthesis process. Other than that, the oxalate ligand can link two or more different magnetic metals, and construct more complex magnetic materials and other multifunctional materials. In addition, the oxalate ligand is compatible with many other non-magnetic metals or organic ligands, which will result in more multifunctional materials.

One example of oxalate based molecular magnet is $KFe(C_2O_4)F$.[106,107] Fig. 1-9 shows the structure of the compound obtained from single crystal X-ray diffraction. There are two magnetic interaction pathways through the oxalate ligand: one is from the *syn-anti* carboxylate bridging Fe−O−C−O−Fe while the other is oxalate *cis* bridging Fe−O−C−C−O−Fe. Through the magnetic bridging, the Fe^{2+} ions form a triangular lattice or distorted kagome in the 2 D $[Fe(C_2O_4)]^{\infty}$ layers within the *bc* plane, which may yield the spin frustration behaviour. Along the *a* axis, the fluoride anions could also be a magnetic bridge through the Fe−F−Fe chains. The preliminary magnetic characterisation also confirmed an overall antiferromagnetic interaction system at high temperature with Weiss constant $\theta \approx -300$ K, and magnetic ordering transition at $T_N \approx 20$ K. The frustration index, $f = |\theta|/ T_N \approx 15$ indicates a strong spin frustration.[106] Furthermore, powder neutron diffraction (PND) and muon spin rotation (μSR) analysis showed two competing antiferromagnetic pathways: the quasi-two-dimensional distorted triangular layers in *bc* plane (oxalate) and the quasi-one-dimensional Fe−F−Fe chains. Also, the strongest antiferromagnetic spin chains are along the *a* axis, which indicates the antiferromagnetism is mainly mediated by the fluoride anions.[107]

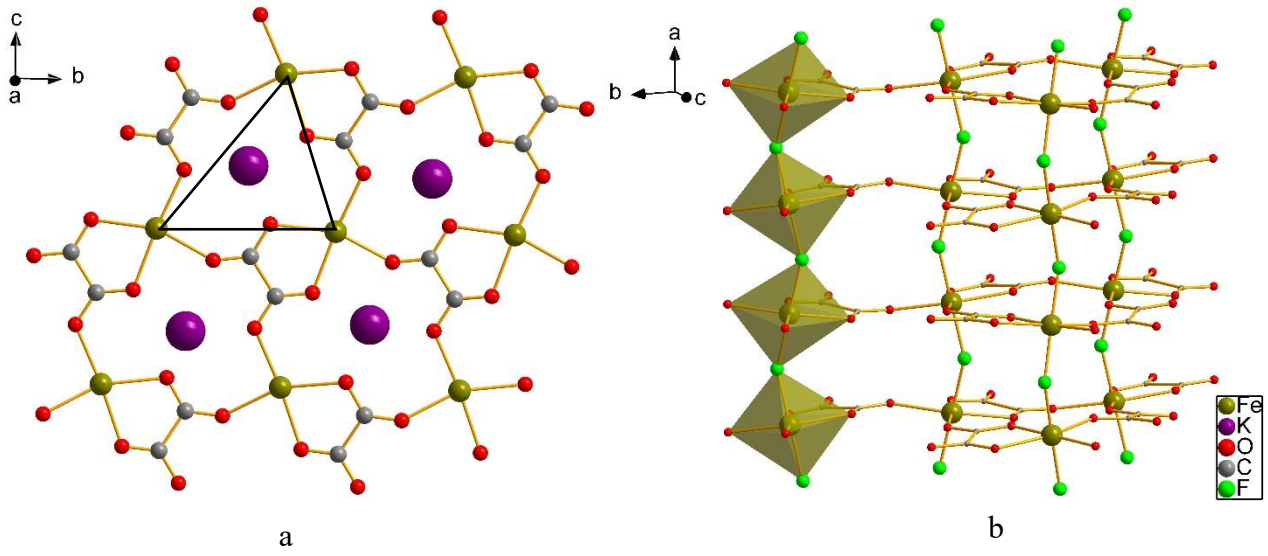

Fig. 1-9 The crystal structure of $KFe(C_2O_4)F$ viewed (a) in the *bc* plane (single layer) and (b) showing the corner-sharing Fe^{2+} octahedra running along the *a* axis (Fe^{2+} octahedra formed via two F linkers and four oxygens from oxlate ligands). The potassium is omitted in (b) for clarity. The figure is reproduced from reference 106.

Another example is a series of oxalate-based 2D compounds with more than one metal in each, the $[N(n\text{-}Bu)_4][M^{II}V^{III}(ox)_3]$ (M^{II} = Fe, Co, Ni, Cu).[108] These compounds are stable in air and can be very easily synthesised by aqueous methods. In these compounds, each metal ion is surrounded by three oxalates and extended in two-dimensions to form a hexagonal ring (Fig. 1-10). The $[N(n\text{-}Bu)_4]^+$ cation is located above the centre of each hexagonal ring. The magnetic characterisations indicate there could be ferro- or antiferro- magnetic couplings between the metal centres based on different metal combinations. The large void in the hexagonal ring provides a useful space for further modification of these compounds. For example, these spaces could be filled by some other amine to introduce ferroelectric properties. The series of the compounds give an oxalate skeleton with potential for multifunctionality.

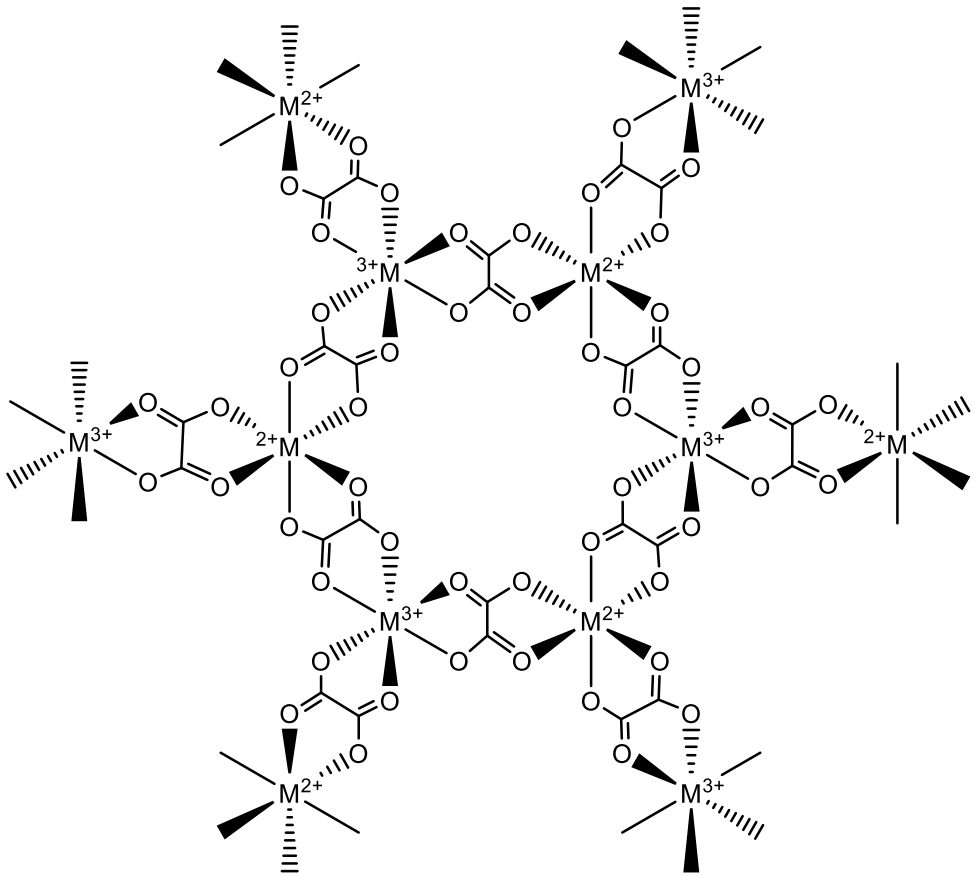

Fig. 1-10 Proposed 2-D structure of $[M^{II}M^{III}(ox)_3]$. The $[N(n\text{-}Bu)_4]^+$ cation is omitted for clarity.

In 2009, Kitagawa *et al*. also reported a series of bimetallic oxalate complexes based on hydrophilic tri(3-hydroxypropyl)ammonium ($NH(prol)^{3+}$), $\{NH(prol)_3\}[M^{II}Cr^{III}(ox)_3]$ (M^{II} = Mn^{II}, Fe^{II}, Co^{II}).[109] The metal centres and oxalate ligands also link with each other and form a hexagonal ring structure with honeycomb cavities. There are disordered H_2O molecules in the cavities. The $NH(prol)^{3+}$ ion assumes a tripodal configuration, with a 3-fold axis along the N-H bond (Fig. 1-11). Magnetic studies demonstrate that all three compounds exhibit overall ferromagnetic ordering, with T_C values of 5.5 K, 9.5 K, and 10K for MnCr, FeCr, and CoCr complexes, respectively. Furthermore, these compounds show a proton conductivity of 1.2×10^{-10} to 4.4×10^{-10} S cm^{-1} even under 40% relative humidity (RH) and the value increases with RH to a much higher value of $\sim 1 \times 10^{-4}$ S cm^{-1} under ~75% RH. This is the first example of a

coordination polymer exhibiting the coexistence of ferromagnetism and high proton conduction. It is also another example of multifunctional oxalate-based CPs.

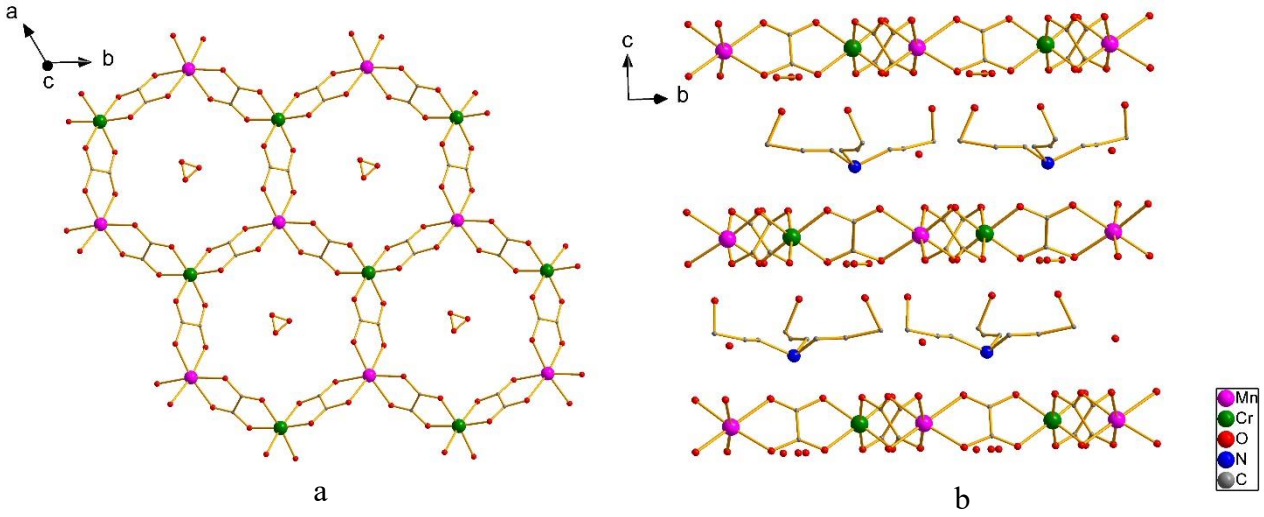

Fig. 1-11 (a) The crystal structure of $\{NH(prol)_3\}[Mn^{II}Cr^{III}(ox)_3]\cdot 2H_2O$ viewed in the *ab* plane (single layer) and (b) in *bc* plane. The ammonium cation is omitted in (a) for clarity. The figure is reproduced from reference 109.

Apart from the magnetic-related applications, there are also some other oxalate compounds that could be potentially used in ion batteries,[110,111] which makes the oxalate ligand a more fascinating element in functional materials construction. Based on those reasons, we are going to present some oxalate-based CPs in this thesis and explore the relationship between the crystal structures and the magnetic properties of these.

1-4 Metal Fluorides

In recent years, the research into metal fluorides has grown rapidly, especially into the organically-templated metal fluorides and oxyfluorides. Not only because the F^- can be used to construct some zeolites and MOFs, but it may also contribute to some interesting physical properties, such as ferroelectricity and magnetism.[112,113] One example is the simple vanadium

based oxyfluoride compounds, [H$_2$*en*][VOF$_4$(H$_2$O)][114] (*en* = ethylenediamine) and [H$_2$*pipz*][VOF$_4$(H$_2$O)][115] (*pipz* = piperazine). Both exhibit monomeric structures with isolated [VOF$_4$(H$_2$O)] octahedra, connected with protonated organic ligands through H bonds (Fig. 1-12). However, the [H$_2$*en*][VOF$_4$(H$_2$O)] crystallises in a polar space group $P2_1$ and exhibits a strong second-harmonic generation (SHG) signal while [H$_2$*pipz*][VOF$_4$(H$_2$O)] crystallises in a centrosymmetric space group $P\bar{1}$. Such H bond mediated polar ordering is quite intriguing and further work in related systems will be introduced in this thesis.

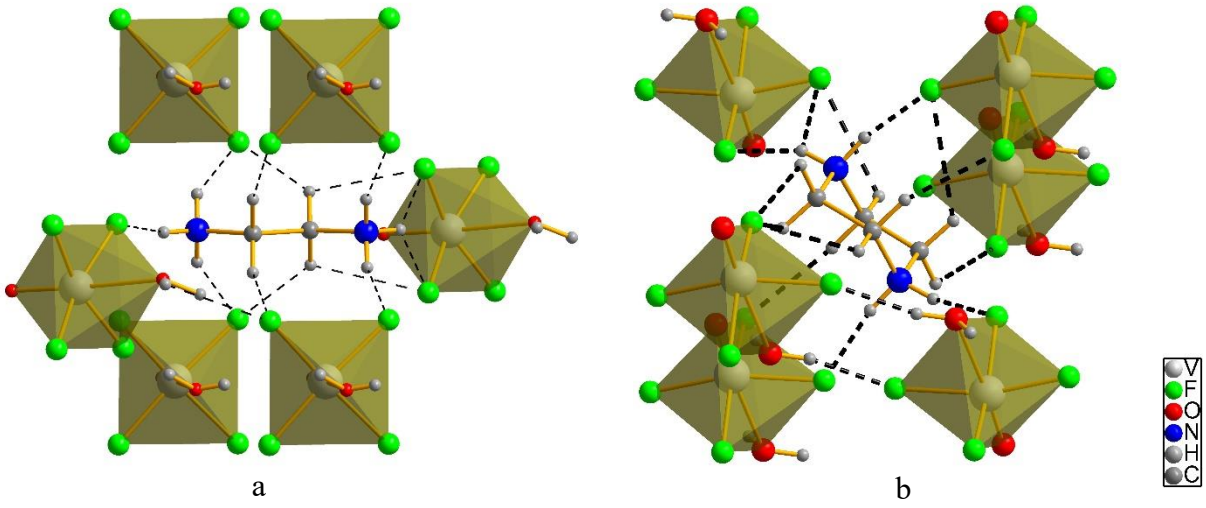

Fig. 1-12 (a) The crystal structure of [H$_2$*en*][VOF$_4$(H$_2$O)] and (b) the crystal structure of [H$_2$*pipz*][VOF$_4$(H$_2$O)]. The H bonds are shown as black dashes. The figure is reproduced from reference 114.

Another interesting vanadium oxyfluoride example is [H$_2$*pipz*]$_3$[V$_4$F$_{17}$O]·1.5H$_2$O.[112] The inorganic components of this compound are mixed valence [$V_3^{III}V^{IV}F_{17}O]_n^{6n-}$ anions (Fig. 1-13). The anions are constructed by corner- and edge- sharing [VF$_6$] and [VF$_5$O] octahedra and generate 2D [V$_{18}$F$_{18}$] rings. The free water molecules are in the vacancies of the rings and interact with nonbonding F by H bonds, and [H$_2$*pipz*]$^{2+}$ cations are located between the rings. In the 2D rings we can find some "Y shaped" tetrameric units built by four octahedra. We shaded the "Y shape" octahedral units by two colours (purple and yellow) in the 2D ring for

clarity. The magnetic measurements show a dominant antiferromagnetic interaction of the compound.

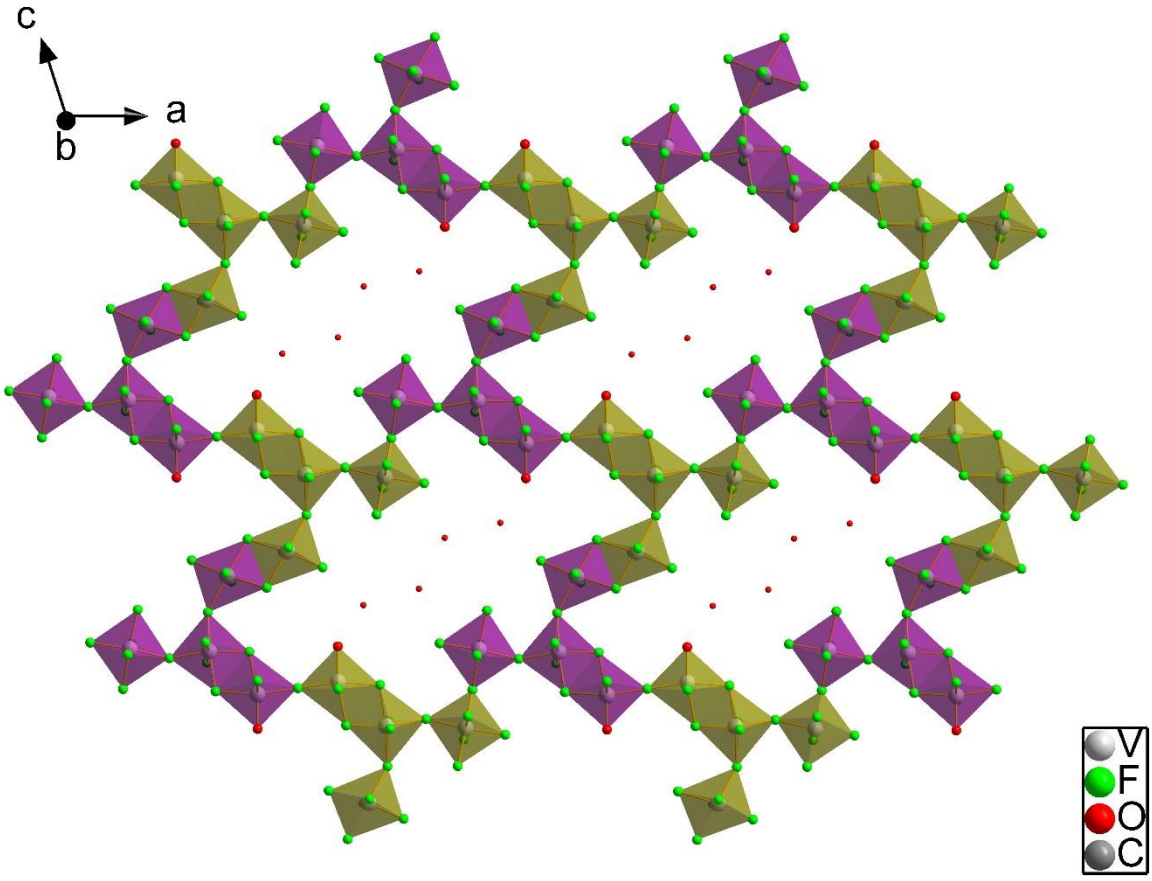

Fig. 1-13 The 2D layers with free water molecules of $[H_2pipz]_3[V_4F_{17}O]\cdot 1.5H_2O$. The octahedra with different colours show how the Y shaped units are connected. Figure drawn using data from the Cambridge Crystallographic Database (CSD), structure 719536.

1-5 Thesis Overview

The work presented in this thesis describes the use of hydrothermal and solvothermal reactions to synthesise two types of organic-inorganic hybrid coordination polymers (CP): hybrid layered fluoride perovskites and oxalate fluoride coordination polymers, as well as some metal fluoride compounds arising as by-products. Characterisation will involve crystal structure determination and physical property measurements.

In chapter 2, information regarding experimental techniques used in this work will be presented. This will include background information about crystallography, including basic theory for single crystal structure determination and powder patterns. Neutron diffraction techniques will be presented with regard to both crystal and magnetic structure determination. Finally, a brief introduction of superconducting quantum interference devices (SQUID) used in magnetic measurements will be presented.

In chapter 3, the syntheses, crystal structures and the magnetic properties of some 2D layered fluoroperovskites containing different interlayer organic cations and some by-products will be described. Firstly, the syntheses of the compounds which are constructed by hydro/solvothermal reactions. Then, the single crystal structures of the compounds will be presented, followed by the crystal structures changing with temperature changing using X-ray and neutron diffraction characterisations. Finally, the magnetic properties of selected compounds using SQUID and neutron diffraction measurements.

The syntheses, crystal structures and the magnetic properties of some oxalate ligand-based compounds will be described in chapter 4. Firstly, the syntheses and how to get the desired products, based on the same starting materials. Then, the crystal structures and magnetic characterisations will be described. Finally, the relationship between the crystal structures and magnetic properties of the compounds will be investigated and a comparison with other similar known oxalate-based compounds will also be shown.

In chapter 5, a series of organic cation-templated metal fluorides are reported. The syntheses will also be discussed firstly, followed by the effect of the H bonds on polar ordering mediations. Finally, a comparison between similar structures (synthesised and known) will be given.

The chapter 6 contains the key results and summary of the thesis and an outline for future work.

1-6 References

1. S.-H. Feng and G.-H. Li, in *Modern Inorganic Synthetic Chemistry: Second Edition*, eds. R. Xu and Y. B. T.-M. I. S. C., Elsevier, Amsterdam, 2017, ch. 4, pp. 73–104.
2. E. D. Kolb and R. A. Laudise, *J. Cryst. Growth*, 1976, **33**, 145-149.
3. J. C. Jumas, A. Goiffon, B. Capelle, A. Zarka, J. C. Doukhan, J. Schwartzel, J. Détaint and E. Philippot, *J. Cryst. Growth*, 1987, **80**, 133–148.
4. T. Sasaki, S. Ohara, T. Naka, J. Vejpravova, V. Sechovsky, M. Umetsu, S. Takami, B. Jeyadevan and T. Adschiri, *J. Supercrit. Fluids*, 2010, **53**, 92-94.
5. Y. Moreno, A. Vega, S. Ushak, R. Baggio, O. Peña, E. Le Fur, J. Y. Pivan and E. Spodine, *J. Mater. Chem*., 2003, **13**, 2381–2387.
6. Y. Kakizawa, K. Miyata, S. Funtkawa and K. Kataoka, *Adv. Mater*., 2004, **16**, 699–702.
7. X. Liu, W. Xu, S. Xu, X. Yu, Y. Deng, X. Wu, F. Liang and Q. Wu, *Inorg. Chem*., 2020, **59**, 5721–5727.
8. Y.-Y. Guo, L.-J. Yang, S. Biberger, J. A. McNulty, T. Li, K. Schötz, F. Panzer and P. Lightfoot, *Inorg. Chem*., 2020, **59**, 12858–12866.
9. G. Férey, *Chem. Mater*., 2001, **13**, 3084–3098.
10. C. N. R. Rao, S. Natarajan and R. Vaidhyanathan, *Angew. Chem. Int. Ed*., 2004, **43**, 1466–1496.
11. S. Kitagawa, R. Kitaura and S. I. Noro, *Angew. Chem. Int. Ed*., 2004, **43**, 2334–2375.
12. Y. G. Huang, F. L. Jiang and M. C. Hong, *Coord. Chem. Rev*., 2009, **253**, 2814–2834.
13. W. P. Chen, J. Singleton, L. Qin, A. Camón, L. Engelhardt, F. Luis, R. E. P. Winpenny and Y. Z. Zheng, *Nat. Commun*., 2018, **9**, 1–6.
14. L. Qin, G. J. Zhou, Y. Z. Yu, H. Nojiri, C. Schröder, R. E. P. Winpenny and Y. Z. Zheng, *J. Am. Chem. Soc*., 2017, **139**, 16405–16411.

15. S. R. Batten, N. R. Champness, X. M. Chen, J. Garcia-Martinez, S. Kitagawa, L. Öhrström, M. O'Keeffe, M. P. Suh and J. Reedijk, *Pure Appl. Chem*., 2013, **85**, 1715-1724.
16. S. L. James, *Chem. Soc. Rev*., 2003, **32**, 276-288.
17. S. Fantacci, F. De Angelis, J. Wang, S. Bernhard and A. Selloni, *J. Am. Chem. Soc*., 2004, **126**, 9715–9723.
18. H. Han, S. Zhang, H. Hou, Y. Fan and Y. Zhu, *Eur. J. Inorg. Chem*., 2006, 1594–1600.
19. Y. Ammari, N. Baaalla, E. K. Hlil and S. Abid, *Sci. Rep*., 2020, **10**, 1-12.
20. C. Dey, T. Kundu, B. P. Biswal, A. Mallick and R. Banerjee, *Acta Crystallogr. Sect. B Struct. Sci. Cryst. Eng. Mater*., 2014, **70**, 3-10.
21. E. J. Carrington, I. J. Vitórica-Yrezábal and L. Brammer, *Acta Crystallogr. Sect. B Struct. Sci. Cryst. Eng. Mater*., 2014, **70**, 404-422.
22. R. Lyndon, K. Konstas, B. P. Ladewig, P. D. Southon, P. C. J. Kepert and M. R. Hill, *Angew. Chem. Int. Ed*., 2013, **52**, 3695–3698.
23. L. Li, S. Tang, C. Wang, X. Lv, M. Jiang, H. Wu and X. Zhao, *Chem. Commun*., 2014, **50**, 2304-2307.
24. B. Liu, R. Zhao, K. Yue, J. Shi, Y. Yu and Y. Wang, *Dalton. Trans*., 2013, **42**, 13990-13996.
25. K. Leus, Y. Y. Liu and P. Van Der Voort, *Catal. Rev*., 2014, **56**, 1-56.
26. A. Aijaz and Q. Xu, *J. Phys. Chem. Lett*., 2014, **5**, 1400-1411.
27. L. L. Liu, C. X. Yu, F. J. Ma, Y. R. Li, J. J. Han, L. Lin and L. F. Ma, *Dalton. Trans*., 2015, **44**, 1636-1645.
28. D. Liu, K. Lu, C. Poon and W. Lin, *Inorg. Chem*., 2014, **53**, 1916-1924.

29. Z. F. Liu, M. F. Wu, S. H. Wang, F. K. Zheng, G. E. Wang, J. Chen, Y. Xiao, A. Q. Wu, G. C. Guo and J. S. Huang, *J. Mater. Chem. C*., 2013, **1**, 4634-4639.
30. X. Zhang, W. Wang, Z. Hu, G. Wang and K. Uvdal, *Coord. Chem. Rev*., 2015, **284**, 206-235.
31. L. E. Kreno, K. Leong, O. K. Farha, M. Allendorf, R. P. Van Duyne and J. T. Hupp, *Chem. Rev*., 2012, **112**, 1105-1125.
32. P. L. Feng, K. Leong and M. D. Allendorf, *Dalton. Trans*., 2012, **41**, 8869-8877.
33. Y. Cui, Y. Yue, G. Qian and B. Chen, *Chem. Rev*., 2012, **112**, 1126-1162.
34. X. Shen and B. Yan, *Dalton. Trans*., 2015, **44**, 1875-1881.
35. G. Nickerl, I. Senkovska and S. Kaskel, *Chem. Commun*., 2015, **51**, 2280-2282.
36. Y. Z. Zheng, Z. Zheng and X. M. Chen, *Coord. Chem. Rev*., 2014, **258-259**, 1-15.
37. D. I. Alexandropoulos, L. Cunha-Silva, A. Escuer and T. C. Stamatatos, *Chem. - A Eur. J*., 2014, **20**, 13860-13864**.**
38. W. H. Yan, S. S. Bao, J. Huang, M. Ren, X. L. Sheng, Z. S. Cai, C. S. Lu, Q. J. Meng and L. M. Zheng, *Dalton. Trans*., 2013, **42**, 8241-8248.
39. N. Stock and S. Biswas, *Chem. Rev*., 2012, **112**, 933–969.
40. P. Kanoo, R. Haldar, S. T. Cyriac and T. K. Maji, *Chem. Commun*., 2011, **47**, 11038-11040.
41. Q. Chen, F. Jiang, L. Chen, M. Yang and M. Hong, *Chem. - A Eur. J*., 2012, **18**, 9117-9124.
42. D. Liu, J. P. Lang and B. F. Abrahams, *Chem. Commun*., 2013, **49**, 2682-2684.
43. Y. C. Pang, X. Hou, L. Qin, C. Wu, W. Xue, Y. Z. Zheng, Z. Zheng and X. M. Chen, *Chem. Commun*., 2014, **50**, 2910-2912.

44. J. W. Anthony, R. A. Bideaux, K. W. Bladh and M. C. Nichols., *Handbook of Mineralogy*, Mineralogical Society of America, Chantilly, VA 20151-1110, USA, 2003.
45. C. J. Bartel, C. Sutton, B. R. Goldsmith, R. Ouyang, C. B. Musgrave, L. M. Ghiringhelli and M. Scheffler, *Sci. Adv.*, 2019, **5 (2)**, eaav0693.
46. V. M. Goldschmidt, *Naturwissenschaften*, 1926, **14**, 477-485.
47. G. H. Jonker and J. H. Van Santen, *Physica*, 1950, **16**, 337-349.
48. G. Blasse, *J. Phys. Chem. Solids*, 1950, **26**, 1969-1971.
49. D. Serrate, J. M. De Teresa and M. R. Ibarra, *J. Phys.: Condens. Matter*, 2007, **19**, 023201.
50. R. E. Cohen, *Nature*, 1992, **358**, 136–138.
51. Z. Fan, J. Xiao, K. Sun, L. Chen, Y. Hu, J. Ouyang, K. P. Ong, K. Zeng and J. Wang, *J. Phys. Chem. Lett.*, 2015, **6**, 1155–1161.
52. H. Röhm, T. Leonhard, A. D. Schulz, S. Wagner, M. J. Hoffmann and A. Colsmann, *Adv. Mater.*, 2019, **31**, 1806661.
53. C. C. Homes, T. Vogt, S. M. Shapiro, S. Wakimoto and A. P. Ramirez, *Science*, 2001, **293**, 673-676.
54. L. Wu, Y. Zhu, S. Park, S. Shapiro, G. Shirane and J. Tafto, *Phys. Rev. B - Condens. Matter Mater. Phys.*, 2005, **71**, 014118.
55. A. Miyata, A. Mitioglu, P. Plochocka, O. Portugall, J. T. W. Wang, S. D. Stranks, H. J. Snaith and R. J. Nicholas, *Nat. Phys.*, 2015, **11**, 582–587.
56. M. E. Ziffer, J. C. Mohammed and D. S. Ginger, *ACS Photonics*, 2016, **3**, 1060–1068.
57. Z. Yang, A. Surrente, K. Galkowski, N. Bruyant, D. K. Maude, A. A. Haghighirad, H. J. Snaith, P. Plochocka and R. J. Nicholas, *J. Phys. Chem. Lett.*, 2017, **8**, 1851–1855.
58. Z. Fan, K. Sun and J. Wang, *J. Mater. Chem. A*, 2015, **3**, 18809–18828.

59. N. A. Benedek, J. M. Rondinelli, H. Djani, P. Ghosez and P. Lightfoot, *Dalton. Trans*., 2015, **44**, 10543–10558.

60. F. Lichtenberg, A. Herrnberger and K. Wiedenmann, *Prog. Solid State Chem*., 2008, **36**, 253-387.

61. I. A. Rodionov and I. A. Zvereva, *Russ. Chem. Rev*., 2016, **85**, 248–279.

62. S. N. Ruddlesden and P. Popper, *Acta Crystallogr*., 1957, **10**, 538-539.

63. S. N. Ruddlesden and P. Popper, *Acta Crystallogr*., 1958, **11**, 54-55.

64. M. Dion, M. Ganne and M. Tournoux, *Mater. Res. Bull*., 1981, **16**, 1429-1435.

65. A. J. Jacobson, J. T. Lewandowski and J. W. Johnson, *J. Less-Common Met*., 1986, **116**, 137-146.

66. A. J. Jacobson, J. W. Johnson and J. T. Lewandowski, *Mater. Res. Bull*., 1987, **22**, 45-51.

67. B. Aurivillius, *Ark. Kemi*., 1949, **1**, 463-480.

68. Y. Y. Guo, A. S. Gibbs, J. M. Perez-Mato and P. Lightfoot, *IUCrJ*, 2019, **6**, 438-446.

69. D. Weber, *Zeitschrift fur Naturforsch. - Sect. B J. Chem. Sci*., 1978, **33**, 1443-1445.

70. A. Kojima, K. Teshima, Y. Shirai and T. Miyasaka, *J. Am. Chem. Soc*., 2009, **131**, 6050-6051.

71. N. Kitazawa, *Jpn. J. Appl. Phys*., 1996, **35**, 6202-6207.

72. D. B. Mitzi, D. R. Medeiros and P. R. L. Malenfant, *Inorg. Chem*., 2002, **41**, 2134-2145.

73. K. Tichý, J. Beneš, W. Hälg and H. Arend, *Acta Crystallogr. Sect. B Struct. Crystallogr. Cryst. Chem*., 1978, **34**, 2970–2981.

74. D. Solis-Ibarra and H. I. Karunadasa, *Angew. Chem. Int. Ed*., 2014, **136**, 1718-1721.

75. N. Mercier, N. Louvain and W. Bi, *CrystEngComm*, 2009, **11**, 720–734.

76. A. Lemmerer and D. G. Billing, *CrystEngComm*, 2010, **12**, 1290–1301.

77. B. Tieke and G. Chapuis, *Mol. Cryst. Liq. Cryst*., 1986, **137**, 101-116.

78. X. Liu, S. Chen, J. Hauser, V. Laukhin, S. Decurtins, U. Aschauer and S. X. Liu, *Cryst. Growth Des*., 2016, **16**, 5230–5237.

79. B. Vargas, R. Torres-Cadena, J. Rodríguez-Hernández, M. Gembicky, H. Xie, J. Jiménez-Mier, Y. S. Liu, E. Menéndez-Proupin, K. R. Dunbar, N. Lopez, P. Olalde-Velasco and D. Solis-Ibarra, *Chem. Mater*., 2018, **30**, 5315-5321.

80. P. Vishnoi, J. L. Zuo, T. A. Strom, G. Wu, S. D. Wilson, R. Seshadri and A. K. Cheetham, *Angew. Chem. Int. Ed.*, 2020, **132**, 9059–9066.

81. L. Theofylaktos, K. O. Kosmatos, E. Giannakaki, H. Kourti, D. Deligiannis, M. Konstantakou and T. Stergiopoulos, *Dalton. Trans*., 2019, **48**, 9516–9537.

82. R. Gegevičius, M. Franckevičius, J. Chmeliov, W. Tress and V. Gulbinas, *J. Phys. Chem. Lett*., 2019, **10**, 1779–1783.

83. Z. Zhang, X. Li, X. Xia, Z. Wang, Z. Huang, B. Lei and Y. Gao, *J. Phys. Chem. Lett*., 2017, **8**, 4300–4307.

84. M. Wang, P. Zeng, S. Bai, J. Gu, F. Li, Z. Yang and M. Liu, *Sol. RRL*, 2018, **2**, 1800217.

85. C. Zuo and L. Ding, *Angew. Chem. Int. Ed*., 2017, **56**, 6528-6532.

86. D. B. Mitzi, *Inorg. Chem*., 2000, **39**, 6107-6113.

87. F. A. Mautner, R. Cotés, L. Lezama and T. Rojo, *Angew. Chem. Int. Ed*., 1996, **35**, 78-80.

88. M. Daub and H. Hillebrecht, *Angew. Chem. Int. Ed*., 2015, **54**, 11016-11017.

89. D. Umeyama, Y. Lin and H. I. Karunadasa, *Chem. Mater*., 2016, **28**, 3241-3244.

90. T. Li, R. Clulow, A. J. Bradford, S. L. Lee, A. M. Z. Slawin and P. Lightfoot, *Dalton. Trans*., 2019, **48**, 4784–4787.

91. Y. I. Dolzhenko, T. Inabe and Y. Maruyama, *Bull. Chem. Soc. Jpn*., 1986, **59**, 563-567.

92. D. Liang, Y. Peng, Y. Fu, M. J. Shearer, J. Zhang, J. Zhai, Y. Zhang, R. J. Hamers, T. L. Andrew and S. Jin, *ACS Nano*, 2016, **10**, 6897–6904.

93. O. Nazarenko, M. R. Kotyrba, M. Wörle, E. Cuervo-Reyes, S. Yakunin and M. V. Kovalenko, *Inorg. Chem*., 2017, **56**, 11552–11564.

94. W. S. Yang, B. W. Park, E. H. Jung, N. J. Jeon, Y. C. Kim, D. U. Lee, S. S. Shin, J. Seo, E. K. Kim, J. H. Noh and S. Il Seok, *Science*, 2017, **356**, 1376–1379.

95. H. Tsai, W. Nie, J. C. Blancon, C. C. Stoumpos, C. M. M. Soe, J. Yoo, J. Crochet, S. Tretiak, J. Even, A. Sadhanala, G. Azzellino, R. Brenes, P. M. Ajayan, V. Bulović, S. D. Stranks, R. H. Friend, M. G. Kanatzidis and A. D. Mohite, *Adv. Mater*., 2018, **30**, 1704217.

96. C. C. Stoumpos, D. H. Cao, D. J. Clark, J. Young, J. M. Rondinelli, J. I. Jang, J. T. Hupp and M. G. Kanatzidis, *Chem. Mater*., 2016, **28**, 2852–2867.

97. X. Li, J. Hoffman, W. Ke, M. Chen, H. Tsai, W. Nie, A. D. Mohite, M. Kepenekian, C. Katan, J. Even, M. R. Wasielewski, C. C. Stoumpos and M. G. Kanatzidis, *J. Am. Chem. Soc*., 2018, **140**, 12226–12238.

98. R. D. Willett, O. L. Liles and C. Michelson, *Inorg. Chem*., 1967, **6**, 1885-1889.

99. L. J. De Jongh, A. C. Botterman, F. R. De Boer and A. R. Miedema, *J. Appl. Phys*., 1969, **40**, 1363-1365.

100. L. J. De Jongh and A. R. Miedema, *Adv. Phys*., 1974, **23**, 1-260.

101. S. R. Desjardins, K. W. Penfield, S. L. Cohen, E. I. Solomon and R. L. Musselman, *J. Am. Chem. Soc*., 1983, **105**, 4590–4603.

102. H. Arend and H. Gränicher, *Ferroelectrics*, 1976, **13**, 537–539.

103. H. Arend, H. Von Känel and P. Wachter, *Phys. Status Solidi B*, 1976, **74**, 151-157.

104. R. Kind, S. Plesko, P. Günter, J. Roos and J. Fousek, *Phys. Rev. B: Condens. Matter Mater. Phys*., 1981, **23**, 5301-5315.

105. H. Cui, Z. Wang, K. Takahashi, Y. Okano, H. Kobayashi and A. Kobayashi, *J. Am. Chem. Soc*., 2006, **128**, 15074–15075.

106. W. Yao, L. Clark, M. Xia, T. Li, S. L. Lee and P. Lightfoot, *Chem. Mater*., 2017, **29**, 6616–6620.

107. K. Tustain, L. Farrar, W. Yao, P. Lightfoot, I. Da Silva, M. T. F. Telling and L. Clark, *Inorg. Chem*., 2019, **58**, 11971–11977.

108. K. S. Min and J. S. Miller, *Dalton Trans*., 2006, 2463–2467.

109. H. Ōkawa, A. Shigematsu, M. Sadakiyo, T. Miyagawa, K. Yoneda, M. Ohba and H. Kitagawa, *J. Am. Chem. Soc*., 2009, **131**, 13516-13522.

110. W. Yao, M. T. Sougrati, K. Hoang, J. Hui, P. Lightfoot and A. R. Armstrong, *Chem. Mater*., 2017, **29**, 9095–9101.

111. W. Yao, A. R. Armstrong, X. Zhou, M. T. Sougrati, P. Kidkhunthod, S. Tunmee, C. Sun, S. Sattayaporn, P. Lightfoot, B. Ji, C. Jiang, N. Wu, Y. Tang and H. M. Cheng, *Nat. Commun*., 2019, **10**, 1–9.

112. P. DeBurgomaster, W. Ouellette, H. Liu, C. J. O'Connor, G. T. Yee and J. Zubieta, *J. Inorg. Chim. Acta*, 2010, **363**, 1102–1113.

113. J. F. Scott and R. Blinc, *J. Phys. Condens. Matter*, 2011, **23**, 113202.

114. N. F. Stephens, M. Buck and P. Lightfoot, *J. Mater. Chem*., 2005, **15**, 4298–4300.

115. D. W. Aldous, N. F. Stephens and P. Lightfoot, *Dalton. Trans*., 2007, 4207–4213.

Chapter 2 Theory and Experimental Techniques

2-1 Synthesis

The majority of products presented in this thesis were synthesised by hydro/solvothermal reactions. The containers used for these reactions were 15 mL, 30 mL and 50 mL Teflon-lined stainless-steel autoclaves with solvent filling less than 80%. The filled and sealed autoclaves were placed into a preheated oven and kept at a constant temperature (100-190 °C) for 1-7 days' reaction. The solvents used were deionised water (H_2O), methanol (MeOH), ethanol (EtOH), acetone (C_3H_6O), acetonitrile (CH_3CN), dimethyl sulfoxide (DMSO) toluene and ethylene glycol (EG) or any combination of two of these.

The layered solution method also been used for synthesis in some instances for which hydro/solvothermal synthesis produced poor quality single crystals. Crystals were grown at the interface of two immiscible solvents with different solubilities. Products based on this method are often pure, but with low yield, and it also takes a long time to get well crystallised structures.

2-2 Crystallography

Crystallography is the study and determination of the arrangement of atoms in crystalline solids. It can also be regarded as an essential tool in crystal synthesis and characterisation. The object of crystallography, the crystal, consists of an array of atoms (or single atom) that repeats periodically in three dimensions. In a crystal structure, the smallest repeating unit having the full symmetry of the crystal is called the unit cell. The unit cell is described by six cell parameters: three for the unit lengths in different dimensions (a, b, c) and three for the angles between them (α, β, γ). Based on different unit lengths and the angles, there are seven corresponding crystal systems: triclinic, monoclinic, orthorhombic, tetragonal, cubic, trigonal and hexagonal (Fig. 2-1 and Table 2-1).

2-2-1 Crystallographic Space Groups

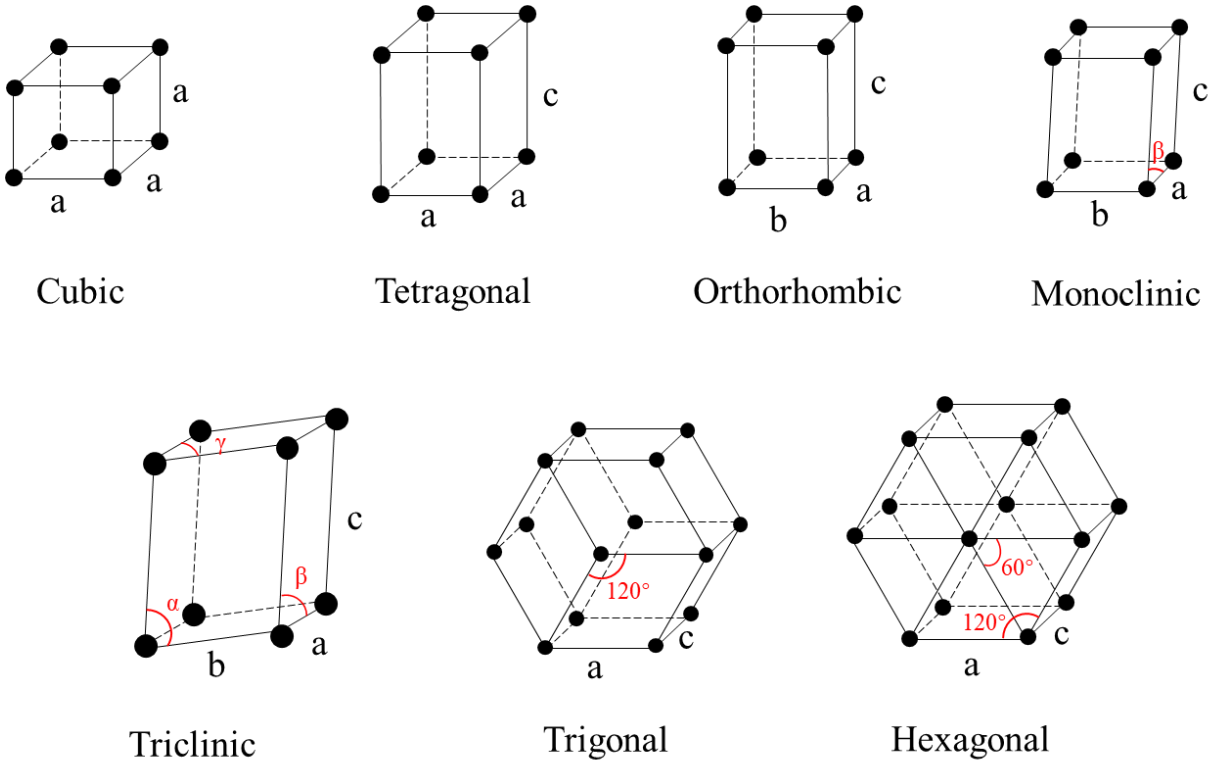

Fig. 2-1 The seven crystal systems.

If five extra symmetry centres: primitive (*P*), body centred (*I*), face centred (*F*), side centred (*C*) and rhombohedral (*R*) are combined with the seven crystal systems, fourteen Bravais lattices are obtained (Table 2-1 and Fig. 2-2).

Point group is a geometry concept, which indicates a group of geometric symmetries (*e.g.* rotation axes, mirrors, etc.) that keep at least one point fixed. In crystallography, there are in total 32 crystallographic point groups. However, the point groups do not include translation symmetry. With the introduction of more translational symmetry elements (lattice centring, screw axes and glide planes), the 230 space groups are constructed. The space groups are the combination of point groups with Bravais lattices and other translational symmetry, which can be used to describe the symmetry of any conventional crystal structure. All the information about the 230 space groups is given in the International Tables for Crystallography.[1]

Table 2-1 The information of seven crystal systems.

Crystal System	Bravais Lattice Types	Unit Cell	Required Symmetry
Triclinic	*P*	$a \neq b \neq c$ $\alpha \neq \beta \neq \gamma \neq 90^\circ$	None
Monoclinic	*P*, *C*	$a \neq b \neq c$ $\alpha = \gamma = 90^\circ\ \beta \neq 90^\circ$	One twofold axis or one mirror plane
Orthorhombic	*P*, *C*, *I*, *F*	$a \neq b \neq c$ $\alpha = \beta = \gamma = 90^\circ$	Three twofold axes or mirror planes
Tetragonal	*P*, *I*	$a = b \neq c$ $\alpha = \beta = \gamma = 90^\circ$	One fourfold axis
Trigonal	*P*	$a = b \neq c$ $\alpha = \beta = 90^\circ\ \gamma = 120^\circ$	One threefold axis
(Rhombohedral)	*R*	$a = b = c$ $\alpha = \beta = \gamma \neq 90^\circ$	One threefold axis
Hexagonal	*P*	$a = b \neq c$ $\alpha = \beta = 90^\circ\ \gamma = 120^\circ$	One sixfold axis
Cubic	*P*, *I*, *F*	$a = b = c$ $\alpha = \beta = \gamma = 90^\circ$	Three fourfold axes

The crystal systems and lattice systems are very similar, but still have some differences. For example, the hexagonal family is the combination of hexagonal and trigonal cases in crystal system or the hexagonal and rhombohedral cases in Bravais lattice. The unit cell rules for trigonal and rhombohedral are different. In addition, the rhombohedral case in Bravais lattice could be regarded as a subdivision of the trigonal case in crystal system. There are 25 space groups in trigonal, 7 of them belong to the rhombohedral Bravais lattice and the other 18 belong to the hexagonal Bravais lattice. For example, the space groups of α-quartz are $P3_121$ or $P3_221$ (depending on the chiral state), both belong to trigonal but not rhombohedral.

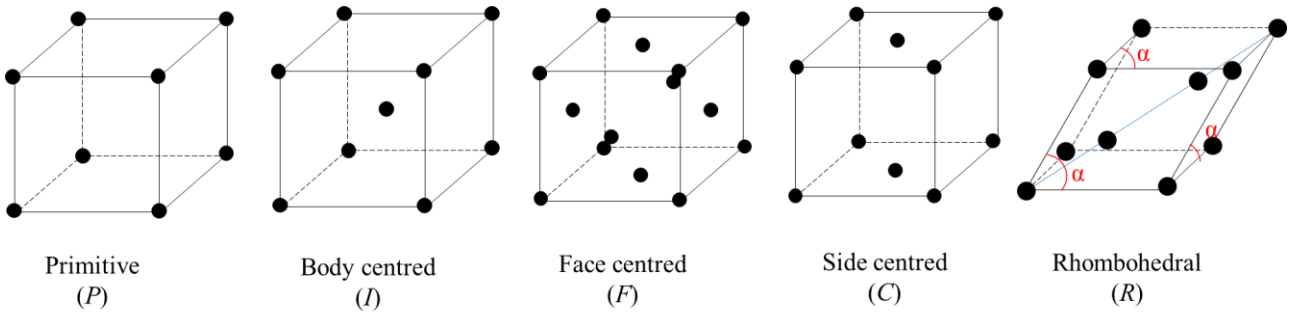

Fig. 2-2 The five symmetry centres in Bravais Lattices.

Many crystalline materials have phase transition behaviours with the changing of temperature, pressure, or other ambient environments, accompanied by the changing of cell parameters, space groups or even crystal systems. Changing the space group will also often cause a change in the intrinsic physical properties of the crystalline materials. For example, changing the space group breaks the symmetry of the structure and hence may cause a change in the magnetic properties.[2] If the space group is changed from polar to nonpolar, there would potentially be a ferroelectric to paraelectric transition.[3]

For a known crystalline material, all the crystallographic information can be found in a crystallographic information framework (CIF) file, a standard file format in crystallography developed by the international union of crystallography (IUCr).[4]

2-2-2 Magnetic Space Groups

For magnetic crystalline materials, there is an extension to the space group; the magnetic space group. This is also known as the Shubnikov group, which is used to classify the symmetries of a crystal both in terms of atomic structure and electron spins. In the magnetic space group, a new symmetry operation- "time reversal" is involved, which enlarges the number of possible groups from 230 to 1651.[5] The time reversal is a non-geometric symmetry transformation, which will only reverse the magnetic moment without affecting the geometric structure of the crystal. In the magnetic space groups, the lattice points are "painted" into black or white to represent the up and down spin directions.[6] Thus, the magnetic space group can be divided into three categories: the 230 colourless groups contain only crystallographic geometry

spatial symmetry, another 230 corresponding invariant antisymmetric grey groups, and the rest 1191 black-white colourful groups. When the magnetic phase and crystallographic phase are commensurate, the magnetic groups can be used to describe the magnetic structure. However, for the incommensurate ordering structures, such as helical spin, two- or three-dimensional irreducible representations, the simple magnetic groups are not applicable and the magnetic superspace groups should be used instead.[7] The CIF file containing magnetic space group information is called mCIF.

2-3 X-ray Diffraction

2-3-1 Introduction

X-rays are a very useful tool to characterise crystal structures. The X-rays are high energy (100 eV-200 keV) electromagnetic radiation. In general, we can observe two types of X-rays, the characteristic X-rays and the Brehmsstrahlung X-rays (also known as the continuum part). The standard X-ray source was normally created in a glass or ceramic vacuum X-ray tube, in which some electrons were released by passing an electrical current through a metal filament. The electrons were accelerated under a high voltage (40 kV-60 kV) environment, collided with a metal target and X-rays emitted.

The characteristic X-rays were generated by accelerated electrons knocking on the target metal, with the orbital electrons in the inner 1s (K shell) ejected, forming a vacancy. Then the orbital electrons in neighbouring 2p (L shell) and 3p or 3d shells (M shell) will "drop down" and fill the vacancy. At the same time, the filling electrons lose the energy corresponding to the gaps between shells and emit an X-ray with that fixed energy. The X-rays based on L-K, M-K and M-L transitions have different wavelengths called Kα, Kβ and Lα respectively (Fig. 2-3 (a)). Kα is composed by Kα1 and Kα2 due to the different spin states of the electrons. (Fig. 2-3 (b)) The wavelengths of Kα1 and Kα2 are very close and the intensities

of Kα2 are nearly half of Kα1 for all elements.[8] Thus, the combined Kα are often used in X-ray diffractometry with the wavelength as the average of the Kα1 and Kα2 wavelengths. Comparing with Kα, the intensities of Kβ are much weaker; as for the Lα emitting, the X-ray energies are around or even below the limit of detection for most detectors.

Except for the above effective collisions, there are also some other interactions between the accelerated electrons and the metal target. For example, some electrons on the metal target are knocked out during the collision and causing minor or major energy changes in the same time. Those unwanted X-rays are called Brehmsstrahlung X-rays or continuous X-ray,[9] which are shown in the continuous curve of the (Fig. 2-3 (b)).

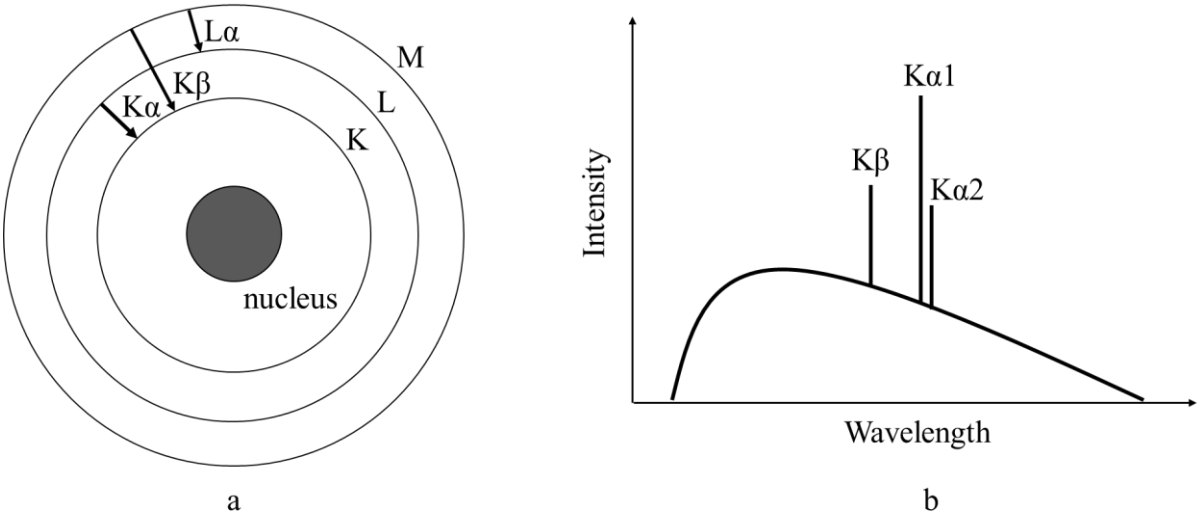

Fig. 2-3 The scheme of the generation of X-rays, (a) is the model of one atom (the M shell comprises 3s, 3p and 3d shells); (b) is the plot of the intensity and the wavelength of different X-rays.

So far, the most common metal targets are made by copper and molybdenum, and they provide X-rays with wavelengths of 1.54185 (1.54059 for monochromated Kα1) and 0.71073 Å, respectively, which is similar with the spacings between the atoms in crystalline materials.[10] So, once a monochromatic X-ray beam is applied to the crystalline materials, there will be some interference effects between the planes of atoms and X-rays. More exactly, the scattering

interaction occurs between the X-rays and the electron density of the atoms. That is the reason why X-ray diffraction is a common method to determine the crystal structures.

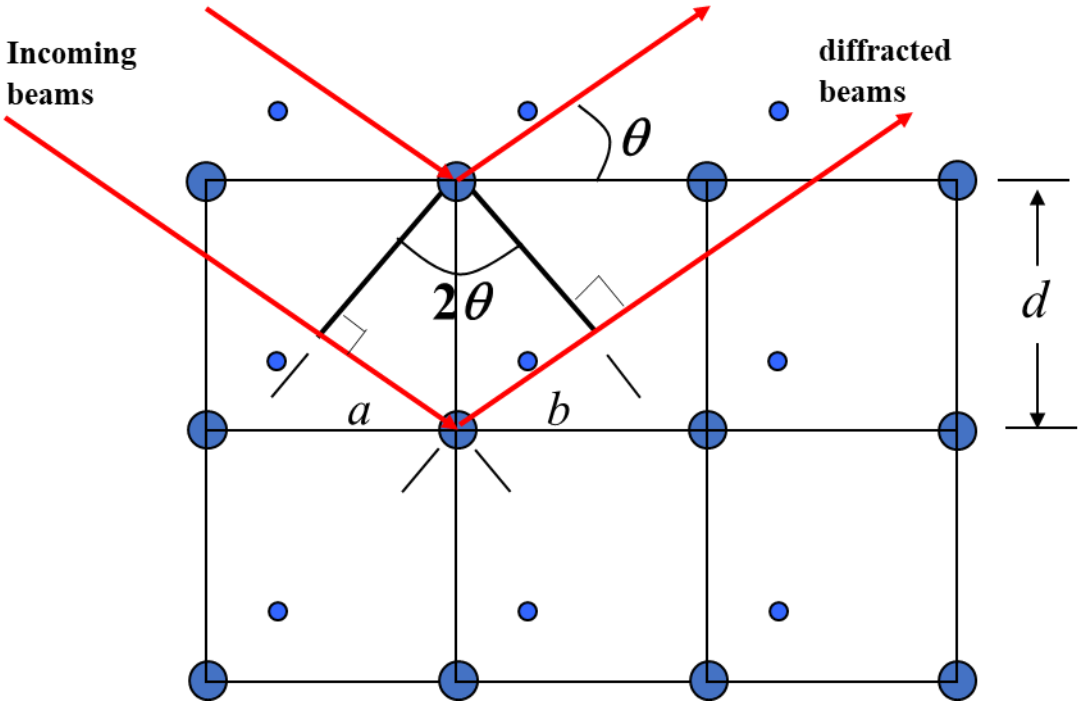

Fig. 2-4 X-ray scattering by the planes of atoms.

2-3-2 Bragg's Law

In crystalline materials, all the atoms are ordered and aligned periodically. This periodic nature of the internal structure may induce a three-dimensional grid with the unit cell as the basic repeating unit. In the grid, many groups of the planes in various orientations with an inter-planar spacing (*d*) could be found.

Bragg's law is a formula which can be used to describe the interaction between the electrons of the crystalline atoms and X-ray diffraction. In Bragg's law, these planes can be considered as semi-transparent mirrors, which will reflect the incident X-rays (Fig. 2-4).[11] The planes are aligned periodically, which makes the *d* value constant for a particular set of planes. In Fig. 2-4 three planes and two waves are shown. The second wave has a longer path than the first wave during the entire reflection process, with a difference value ($a + b$). The two waves

will undergo constructive interference, so the path difference must be equal to an integer number (n) of the X-ray wavelength (λ). Thus, we can deduce equation (2−1)

$$a + b = n\lambda \qquad (2-1)$$

Plus, the geometric relationships between a, b and d can be expressed by equation (2−2) and (2−3)

$$a = b = d\sin\theta \qquad (2-2)$$

$$a + b = 2d\sin\theta \qquad (2-3)$$

Then, Bragg's law, also known as the Bragg equation (equation (2−4)), will be reached by the combination of equation (2−1) and (2−3)

$$n\lambda = 2d\sin\theta \qquad (2-4)$$

When the Bragg equation is satisfied, diffraction will take place. In a three-dimensional crystal lattice, the diffraction can be labelled by three indices *hkl*.

2-3-3 Single Crystal X-ray Diffraction

X-ray diffraction is a very important method to analyse single crystal structures. The basic idea is based on the Bragg equation, as λ and θ are known, scattering from different d-spacings are detected by a two-dimensional X-ray detector, showing as spots in the images (Fig. 2-5). Those spots are the Fourier transformation of the electron density distribution. When enough valid images are collected, the three-dimensional diffraction of the single crystal can be mapped. The structure can then be solved from this data with the constituent chemical

element information, and the CIF file of the structure will be generated based on the refined structure model. The Fourier transformation is a tool to connect the arrangement of the atoms in the unit cell and the intensities of the X-ray diffraction pattern. The diffraction pattern is the Fourier transform of the electron density and can be expressed in mathematics:

$$F(hkl) = \int_{cell} \rho(xyz) \cdot exp[2\pi i(hx + ky + lz)]\,\mathrm{d}V \qquad (2-5)$$

Here, the $F(hkl)$ is the amplitude and phase structure factor of the reflection with indices h, k and l; $\rho(xyz)$ represents the electron density distribution of a specific point in the unit cell; $exp[2\pi i(hx+ky+lz)]$ is the complex number of the $\rho(xyz)$; V is the volume of the unit cell. From the above equation, the structure factor of any single atom could be deduced from the coordination site of the atom and vice versa, the electron density distribution could be expressed through the structure factor from the reverse Fourier transformation, in mathematics:

$$\rho(xyz) = \frac{1}{V} \sum_{h,k,l} |F(hkl)| \cdot \exp[i\varphi(hkl)] \cdot \exp[-2\pi i(hx + ky + lz)] \qquad (2-6)$$

$$I(hkl) \propto |F(hkl)|^2 \qquad (2-7)$$

In the equation, all the other elements have corresponding part in the Fourier transformation equation (2−5). The $F(hkl)$ in (2−5) is the combination structure factor of amplitude $|F(hkl)|$ and phases $\varphi(hkl)$ in (2−6). The correct amplitude structure factor $|F(hkl)|$ could be deduced from the intensities of the diffraction peaks I by (2−7); however, the intrinsic phases $\varphi(hkl)$ of the reflection are not measurable from the diffraction experiment. This means even when the diffraction pattern has been measured, the image of the electron density cannot be calculated simply from the reverse Fourier transformation, which is also known as the

"phase problem". To solve the phase problem, the Patterson synthesis and the direct methods are used.

In Patterson synthesis, the squared observed diffracted beam amplitudes $|F_O|^2$ is used with all the phases set (φ) equal to zero and the mathematical expression is (2−8). The Patterson method shows the electron density peaks and the shapes of electron density peaks are very similar with the Patterson peaks, but are nearly half as broad. Furthermore, all the atoms in Patterson synthesis are in pairs, which will generate n^2 position vectors in a unit cell containing n atoms. In those vectors, the self-peak of each atom is the strongest. However, there are n^2-n other peaks, which builds many broad overlap peaks but not all of these can be resolved in the Patterson map. Therefore, the Patterson mapping is normally used to determine the structures with heavy atoms, those which generate significant peaks due to the vectors between them.

$$P(xyz) = \frac{1}{V}\sum_{h,k,l}|F_O(hkl)|^2 \cdot \exp[-2\pi i(hx + ky + lz)] \qquad (2-8)$$

The direct method is the usual method for most software to solve single crystal structures. It is a general name for several methods which are trying to directly find the phase information of the reflection. Even though the phase factor is unknown, it is contained in the electron density distribution. As the electron density must be positive, so too must the sum of correct set of phases, which constrains the relationships between the phase factors. The direct method is based on this, and it can be regarded as a trial-and-error method. The basic idea is to firstly find the most important reflections (those which contribute most to the Fourier transform), then calculate the probable relationships of their phase factors and try different possible phase factors to fit the probable relationships and select the most satisfactory phase factors. The most promising combinations are finally selected to generate the structure factors and to be used to map the electron density distribution through the Fourier transform.

After the phase problem is solved, the partial structure is obtained, which is also known as the initial model structure. To reveal the entire structure, the least-squares analysis is applied. If the model structure is the correct one, we can calculate the theoretical diffraction pattern and get the structure factor F_C through the Fourier transform. Combining with the observed amplitude factor F_O (phase factor is unknown), we can define a residual factor called *R* factor (2−9) to evaluate how similar the F_C and F_O are. For a good quality single crystal which is well measured and the model is correct, the crystal structure will be obtained and the final *R*1 value should be around 0.02-0.07.

$$R1 = \frac{\sum ||F_O| - |F_C||}{\sum |F_O|} \qquad (2-9)$$

Another residual factor *wR*2 (2−10) is deduced from F^2, which contains only the information of amplitude factors and ignores the phase factors. In addition, the F^2 is multiplied by their weighting factors, *w*, based on their standard uncertainties (s.u.s). For the same single crystal in the same model, the value of *wR*2 is normally higher than *R*1.

$$wR2 = \sqrt{\frac{\sum w(F_O^2 - F_C^2)}{\sum w\,(F_O^2)^2}} \qquad (2-10)$$

Using the value of *R*1 and *wR*2 as the guide, the process of finding the correct crystal structure from the single crystal X-ray diffraction is called single crystal refinement. After the *R*1 and *wR*2 are reduced in a resonable value, a CIF file of the refined structure can be generated and sent to checkCIF[12] for structure examination. CheckCIF is a service provided by the IUCr to evaluate if a CIF is internally consistent and also if the data fits the defined standards. In total there are four different alert levels (A, B, C and G) in the data validation report: level A and B alerts are most likely serious and potentially serious problems respectively; level C alerts require checking to make sure they are not caused by omission or oversight; level G alerts are

related to general information, also needed to be checked to make sure they are not something unexpected.

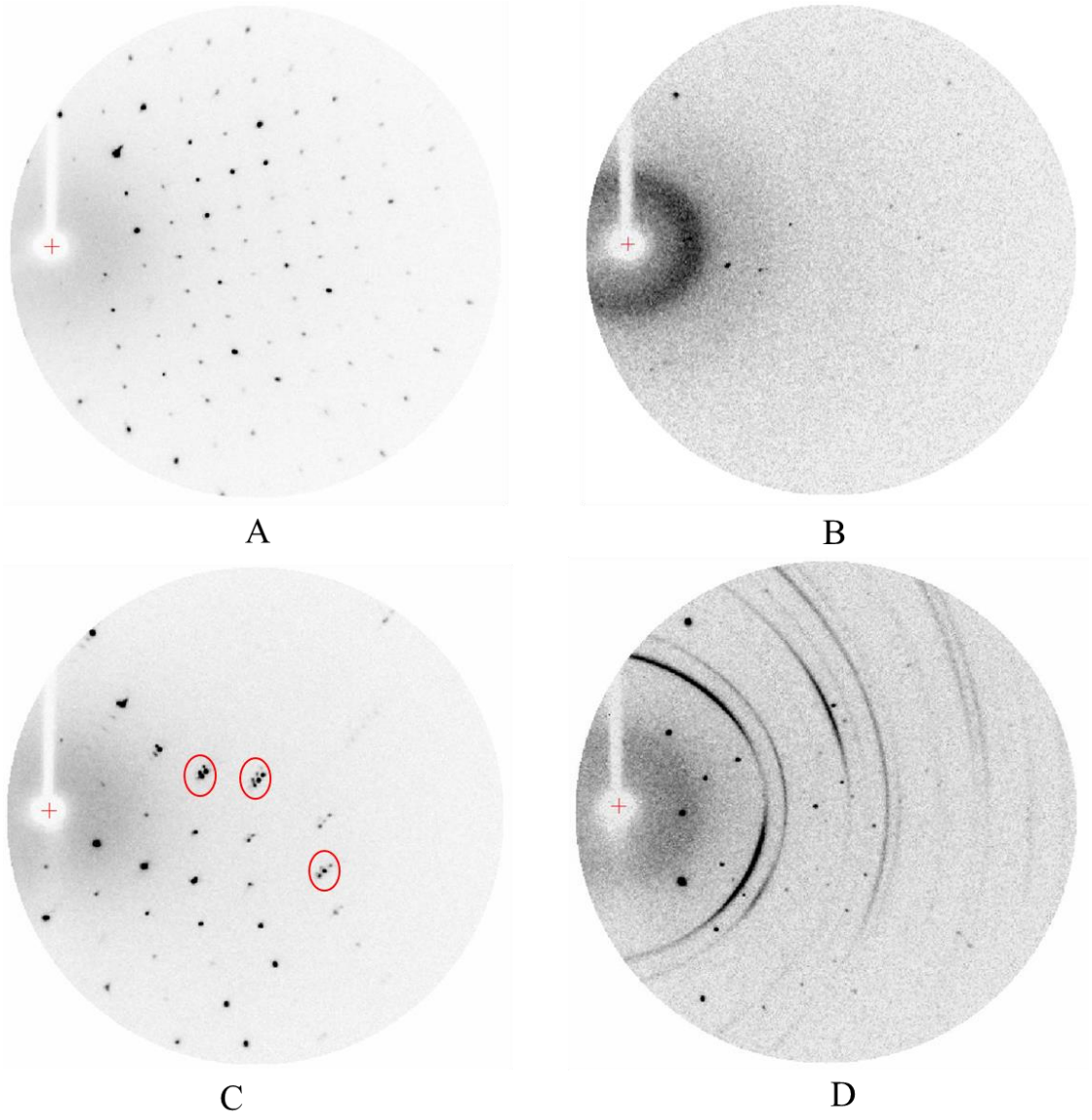

Fig. 2-5 Some examples of single crystal X-ray diffraction patterns, in which (a) is good diffraction, (b) is poor diffraction, (c) is the diffraction for a twin crystal (red circles) and (d) is the diffraction for a partly powderised single crystal.

In fact, the practical refinement is more complex than the theory. For example, some single crystals have strongly disordered atoms or molecular groups, some crystals are of poor quality, some crystals are grown in twin style, some crystals are partly powderised (Fig. 2-5)

etc. To obtain the correct crystal structures under such circumstances, some specific mathematical methods and some constraints are needed during the refinement. In addition, the signals of hydrogen atoms are normally weak in X-ray diffraction because of the low scattering power and lack of core electrons of hydrogens. If the data quality is good enough, the hydrogens could be directly located from Fourier difference maps and refined, with the consideration of chemical environment and geometric constraints. If the data quality is less good, the hydrogens are normally placed in calculated positions with a distance restraint, also based on the geometric considerations of the crystal structures.

All the crystal structures of the compounds described in this thesis were obtained by single crystal X-ray diffraction. Transparent crystallites of the samples were selected under a microscope and mounted on nylon loops coated by inert crystal oil. Diffraction data at 173 K and 298 K were collected on a Rigaku SCX Mini diffractometer using a sealed tube X-ray source and Mo Kα radiation, with a charge-coupled device (CCD) detector; the data at 93 K were collected by a Rigaku FRX diffractometer with a rotating anode source and Mo Kα radiation, with a hybrid photon counting (HPC) detector. Rigaku CrystalClear-SM Expert 2.1 b45 was employed to index and process the data. Structures were then solved by Patterson or direct methods and refined using SHELXL-2018[13] incorporated in the WinGX program.[15] Platon was used to check space groups and deal with crystallographic twinning problems of some structures.[14] All the hydrogens on carbons were added by theoretical riding models. For the hydrogens on heteroatoms (N, O), most were located from the difference Fourier map with constrains, while some few examples with less good quality data were placed in calculated positions. For some disordered non-coordinated waters, hydrogens were not modelled.

2-3-4 Powder X-ray Diffraction (PXRD) and Rietveld Method

Powder X-ray diffraction is also a common method of crystal characterisation. In general, powder crystalline samples are much more common than good quality single crystal samples from experimental synthesis, which makes powder diffraction more widely used. In single crystal diffraction, the intensity of the spots can be transferred into the Miller indices *hkl*. The measured reflections can be compared with other possible symmetry equivalent reflections. Then after the Laue check on the symmetry of the crystal, the correct Laue class for the crystal can be deduced. However, the individual intensities cannot be obtained in powder diffraction, and all the symmetry equivalent reflections have the same *d* spacing. Hence, it is not possible to use the Laue check to find the symmetry of the crystal like in single crystal diffraction. Thus, single crystal diffraction is normally used to identify atoms in the crystal and their locations, as well as bond lengths and angles. Powder diffraction is often used for checking sample crystallinity and purity. In addition, the measurement of powder diffraction is normally less time consuming and much easier compared with single crystal diffraction measurements.

The general idea for powder diffraction analysis is to use the experimental data to compare with theoretical data from CIF files and then minimise the difference between them by refinement of a crystallographic model. The most used refinement method is Rietveld refinement, which uses a least squares approach to refine the model. The mathematical expression for the refinement is shown in (2−11),

$$S = \sum_i w_i \left[y_i(o) - y_i(c)\right]^2 \qquad (2-11)$$

in which S is the weighted (w_i) difference between the observed ($y_i(o)$) and calculated ($y_i(c)$) intensities.[16] Similar with the single crystal X-ray diffraction, the quality of the fit between the observed and calculated intensities is evaluated by the R-factor, the unweighted-profile, $R1$ and weighted-profile, R_{wp} are defined as (2−12) and (2−13), respectively.

$$R1 = \frac{\sum y_i(o) - y_i(c)}{\sum y_i(o)} \qquad (2-12)$$

$$R_{wp} = \sqrt{\frac{\sum_i w_i \left[y_i(o) - y_i(c)\right]^2}{\sum_i w_i \left[y_i(o)\right]^2}} \qquad (2-13)$$

However, if a high background is included, it will automatically produce a low R_{wp}, which may cause an extremely misleading result. Thus, another R-factor, the statistically expected R value, R_{exp}, is introduced to solve this problem and is expressed as (2−14),

$$R_{exp} = \sqrt{\frac{(N - P + C)}{\sum_i^N w_i \left[y_i(o)\right]^2}} \qquad (2-14)$$

where N is the number of observations, P the number of parameters in the refinement, C is the number of constraints applied in the refinement. The ratio between R_{wp} and R_{exp} is the goodness of fit, χ^2 is defined as (2−15):

$$\chi^2 = \frac{\sum_i w_i \left[y_i(o) - y_i(c)\right]^2}{(N - P + C)} \qquad (2-15)$$

If the experimental data are perfectly fitted with the calculated data, the ideal χ^2 is achieved with a value of one.

All the structural refinements of the powder diffraction data in this thesis were achieved by using the General Structure Analysis System (GSAS) and its graphical user interface (EXPGUI).[17] The theoretical CIF files are from single crystal X-ray diffraction data, verified by checkCIF or directly downloaded from the Cambridge Crystallographic Data Centre (CCDC)[18] and Inorganic Crystal Structure Database (ICSD)[19]. The refined parameters include background, scale factor, CW profile functions, cell parameters, atomic positions and Uiso of non-hydrogen atoms. The powder samples were measured by many different PXRD facilities based on different situations: for the samples with a large amount (0.1~0.5 g) available, the samples were placed in a rotatable disc sample holder and the PXRD data were collected on a PANalytical Empyrean with Cu X-ray primary beam monochromator (CuKα1); for small

sample amounts (less than 0.1 g), the samples were sealed in glass capillaries with low X-ray diffraction background and the PXRD data were collected on STOE STADIP with Cu X-ray primary beam monochromator (CuKα1) and PANalytical Empyrean with Mo X-ray primary beam monochromator (Mo Kα1,2). In addition, all the samples were measured at room temperature.

2-3-5 Synchrotron X-ray Diffraction

In contrast to normal X-rays, synchrotron X-rays are very powerful and produced by high energy electrons. Fig. 2-6 shows the principle structure of the UK's national synchrotron, the Diamond Light Source,[20] in which the X-rays are generated in a complex way. Firstly, the electron gun emits liberated electrons, then the electrons are accelerated by earthed anodes and form an electron stream with the energy of 90 keV. The linac accelerates the electrons to 100 MeV and injects them into the booster synchrotron, in which the electron stream will be accelerated to 3 GeV and sent into the storage ring. The storage ring is a > 560 metres closed loop with large electromagnets in it to curve the electron stream. During the process of electrons travelling through the magnetic loop, X-ray beams are produced and directed toward different beamlines for different kinds of research. Compared with normal X-ray sources, the synchrotron has greater brilliance, which corresponds to higher resolution. Synchrotron X-ray diffraction is an effective way to check the change of crystallographic parameters and phase transitions of the samples with the changing of the environment. The synchrotron experiments in this thesis were carried out at the I11 instrument of the Diamond Light Source. The detectors used for the synchrotron powder X-ray experiments in this thesis are multi-analyser crystal (MAC) detectors.

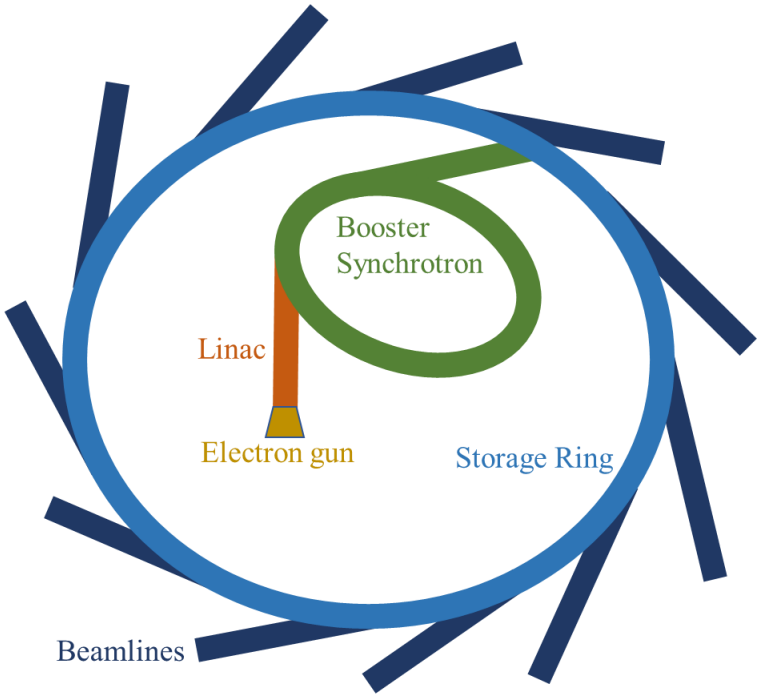

Fig. 2-6 Schematic of the components of the synchrotron at Diamond Light Source[20]

2-4 Neutron Diffraction

The neutron has approximately one atomic mass unit with a half spin state, which makes neutron diffraction an important tool to characterise the atomic and magnetic structures of materials. Different from X-ray diffraction, where the interaction is with the electrons surrounding the atom, neutrons interact with the nucleus. Normally, based on the periodic table, atoms with larger atomic number (heavy atoms) contribute larger intensity in X-ray diffraction. However, the neutron diffraction intensity is not based on the periodic table order, it is more related to the nuclear composition of the atom, for example, the neutron scattering lengths for ^{1}H and ^{2}H (Deuterium, D) are very different. Thus, many organic containing materials need to be deuterated before the neutron diffraction experiment to eliminate the high background due to the high incoherent scattering of ^{1}H. As neutron diffraction is more sensitive for some light atoms, it can supplement the information which X-ray is missing.[21]

2-4-1 ISIS Neutron and Muon Source

The neutron experiments in this thesis were carried out at the General Materials Diffractometer (GEM) at the ISIS Neutron and Muon Source at the STFC Rutherford Appleton Laboratory (RAL). At ISIS, the neutrons were generated by the spallation process of high energy protons. The protons originate from the hydrogen gas which further accepted electrons to form a beam of H^- ions. Then the H^- beam was accelerated to 70 MeV in the form of 200 μs long, 22 mA pulses by the Radio Frequency Quadrupole (RFQ) and linac accelerators and sent into the synchrotron, where the electrons were stripped off by a thick aluminium oxide stripping foil and the protons generated. Finally, the protons were accelerated by RF cavities and magnetic field to 100 μs long, 200 μA pulses and then delivered to the neutron targets.[22]

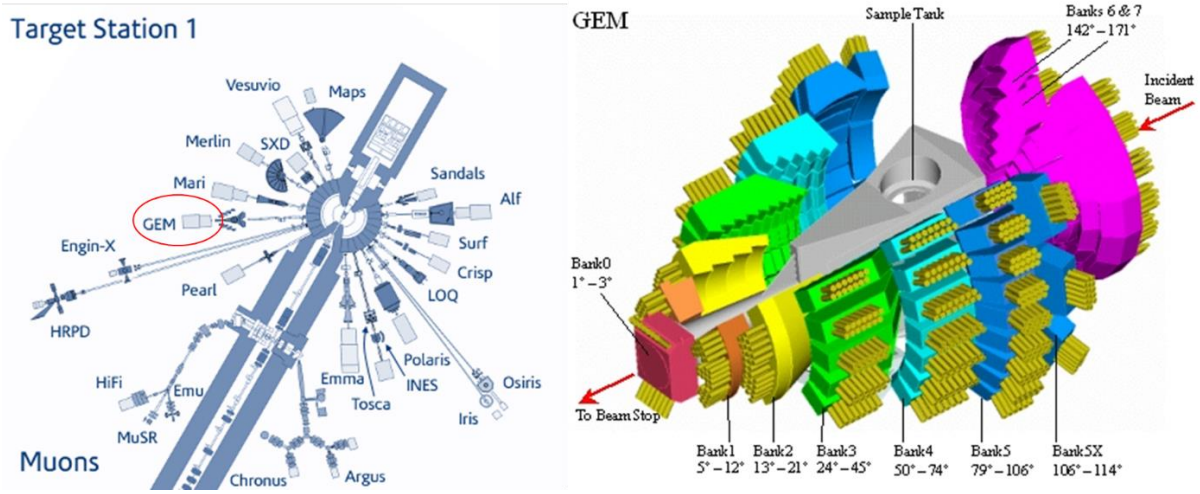

Fig. 2-7 Schematic representation of the Target Station1 (TS1) of ISIS (left)[23] and the GEM instrument (right)[24]. The images are reproduced with permission of the rights holder.

In TS1, neutrons are produced when the proton beam hits a series of thick tungsten plates placed in a pressure vessel and spread to 18 beam channels (Fig. 2-7 left). GEM is one of the 18 beam channels, which is designed for the study of crystalline powders and amorphous materials through high-intensity and high-resolution neutron diffraction (Fig. 2-7 right). The incident beam of GEM is rectangular with the maximum size is 40 mm × 20 mm and can be

adjusted by five remotely controlled apertures and one beam-scraper. There are also two disc choppers and one nimonic chopper, which can be used the limit the wavelength range of GEM in 0.1-3.5 Å. After a 17.0 metres flight path (the distance between the moderator and the sample point, *L*), the incident beam hits the sample and the diffraction signal is received by the detectors (8 banks) covering the angle range from 1.1˚ to 169.3 ˚.[25]

2-4-2 Time of Flight (TOF) Neutron Diffraction

The TOF technique in neutron diffraction is applied to determine the wavelength (λ) by controlling the flight path (L) associating with the time (t) during the neutron travelling through this distance, by the de Broglie relationship (2−16):

$$\lambda = \frac{h}{mv} = \frac{h}{m\frac{L}{t}} = \frac{ht}{mL} \quad (2-16)$$

Combining with the Bragg equation (2−4), the *d*-spacing can be deduced by (2−17):

$$d = \frac{n\lambda}{2sin\theta} = \frac{nht}{2mLsin\theta} \quad (2-17)$$

In which, *h* is the Planck's constant, *v* is the speed and *m* the mass of neutron. Similar to powder X-ray diffraction data, powder neutron diffraction data can also be analysed by Rietveld refinement.

2-5 ISOTROPY Software Suite

In general, the theoretical crystallographic models for Rietveld refinement are taken from known CIF files, but in some cases when there are large changes in bond lengths, bond angles or atom displacements these are not suitable as a starting point for the refinement. Under such circumstances, the ISOTROPY Software Suite can be used to explore the possible space groups and distortions of the crystalline structures. The user interface can visualise the predicted peaks by manipulating the relevant distortion modes, giving atom positions and the

corresponding CIF files for further refinements.[26] In addition, the software suite can also predict and create mCIF including the magnetic superspace groups for magnetic materials.

2-6 Magnetic Properties

2-6-1 Introduction

Magnetism is a common physical property for materials and coordination polymers (CPs) containing magnetic metal centres. The magnetic moment (μ), a vector produced by the nucleus and electrons of an atom/molecule, is an important physical parameter to describe the orientation (expressed in arrow format (↑)) and the strength of a magnet. Comparing with the electron magnetic moment, the contribution of the nuclear magnetic moment is negligible as they are five orders weaker in magnitude. Thus, the magnetic moment is normally equal to the electron magnetic moment, which is the vector sum of the orbital magnetic moment (L) and the spin magnetic moment (S).

Apart from μ, another physical parameter, the magnetic susceptibility (χ), is also a common parameter to describe the magnetic properties of the materials. The magnetic susceptibility is a second order tensor which describes the magnetisation (M) of a magnetic material in a magnetic field (H) and expressed in (2−18) [27]:

$$\chi = \frac{\partial M}{\partial H} \qquad (2-18)$$

when the magnetic field is weak enough and χ is independent of H, it can be expressed as (2−19):

$$\chi = M/H \qquad (2-19)$$

Based on the origin of the magnetism, the arrangement of μ and the value of χ, there are five different magnetic types: diamagnetic, paramagnetic, ferromagnetic, ferrimagnetic and antiferromagnetic (Fig. 2-8).

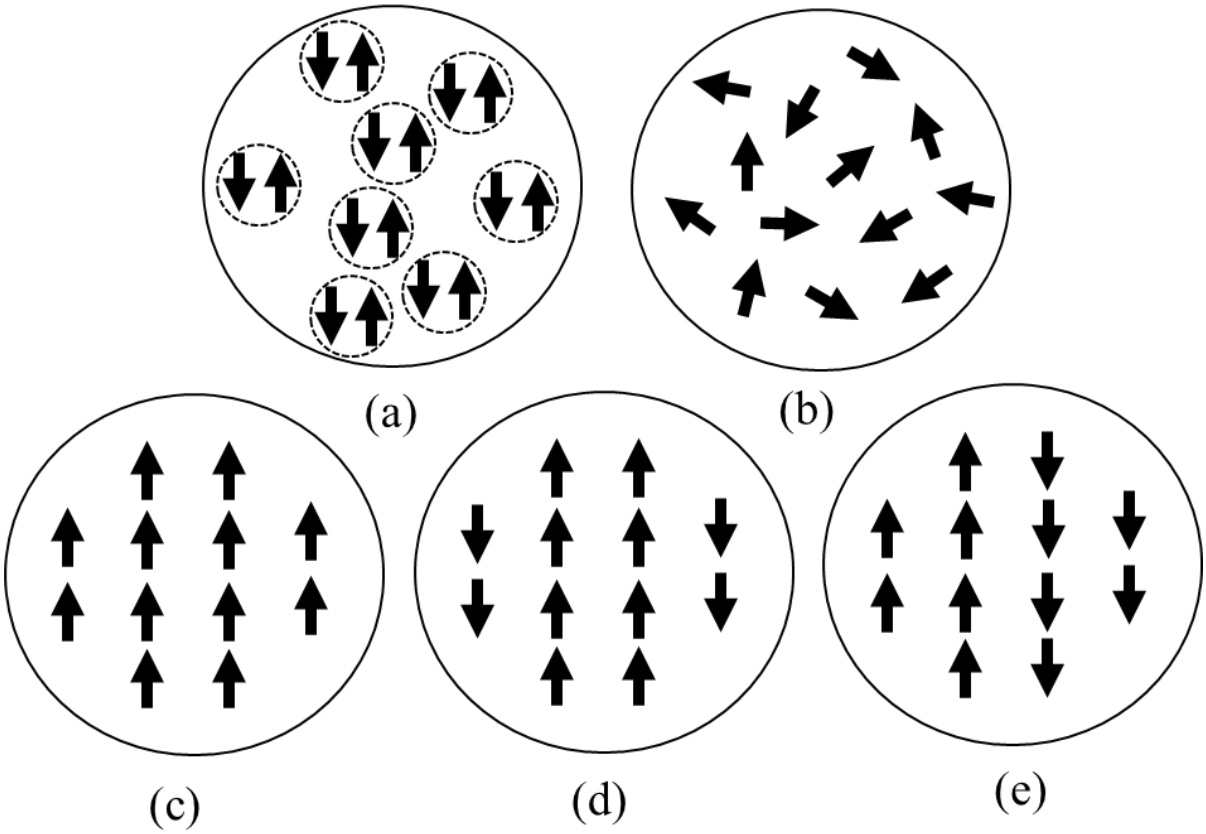

Fig. 2-8 Schematic spin arrangements for (a) diamagnetic, (b) paramagnetic, (c) ferromagnetic, (d) ferrimagnetic, and (e) antiferromagnetic interactions.

For the diamagnetic materials, each electron in the atom/molecule orbital is paired with another one with opposite spin state based on Pauli exclusion principle (Fig. 2-8 (a)). In a magnetic field, the diamagnetic materials are repelled and form an induced internal magnetic field in the opposite direction, which produces a constant negative magnetic susceptibility (χ_d) no matter how the temperature changes (Fig. 2-9 (a)). As all the materials have paired electrons, diamagnetism is a common property in all materials and always contributes a constant small negative χ_d under a magnetic field.

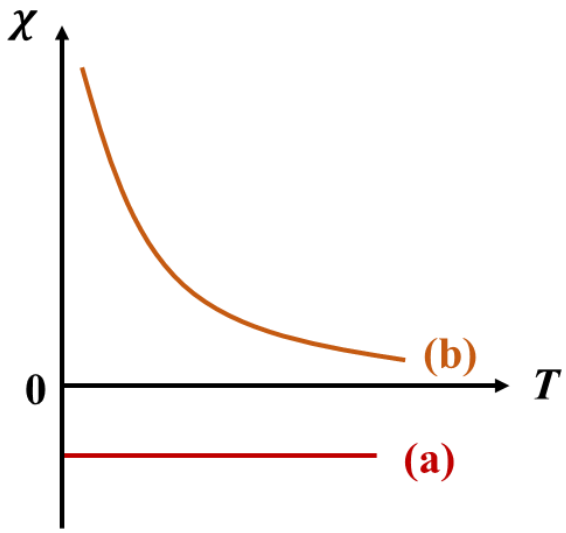

Fig. 2-9 The magnetic susceptibility (χ) as a function of temperature (T) for (a) diamagnetic materials and (b) paramagnetic materials

2-6-2 Curie's Law

In the paramagnetic state, the unpaired electrons with the spins in random directions have no magnetic interaction with each other (Fig. 2-8 (b)). Once an external magnetic field is applied, all the unpaired spins will align along the magnetic field direction and an induced weak internal magnetic field with the same direction is formed. When the external magnetic field is changing direction, the spin direction and internal magnetic field changes to the same direction as well. Once the external magnetic field is removed, the internal magnetic field is also removed, and the spins return to random directions. In this paramagnetic situation, the magnetic susceptibility (χ_p) is inversely proportional to the temperature (Fig. 2-9 (b)), and can be expressed by (2−20), also known as the Curie's law:

$$\chi_p = \frac{Ng^2\beta^2}{3kT} S(S+1) = C/T \qquad (2-20)$$

where N is the Avogadro number, g is the Landé factor (g = 2.0023 for spin only systems), β is the Bohr magneton, k is the Boltzmann constant, S is the spin quantum number and C is the Curie constant which is expressed in (2−21):

$$C = \frac{Ng^2\beta^2}{3k}S(S+1) \qquad (2-21)$$

In addition, the magnetic moment, also known as the effective magnetic moment μ_{eff}, is only contributed to by the electron spin magnetic moment, which can be expressed by (2−22). The effective magnetic moment (μ_{eff}) is similar to the electron spin magnetic moment for most first row transition metal cations, which is what this thesis discusses, but this is not true for second and third row transition metal cations or the f-block elements.

$$\mu_{eff} = \sqrt{3kT\chi_p/N\beta^2} = g\sqrt{S(S+1)} \qquad (2-22)$$

Furthermore, if the single crystal structure or the composition of the magnetic sample is known, we can use the measured magnetic data combined with the molecular mass of the sample to calculate the molar magnetic susceptibility (χ_m) and the paramagnetic susceptibility (χ_p) after the diamagnetic correction (2−23). The equations (2−20) and (2−23) can also be used to deduce the purity of the magnetic sample.

$$\chi_p = \chi_m - \chi_d \qquad (2-23)$$

For the paramagnetic materials, all the unpaired spins are isolated no matter how the temperature and external magnetic field change. However, for some materials, the external magnetic field or lowering of temperature may cause the spins to interact with each other in a particular alignment, then the state may change from paramagnetic to a particular ordering, based on different materials. If all the unpaired spins are aligning in parallel, then the ordering is ferromagnetic (Fig. 2-8 (c)). If most unpaired spins are aligning in the same direction, but others are in the opposite way, then it is ferrimagnetic ordering (Fig. 2-8 (d)). However, for more typical ferrimagnets, the spins are antiparallel to each other but are not equal in magnitude. If the alignment is in an anti-parallel way, then it is antiferromagnetic ordering (Fig. 2-8 (e)). Ideally, the ferromagnetic and ferrimagnetic ordering will exhibit strong spontaneous magnetisation, while antiferromagnetic ordering does not. However, the actual situation is

more complex for antiferromagnetic ordering, for example, some spin-canting, spin-frustration or spin-spiral systems will also cause magnetic phase transitions with strong spontaneous magnetisations. The antiferromagnetic coupling between two neighbour magnetic cations through a non-magnetic anion is usually caused by superexchange interaction, which is also the dominant type of magnetic coupling expected to be present in the materials in this thesis.

2-6-3 Magnetic Hysteresis Loop

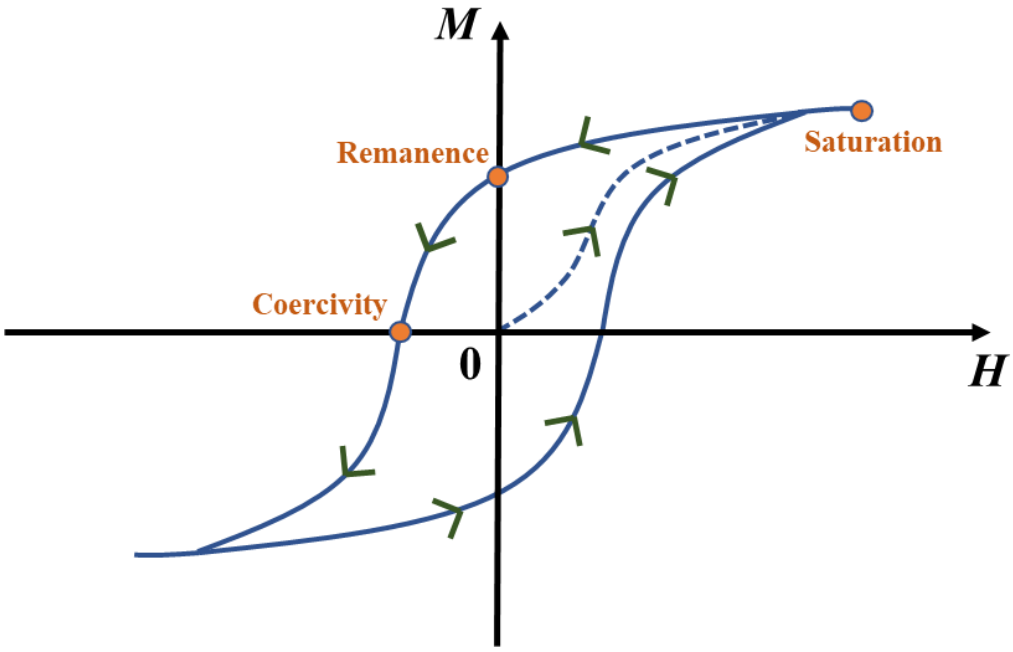

Fig. 2-10 Schematic example of a hysteresis loop.

In ferromagnetic materials, there are many small regions called magnetic domains, which are separated by domain walls. The magnetisation direction in each domain is uniform, but the magnetisation directions in different domains may different. The magnetic domain causes the spontaneous magnetisation of ferromagnetic materials which direction is the vector sum of all the domains. The spontaneous magnetisation responds to the external magnetic field by rotating. Thus, a magnetic hysteresis will occur when a changing external magnetic field is applied. Fig. 2-10 shows the relationship between the applied magnetic field strength H and the magnetisation M of such materials. Assuming the magnet is demagnetised ($H = M = 0$) in

a non-magnetic environment, a magnetic field is applied to the magnet, with H increasing monotonically. Then M of the magnet will correspondingly increase (dashed curve in Fig. 2-10) until M reaches a maximum at the magnetisation saturation point. At the saturation point, if H is reduced at the same rate, M follows the decreasing (solid curve) until $H = 0$, where M remains positive; this is called the remanence. With H cycling further (increasing in the opposite direction) by same rate, M still follows the changing (solid curve) until H reaches another saturation point. If H is continually changed at a constant rate throughout the range of both saturation points, in two opposite directions, then the hysteresis loop is mapped out. In a hysteresis loop, where $M = 0$, the value of H is the coercivity.

2-6-4 Curie-Weiss Law

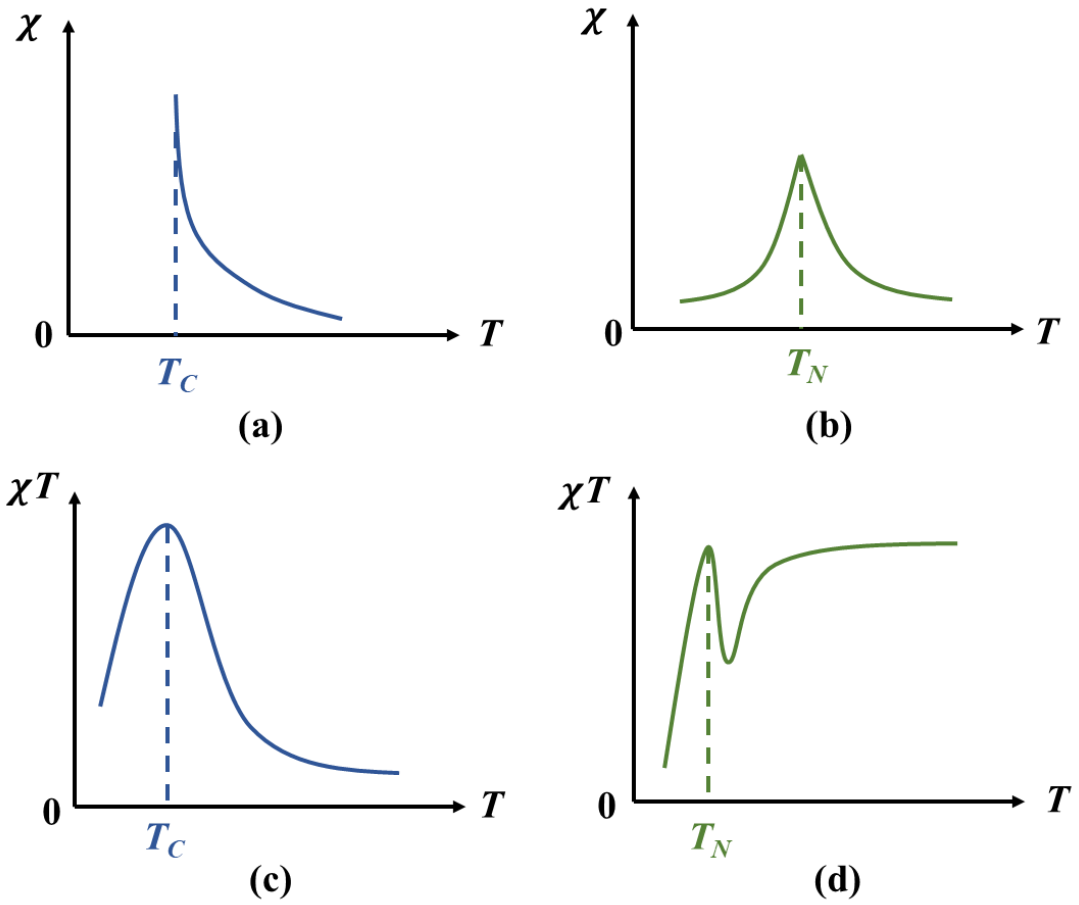

Fig. 2-11 The χ versus T plot for (a) ferromagnetic and (b) antiferromagnetic materials and χT versus T plot for (c) ferromagnetic and (d) antiferromagnetic materials, respectively.

For the ferromagnetic and antiferromagnetic materials, the ordering temperatures are called the Curie temperature (T_C) and Néel temperature (T_N) respectively (Fig. 2-11 (a) and (b)). For the ferrimagnetic materials, the ordering temperatures are also called T_C, because the bulk properties of ferrimagnetic materials resemble ferromagnetic materials.

Ideally, the magnetic material should be in the paramagnetic state with all the spins isolated when the temperature is higher than T_C or T_N, if applicable. However, perfect separation is very rare, and the interactions between the magnetic centres already exist even above the magnetic ordering temperature. According to Curie law, equation (2−19), the $\chi T = f(T)$ plot should be a line parallel to the T axis for the paramagnetic material, but the patterns Fig. 2-11 (c) and (d) don't fit with this. Thus, another parameter θ is involved to modify the Curie law, which is defined in (2−24).

$$\theta = \frac{zJS(S+1)}{3k} \qquad (2-24)$$

in which, z is the number of nearest neighbours around a given magnetic molecule in the crystal lattice, J is the interaction parameter between two nearest neighbouring magnetic centres. Thus, the χ can be described by the equation (2−25), known as the Curie-Weiss law:

$$\chi = \frac{Ng^2\beta^2S(S+1)}{3kT - zJS(S+1)} = C/(T-\theta) \qquad (2-25)$$

This is also the reason why $\chi T = f(T)$ plot useful when analysing magnetic properties: The plot directly to show the magnetic interaction type. For ferromagnetic materials, χT monotonically increases with temperature cooling at higher temperature range, until near T_C, where χT increases abruptly up to maximum then decreases abruptly and left a peak at T_C (Fig. 2-11 (c)). For antiferromagnetic materials, χT monotonically decreases with temperature cooling at higher temperature range, until near T_N, where χT also increases abruptly up and then decreases abruptly and left a peak at T_N (Fig. 2-11 (d)).

The plot of $\chi^{-1} = f(T)$ can directly show the Curie-Weiss law applied to the materials with different magnetic orderings (the slope is C^{-1}). From the plot, we can conclude that a positive θ indicates ferromagnetic interactions while negative θ indicates antiferromagnetic interactions (Fig. 2-12).

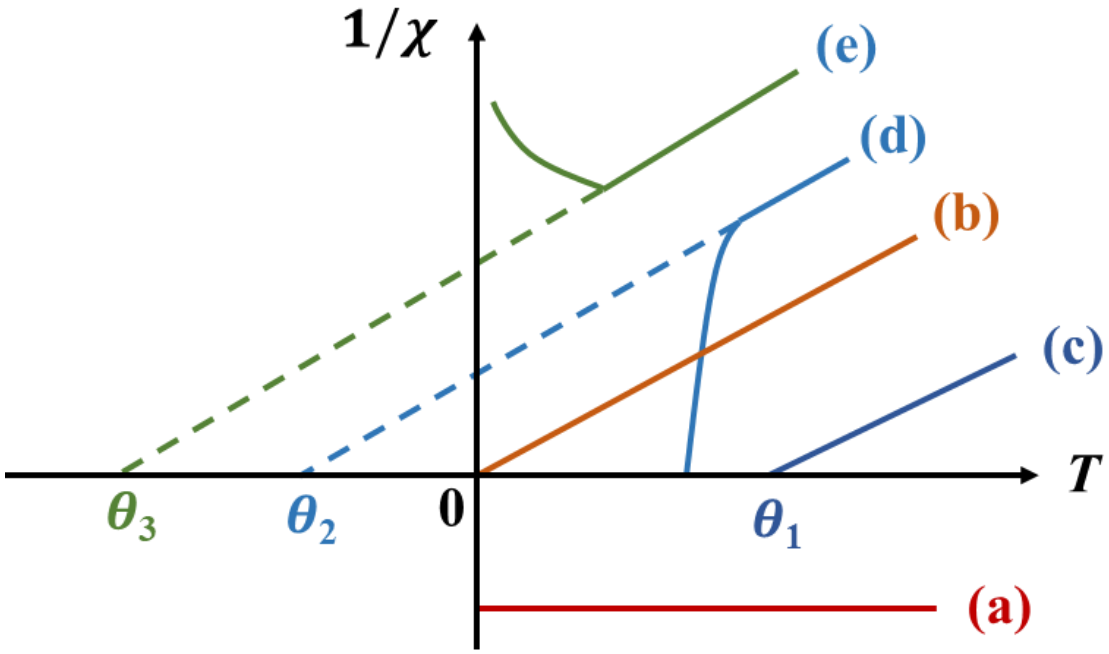

Fig. 2-12 The $1/\chi$ versus T plot for (a) diamagnetic, (b) paramagnetic, (c) ferromagnetic, (d) ferrimagnetic and (e) antiferromagnetic materials.

2-6-5 Superconducting Quantum Interference Device (SQUID)

All the magnetic data in the thesis were measured by using a Quantum Design MPMS SQUID magnetometer in the School of Physics, University of St Andrews. The SQUID can measure the magnetic susceptibility of a single crystal or powder sample in the temperature ranging 1.5 K to 300 K, providing the magnetic field up to 7 Tesla parallel to the sample. For the magnetic measurement, each powder sample was ground carefully to eliminate the magnetic anisotropy effect, then 20~30 mg sample was sealed in a capsule to make sure the

sample was fixed even in magnetic field. Then the capsule was placed in the middle of a straw and measured in a vacuum environment.

2-7 Bond Valence Method

The bond valence method is a simple and common way to estimate the oxidation states of atoms, especially the metal atoms of the CPs. It is a very useful technique to help to identify the chemical formulae of single crystal structures and the spin state of the metals. The general expression is in equation (2−26):

$$V = \sum(v_i) \qquad (2-26)$$

in which V is the valence of an atom, v_i is the individual bond valence of a surrounding atom. The v_i can be deduced from the observed bond lengths by equation (2−27):

$$v_i = \exp\left(\frac{R_0 - R_i}{B}\right) \qquad (2-27)$$

where R_i is the bond length between two neighbouring atoms, R_0 and B are the valence parameters in a table.[28]

2-8 CHN Elemental Analysis

CHN elemental analysis is a standard method to determine the sample purity by measuring the mass fractions of carbon, hydrogen, and nitrogen of a sample. The sample is weighted and combusted with exact amount of oxygen at a high temperature in which both organic and inorganic substances are converted into elemental gases. The elemental gases are separated in a chromatographic column, and the mass ratio of CHN for the sample is determined. It is an important complementary technique to X-ray diffraction when there is an amorphous impurity present. The elemental analysis was carried out by the modern Carlo Erba Flash 2000 Elemental Analyser at London Metropolitan University, by Mr Stephen Boyer.

2-9 References

1. T. Hahn, in *International Tables for Crystallography Volume A: Space-group symmetry*. T. Hahn, Springer Netherlands, Dordrecht, 2002, pp. 112–717.
2. X. Ren, Q. Meng, Y. Song, C. Lu, C. Hu and X. Chen, *Inorg. Chem.*, 2002, **41**, 5686–5692.
3. C. A. L. Dixon, J. A. McNulty, K. S. Knight, A. S. Gibbs and P. Lightfoot, *Crystals*, 2017, **7**, 1–11.
4. S. R. Hall, F. H. Allen and I. D. Brown, *Acta Crystal. Sect A: Found. Adv.*, 1991, **47**, 655-685.
5. E. F. Bertaut, *Acta Cryst. Sect. A: Found. Adv.*, 1968, **24**, 217–231.
6. D. B. Litvin, *Acta Cryst. Sect. A: Found. Adv.*, 2001, **57**, 729–730.
7. J. M. Perez-Mato, J. L. Ribeiro, V. Petricek and M. I. Aroyo, *J. Phys.: Condens. Matter.*, 2012, **24**, 163201.
8. H. Klug and L. Alexander, *X-Ray diffraction procedures: for polycrystalline and amorphous materials, 2nd Edition*, Willey, New York, 1974.
9. S. J. B. Reed, *Electron microprobe analysis and scanning electron microscopy in geology*, Cambridge University Press, 2005.
10. W. Clegg, *X-Ray Crystallography Second Edition*, Oxford University Press, 2015.
11. (a) A. K. Cheetham, *Solid State Chemistry: Techniques, eds*. A. K. Cheetham, and P. Day, Oxford University Press, Oxford, 1987.
12. Checkcif, https://checkcif.iucr.org/, (accessed March 2020).
13. G. M. Sheldrick, SHELXL-2018, *Program for the Refinement of Crystal Structures*, University of Göttingen, Göttingen, Germany, 2018.

14. (a) A. L. Spek, *J. Appl. Cryst*. 2003, **36**, 7-13; (b) A. L. Spek, *Acta Crystallogr., Sect. D*, 2009, **65**, 148-155; (c) A. L. Spek, *Inorg. Chim. Acta*, 2018, **470**, 232-237; (d) A. L. Spek, *Acta Crystallogr., Sect. E*., 2020, **76**, 1-11.
15. L. J. Farrugia, *J. Appl. Cryst*., 2012, **45**, 849-854.
16. L. B. McCusker, R. B. Von Dreele, D. E. Cox, D. Louër and P. Scardi, *J. Appl. Cryst*., 1999, **32**, 36-50.
17. (a) A.C. Larson and R.B. Von Dreele, *General Structure Analysis System (GSAS)*, Los Alamos National Laboratory Report LAUR 86-748, 2000. (b) B. H. Toby, *J. Appl. Cryst*., 2001, **34**, 210-213.
18. C. R. Groom, I. J. Bruno, M. P. Lightfoot and S. C. Ward, *Acta Crystallogr., Sect. B: Struct. Sci., Cryst. Eng. Mater*., 2016, **72**, 171-179.
19. D. Zagorac, H. Müller, S. Ruehl, J. Zagorac and S. Rehme, *J. Appl. Cryst*. 2019, **52**, 918-925.
20. How diamond works, https://www.diamond.ac.uk/Home/About/How-Diamond-Works, (accessed March 2020).
21. Introduction of neutron diffraction, https://www.isis.stfc.ac.uk/Pages/Neutron-diffraction.aspx, (accessed March 2020).
22. How ISIS works – in depth, https://www.isis.stfc.ac.uk/Pages/How-ISIS-works--in-depth.aspx, (accessed March 2020).
23. The schematic representation of ISIS Instruments, https://www.isis.stfc.ac.uk/Pages/Instruments.aspx, (accessed March 2020).
24. The schematic representation of GEM, http://wwwisis2.isis.rl.ac.uk/disordered/gem/GEMdraw/GEMAnnColPic.pdf, (accessed March 2020).
25. Introduction of GEM, https://www.isis.stfc.ac.uk/Pages/Gem.aspx, (accessed March 2020).

26. (a) H. T. Stokes, D. M. Hatch, and B. J. Campbell, *ISODISTORT, ISOTROPY Software Suite*, iso.byu.edu. (b) B. J. Campbell, H. T. Stokes, D. E. Tanner and D. M. Hatch, *J. Appl. Cryst*., 2006, **39**, 607-614.
27. O. Kahn, *Molecular Magnetism*, VCH Publishers, Inc., 1993.
28. I. D. Brown, *The Chemical Bond in Inorganic Chemistry: The Bond Valence Model*, published by Oxford University Press, 2002.

Chapter 3 Organic-Inorganic Hybrid Fluoride Layered Perovskites

3-1 Introduction

Amongst the present research, there are many organic-inorganic hybrid layered perovskites with heavier halides (Cl^-, Br^-, I^-). However, there is no report yet about the hybrid fluoride layered perovskite with the exception of some of the work described below.[1] Thus, in this chapter, the synthesises, structures and magnetic properties of several organic-inorganic hybrid fluoride layered perovskites and some derivatives will be introduced. In previous research, the hybrid layered perovskites with heavier halides are normally synthesised by solution methods (mostly in water) with the starting materials being metal-halide salts, organic A cations and HX (X = halide) acid. But these solution methods are not suitable for the fluoride analogues because of the poor solubilities of metal fluorides (MF_2). Therefore, hydro/solvothermal reactions were chosen here, to carry out the synthesis of hybrid fluoride layered perovskites. In addition, as diamines can interact with the perovskite layers through H-bonds from the protonated amines, and they are also one of the most common organic A cations in existing hybrid layered perovskites, we chose these for exploratory reactions. Thus, three simple diamines:1,2-diaminoethane (*en*), 1,3-diaminopropane (*1,3-DAP*), and 1,4-diaminobutane (*1,4-DAB*) were selected to act as organic A cations and were reacted with the mixture of metal-fluorides (MF_2) and HF acids to synthesise hybrid fluoride layered perovskites in stainless steel autoclaves.

3-2 *en* Based Hybrid Fluoride Layered Perovskites

3-2-1 Synthesis and PXRD Analysis

This series of compounds can be synthesised through similar hydro/solvothermal reactions at 120 °C, 160 °C, and 190 °C with different fractions of unreacted MF_2 (M = Mn, Co, Ni) impurities in the products. Therefore, the Powder X-ray diffraction (PXRD) and elemental analysis are extremely important to confirm the purity of products. Due to the poor solubilities of MF_2 in water and most organic solutions, to reduce the granularity and to react at higher temperature are two effective methods to minimise the MF_2 impurities.

3-2-1-1 (*en*H_2)MnF_4 (1)

0.092 g (1.0 mmol) ground MnF_2, 0.540 mL (8.0 mmol) *en*, 0.4 mL (11.1 mmol) HF (48-51 % wt. in water) and 2 mL H_2O were mixed and sealed in a 23 mL Teflon-lined stainless-steel autoclave and then was placed in a 190 °C oven and maintained for 48 hours. After the autoclave was cooled to room temperature, colourless plate single crystals of **1** with ~1% MnF_2 impurities were obtained by filtration with washing by deionised water.[1] The single crystal structure data were collected at 93 K, 173 K and 298 K by using three different single crystals at different temperatures. The impurity phase was revealed by powder XRD and analysed by Rietveld method with the support of elemental analysis (anal. calc. (%) for $C_2H_{10}F_4MnN_2$: C, 12.44; H, 5.22; N, 14.51. Found: C, 12.33; H, 5.30; N, 14.44).

The crystalline sample for PXRD was ground for 30 mins into a proper powder and loaded into a steel disc with Teflon liner. PXRD data were collected between 3-70° for one hour at room temperature on a Panalytical Empyrean diffractometer, using CuKα1 radiation. Rietveld refinement was carried out using the GSAS package[2] and the EXPGUI interface[3] with the result of wRp = 0.1483, Rp = 0.0818 and χ^2 = 23.52. The fixed crystallographic models were used, based on the CIF file from the single crystal refinement at 298 K, with only profile and lattice parameters being refined. Even though the crystals were ground for a time, a distinct

preferred orientation was still observed, with (h00) reflections exhibiting artificially high intensity (Fig. 3-1); these reflections were excluded from the refinement (Fig. 3-2). A significant peak ($2\theta \sim 18°$) from the Teflon sample holder is also present (Fig. 3-3). The fraction of MnF_2 impurity was determined to be 1.2 (1) % by weight, which supports the purity of the sample, based on elemental analysis. Another batch (with higher MnF_2 impurity content, ~ 9%,) was measured between 3.5-35° for 22 hours at room temperature on another Panalytical Empyrean diffractometer, in transmission (capillary) geometry, using MoKα radiation (Fig. 3-4). In this geometry, the preferred orientation is minimised, and it also supports the much smaller amount of impurity present in the original sample, which was used for magnetic analysis.

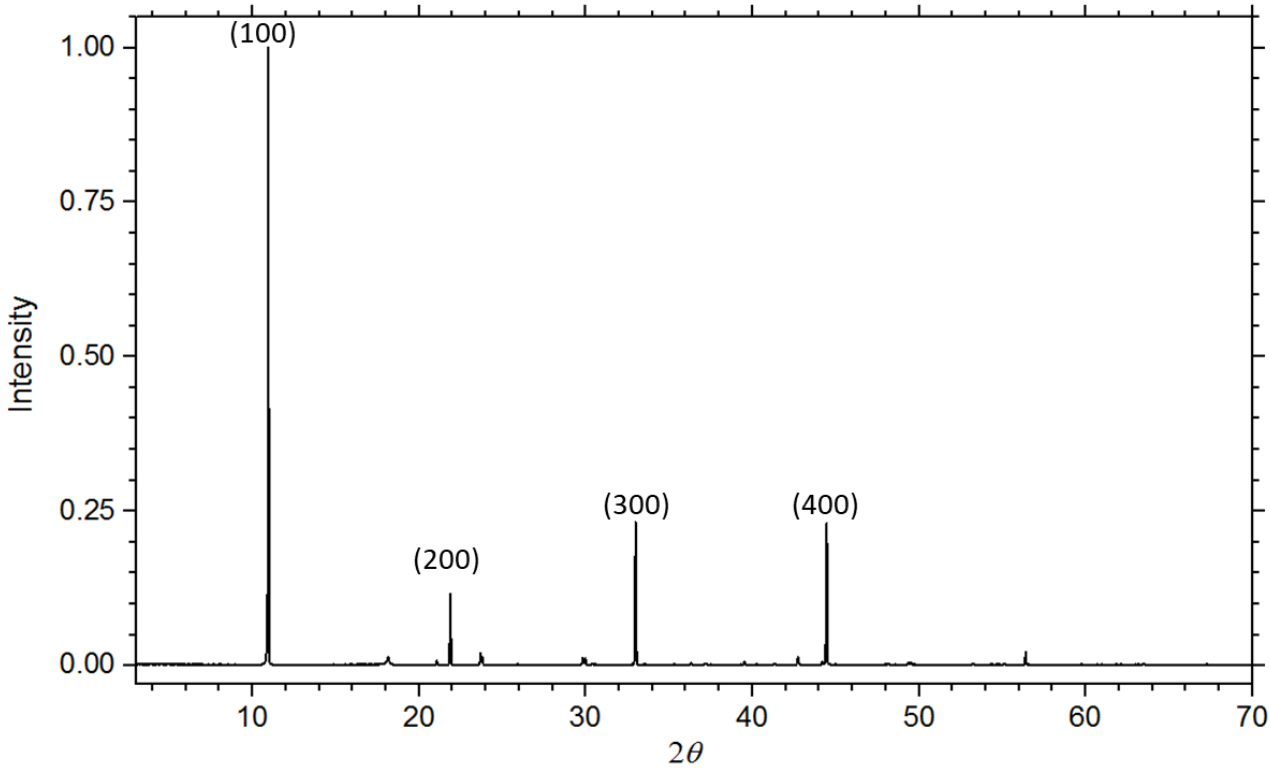

Fig. 3-1 Raw PXRD data (CuKα1) showing the preferred orientation effect (h00 reflections) for **1**.

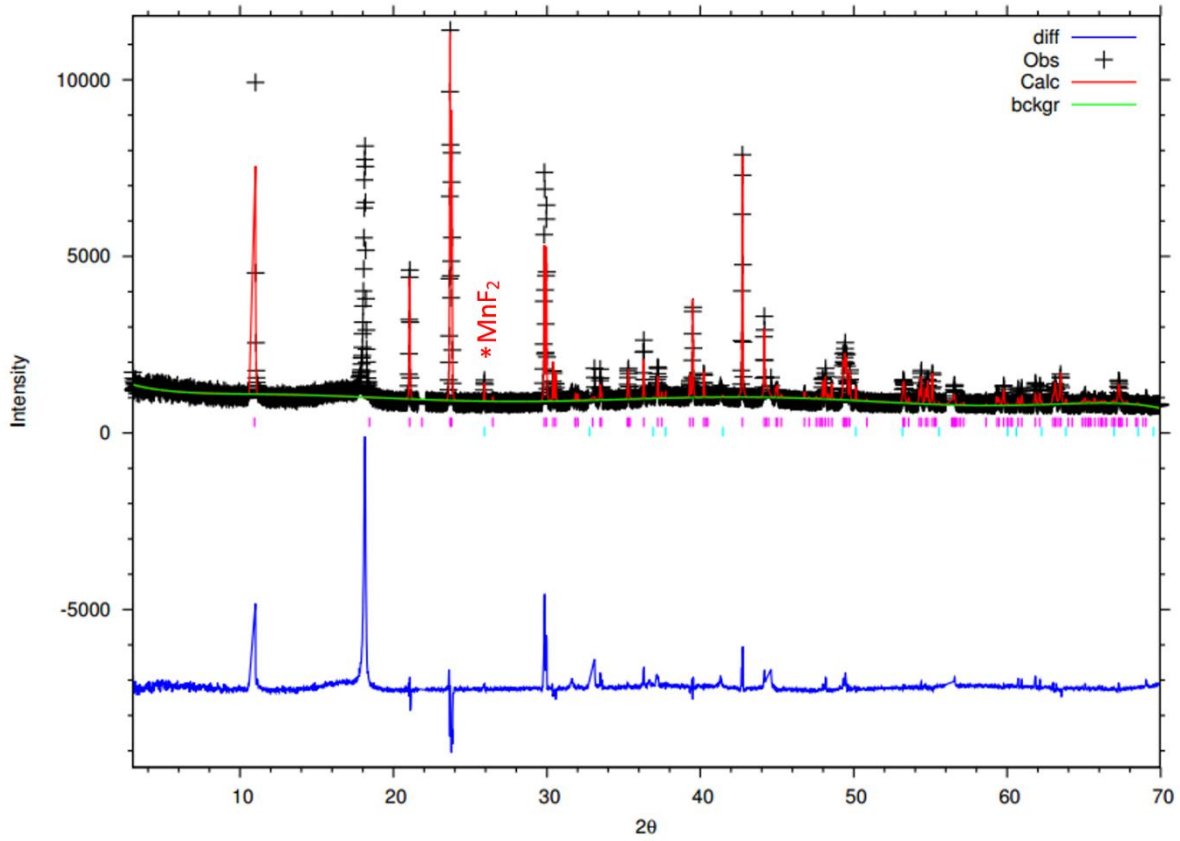

Fig. 3-2 Rietveld plot (PXRD, CuKα1) for **1**. Dominant h00 reflections have been excluded. The peak near $2\theta \sim 18°$ is due to the Teflon sample holder (see Fig. 3-3). The most significant peak of the MnF_2 impurity (~1%) is highlighted.

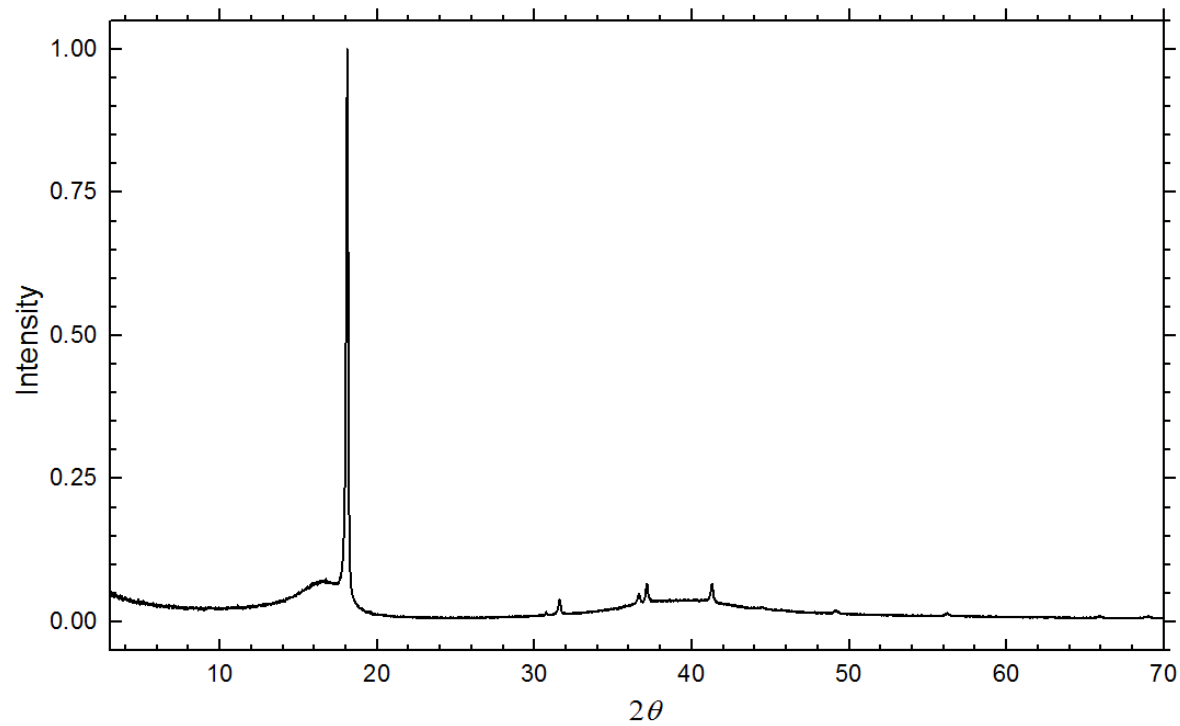

Fig. 3-3 PXRD data (CuKα1) for the Teflon sample holder (see Fig. 3-2).

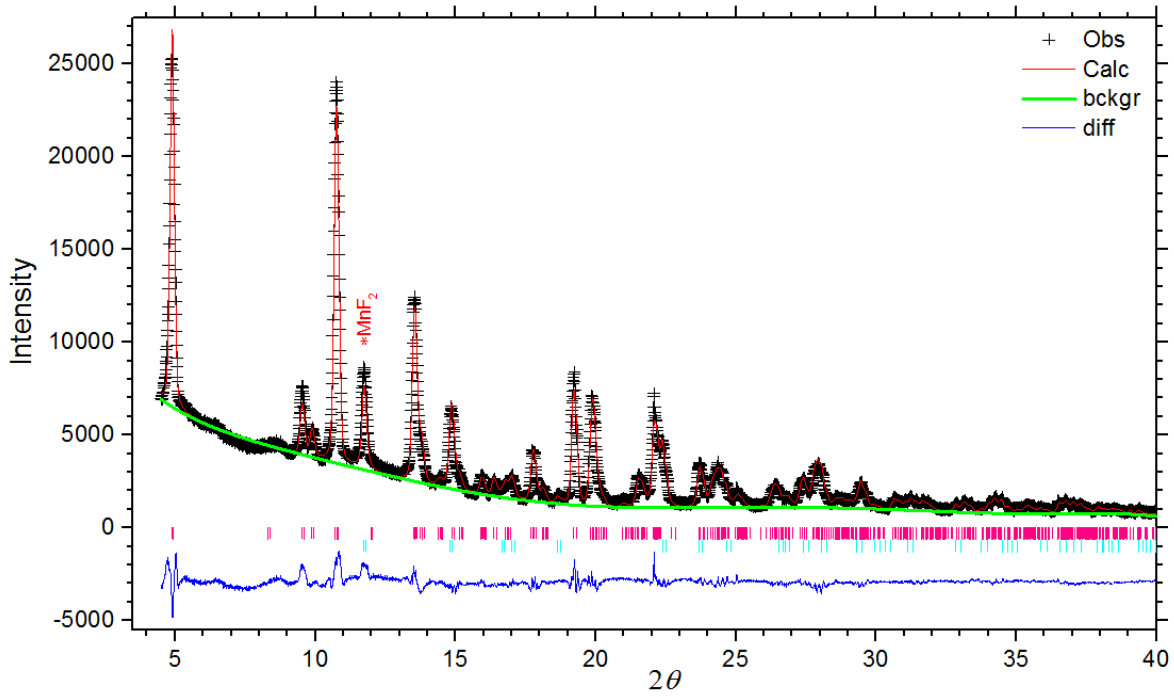

Fig. 3-4 Rietveld plot (PXRD, MoKα) for **1**. The h00 reflections have been included, revealing the lack of preferred orientation in capillary mode. The most significant peak of the MnF_2 impurity (~9%) is highlighted.

3-2-1-2 (*en*H_2)CoF_4 (2)

0.485 g (5.0 mmol) ground CoF_2, 2.7 mL (40.0 mmol) *en*, 2.0 mL (55.6 mmol) HF (48-51 % wt. in water) and 2 mL H_2O were mixed and sealed in a 50 mL Teflon-lined stainless-steel autoclave and then was placed in a 190 °C oven and maintained for 72 hours. The pure product, pink plate single crystals of **2** were generated after cooling to room temperature and washed by ethanol (EtOH). The single crystal structure data were collected at 173 K.

The crystalline samples were also ground for 30 mins into a homogeneous powder and loaded into steel discs with Teflon liners. PXRD (CuKα1) data collection and Rietveld refinement were based on the same conditions as **1**, with a result of wRp = 0.0561, Rp = 0.0263 and χ^2 = 19.45. The fixed crystallographic models were used, based on the CIF file from the

single crystal refinement at 173 K, with only profile and lattice parameters being refined. The preferred orientation was also observed, with (h00) reflections exhibiting artificially high intensity (Fig. 3-5).

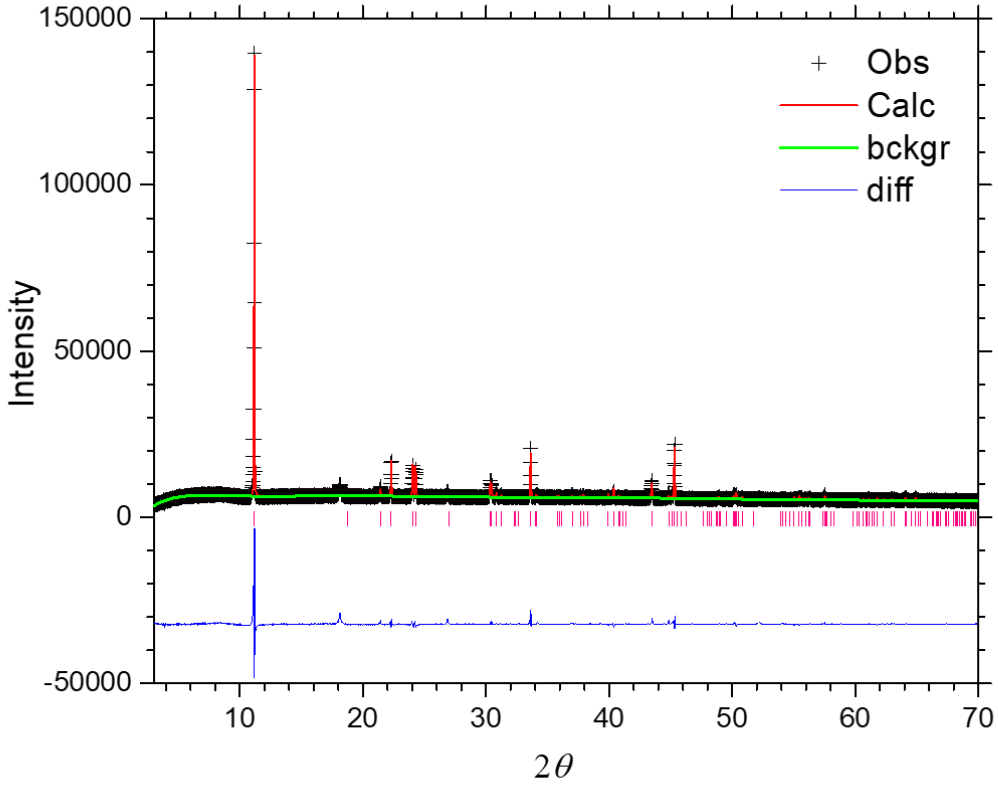

Fig. 3-5 Rietveld plot (PXRD, CuKα1) for **2**. Dominant h00 reflections have been excluded except for (100). The peak near $2\theta \sim 18°$ is due to the Teflon sample holder (see Fig. 3-3).

3-2-1-3 (*en*H$_2$)NiF$_4$ (3)

0.097 g (1.0 mmol) ground NiF_2, 0.4 mL (6.0 mmol) *en*, 0.45 mL (12.5 mmol) HF (48-51 % wt. in water) and 2 mL ethylene glycol (EG) were mixed and sealed in a 50 mL Teflon-lined stainless-steel autoclave, which was placed in a 190 °C oven and maintained for 48 hours. The product, yellow-green plate single crystals of **3**, were generated after cooling to room temperature and washed by EtOH. The single crystal structure data were collected at 173 K

and 298 K. The phase purity was also revealed by powder XRD. Elemental analysis (anal. calc. (%) for $C_2H_{10}F_4NiN_2$: C, 12.21; H, 5.12; N, 14.23. Found: C, 12.15; H, 4.99; N, 14.17) shows a high level of purity.

The crystalline samples were also ground for 30 mins into a powder and loaded into steel discs with Teflon liners. PXRD (CuKα1) data collection and Rietveld refinement were also based on the same conditions as **1**, with a result of wRp = 0.2173, Rp = 0.1343 and χ^2 = 97.61. The fixed crystallographic models were used, based on the CIF file from the single crystal refinement at 298 K, with only profile and lattice parameters being refined. The preferred orientation was also observed, with (h00) reflections exhibiting artificially high intensity (Fig. 3-6).

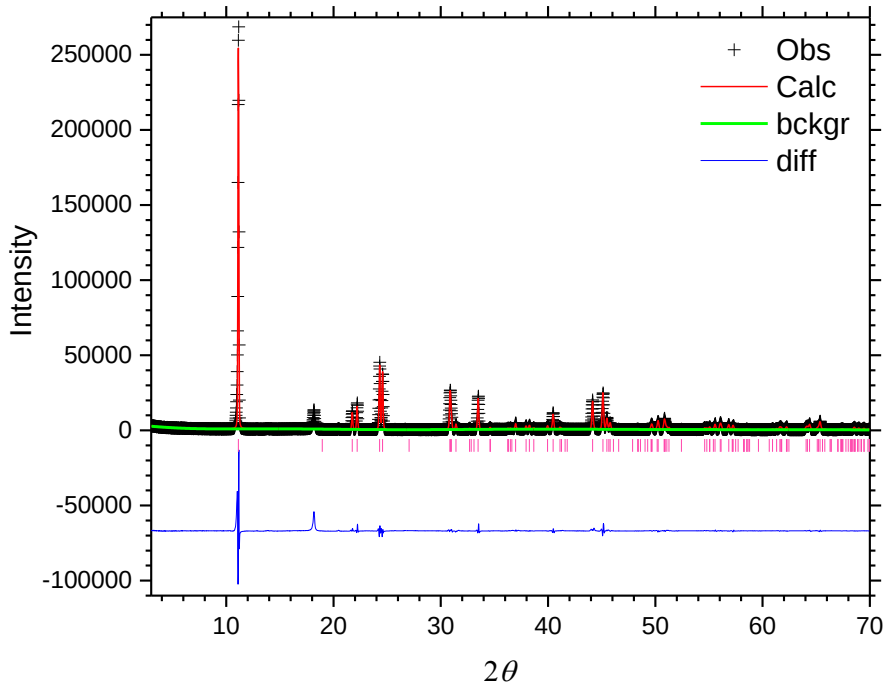

Fig. 3-6 Rietveld plot (PXRD, CuKα1) for **3**. The peak near $2\theta \sim 18°$ is due to the Teflon sample holder (see Fig. 3-3).

3-2-2 Single Crystal Data and Analysis

Single crystal data of **1** were collected at 93 K, 173 K and 298 K with three different single crystals, with no evidence of any structural phase transition, but only small changes of bond lengths and bond angles within the temperature range. As compounds **1**-**3** are isostructural, only one single crystal of **2** was measured at 173 K, and one single crystal of **3** was measured at 173 K and 298 K (Table 3-1). The unit cells for the three compounds were found to be metrically pseudo-tetragonal, however, all the metal-fluoride bond lengths and bond angles are found unreasonable in tetragonal models, leading to unacceptable fits. In further progress, the only satisfactory model was found to be monoclinic with space group $P2_1/c$. Among all the cell parameters, *a* is the longest axis, *b* and *c* are similar in length, but *b* is slightly longer than *c*. This rule is applicable for all temperatures.

During the single crystal measurements, even though all measured single crystals looked good under the microscope, most of them were found twinned (except for **1** (93 K)) after the single crystal structure measurements. Thus, before single crystal refinements, all the twin data were processed by the TWINROTMAT algorithm in the PLATON suite,[4] via the following matrices:

$$\begin{pmatrix} -1 & 0 & 0 \\ 0 & -1 & 0 \\ -0.002 & 0 & 1 \end{pmatrix}$$ for **1** (173 K), $$\begin{pmatrix} -1 & 0 & 0 \\ 0 & -1 & 0 \\ 0.005 & 0 & 1 \end{pmatrix}$$ for **1** (298 K),

$$\begin{pmatrix} 1 & 0 & 0.034 \\ 0 & -1 & 0 \\ 0. & 0 & -1 \end{pmatrix}$$ for **2**, and $$\begin{pmatrix} 1 & 0 & 0 \\ 0 & -1 & 0 \\ 0.007 & 0 & 1 \end{pmatrix}$$ for **3** (173 K and 298 K)

Table 3-1 Crystallographic data and refinement details of compounds **1**, **2** and **3**.

Compound (*T*)	**1** (93 K)	**1** (173 K)	**1** (298 K)	**2** (173 K)	**3** (173 K)	**3** (298 K)
Formula	$(C_2H_{10}N_2)MnF_4$	$(C_2H_{10}N_2)MnF_4$	$(C_2H_{10}N_2)MnF_4$	$(C_2H_{10}N_2)CoF_4$	$(C_2H_{10}N_2)NiF_4$	$(C_2H_{10}N_2)NiF_4$
Formula weight	193.06	193.06	193.06	197.05	196.81	196.81
Density (g cm^{-3})	2.197	2.190	2.190	2.349	2.416	2.406
Crystal system	Monoclinic	Monoclinic	Monoclinic	Monoclinic	Monoclinic	Monoclinic
Space group	$P2_1/c$	$P2_1/c$	$P2_1/c$	$P2_1/c$	$P2_1/c$	$P2_1/c$
a/Å	8.1735(18)	8.1634(7)	8.1632(7)	8.0384(5)	8.0461(8)	8.0449(8)
b/Å	5.9868(13)	5.9917(5)	6.0028(5)	5.8987(4)	5.8058(5)	5.8218(6)
c/Å	5.9637(14)	5.9622(5)	5.9759(5)	5.8754(4)	5.7911(6)	5.7995(6)
β/°	90.2876(6)	89.937(11)	90.183(13)	90.703(12)	90.298(14)	90.336(16)
V/$Å^3$	291.82(11)	291.63(4)	292.83(4)	278.57(3)	270.52(5)	271.62(5)
Z	2	2	2	2	2	2
Measured ref	3454	2735	2786	2288	2307	2312
Independent ref	526	653	666	475	479	480
	[*R*(int) = 0.027]	[*R*(int) = 0.049]	[*R*(int) = 0.082]	[*R*(int) = 0.046]	[*R*(int) = 0.106]	[*R*(int) = 0.155]
GOOF	1.123	0.995	1.048	1.036	1.029	0.956
Final *R* indices ($I > 2\sigma(I)$)	*R*1 = 0.0141, *wR*2 = 0.0409	*R*1 = 0.0202. *wR*2 = 0.0470	*R*1 = 0.0338, *wR*2 = 0.0847	*R*1 = 0.0434, *wR*2 = 0.1281	*R*1 = 0.0480, *wR*2 = 0.1030	*R*1 = 0.0491, *wR*2 = 0.1029

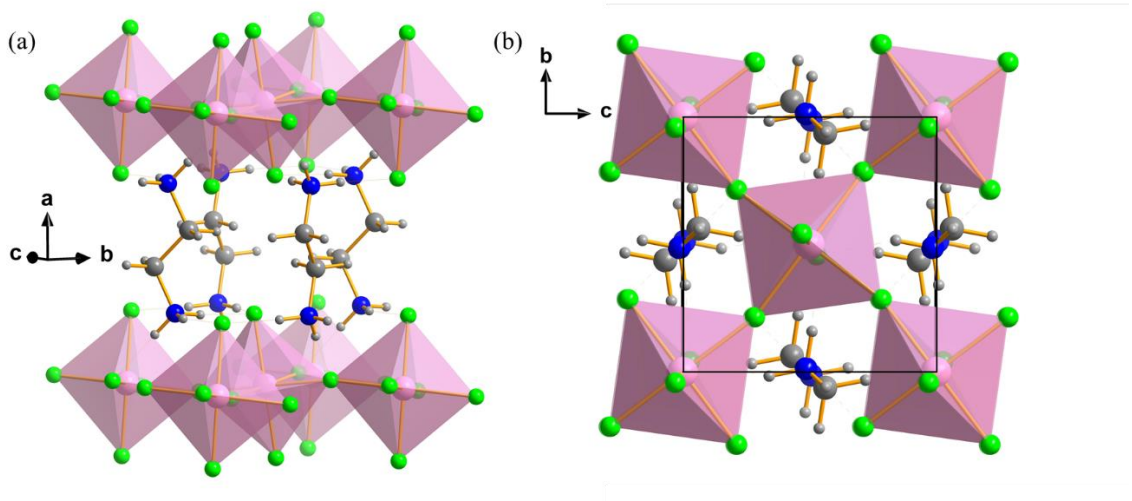

Fig. 3-7 Crystal structure of (*en*H_2)MF_4. (a) perpendicular to *a* and (b) along *a*.

The single crystal structure of (*en*H_2)MF_4 is shown in Fig. 3-7, which may be regarded as a layered perovskite of the Dion-Jacobson (DJ) family, with n = 1 (see chapter 1 for detail). Every M^{2+} (M = Mn, Co, Ni) cation is 6-coordinated with F^- ions, forming $MF_2F_{4/2}$ octahedra. All the octahedra are corner-shared and form single perovskite $[MF_4]_\infty$ layers in the *bc*-plane, which are separated by the protonated *en*H_2^{2+} cations along the *a*-axis. The shortest M-M distances in-plane are 4.2264(3) Å for **1** (173 K), 4.1628(2) Å for **2** (173 K) and 4.1001(3) Å for **3** (173 K), which distances are suitable for constructing 2D magnetic perovskite layers through the M-F-M bridges. However, the shortest M-M through-space distances between the layers are 8.1634(7) Å for **1** (173 K), 8.0384(5) Å for **2** (173 K) and 8.0461(8) Å for **3** (173 K). They are longer than the in-plane distances, and this supports that the materials should have 2D magnetic properties, rather than 3D. By literature review, we found there is no such organic-inorganic hybrid fluoride layered perovskite reported yet. So far, the closest fluoride relative we could find is non-magnetic (*en*H_2)$_{0.5}ScF_4$, in which $[ScF_4]_\infty$ layers were constructed by corner-sharing $ScF_2F_{4/2}$ octahedra and form a 'tungsten-bronze-like' structure.[5]

The unit cell parameters variation with temperature have also been investigated based on the single crystal data. The trend of **1** is unclear so far, because the data are from three

different single crystals, the systematic errors about different crystals may be too large to be used for determining the trend. For compound **3**, the trend of cell parameters like *a*, *b*, *c* axis, *β* and *V* are all larger at higher temperature. If the temperature is constant, cell parameters for different metal compounds are decreasing with the metal atomic number increasing, which is likely due to the effective atom radius decreasing with the metal atomic number increasing.[6] Table 3-2 shows selected bond lengths (Å) and bond angles (°), which also coincide with the cell parameter trends based on different metals. More details will be discussed later from the synchrotron X-ray data study.

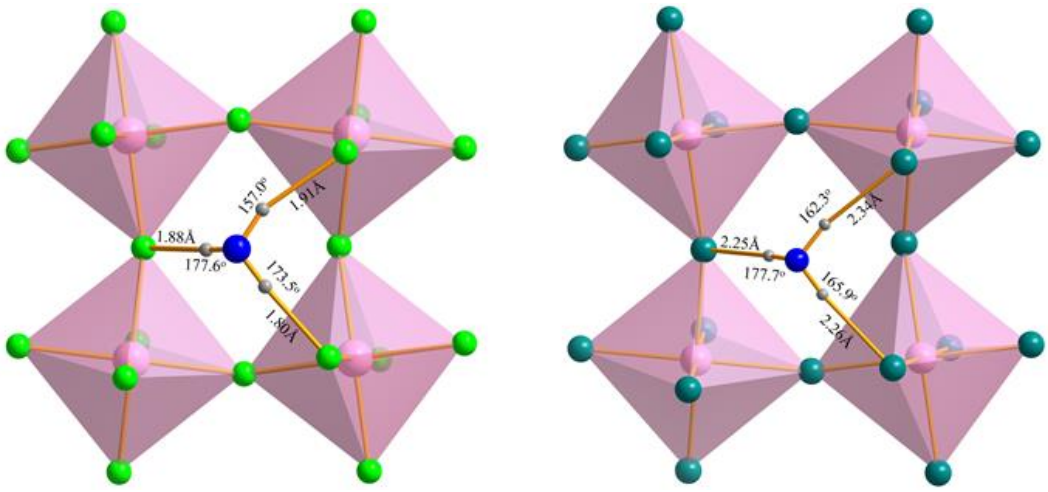

Fig. 3-8 H-bonding in (*en*H_2)MnF_4 (left) and (*en*H_2)$MnCl_4$ (right) at ambient temperature.[7]

The single crystal structure of a chloride derivative (*en*H_2)$MnCl_4$ has been investigated in 1978, which structure was also solved from a twinned crystal.[10] The chloride compound is crystallised in the non-standard monoclinic, $P2_1/b$ space group with unit-cell parameters: a = 8.609 (2), b = 7.130 (2), c = 7.192 (2) Å and γ = 92.69 (2)˚ at room temperature. Here, the *a* axis is the longest in length and *c* is slightly longer than *b*, which is the reason why the space group is $P2_1/b$, different from **1** ($P2_1/c$). The chloride derivative also has longer lengths of all the three axes due to Mn-Cl bonds being longer compared with the Mn-F bonds of **1**. In addition, the angles of N-H---Cl are slightly deviated from N-H---F, but the H-bonds network is in the

same style (Fig. 3-8). All these characteristics prove that the (enH_2)MnF_4 and (enH_2)$MnCl_4$ are isostructural with different halogens.

Except for (enH_2)$MnCl_4$, there are also many other hybrid chloride perovskites have been reported, which contain longer chain protonated diamines ($NH_3(CH_2)_nNH_3MCl_4$, n = 3-7).[7-9] All these structures can usefully be considered as derived from the aristotype $TlAlF_4$ structure, a n=1 DJ phase perovskite structure in which the $[AlF_4]_\infty$ octahedral layers are separated by Tl^+ cations (Fig. 3-9). The aristotype structure crystallises in *P4/mmm* space group, with the 2D perovskite layers in the *ab* plane and stacking along the *c* direction. In further discussions, all the perovskite layer directions will be based on the aristotype for clarity (i.e. layers stacked along *c*).

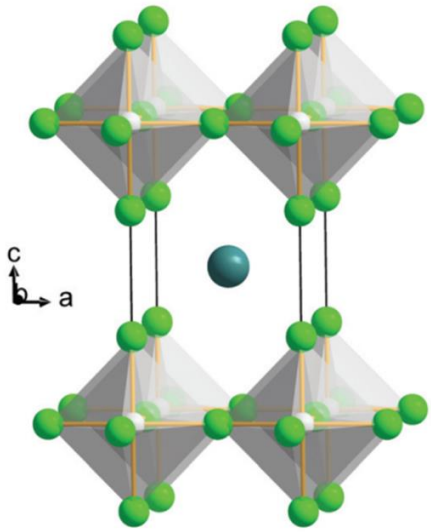

Fig. 3-9 Crystal structure of the aristotype n=1 DJ phase.

Previously, Glazer and Howard have systematically investigated the octahedral tilting of perovskites.[10, 11] Deblieck also studied the DJ family of layered perovskites and listed 75 possible ABX_4 structures, which includes the superstructures with different tilting of adjacent layers along the layer-stacking direction (i.e. doubling the *c*-axis).[12]

As (enH_2)MF_4 is the first example of hybrid fluoride layer perovskite, we investigated the octahedral tilting and compared the tilting with other known (inorganic) fluorides, which are also derived from parent perovskites with n = 1 (compounds with doubling of the c-axis are excluded). There are three different distortion modes with the tilting notations adapted from Glazer's notation,[10] for example, along the a-axis they are shown as "a^0" (no tilting), "a^+" (in-phase tilting) and "a^-" (out-of-phase tilting) (Fig. 3-10). All the distortions are derived from the aristotype ABX_4 ($P4/mmm$) and tilting in at least one of the three distortion modes, and the result is shown in Table 3-3. Here, (enH_2)MF_4 belongs to the to tilt system a^-a^-c. As all the fluoride perovskites listed here belong to DJ phase with n = 1, thus, 'c' means rotation around c direction and 'c^0' means no tilting.

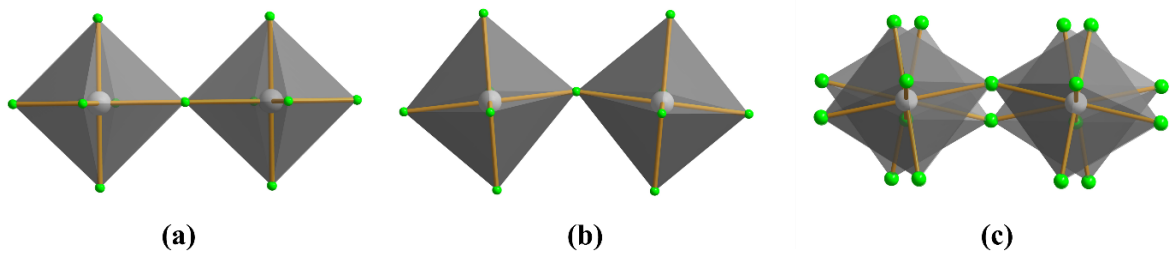

Fig. 3-10 Three different types of octahedral tilts view along the a-axis: (a) a^0, (b) a^+ and (c) a^-.

Table 3-2 Selected bond lengths (Å) and bond angles (°).

	1 (93 K)	**1** (173 K)	**1** (298 K)	**2** (173 K)	**3** (173 K)	**3** (298 K)
M-F2	2.1030(8)	2.0991(11)	2.100(2)	2.003(3)	1.973(4)	1.972(4)
M-F1	2.1449(6)	2.1426(9)	2.1462(18)	2.093(2)	2.057(6)	2.056(7)
M-F1	2.1458(6)	2.1480(9)	2.1510(17)	2.106(2)	2.065(6)	2.072(6)
M-F-M	4.2251(7)	4.2264(3)	4.2351(3)	4.1628(2)	4.1001(3)	4.1088(3)
M-F-M angle	159.94(4)	160.15(5)	160.50(11)	165.00(16)	168.3(3)	168.9(3)
N1-(H)---F1	2.7652(14)	2.757(2)	2.765(4)	2.759(7)	2.788(10)	2.804(12)
N1-(H)---F2	2.6795(13)	2.6828(16)	2.687(3)	2.702(5)	2.713(8)	2.718(9)
N1-(H)---F2	2.7408(16)	2.741(4)	2.750(7)	2.753(11)	2.77(2)	2.75(2)
N1-H-F1 angle	177.8	177.9	177.6	176.3	174.4	175.3
N1-H-F2 angle	173.2	173.0	173.5	171.1	167.9	168.9
N1-H-F2 angle	157.8	157.6	157.0	158.0	160.7	160.7

Table 3-3 Examples of different octahedral tilts in *n*=1 RP phases. The numbers in brackets refer to the number of examples found in ICSD.

Tilt system	Space group	Metrics	Examples
$a^0a^0c^0$	*P4/mmm*	*a a c*	$TlAlF_4$[13] (6)
a^0a^0c	*P4/mbm*	$\sqrt{2}a\ \sqrt{2}a\ c$	$KAlF_4$[14] (3)
$a^-a^0c^0$	*Cmma*	$2a\ 2a\ c$	
$a^-a^-c^0$	*Pmna*	$\sqrt{2}a\ c\ \sqrt{2}a$	
$a^-b^-c^0$	*P2/c*	$\sqrt{2}a\ c\ 2a$	
$a^+a^0c^0$	*Pmma*	$2a\ a\ c$	
$a^+a^+c^0$	*P4/nmm*	$2a\ 2a\ c$	NH_4CrF_4[15] (4)
$a^+b^+c^0$	*Pmmn*	$2a\ 2a\ c$	
a^-b^0c	*C2/m*	$2a\ 2a\ c$	
a^-a^-c	$P2_1/c$	$c\ \sqrt{2}a\ \sqrt{2}a$	$(enH_2)MF_4$
a^-b^-c	$P\bar{1}$	$\sqrt{2}a\ \sqrt{2}a\ c$	
a^+b^+c	*Pmmn*	$2a\ 2a\ c$	$CsFcF_4$[16] (0)
$a^+b^-c^0$	*Pbcm*	$c\ 2a\ 2a$	$RbFeF_4$[17] (1)

3-2-3 Synchrotron Powder X-ray Data and Analysis

In order to explore the detailed changes in cell parameters as a function of temperature, synchrotron PXRD data were collected on compounds **1** and **2**. The synchrotron experiments were carried out at I11 instrument of the Diamond Light Source. Compound **2** was firstly measured with a PheniX cryostat, for which well ground compound **2** powder was coated on an aluminium wire (to improve thermal contact) through a small amount of vacuum grease. Then the sample wire was mounted on to the PheniX brass sample holder, which was coved by an outer shield and evacuated to 1.4×10^{-4} mbar. The diffraction data were collected between 20 K and room temperature (RT). The sample was firstly measured at RT, then cooled for 90 minutes to 20 K, measuring from 20 K to 90 K with 2 K intervals between the measured temperatures, and from 90 K to 250 K with 10 K gaps. The scanning time for each temperature was 15 mins.

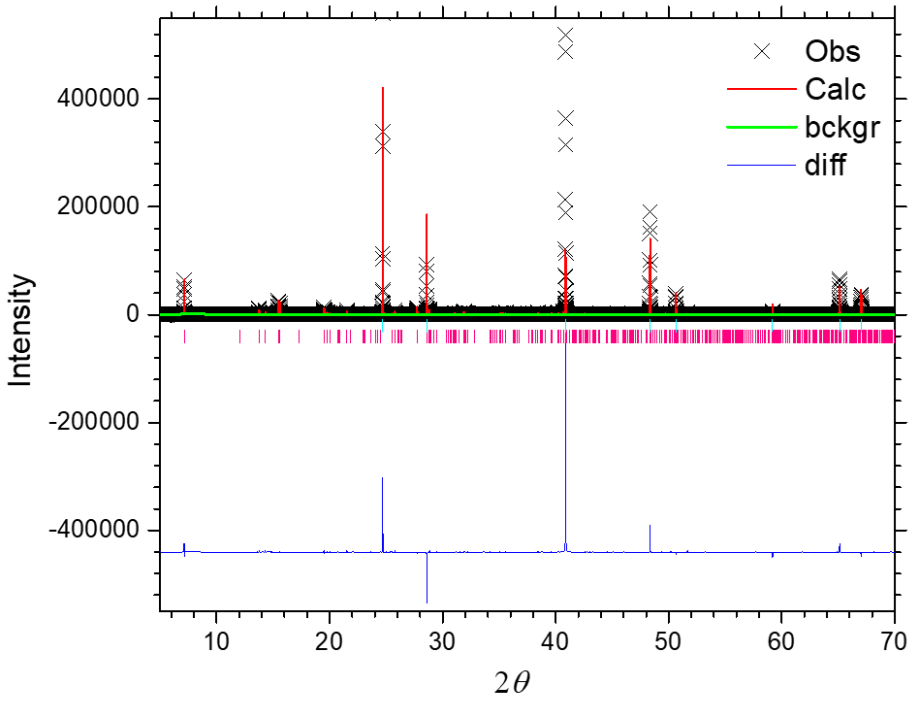

Fig. 3-11 Rietveld plot for **2** on Al wire. (The peak positions of Al are shown by blue).

The Rietveld refinement shows the fraction of Al is 72.2(5) % by weight, with a result of w*Rp* = 0.3873, *Rp* = 0.2622 and χ^2 = 241.2 (Fig. 3-11) based on room temperature data. Such a fitting result could not be used to analyse the crystal structure of **2** due to the high χ^2. As the signals of Al are much stronger than **2**, the Al peaks were eliminated for clarity (Fig. 3-12). Rietveld refinements were applied for 20 K and RT diffraction data without Al peaks, resulting in w*Rp* = 0.1647, *Rp* = 0.1221 and χ^2 = 22.22 for 20 K and w*Rp* = 0.1553, *Rp* = 0.1159 and χ^2 = 23.62 for RT. There are no new peaks and no obvious peak positions changing between 20 K and RT diffraction patterns, except due to thermal expansion effects. In addition, there is no phase transition between the two temperatures and all the refined cell parameters at RT are larger than 20 K except for the *a* axis length (Table 3-4). However, the intensities of several diffraction peaks at 20 K are lower than the relative peaks at RT, and the precision for axis lengths at 20 K is also lower than RT, which indicate that the sample is probably suffering some decomposition during the measurement (Fig. 3-12).

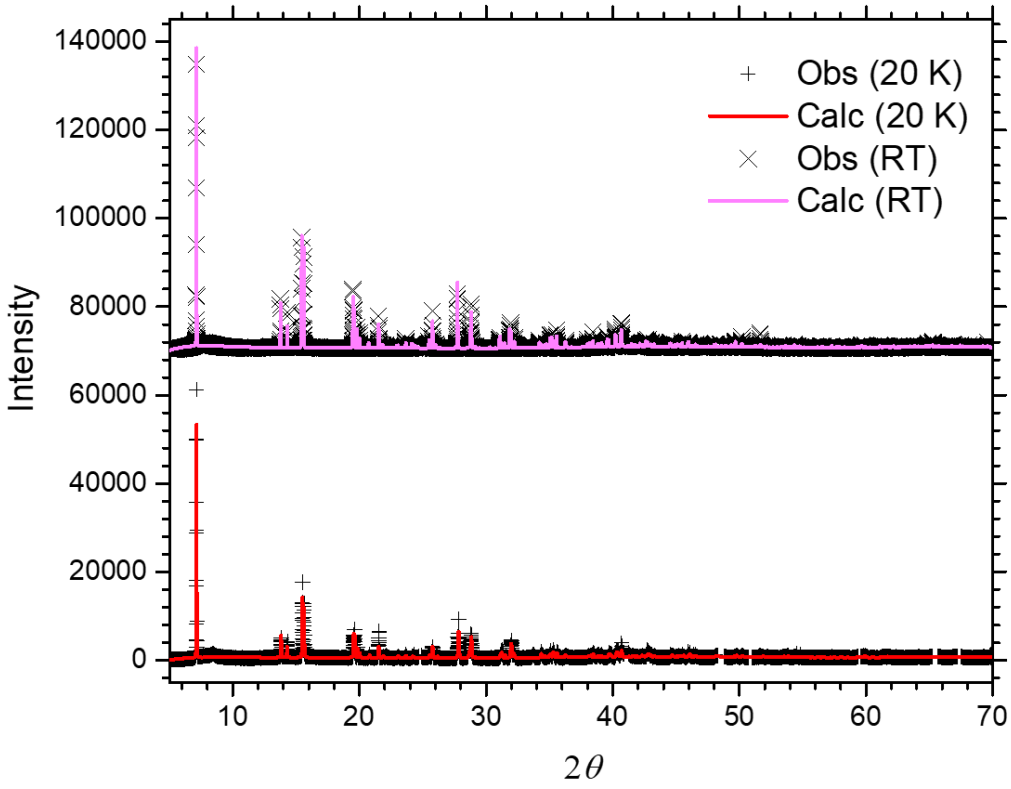

Fig. 3-12 Rietveld plot for **2** at room temperature (above) and 20 K (below). (The peaks of Al are eliminated).

Table 3-4 Lattice parameters obtained from Rietveld refinement of synchrotron diffraction PheniX data for **2** at 20 K and RT.

***T* (K)**	**Space Group**	***a* (Å)**	***b* (Å)**	***c* (Å)**	***β* (˚)**	**V(Å^3)**
20	$P2_1/c$	8.0357(1)	5.8911(2)	5.8709(2)	90.756(2)	277.897(8)
RT	$P2_1/c$	8.03525(5)	5.90847(6)	5.89399(6)	90.925(1)	279.787(3)

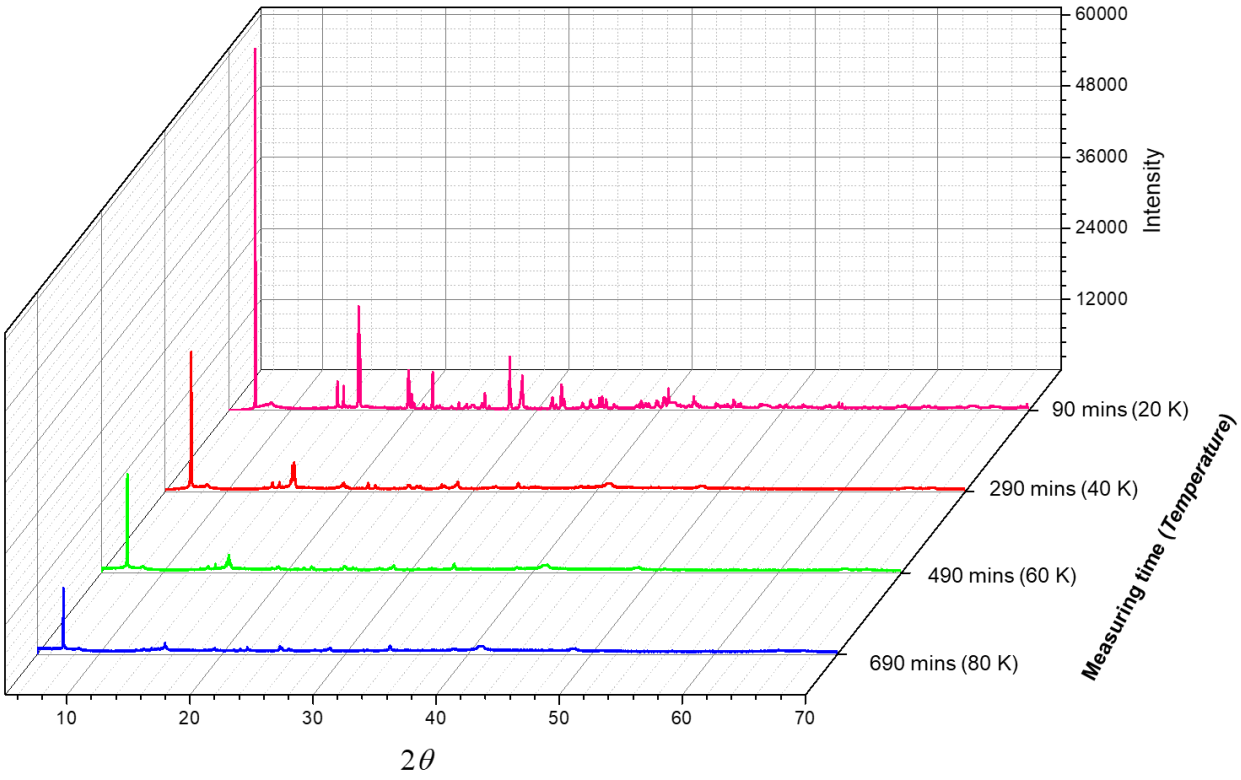

Fig. 3-13 Powder diffraction patterns for **2** measuring for 90, 290, 490 and 690 mins. (The peaks of Al are excluded).

While analysing the data measured at other temperatures, we found that the intensities of peaks were decreasing, and many peaks were becoming amorphous during the measurement. This indicated the sample could be decomposed into amorphous phases by the high energy X-rays. At 80 K (measuring for 690 mins), the (100) peak (2θ = 7.15) is the only well defined peak, which confirms the decomposition of the sample. In addition, it also suggests there is no phase transition between 20 K to 80 K (Fig. 3-13). After the measurement we found the colour of part sample was turned to orange from purple, which also corresponds with the decomposition hypothesis.

In further progress, well ground powder samples of **1** and **2** were coated on glass capillaries and measured from 90 K to 300 K and 80 K to 300 K with 10 K gaps, respectively.

In this case, the temperature was controlled by cryostream (liquid nitrogen), and the scanning time was two minutes for each temperature to avoid the decomposition of samples. Rietveld refinements were applied for all diffraction data and carried out by GSAS[2] and EXPGUI software suites[3], with an example Rietveld plot of **2** at 80 K depicted in Fig. 3-14. Table 3-5 and Table 3-6 describe cell parameters and the goodness-of-fit values at each temperature for **1** and **2**, respectively. The changing of lattice parameters are also depicted in Fig. 3-15, from which we can conclude the lengths of all the three cell edges, β angles and volumes for both compounds are increasing in two nearly linear regions with the critical temperatures are 140 K for **1** and 160 K for **2.**

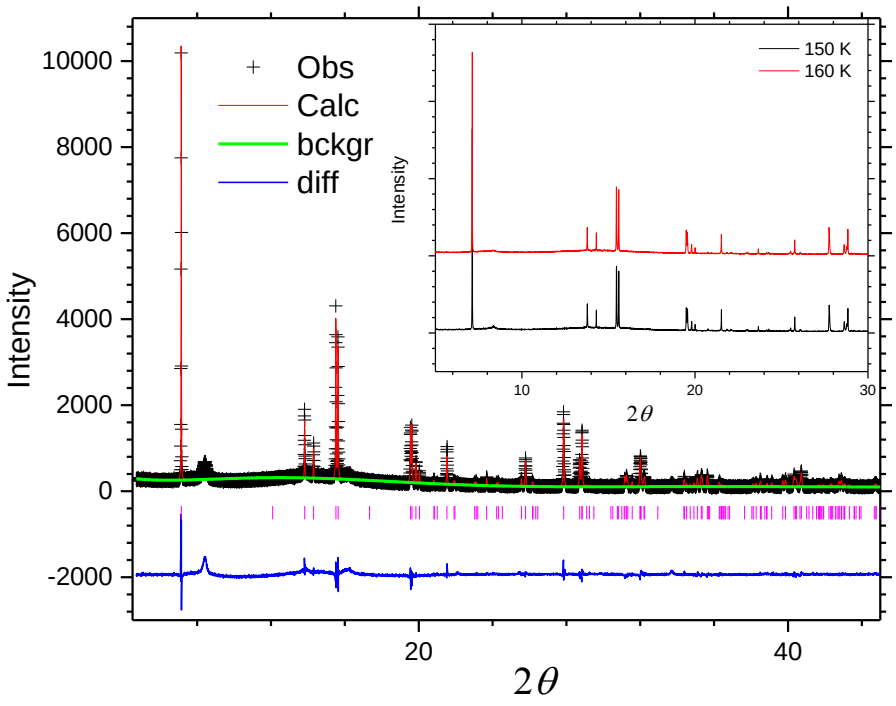

Fig. 3-14 Rietveld plot for **2** at 80 K. (The inset shows the diffraction patterns of 150 K and 160 K).

In order to figure out what caused the phenomenon, we tried to analyse the data around the critical temperatures (140, 150, 160 and 170 for **2**). The diffraction patterns of 150 K and 160 K are depicted in the inset part of Fig. 3-14, which shows no obvious changes in peak position and peak intensities. The changes of atomic positions and Uiso between 150 and 160 K are similar with 140 and 150 K. Crystal structures of those temperatures are also depicted based on simulated CIF files, from which no obvious changings of tilting were observed. All the relevant parameter changes based on corresponding temperatures of **1** were also similar. These results may suggest the lattice parameters change around critical temperatures are larger than other temperatures but not phase transitions.

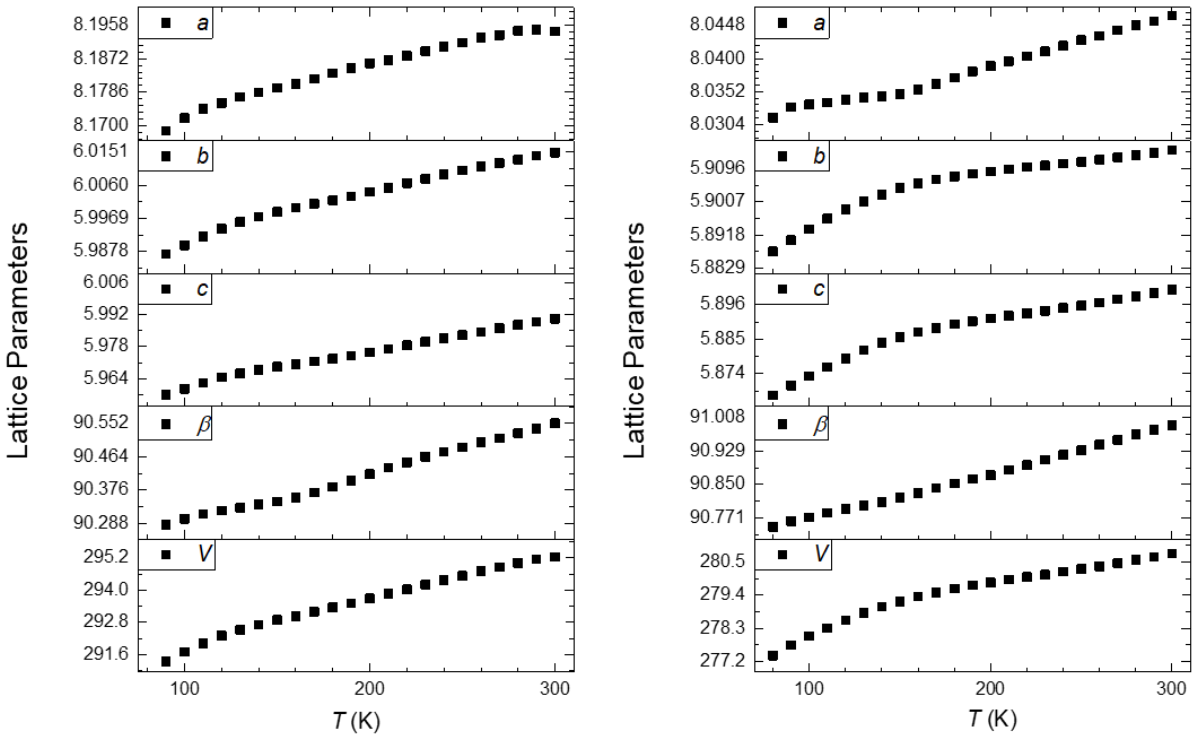

Fig. 3-15 Lattice parameters obtained from Rietveld refinement of synchrotron diffraction over the temperature range 90-300 K for **1** (left) and 80-300 K for **2** (right).

Table 3-5 Cell parameters and the goodness-of-fit values obtained from Rietveld refinement of synchrotron data for **1**.

T **(K)**	***a*** **(Å)**	***b*** **(Å)**	***c*** **(Å)**	***β*** **(°)**	**V(Å^3)**	**w*Rp***	***Rp***	χ^2
90	8.16863(5)	5.98720(4)	5.95694(4)	90.284(1)	291.334(2)	0.1657	0.1262	5.612
100	8.17193(4)	5.98954(4)	5.95955(3)	90.300(1)	291.693(2)	0.1611	0.1215	5.324
110	8.17426(4)	5.99192(4)	5.96216(4)	90.312(1)	292.019(2)	0.1650	0.1245	5.508
120	8.17581(5)	5.99407(4)	5.96453(4)	90.321(1)	292.296(2)	0.1643	0.1232	5.472
130	8.17735(5)	5.99591(4)	5.96631(4)	90.329(1)	292.527(2)	0.1658	0.1240	5.540
140	8.17852 (5)	5.99737(4)	5.96790(4)	90.337(1)	292.718(2)	0.1667	0.1253	5.549
150	8.17968(5)	5.99873(4)	5.96920(4)	90.345(1)	292.889(2)	0.1713	0.1278	5.857
160	8.18080(5)	5.99988(4)	5.97032(4)	90.356(1)	293.040(2)	0.1734	0.1293	5.953
170	8.18197(5)	6.00091(5)	5.97152(4)	90.369(1)	293.191(3)	0.1726	0.1293	5.847
180	8.18350(5)	6.00193(5)	5.97272(5)	90.384(1)	293.354(3)	0.1746	0.1302	5.960
190	8.18479(6)	6.00296(5)	5.97411(5)	90.400(1)	293.518(3)	0.1747	0.1295	5.907
200	8.18600(6)	6.00415(5)	5.97552(5)	90.418(1)	293.689(3)	0.1756	0.1300	5.940
210	8.18691(6)	6.00532(5)	5.97708(5)	90.435(1)	293.855(3)	0.1724	0.1289	5.729
220	8.18798(6)	6.00660(5)	5.97857(5)	90.449(1)	294.028(3)	0.1733	0.1291	5.752
230	8.18917(7)	6.00783(6)	5.98008(6)	90.464(1)	294.205(3)	0.1739	0.1292	5.830
240	8.19031(7)	6.00898(6)	5.98156(6)	90.477(1)	294.375(3)	0.1738	0.1300	5.849
250	8.19130(7)	6.01009(6)	5.98305(6)	90.489(1)	294.537(3)	0.1748	0.1301	5.846
260	8.19260(8)	6.01112(6)	5.98447(6)	90.502(1)	294.704(4)	0.1766	0.1316	6.003
270	8.19332(8)	6.01212(7)	5.98605(7)	90.513(1)	294.856(4)	0.1750	0.1311	5.917
280	8.19438(8)	6.01311(7)	5.98751(7)	90.526(1)	295.014(4)	0.1741	0.1300	5.799
290	8.19471(8)	6.01409(7)	5.98890(7)	90.537(1)	295.143(4)	0.1710	0.1276	5.632
300	8.19421(8)	6.01496(8)	5.99019(8)	90.552(1)	295.230(4)	0.1641	0.1236	5.220

Table 3-6 Cell parameters and the goodness-of-fit values obtained from Rietveld refinement of synchrotron data for **2**.

T **(K)**	***a*** **(Å)**	***b*** **(Å)**	***c*** **(Å)**	***β*** **(°)**	**V(Å^3)**	**w*Rp***	***Rp***	χ^2
80	8.03139(9)	5.88739(9)	5.86716(9)	90.749(2)	277.399(5)	0.1457	0.1118	3.591
90	8.03294(8)	5.89042(9)	5.87021(9)	90.763(1)	277.739(4)	0.1485	0.1130	3.698
100	8.03330(8)	5.89342(8)	5.87328(8)	90.772(1)	278.037(4)	0.1504	0.1151	3.782
110	8.03357(8)	5.89620(8)	5.87612(8)	90.782(1)	278.312(4)	0.1521	0.1163	3.786
120	8.03400(8)	5.89866(8)	5.87886(8)	90.791(1)	278.572(4)	0.1531	0.1168	3.826
130	8.03430(7)	5.90076(8)	5.88153(8)	90.800(1)	278.808(4)	0.1527	0.1166	3.804
140	8.03446(7)	5.90269(8)	5.88379(8)	90.808(1)	279.011(4)	0.1504	0.1155	3.642
150	8.03487(7)	5.90437(7)	5.88564(7)	90.818(1)	279.191(4)	0.1473	0.1135	3.496
160	8.03551(7)	5.90569(7)	5.88730(7)	90.829(1)	279.354(4)	0.1429	0.1102	3.292
170	8.03636(6)	5.90669(7)	5.88854(7)	90.841(1)	279.489(4)	0.1418	0.1097	3.204
180	8.03724(6)	5.90752(7)	5.88985(7)	90.852(1)	279.620(4)	0.1403	0.1091	3.143
190	8.03811(6)	5.90825(7)	5.89072(7)	90.863(1)	279.725(4)	0.1381	0.1074	3.039
200	8.03891(7)	5.90882(7)	5.89165(7)	90.872(1)	279.824(4)	0.1403	0.1094	3.121
210	8.03961(6)	5.90939(7)	5.89247(7)	90.884(1)	279.913(3)	0.1382	0.1077	3.040
220	8.04033(6)	5.90998(7)	5.89325(7)	90.896(1)	280.002(3)	0.1365	0.1055	2.959
230	8.04105(6)	5.91044(7)	5.89400(7)	90.908(1)	280.084(3)	0.1375	0.1064	2.993
240	8.04187(6)	5.91088(6)	5.89492(6)	90.920(1)	280.176(3)	0.1358	0.1055	2.930
250	8.04267(6)	5.91138(6)	5.89577(6)	90.931(1)	280.268(3)	0.1373	0.1062	2.977
260	8.04333(6)	5.91199(6)	5.89670(6)	90.944(1)	280.362(3)	0.1345	0.1041	2.854
270	8.04413(6)	5.91262(6)	5.89768(6)	90.955(1)	280.466(3)	0.1339	0.1041	2.838
280	8.04485(6)	5.91325(6)	5.89870(6)	90.968(1)	280.568(3)	0.1330	0.1035	2.785
290	8.04542(6)	5.91387(6)	5.89973(6)	90.979(1)	280.665(3)	0.1340	0.1046	2.839
300	8.04625(6)	5.91460(6)	5.90074(6)	90.990(1)	280.776(3)	0.1347	0.1051	2.880

3-2-4 Magnetic Data and Analysis

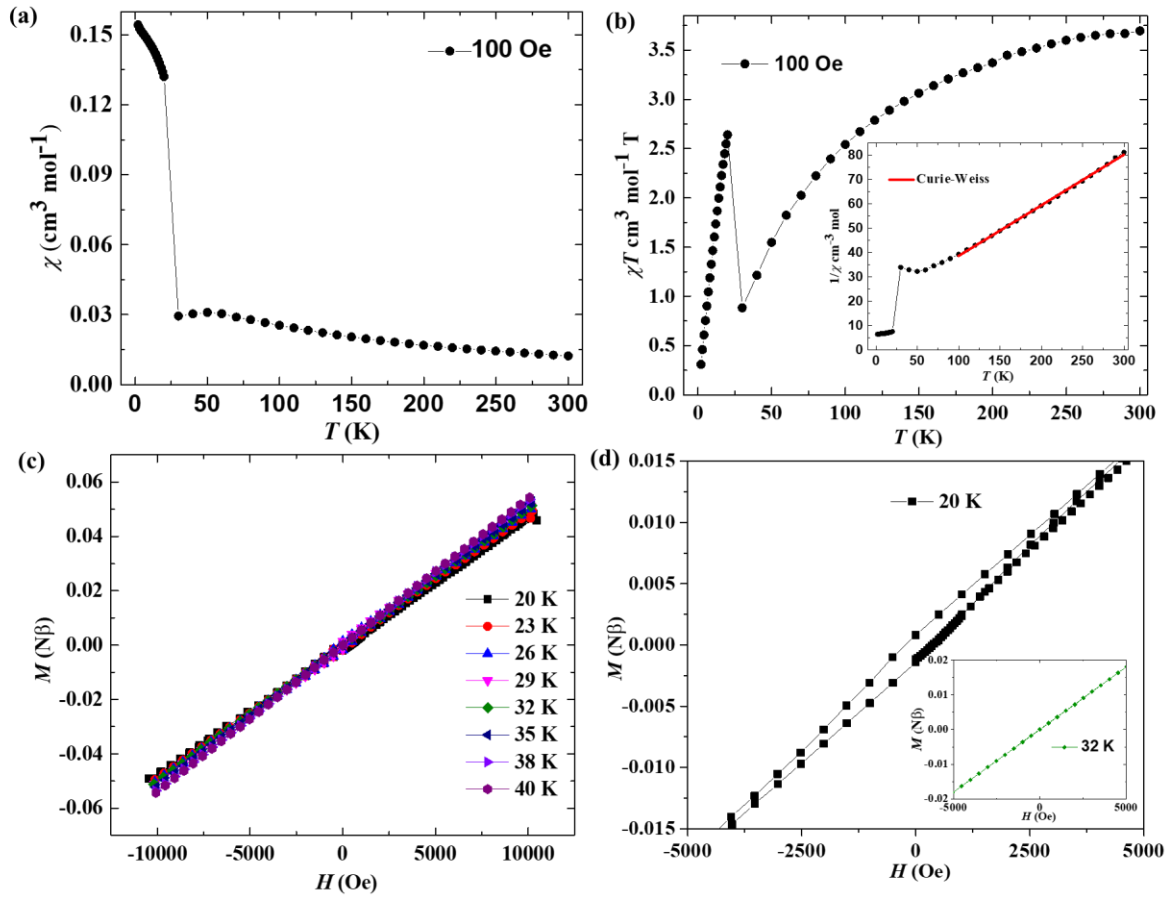

Fig. 3-16 The plots of magnetic data of **1**: (a) χ versus T. (b) χT versus T (The inset shows the Curie-Weiss fit to $1/\chi$). (c) Magnetisation (M) versus magnetic field (H) at several temperature. (d) hysteresis loop of **1** at 20 K.

The magnetic properties of compound **1** have been investigated by SQUID magnetometry. In a 100 Oe magnetic field, the magnetic susceptibility (χ) of **1** is plotted as a function of temperature (T) in the range of 2 K to 300 K (Fig.3-16 (a)), in which χ is increasing with the decreasing of T and has a sudden jump at ~20 K. The inverse susceptibility plot (the inset of Fig.3-16 (b)) has a linear temperature dependence in the range of 100 K-300 K, which is fitted with the Curie-Weiss law. The Landé factor, g = 2.1 (S = 5/2) and effective moment, μ_{eff} = 6.2 μ_B, which deviates slightly from the expected spin-only value (5.92 μ_B). The Curie

constant, $C = 4.81$ cm^3 mol^{-1} K and the Weiss constant, $\theta = -85.59$ K, which indicates an overall antiferromagnetic exchange interaction. The χT *vs.* T plot (Fig.3-16 (b)) also proves the antiferromagnetic interaction from 30 K to 300 K. As T is lowered, χT decreases smoothly and reaches to a minimum of 0.88 cm^3 mol^{-1} K (2.65 μ_B) around 30 K. However, the value of χT increases rapidly on further cooling and reaches to 2.64 cm^3 mol^{-1} K (4.59 μ_B), then continues decreasing smoothly with cooling, which causes a sharp peak at 20 K (T_N). The peak indicates a magnetic phase transition to a state of long-range ordering and the continual decreasing below 20 K results from the saturation of χ. As the μ_{eff} at T_N is less than the spin-only value, it is very likely a canted-antiferromagnetic ordering. In addition, the χT value at 300 K is 3.68 cm^3 mol^{-1} K, lower than C, which suggests the antiferromagnetic interactions could exist at room temperature. The Magnetisation (M) was also investigated in the magnetic field (H) of $\pm$ 10000 Oe (Fig.3-16 (c) and (d)), which shows a very tiny magnetic hysteresis below T_N which disappears at 32 K, corresponding to the weak canted-antiferromagnetic ordering at low temperature.

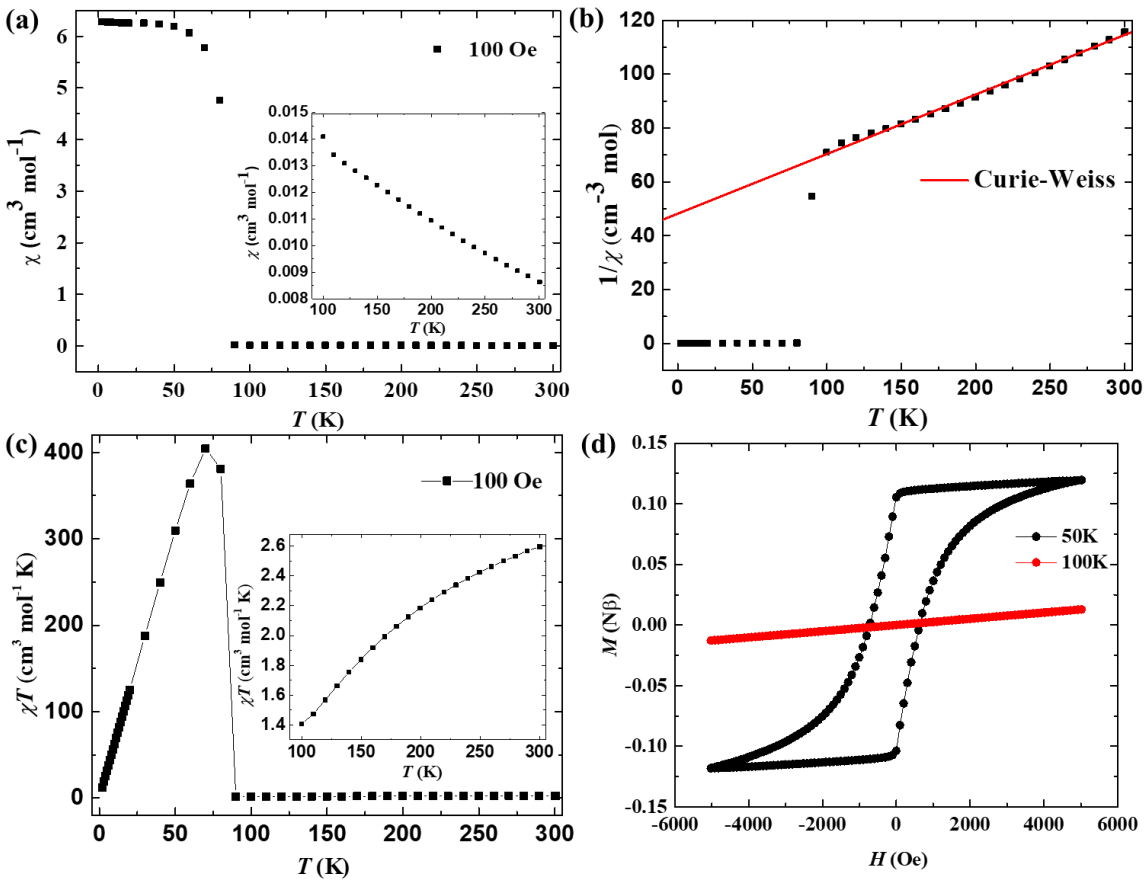

Fig. 3-17 The plots of magnetic data of **2**: (a) χ versus T (The inset shows the plot at high temperature). (b) $1/\chi$ versus T and the Curie-Weiss fit to $1/\chi$. (c) χT versus T (The inset shows the plot at high temperature). Magnetisation (M) versus magnetic field (H) at 100 K and hysteresis loop at 50 K.

The magnetic properties of **2** have also been investigated. Fig. 3-17 (a) depicts the χ versus T plot in the range of 2 K $\leq T \leq$ 300 K in a 100 Oe magnetic field, which also shows a linear temperature dependence in the high temperature region (the inset of Fig.3-17 (a)). However, there is a huge jump of the susceptibility ~80 K, which even makes the curve plot at high temperature look flat and indicates a significant magnetic phase transition at low temperature. The T > 150 K part of the inverse susceptibility plot was fitted with the Curie-Weiss law (Fig. 3-17 (b)), with derived parameters C = 4.35 $cm^3 mol^{-1}$ K and the Weiss constant, $\theta = -199$ K, also indicating an overall antiferromagnetic interactions like **1**. The Landé factor,

g = 2.9 (S = 3/2), and effective moment, μ_{eff} = 5.9 μ_B calculated from the Curie constant, are significantly higher than spin-only value (3.87 μ_B) due to a strong orbital contribution. The high-spin octahedron Co^{2+} (d^7, $^4T_{1g}$) is in degenerate ground state, in which the orbital angular momentum is not quenched and cause a significant orbital contribution.

At 300 K, χT is 2.60 $cm^3 mol^{-1}$ K (4.56 μ_B), much lower than C, indicating a significant antiferromagnetic coupling between the Co^{2+} ions at room temperature. Upon cooling, the χT monotonically decreases down to 90 K, where the minimum is reached, χT = 1.65 $cm^3 mol^{-1}$ K (3.63 μ_B), then χT increases abruptly up to a maximum of 404.61 $cm^3 mol^{-1}$ K (56.89 μ_B) at 70 K (T_N), followed by a decreasing trend with further cooling (Fig. 3-17 (c)). The monotonically decreasing trend corresponds to the antiferromagnetic interaction between the cobalt ions becoming stronger (The inset of Fig.3-17 (c)), the peak at T_N corresponds to a magnetic long-range ordering and the following decrease is due to the saturation of χ. In addition, μ_{eff} at T_N is much larger than the spin-only value due to Co^{2+} retaining significant orbital angular momentum. This suggests either long-range ordering (spin-canted antiferromagnet) or a spin-flop effect causing a magnetic phase transition from antiferromagnet to ferromagnet. A similar spin-flop effect has also been observed in another organic-inorganic hybrid layered perovskite $(C_2H_5NH_3)_2CuCl_4$.[18] Fig. 3-17 (d) shows the field dependence (-5000 Oe to 5000 Oe) of the Magnetisation (M), which discloses a strong magnetic hysteresis at 50 K that disappears at 100 K, corresponding to the magnetic ordering below T_N.

Further detailed investigation of magnetic properties of both compounds were carried out by neutron diffraction.

3-2-5 Neutron Diffraction Data and Analysis

To explore the detailed magnetic properties of the two compounds, powder samples of **1** and **2** were characterised by neutron diffraction, which was carried out at GEM (bank 1 to

bank 5, all the Rietveld plots depicted here were based on bank 3) of ISIS Neutron and Muon Source (Chapter 2, **2-3-1**). Before the measurement, a pre-test of 5 g normal and 5 g deuterated compound **1** was performed at room temperature to check the influences of H atoms in neutron diffraction. The deuterated sample was synthesised in a similar solvothermal method as the previous sample by only changing H_2O solvent to D_2O. Thus, in the deuterated sample, some N-H of the ethylenediamine were substituted by N-D.

Rietveld refinements were also carried out for both samples with profile, lattice parameters, atomic positions and Uiso being refined, by GSAS[2] and EXPGUI software suites[3]. The fraction of deuterium was refined for the deuterated sample and the atomic positions and Uiso for relative H/D atoms were constrained to be the same. The results showed that the deuterated sample has a smaller background (Fig. 3-18 top (normal sample) and mid (deuterated sample)) and it is more suitable for neutron diffraction to explore the magnetic properties of the compound. In addition, the goodness of fit, χ^2 = 1.330 for the normal sample and χ^2 = 1.145 for deuterated one based on the overall data from bank 1 to bank 5, which suggested good purities of both samples; the fraction of overall deuterium was also calculated around 76 % based on the refined data.

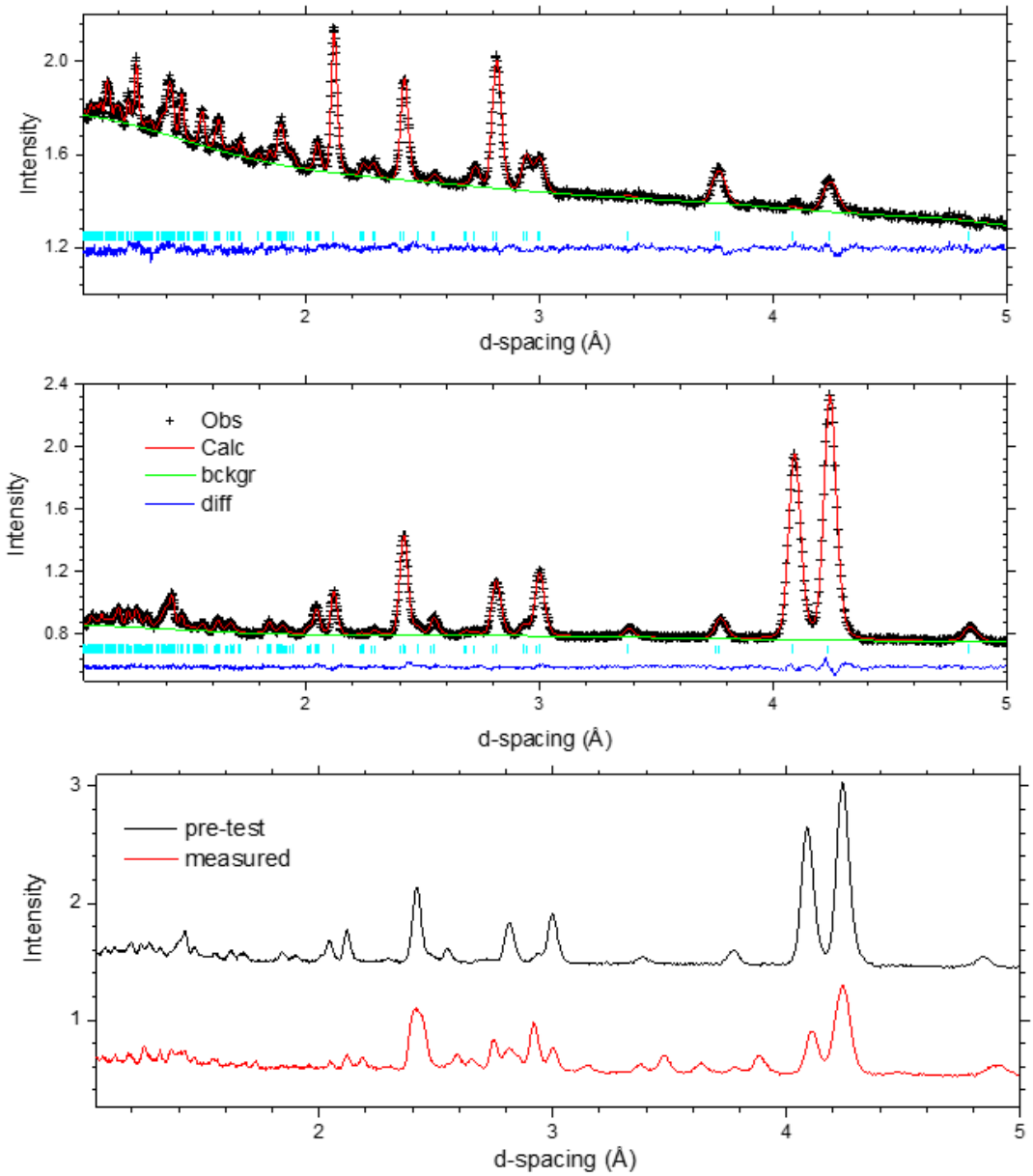

Fig. 3-18 The bank 3 data from GEM neutron diffraction experiment for **1**. Rietveld plot for normal sample (top) and deuterated sample (mid) at 300 K; diffraction patterns for pre-test (300 K) and measured (180 K) data of deuterated sample (bottom).

Thus, another batch of 5 g deuterated **1** synthesised by the same method of the pre-test sample was applied for formal measurement. The highest temperature of formal measurement is 180 K, at which temperature the crystal structure and diffraction peaks should be same at 300 K. However, some obvious impurity peaks were observed in the formal measured sample

of deuterated **1** (180 K) (Fig. 3-18 bottom). Since the impurities cannot be identified, the changes of the peaks of them versus temperature are unpredictable, which will consequently confuse the magnetic properties analysis at low temperature. Thus, those data cannot unfortunately be used to analyse the magnetic properties. However, the Rietveld refinements of the corresponding data of **2** showed good purity of the sample, which can therefore be used to analyse **2** and also to infer similarities for compound **1** due to the isostructural properties and similar magnetic property trends of them.

A weight of 5 g deuterated **2** sample was synthesised through similar solvothermal reaction for neutron diffraction characterisation. The sample was measured in the temperature range 20 K-180 K. Because longer neutron runs will allow more accurate data, two measurements with different time scales were performed for the sample; short run (170 μA) for most normal temperatures and long run (340 μA) for only the highest temperature (180 K), lowest temperature (20 K), and estimated phase transition temperatures (80 K, 82 K, 83 K, 84 K, 85 K, 87 K, 89 K, 91 K, and 93 K). Rietveld refinements of crystal structures were applied for the sample, with profile, lattice parameters, atomic positions and Uiso (the fraction of deuterium was refined around 55 % based on data of 180 K) by GSAS and EXPGUI software suites.[2, 3]

Table 3-7 Cell parameters and the χ^2 values obtained from Rietveld refinement of neutron data for **2**.

***T* (K)**	***a* (Å)**	***b* (Å)**	***c* (Å)**	***β* (°)**	**V(Å^3)**	**χ^2**
20	8.0159(4)	5.8850(3)	5.8643(3)	90.748(3)	276.62(3)	1.714
30	8.0161(4)	5.8849(3)	5.8643(3)	90.751(3)	276.62(3)	1.746
40	8.0165(4)	5.8854(3)	5.8644(3)	90.748(3)	276.66(3)	1.730
50	8.0172(4)	5.8855(3)	5.8650(3)	90.748(3)	276.72(3)	1.720
60	8.0176(4)	5.8861(3)	5.8654(3)	90.749(3)	276.78(3)	1.657
70	8.0180(3)	5.8863(3)	5.8655(3)	90.750(3)	276.81(3)	1.564
72	8.0186(3)	5.8867(3)	5.8656(3)	90.752(3)	276.85(3)	1.538
74	8.0186(3)	5.8864(3)	5.8654(3)	90.749(3)	276.83(3)	1.536
76	8.0187(3)	5.8863(3)	5.8657(3)	90.753(3)	276.84(3)	1.475
78	8.0193(3)	5.8869(3)	5.8662(3)	90.755(3)	276.91(3)	1.454
80	8.0193(3)	5.8867(2)	5.8661(2)	90.752(2)	276.90(3)	2.005
82	8.0191(3)	5.8867(2)	5.8652(2)	90.745(2)	276.85(2)	1.726
83	8.0194(2)	5.8871(2)	5.8656(2)	90.747(2)	276.90(2)	1.404
84	8.0202(2)	5.8874(2)	5.8657(2)	90.746(2)	276.94(2)	1.228
85	8.0201(2)	5.8872(2)	5.8654(2)	90.747(2)	276.92(2)	1.235
87	8.0202(2)	5.8872(2)	5.8657(2)	90.746(2)	276.94(2)	1.184
89	8.0206(2)	5.8873(2)	5.8656(2)	90.751(2)	276.95(2)	1.177
91	8.0208(2)	5.8872(2)	5.8658(2)	90.751(2)	276.96(2)	1.208
93	8.0207(2)	5.8873(2)	5.8657(2)	90.752(2)	276.96(2)	1.179
95	8.0210(3)	5.8874(2)	5.8661(2)	90.749(2)	276.99(3)	0.9767
100	8.0210(3)	5.8872(2)	5.8661(2)	90.747(2)	276.98(3)	1.016
120	8.0226(3)	5.8884(2)	5.8680(2)	90.756(2)	277.18(2)	0.9442
150	8.0237(3)	5.8908(2)	5.8704(2)	90.772(2)	277.44(3)	0.9558
180	8.0246(2)	5.8930(2)	5.8732(2)	90.791(2)	277.71(2)	1.186

The cell parameters and the overall goodness of fit values (based on the sum of 5 banks) of the GSAS[2] refined models at each temperature are summarised in Table 3-7. At temperatures higher than the magnetic critical temperature, the changes of the crystal structural lattice parameters basically corresponded with synchrotron PXRD data. However, some data do not follow this rule, which may be caused by the system errors of small temperature gaps (1K or 2K) of some neighbouring temperatures. The χ^2 values at low temperatures are normally larger

than higher temperatures, which are caused by the magnetic peaks' influences. This may also indicate that the refined crystal structure models at lower temperatures are less reliable. In addition, the obvious difference of χ^2 between 83 K and 84 K may suggest the magnetic ordering temperature of **2** is 83 K.

The examples of Rietveld plots of crystal structures at 20 K, 83K, 84 K and 180 K are depicted in Fig. 3-19; three major magnetic peaks were visible at 5.88, 4.75 and 3.30 Å in the 20 K plot. The magnetic peaks at 4.75 and 3.3 Å are overlapping with the crystal structure (110) peak and (210) peak respectively, which explains why the magnetic peaks influenced the refinements of crystal structure at low temperature. The 5.88 Å peak has been indexed on the unit cell but there is no Bragg reflection from the crystallographic structure, presumably due to a systematic absence. Due to the peak at 5.88 Å being present at 83 K but disappearing at 84 K, the Néel temperature of **2** can be deduced as 83 K based on the measured data.

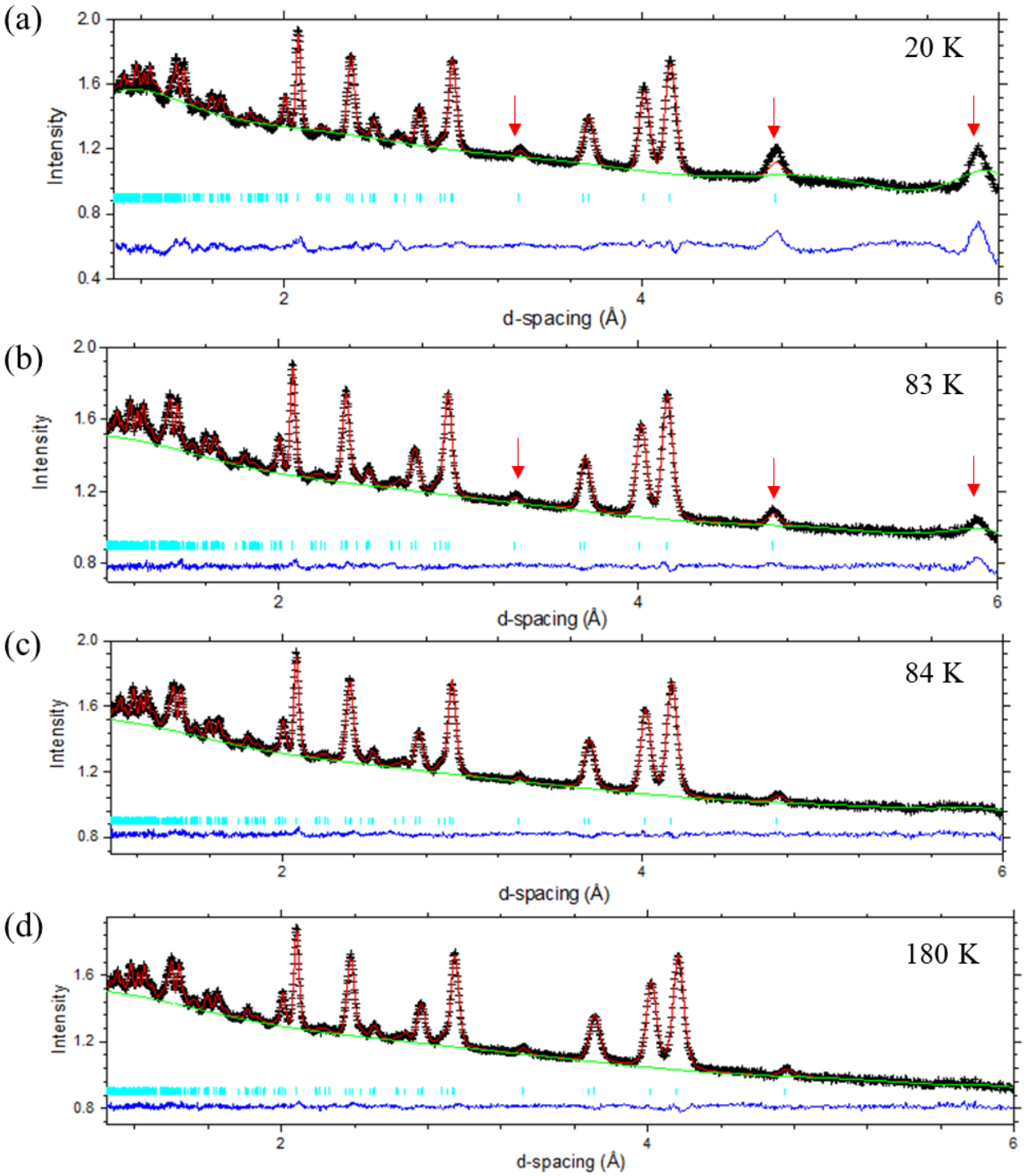

Fig. 3-19 Rietveld plots for neutron diffraction based on bank 3 at (2) 20 K, (b) 83 K, (c) 84 K and (d) 180 K. (major magnetic peaks are shown by red arrows.)

In further progress, the magnetic structure refinements were carried out by Jana2006 software[19]. The magnetic CIF files of different space groups for the refinements were generated

by ISODISTORT[20] based on different magnetic wave vectors, *k*. The parent structure for ISODISTORT was taken from the Rietveld refined model of 180 K data. After the ISODISTORT searching with different *k* vectors, there are two possible magnetic space groups, $P2_1/c$ (14.75) and $P2_1'/c'$ (14.79) with *k* = (0,0,0) (derived from crystal space group $P2_1/c$ (14)) and another 16 possible magnetic super spaces with various *k* vectors. ISODISTORT will generate one CIF file for each possible space group and the distortions and diffraction patterns of these models can be viewed by two interactive visualisation applications: ISOVIZ (structures) and ISOVIZQ (diffraction patterns).[20] In addition, the two applications can be used to predict the magnetic diffraction patterns and interact with the corresponding magnetic moment vectors.

For example, Fig. 3-20 shows the interactive panels for ISOVIZ (top) and ISOVIZQ (bottom) of the magnetic super space *Ps*1 (1.3) with *k* = (1/2, 0, 1/2). In the panels, the crystal or magnetic structures and corresponding diffraction patterns (left part) can be changed and visualised by adjusting the slider-bars (right part). Because the compound **2** has been proved to exhibit no phase transition in the measured temperature range, the only adjustable section is the part of magnetic moment vectors (top six slider-bars). However, the peak at 5.01 Å is not present in the experimental data and it cannot be eliminated. This suggests *Ps*1 is not a suitable candidate space group. Similar phenomena were also observed in the other 15 super space groups: all the predicted diffraction patterns in those magnetic super spaces contain extra theoretical peaks which are not found in the experimental data. In addition, the peak at 5.88 Å in the experimental data is missing in all the 16 magnetic super space groups, no matter how the slider-bar is adjusted. Rietveld refinements of the 20 K data were also carried by Jana2006[19] based on the 16 magnetic super space group CIFs, and none of them achieved convergence. Thus, all the 16 magnetic super space groups are excluded as plausible models, leaving only two monoclinic magnetic space groups.

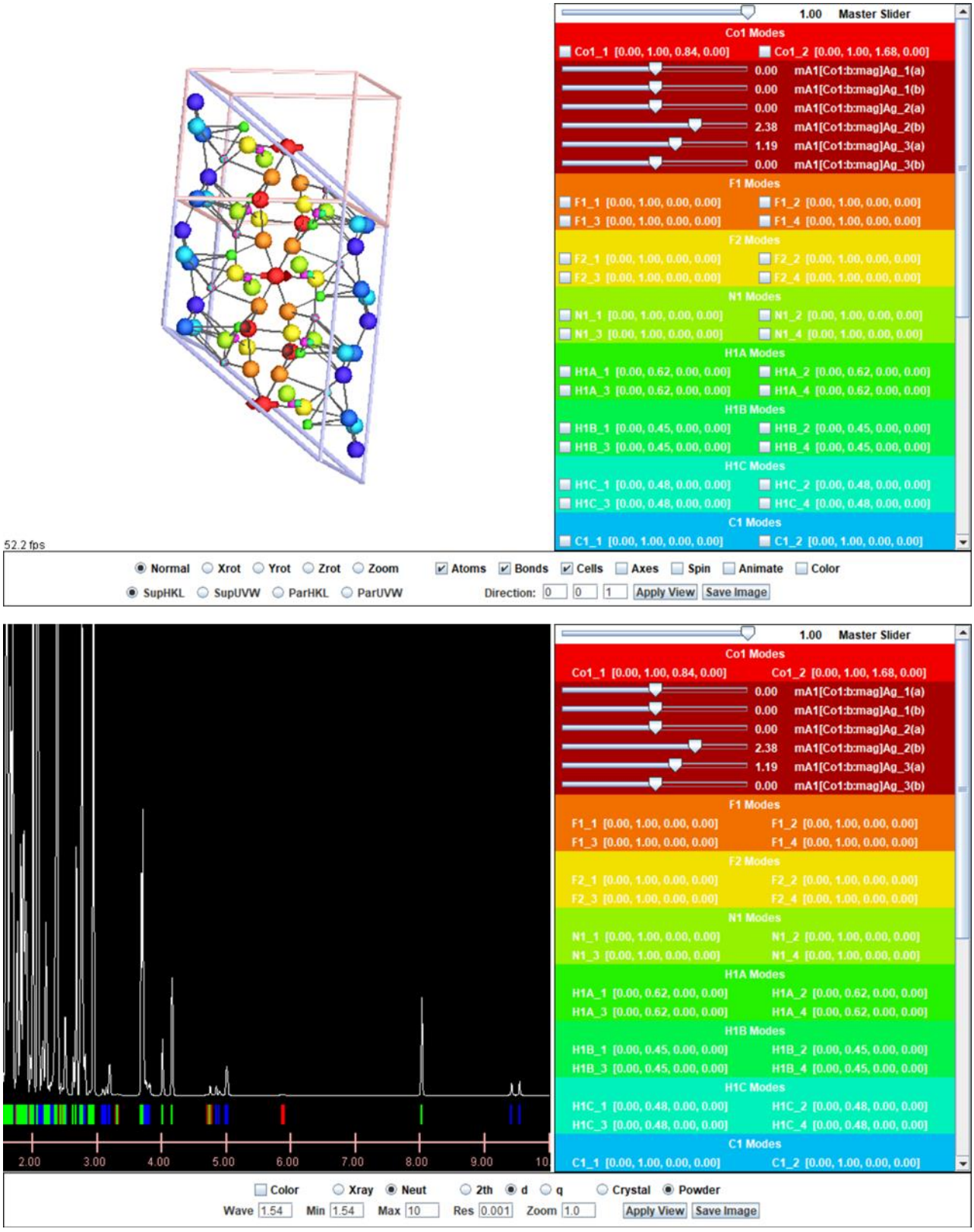

Fig. 3-20 Interactive panels of ISOVIZ (top) and ISOVIZQ (bottom) based on *Ps*1 space group.

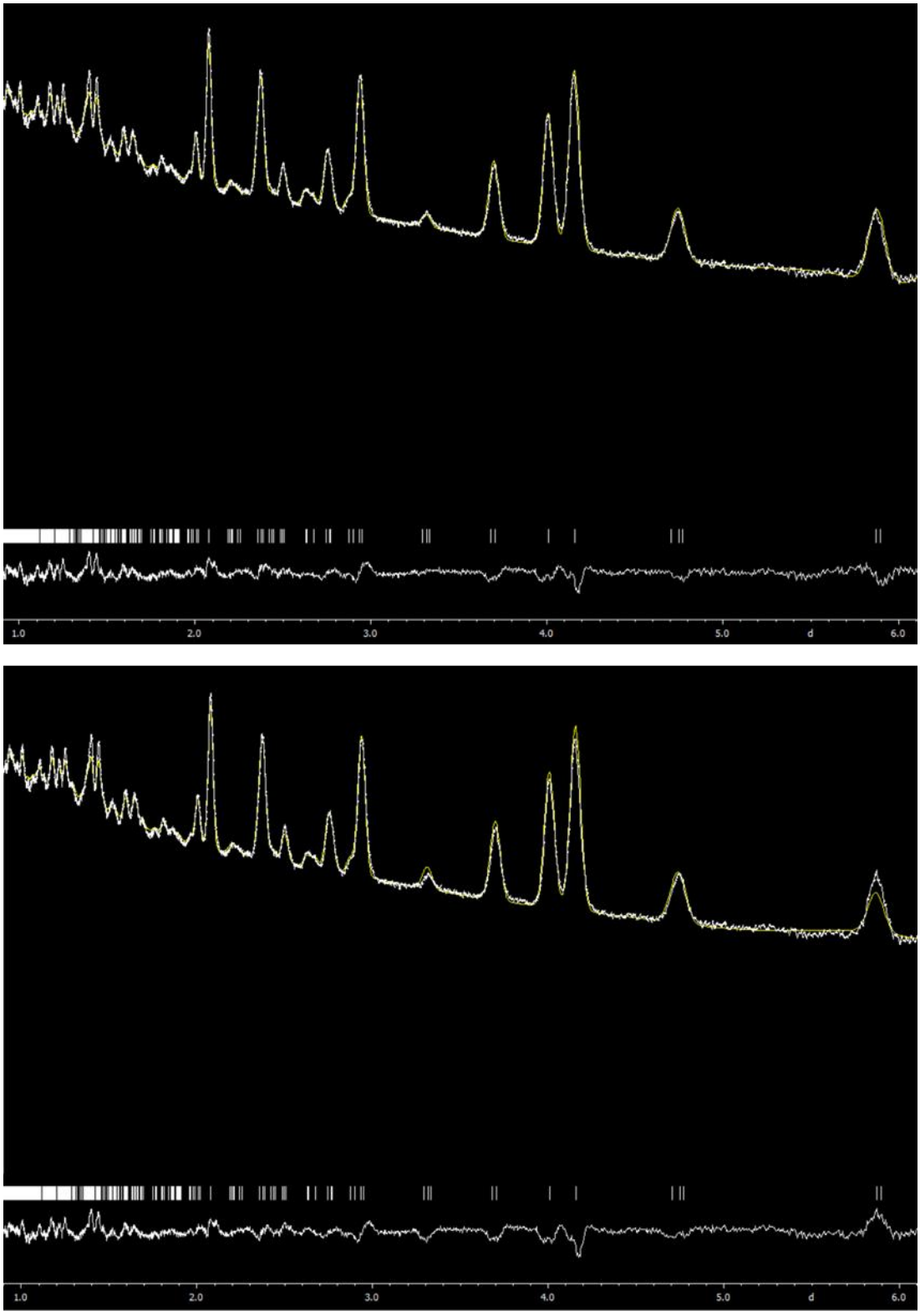

Fig.3-21 Rietveld plots for neutron diffraction (bank 3) of 20 K data in space groups $P2_1/c$ (top) and $P2_1'/c'$ (bottom) by Jana2006.

In order to confirm which is the right space group from $P2_1/c$ and $P2_1'/c'$, ISOVIZ and ISOVIZQ were firstly used to check the interactions between the spin directions and diffraction pattern changes in both space groups. In $P2_1'/c'$ space group, the peak at 5.88 Å is missing in the ground state, which is a reference to the reflection being missing in the absence of magnetic order. However, when the slider-bars are adjusted, the changing of peak intensity at 3.30 Å is more rapid than the intensities at 4.75 Å and 5.88 Å, which consequently means the intensity at 3.30 Å is always higher than the 5.88 Å peak. This conflicts with the experimental results (the intensity of 3.30 Å peak is much lower than 5.88 Å peak). Rietveld refinements of the data at 20 K in both space groups were also carried out by Jana2006 with the result for $P2_1/c$ is Rwp = 1.50, Rp = 1.25 and GOF = 2.26 but the result for $P2_1'/c'$ didn't converge. The Rietveld plots for both space groups are also depicted in Fig. 3-21, which also shows the only suitable space group is $P2_1/c$.

By comparing the plots of Rietveld refinements at 20 K and 83 K. There is no peak shifting, only magnetic peak intensity changes between the two temperatures. The predicted magnetic structures of both temperatures are shown in Fig. 3-22, with Co (Mx0, My0, Mz0) = (3.52(7), 0, 0.53(1)) at 20 K and (Mx0, My0, Mz0) = (1.65(1), 0, 0.12(7)) at 83 K. The coupling of the magnetic cations within the plane are antiferromagnetic, and the alignment of spins of neighbouring cations within layers are in same direction. The result based on the current model suggests an overall canted antiferromagnetic ordering when the temperature is lower than 83 K. On further cooling, the change of spin direction is tiny, but the magnetisation increase is obvious during cooling. From current magnetic data and analysis, the spin canting can only be inferred from the physical properties obtained.

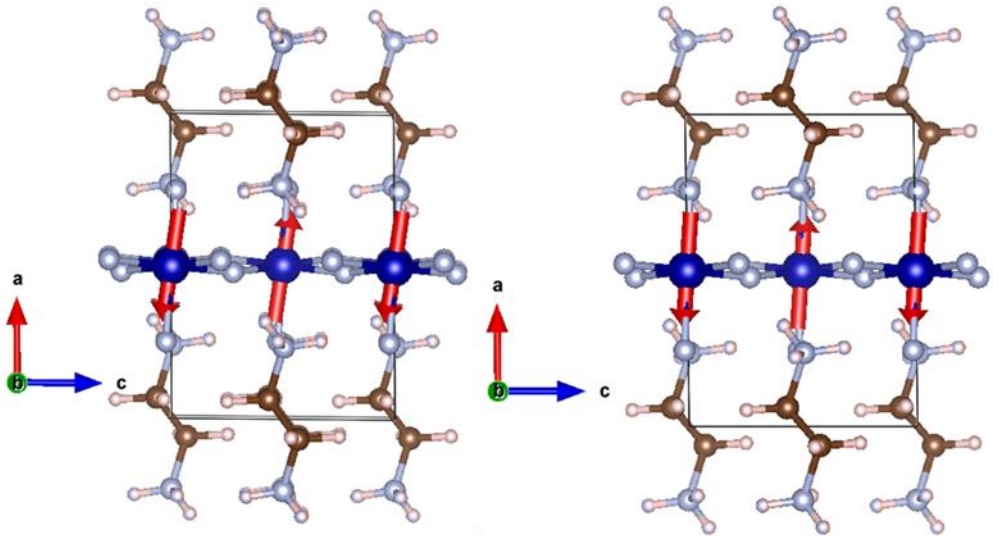

Fig. 3-22 Determined magnetic structures of **2** at 20 K (left) and 83 K (right).

3-3 *1,3-DAP* Based Hybrid Fluoride Layered Perovskites

3-3-1 Synthesis

3-3-1-1 (*1,3-DAP*H_2)MnF_4 (4)

0.460 g (5.0 mmol) ground MnF_2, 2.5 mL (29.8 mmol) *1,3-DAP*, 2.25 mL (62.5 mmol) HF (48-51 % wt. in water), 3 mL H_2O and 3 mL EG were mixed and sealed in a 50 mL Teflon-lined stainless-steel autoclave, which was placed in a 120 °C oven and maintained for 48 hours. The product, colourless plate single crystals of **4** with ~5.4% MnF_2 impurities, was generated after cooling to room temperature and washed by ethanol (EtOH). The single crystal structure data were collected at 173 K and 298 K. The impurity phase was revealed by powder XRD and analysed by the Rietveld method. However, as well as MnF_2, there are some other amorphous phase impurities, which was deduced from elemental analysis (anal. calc. (%) for $C_3H_{12}F_4MnN_2$: C, 17.40; H, 5.84; N, 13.53. Found: C, 15.56; H, 4.76; N, 13.47).

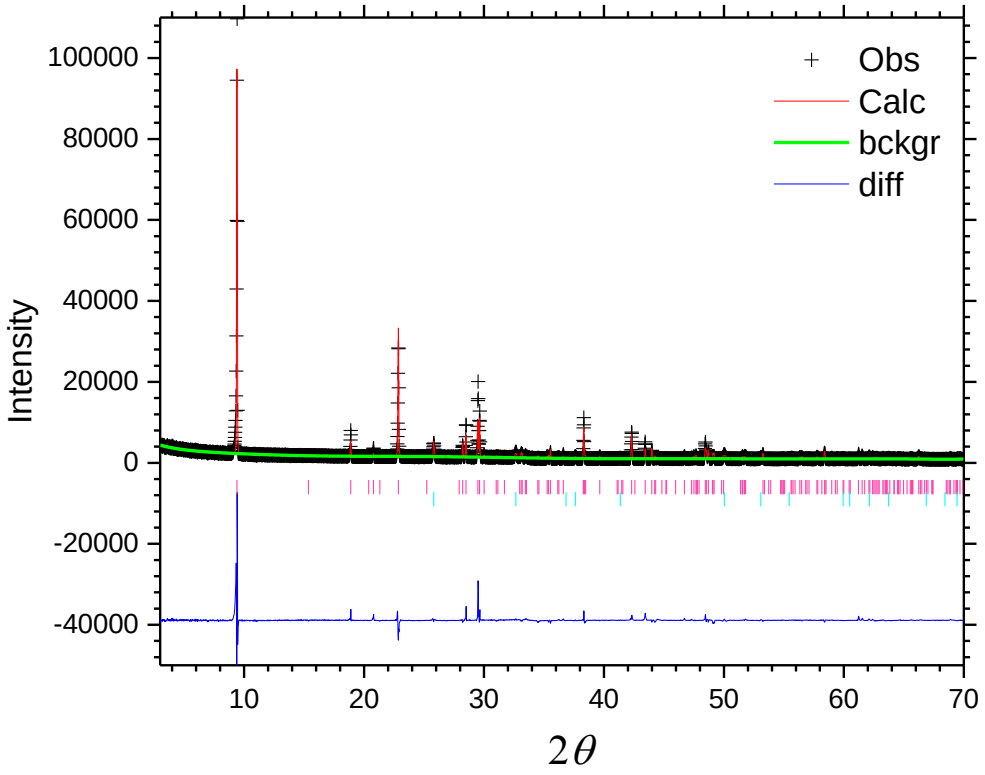

Fig. 3-23 Rietveld plot (PXRD, CuKα1) for **4**.

The crystalline samples were also ground for 30 mins into a homogeneous powder and loaded into a steel disc. PXRD (CuKα1) data collection and Rietveld refinement were based on the same conditions as **1**, with a result of wRp = 0.1408, Rp = 0.0780 and χ^2 = 34.42. The fixed crystallographic models were used, based on the CIF file from the single crystal refinement at 298 K, with only profile and lattice parameters being refined. The preferred orientation was also observed, with (0l0) reflections exhibiting artificially high intensity (Fig. 3-23).

3-3-1-2 (*1,3-DAP*H$_2$)CoF$_4$ (5)

0.194 g (2.0 mmol) ground CoF_2, 1.0 mL (11.9 mmol) *1,3-DAP*, 0.90 mL (25.0 mmol) HF (48-51 % wt. in water), and 4 mL EG were mixed and sealed in a 30 mL Teflon-lined stainless-steel autoclave, which was then placed in a 130 °C oven and maintained for 6 days.

The product, colourless plate single crystals of **5** with ~12% CoF_2 impurities, was generated after cooling to room temperature and washed by Ethanol (EtOH). The single crystal structure data were collected at 173 K and 298 K. The impurity phase was revealed by powder XRD and analysed by the Rietveld method, with the support of elemental analysis (anal. calc. (%) for $C_3H_{12}F_4CoN_2$: C, 17.07; H, 5.73; N, 13.27. Found: C, 11.55; H, 4.07; N, 8.80).

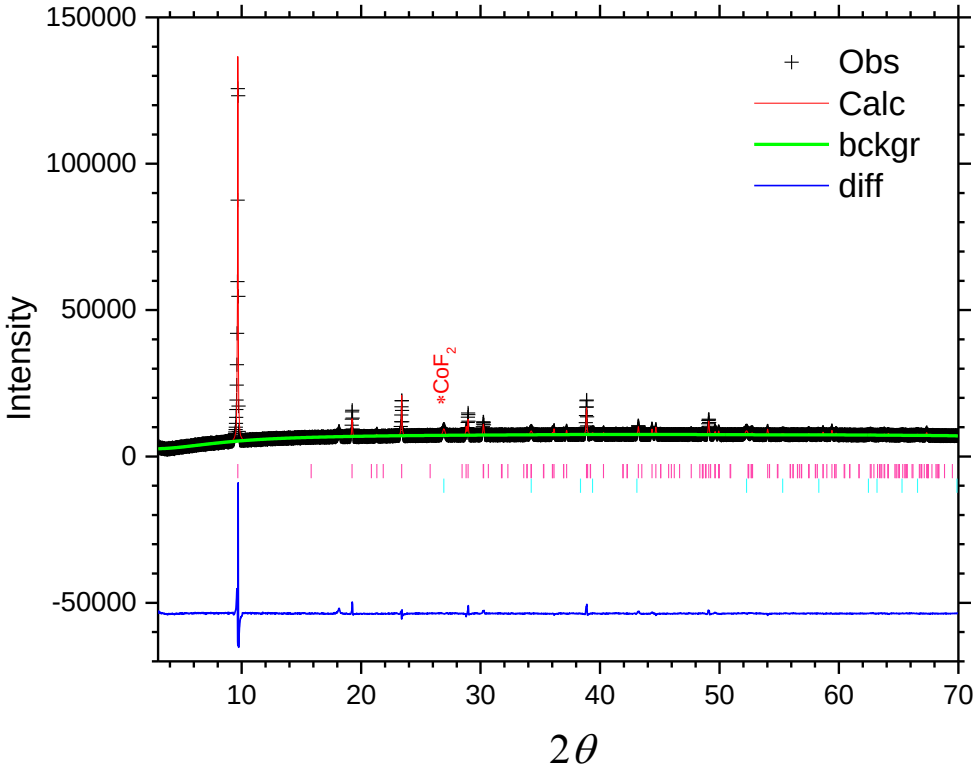

Fig. 3-24 Rietveld plot (PXRD, CuKα1) for **5**. The peak near $2\theta \sim 18°$ is due to the Teflon sample holder (see Fig. 3-3).

The crystalline samples were also ground for 30 mins into a homogeneous powder and loaded into a steel disc with a Teflon liner. PXRD (CuKα1) data collection and Rietveld refinement were based on the same conditions as **1**, with a result of wRp = 0.0619, Rp = 0.0218 and χ^2 = 27.70. The fixed crystallographic models were used, based on the CIF file from the single crystal refinement at 298 K, with only profile and lattice parameters being refined. The

fraction of CoF_2 impurity was determined to be 11.7 (8) % by weight. The preferred orientation was also observed, with (h00) reflections exhibiting artificially high intensity (Fig. 3-24).

3-3-2 Single Crystal Data and Analysis of 4 and 5

Like (*en*H_2)MF_4, single crystal data of (*1,3-DAP*H_2)MF_4 were collected at 173 K and 298 K by using the same facilities, and the structures were processed by same software. Compounds **4** and **5** are also isostructural, and no phase transition was observed in the temperature regime studied. Both compounds crystallised in the orthorhombic system with space group *Pnma*. There are only small changes of cell parameters with temperature (Table 3-8). For the same temperature, all the cell parameters of **5** (Co) are smaller than **4** (Mn), which is same trend with the (*en*H_2)MF_4, reflecting the differences ion ionic radii of the 3*d* metals.

Table 3-8 Crystallographic data and refinement details of compounds **4** and **5**.

Compound (*T*)	**4** (173 K)	**4** (298 K)	**5** (173 K)	**5** (298 K)
Formula	$(C_3H_{12}N_2)MnF_4$	$(C_3H_{12}N_2)MnF_4$	$(C_3H_{12}N_2)CoF_4$	$(C_3H_{12}N_2)CoF_4$
Formula weight	207.09	207.09	211.08	211.08
Density (g cm^{-3})	2.020	2.015	2.147	2.136
Crystal system	Orthorhombic	Orthorhombic	Orthorhombic	Orthorhombic
Space group	*Pnma*	*Pnma*	*Pnma*	*Pnma*
a/Å	6.0080(4)	6.0083(5)	5.9215(4)	5.9384(4)
b/Å	18.7802(13)	18.7807(17)	18.6127(14)	18.5971(15)
c/Å	6.0349(4)	6.0502(5)	5.9258(4)	5.9430(5)
V/$Å^3$	680.93(8)	682.71(10)	653.11(8)	656.33(9)
Z	4	4	4	4
Measured ref	4627	4845	6032	4444
Independent ref	614	621	638	587
	[*R*(int) = 0.158]	[*R*(int) = 0.099]	[*R*(int) = 0.072]	[*R*(int) = 0.058]
GOOF	0.972	1.064	1.004	1.046
Final *R* indices ($I > 2\sigma(I)$)	*R*1 = 0.0388, *wR*2 = 0.0819	*R*1 = 0.0317, *wR*2 = 0.0656	*R*1 = 0.0324, *wR*2 = 0.0715	*R*1 = 0.0328, *wR*2 = 0.0804

(*1,3-DAP*H_2)MF_4 is also a layered perovskite (DJ phase, n = 1) and the single crystal structure is depicted in Fig. 3-25, which shows that the perovskite layer is similar to that in (*en*H_2)MF_4. However, in this structure the perovskite $[MF_4]_\infty$ layers are in the *ac*-plane and the protonated *1,3-DAP*H_2^{2+} amine chains are crystallised along the *b*-axis (normally taken as the *c* direction in the layered perovskite structure). Thus, *b* is the longest axis, *a*, *c* axes are similar in length with *c* is slightly longer than *a*. It should be noted that for each of these structures there is a 'doubling' of the *b*-axis, relative to the corresponding axial length observed in **1-3**. This occurs due to a difference in the octahedral tilt system here, such that alternating layers along *c* are tilted out of the *ac*-plane in opposing senses. For previously reported halide analogues in the formula of $[H_3N(CH_2)nNH_3]MX_4$ with odd *n*, the *c*-axis is also doubled, and phase transitions were observed at higher temperature.[7-9] Due to the lack of sample and MF_2 impurities, the phase transitions of **4** and **5** at higher temperature have not been investigated yet.

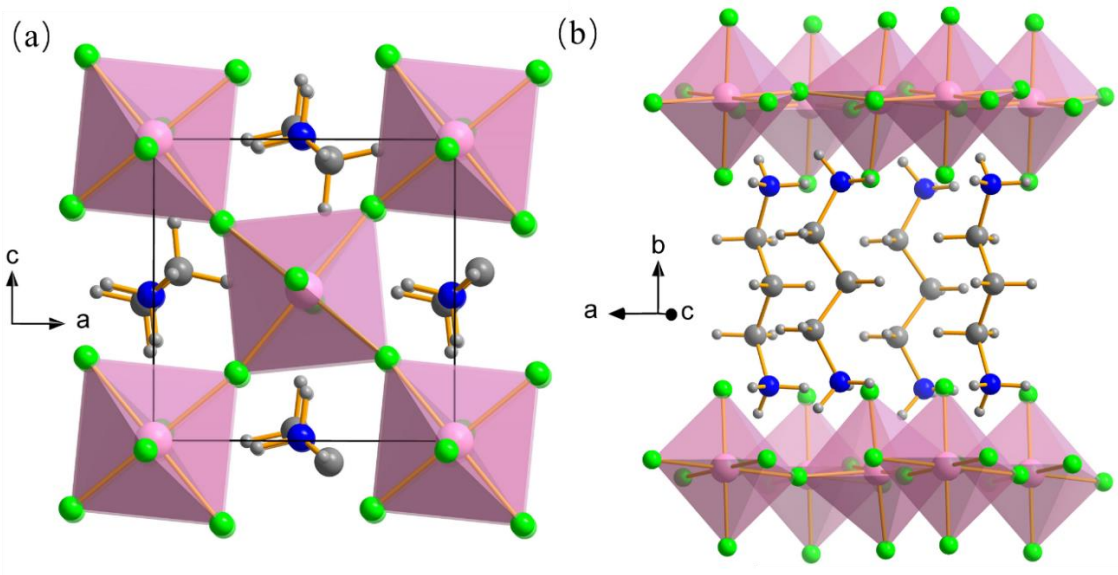

Fig. 3-25 Crystal structure of (*1,3-DAP*H_2)MF_4. (a) along *b* and (b) perpendicular to *b*. Note that only a *b*/2 repeat is shown, since adjacent layers have opposite senses of tilt out of the *ac*-plane.

Table 3-9 Selected bond lengths (Å) and bond angles (°).

	4 (173 K)	**4** (298 K)	**5** (173 K)	**5** (298 K)
M-F2	2.094(3)	2.095(2)	1.9981(16)	1.996(2)
M-F1	2.160(2)	2.1610 (18)	2.1073(14)	2.1143(17)
M-F1	2.162(2)	2.1624 (18)	2.1205(14)	2.1220(17)
M-F-M	4.2264(3)	4.2633(2)	4.1887(2)	4.2007(2)
M-F-M angle	160.27(14)	160.88(10)	164.38(8)	165.12(11)
N1-(H)---F1	2.786(5)	2.807(4)	2.788(3)	2.809(4)
N1-(H)---F2	2.679(4)	2.678(3)	2.683(2)	2.695(3)
N1-(H)---F2	2.738(5)	2.741(3)	2.753(3)	2.756(3)
N1-H-F1 angle	172.6	172.6	173.7	173.1
N1-H-F2 angle	176.7	176.7	176.0	177.4
N1-H-F2 angle	158.0	158.3	158.0	156.9

Selected bond lengths (Å) and bond angles (°) are shown in Table 3-9, which are very similar with the corresponding ethylenediamine series compounds. The shortest M-F-M distances intraplane are 4.2264(2) Å and 4.1887(2) Å (173 K) which are similar with the corresponding ethylenediamine series compounds and should construct similar magnetic connections through M-F-M bridge. The shortest M-M through-space distances between the layers are 9.3901(7) Å and 9.3063(7) Å (173 K) which are much longer than the in-plane distances. This supports that the materials should have 2D magnetic properties, rather than 3D.

3-3-3 Magnetic Data and Analysis

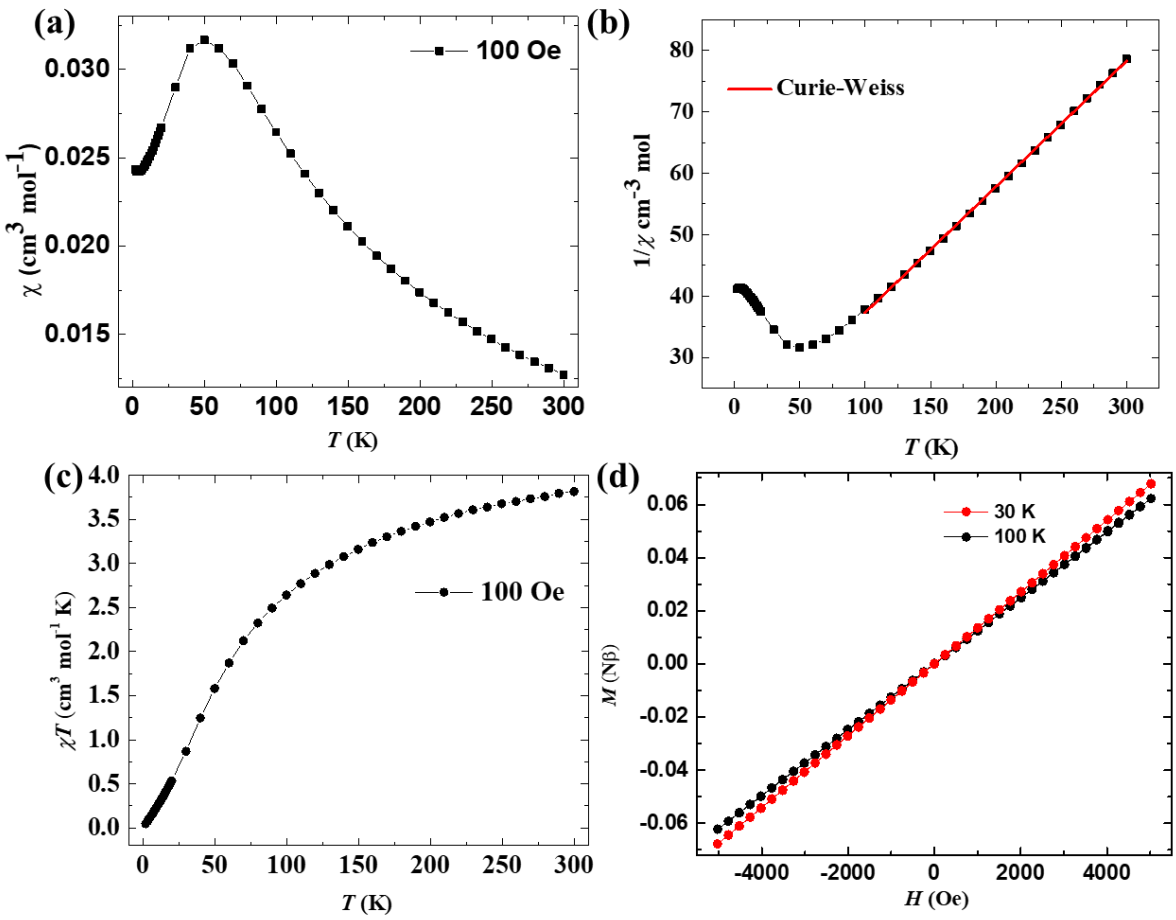

Fig. 3-26 The plots of magnetic data of **4**: (a) χ versus T at 100 Oe. (b) $1/\chi$ versus T and the Curie-Weiss fit to $1/\chi$ at 100 Oe. (c) χT versus T at 100 Oe. (d) Magnetisation (M) versus magnetic field (H) at 30 K (red) and 100 K (black).

The magnetic properties of **4** (with ~5.4 % antiferromagnetic MnF_2 impurities, T_N = 67 K[21]) have also been investigated by SQUID magnetometry. The χ versus T plot in the range of 2 K $\leq T \leq$ 300 K at 100 Oe is depicted in Fig. 3-26 (a). χ monotonically increases during cooling, reaching a maximum at 50 K, then monotonically decreases with cooling. The appearance of a Curie tail at low temperature corresponds to the presence of a small amount of paramagnetic Mn^{2+} impurities. The Curie constant, C = 4.88 $cm^3\,mol^{-1}$ K and Weiss constant, θ = −82.07 K were deduced from the T >100 K part of the $1/\chi$ versus T plot (Fig. 3-26 (b)),

indicating an overall antiferromagnetic exchange interaction. The Landé factor, g = 2.11 and effective moment, μ_{eff} = 6.25 μ_B are nearly the same as those the corresponding Mn^{2+} compound **1**. The χT value at 300 K is 3.82 cm^3 mol^{-1} K and decreases monotonically with cooling with no evidence of magnetic long-range ordering (Fig. 3-26 (c)). The magnetisation (M) versus magnetic field (H) plot also shows no magnetic hysteresis between 30 K to 100 K, which also suggests no magnetic ordering but only overall antiferromagnetic exchange between the Mn^{2+} cations (Fig. 3-26 (d)). It is very unusual that the isothermal magnetisation measurement does not change significantly between the paramagnetic and antiferromagnetic phases, appearing to indicate that compound **4** remains antiferromagnetic well above its ordering temperature.

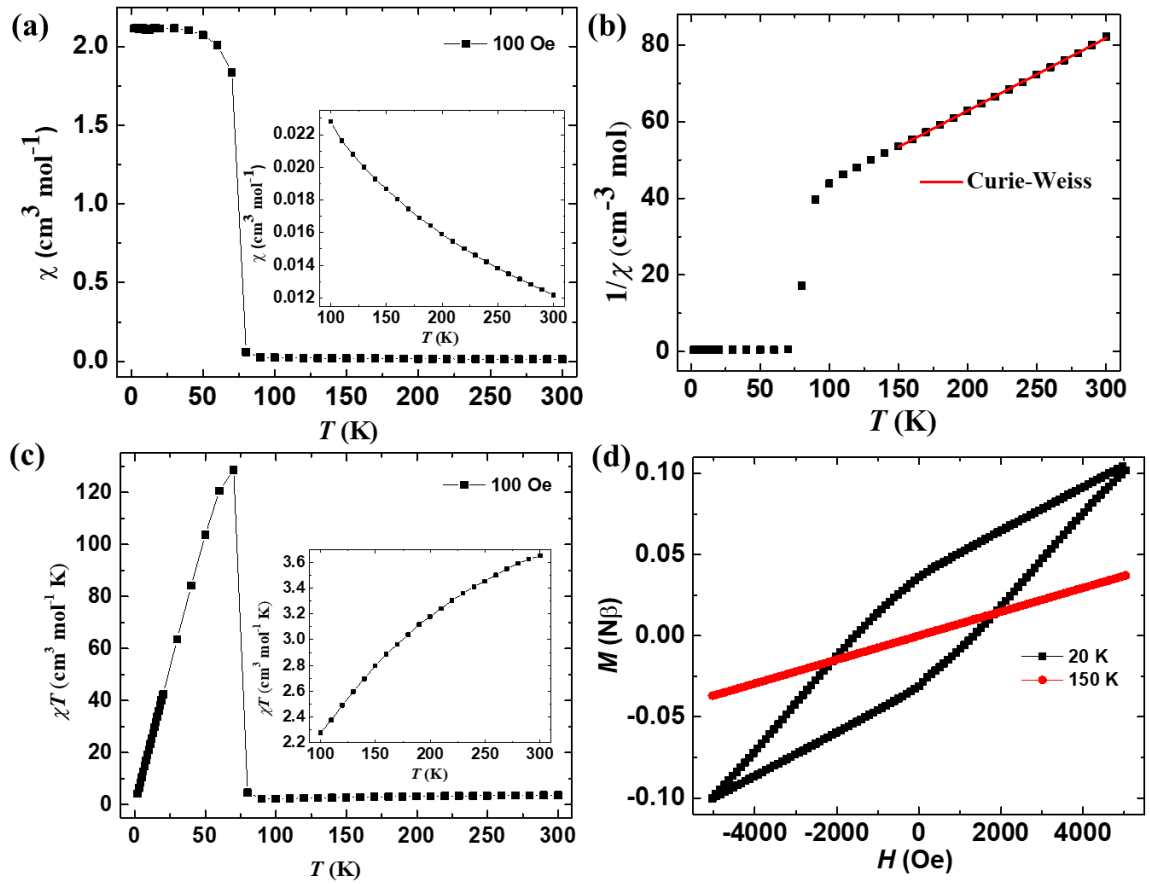

Fig. 3-27 The plots of magnetic data of **5**: (a) χ versus T at 100 Oe (the inset shows the plot at high temperature). (b) $1/\chi$ versus T and the Curie-Weiss fit to $1/\chi$. (c) χT versus T (the inset

shows the plot at high temperature). Magnetisation (*M*) versus magnetic field (*H*) at 150 K and hysteresis loop at 20 K.

The magnetic properties of **5** (with ~12 % antiferromagnetic CoF_2 impurities, T_N = 38.04 K[22]) have also been investigated and depicted in Fig. 3-27. The χ versus *T* plot in the range of 2 K ≤ *T* ≤ 300 K at 100 Oe shows a similar trend to that of compound **2** but at a lower value, which is probably influenced by impurities (Fig. 3-27 (a)). The Curie constant, *C* = 5.28 $cm^3 mol^{-1}$ K and Weiss constant, $\theta = -132.40$ K were calculated from the *T* >150 K part of the $1/\chi$ versus *T* plot (Fig. 3-27 (b)), indicating an overall antiferromagnetic exchange interaction. The Landé factor, g = 3.36 and effective moment, μ_{eff} = 6.50 μ_B, which were calculated from the Curie constant may not reflect the real value due to the impurities. The Néel temperature, T_N = 70 K, was deduced from the χT versus *T* plot (Fig. 3-27 (c)). Fig. 3-27 (d) shows the field dependence (-5000 Oe to 5000 Oe) of the Magnetisation (*M*), which reveals a magnetic hysteresis at 50 K, but weaker than that seen in **2** at the same temperature, perhaps due to the influence of the greater distance between the magnetic layers and the CoF_2 impurities. In summary, **5** is also a spin canting antiferromagnetism like **2**.

3-4 *1,4-DAB* Based Hybrid Fluoride Layered Perovskites

3-4-1 Synthesis

3-4-1-1 (*1,4-DAB*H_2)MnF_4 (6)

The *1,4-DAB*·$(HF)_2$ EG solution was synthesised in an ice/water bath. Firstly, a solution of *1,4-DAB* (5.0 mL, 50.0 mmol) in EG (15 mL) was prepared. Then 3.6 mL (100.0 mmol) HF (48-51 % wt. in water) was slowly added into the EG solution by droplet. Finally, more EG was added to dilute the solution into 50 mL and prepared the *1,4-DAB*·$(HF)_2$ EG solution with the concentration of 2.94 mmol/mL. 0.092 g (1.0 mmol) ground MnF_2 and 2.7 mL (8.0 mmol) *1,4-DAB*·$(HF)_2$ EG solution was mixed and sealed in a 30 mL Teflon-lined stainless-steel autoclave and then was placed in a 120 °C oven for 72 hours. The product, colourless plate

single crystals of **6** with impurities, was generated after cooling to room temperature and washed with ethanol (EtOH). The single crystal structure data were collected at 173 K and 298 K. The product contains a small amount of MnF_2 and other amorphous impurity phases, which was revealed by powder XRD and analysed by Rietveld method with the support of elemental analysis (anal. calc. (%) for $C_4H_{14}F_4MnN_2$: C, 21.73; H, 6.38; N, 12.67. Found: C, 21.59; H, 6.46; N, 12.52).

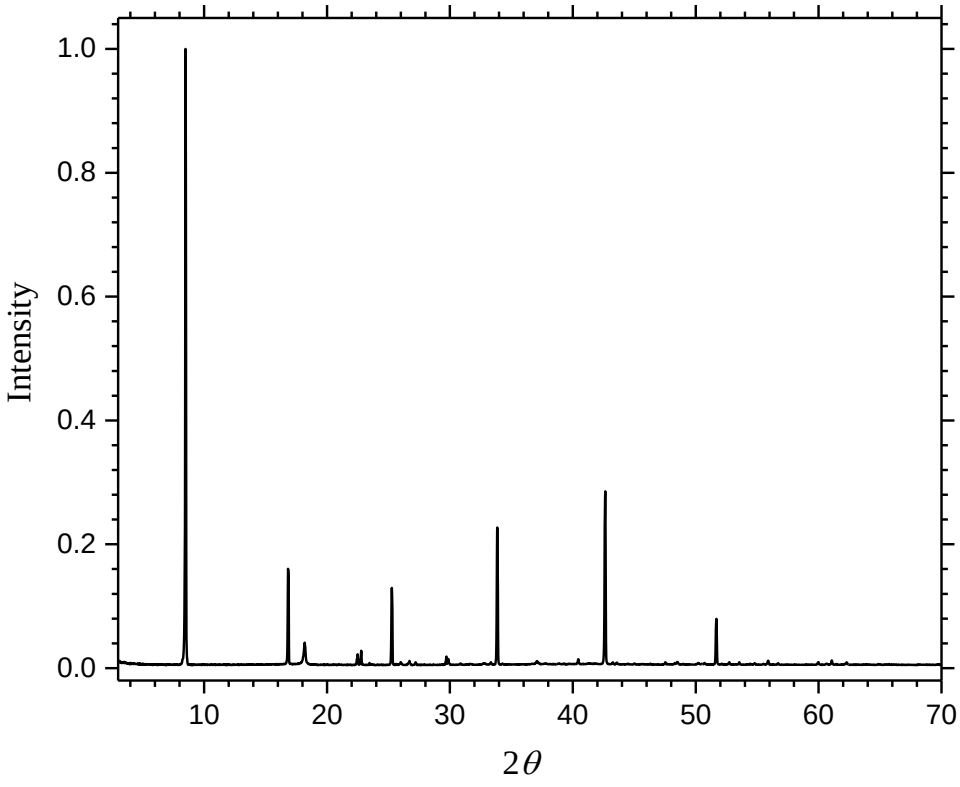

Fig. 3-28 Raw PXRD data (CuKα1) with preferred orientation effect (h00 reflections) for **6**.

The crystalline samples were also ground and loaded into a steel disc with a Teflon liner. PXRD (CuKα1) data collection and Rietveld refinement were based on the same condition as **1**, with a result of wRp = 0.1463, Rp = 0.0831 and χ^2 = 26.23. The fixed

crystallographic models were used, based on the CIF file from the single crystal refinement at 298 K, with only profile and lattice parameters being refined. The fraction of MnF_2 impurity was determined to be 3.4 (6)% by weight. The preferred orientation was also observed, with (h00) reflections exhibiting artificially high intensity (Fig. 3-28); thus, the reflection peak at (100) is excluded from the refinement (Fig. 3-29).

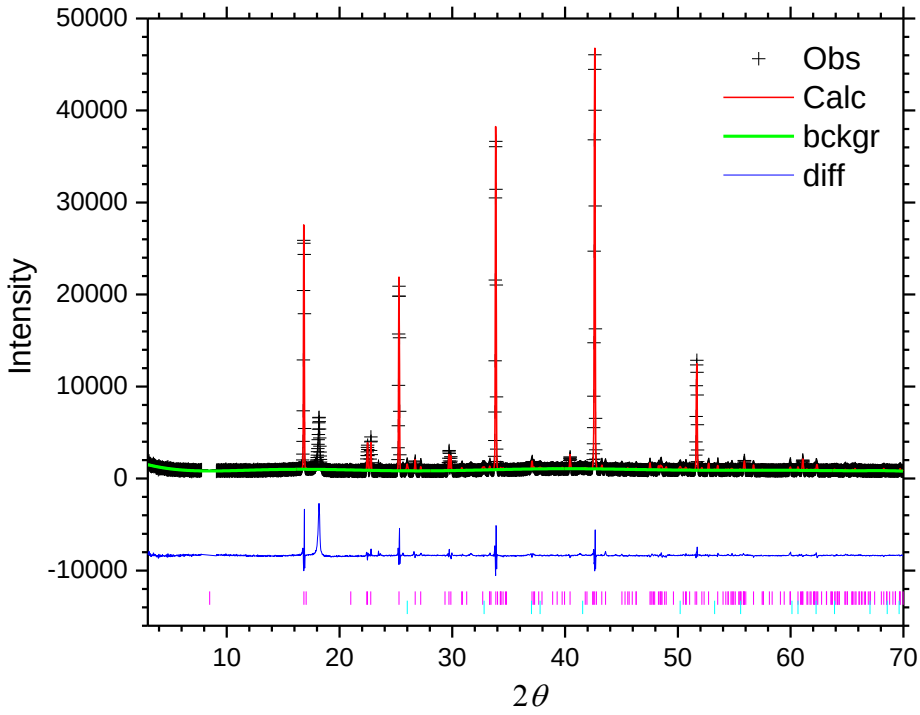

Fig. 3-29 Rietveld plot (PXRD, CuKα1) for **6**. (100) peak has been excluded for clarity. The peak near $2\theta \sim 18°$ is due to the Teflon sample holder (see Fig. 3-3).

3-4-1-2 (*1,4-DAB*H$_2$)CoF$_4$ (7)

0.194 g (2.0 mmol) ground CoF_2, 1.2 mL (12.0 mmol) *1,4-DAB*, 1.35 mL (37.5 mmol) HF (48-51 % wt. in water), and 4 mL EG were mixed and sealed in a 50 mL Teflon-lined stainless-steel autoclave, which was placed in a 130 °C oven and maintained for 6 days. The product, colourless plate single crystals of **7** with ~25% CoF_2 impurities was generated after

cooling to room temperature and washed with ethanol (EtOH). The single crystal structure data were collected at 173 K and 298 K. The CoF_2 impurity was revealed by powder XRD and analysed by the Rietveld method. The elemental analysis (anal. calc. (%) for $C_4H_{14}F_4CoN_2$: C, 21.34; H, 6.27; N, 12.45. Found: C, 12.23; H, 3.90; N, 6.95) suggests some other impurities exist apart from CoF_2.

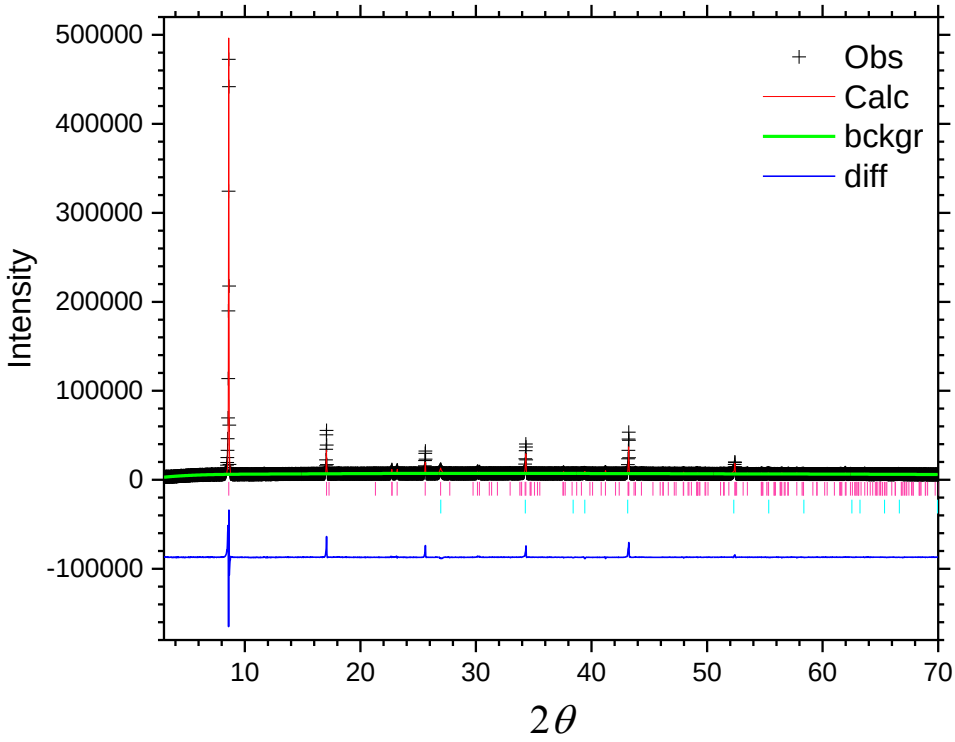

Fig. 3-30 Rietveld plot (PXRD, CuKα1) for **7**.

The crystalline samples were also ground and loaded into a steel disc. PXRD (CuKα1) data collection and Rietveld refinement were based on the same conditions of **1**, with a result of wRp = 0.0937, Rp = 0.0397 and χ^2 = 65.32. The fixed crystallographic models were used, based on the CIF file from the single crystal refinement at 298 K, with only profile and lattice parameters being refined. The fraction of CoF_2 impurity was determined to be 25 (1) % by

weight. The preferred orientation was also observed, with (h00) reflections exhibiting artificially high intensity (Fig. 3-30).

3-4-2 Single Crystal Data and Analysis

Table 3-10 Crystallographic data and refinement details of compounds **6** and **7**.

Compound (*T*)	**6** (173 K)	**6** (298 K)	**7** (173 K)	**7** (298 K)
Formula	$(C_4H_{14}N_2)MnF_4$	$(C_4H_{14}N_2)MnF_4$	$(C_4H_{14}N_2)CoF_4$	$(C_4H_{14}N_2)CoF_4$
Formula weight	221.11	221.11	225.10	225.10
Density (g cm^{-3})	1.909	1.898	2.029	2.018
Crystal system	Monoclinic	Monoclinic	Monoclinic	Monoclinic
Space group	$P2_1/c$	$P2_1/c$	$P2_1/c$	$P2_1/c$
a/Å	10.6452(8)	10.6445(8)	10.5061(7)	10.5009(7)
b/Å	6.0329(4)	6.0475(4)	5.9399(4)	5.9562(4)
c/Å	5.9929(4)	6.0113(4)	5.9078(4)	5.9284(4)
β/°	91.422(6)	91.498(6)	92.251(9)	92.375(9)
V/Å^3	384.75(5)	386.83(5)	368.39(4)	370.48(4)
Z	2	2	2	2
Measured ref	3063	3086	3568	2883
Independent ref	671	673	638	633
	[*R*(int) = 0.053]	[*R*(int) = 0.046]	[*R*(int) = 0.109]	[*R*(int) = 0.092]
GOOF	1.223	1.168	1.022	1.008
Final *R* indices ($I > 2\sigma(I)$)	*R*1 = 0.0327, *wR*2 = 0.0935	*R*1 = 0.0303, *wR*2 = 0.0867	*R*1 = 0.0590, *wR*2 = 0.1472	*R*1 = 0.0630, *wR*2 = 0.1457

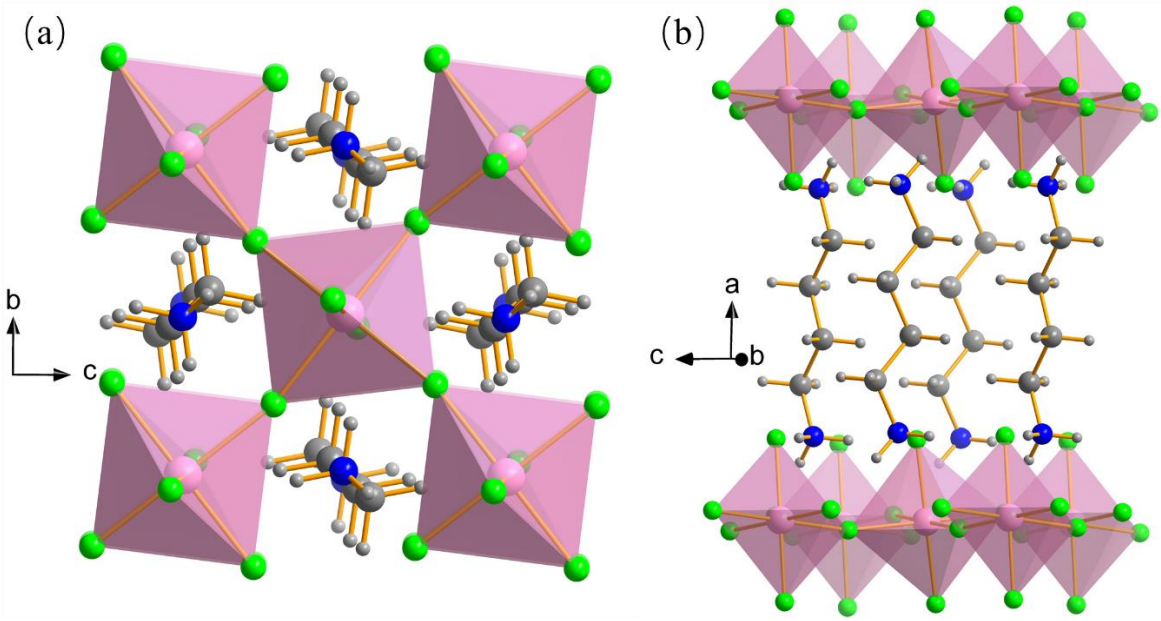

Fig. 3-31 Crystal structure of (*1,4-DAB*)MF_4. (a) perpendicular to *a* and (b) along *a*.

Table 3-11 Selected bond lengths (Å) and bond angles (°).

	6 (173 K)	**6** (298 K)	**7** (173 K)	**7** (298 K)
M-F2	2.0939(19)	2.0964(18)	1.990(3)	1.988(4)
M-F1	2.1549(17)	2.1584(16)	2.102(4)	2.107(4)
M-F1	2.1553(17)	2.1603(16)	2.117(4)	2.122(4)
M-F-M	4.2518(2)	4.2634(2)	4.1888(2)	4.2019(2)
M-F-M angle	161.12(10)	161.64(10)	166.27(19)	166.85(19)
N1-(H)---F1	2.777(4)	2.789(3)	2.786(6)	2.804(7)
N1-(H)---F2	2.687(3)	2.691(3)	2.711(6)	2.713(6)
N1-(H)---F2	2.755(4)	2.768(3)	2.772(7)	2.780(7)
N1-H-F1 angle	174.9	175.1	173.3	173.3
N1-H-F2 angle	175.8	175.1	175.5	176.2
N1-H-F2 angle	156.6	157.2	155.8	155.1

The compounds **6** and **7** are also isostructural, and single crystal structures were determined from one single crystal sample for each compound at 173 K and 298 K, using the same facilities and software as the previous structures in this chapter. The single crystals were crystallised in the monoclinic system with space group $P2_1/c$ at both temperatures, and only

small changes of bond lengths and bond angles were observed at different temperatures (Table 3-10). Similar with the ethylenediamine series compounds, *a* is the longest axis (*c* direction in the conventional description of a layered perovskite structure), *b* is also slightly longer than *c* in both temperatures. In addition, the single crystal of **7** was also found twinned during the processing of data. Thus, the twin data were processed by the TWINROTMAT algorithm in the PLATON suite,[4] via the matrices matrix $\begin{pmatrix} 1 & 0 & 0.14 \\ 0 & -1 & 0 \\ 0 & 0 & -1 \end{pmatrix}$. The crystal structure is depicted in Fig. 3-31. This is another *n* = 1 DJ phase layered perovskite, similar to the previous examples, in which the single perovskite $[MF_4]_\infty$ layers (*bc*-plane) are separated by the protonated (*1,4-DABH*$_2$) along the *a*-axis. The shortest M-F-M distances intraplane are 4.2518(2) Å for **6** (173 K) and 4.1888(2) Å for **7** (173 K) and the shortest M-M through-space distances between the layers are 10.6452(8) Å and 10.5061(7) Å (173 K), which are also similar with the former compounds and should construct similar intraplane 2D magnetic interactions (Table 3-11).

3-4-3 Magnetic Data and Analysis

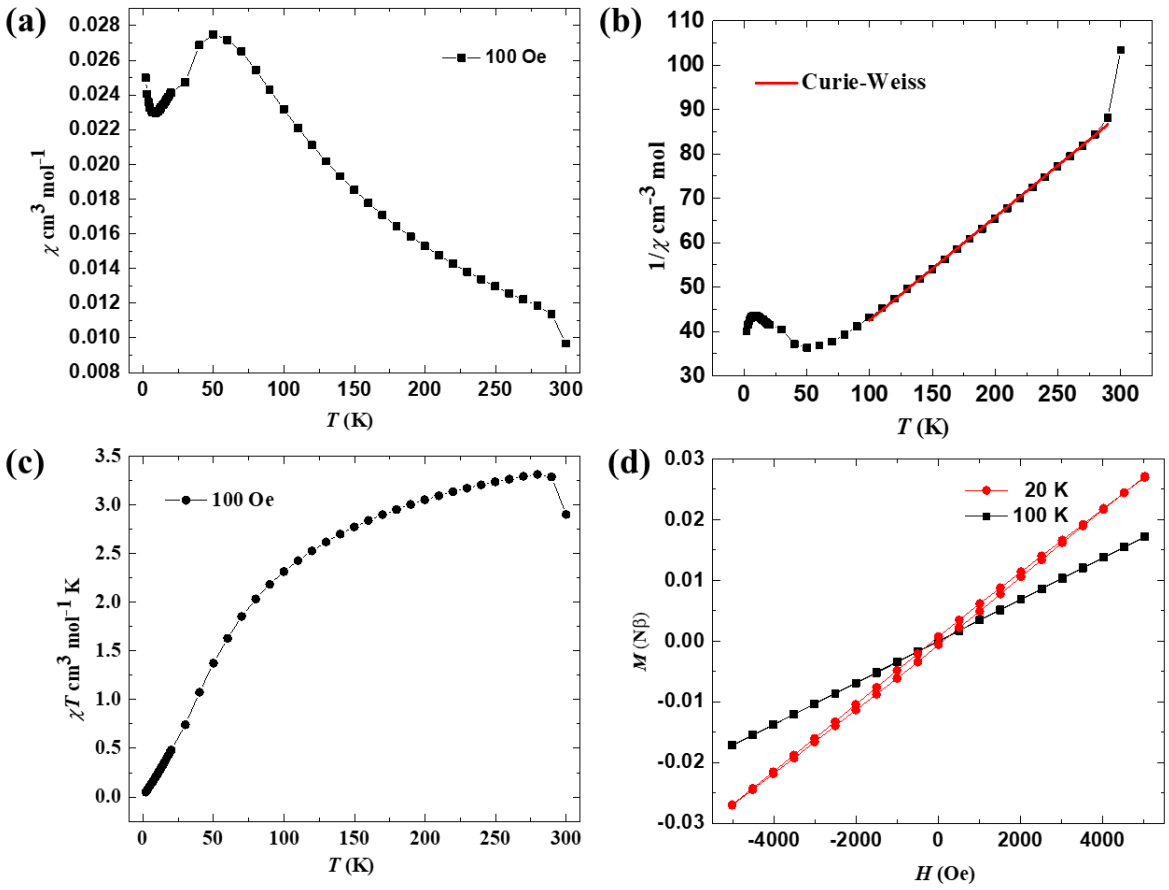

Fig. 3-32 The plots of magnetic data of **6**: (a) χ versus T at 100 Oe. (b) $1/\chi$ versus T and the Curie-Weiss fit to $1/\chi$ at 100 Oe. (c) χT versus T at 100 Oe. (d) Magnetisation (M) versus magnetic field (H) at 20 K (red) and 100 K (black).

The magnetic properties of **6** (with ~4.9 % antiferromagnetic MnF_2 impurities were measured by SQUID magnetometry. The abnormal datum at 300 K may be caused by system error, which will be excluded in further analysis. Fig. 3-32 (a) shows the χ versus T plot in the range of 2 K $\leq T \leq$ 300 K at 100 Oe, in which χ monotonically increases during cooling at high temperature, forming a broad maximum at 50 K, then monotonically decreasing with temperature. The observation of a Curie tail at low temperature corresponds to the presence of a small amount of paramagnetic Mn^{2+} impurities, like **4**. Calculated from the 100 K $\leq T \leq$ 290

K part of the $1/\chi$ versus T plot (Fig. 3-32 (b)), the Curie constant, C = 4.30 $cm^3\ mol^{-1}$ K and Weiss constant, $\theta = -83.23$ K, indicate an overall antiferromagnetic exchange interaction. The Landé factor, is g = 1.98 and effective moment, is μ_{eff} = 5.87 μ_B, which is close to the spin-only value (5.92 μ_B). The χT value decreases monotonically with cooling, which shows no evidence of magnetic long-range ordering (Fig. 3-32 (c)). The magnetisation (M) versus magnetic field (H) plot also shows a tiny magnetic hysteresis at 20 K but disappears at 100 K (Fig. 3-32 (d)). Thus, the low temperature magnetic structure of **6** should be weak antiferromagnetic ordering.

3-5 Derived Products

During the process of researching hybrid fluoride layered perovskites, we found two new Ni-based derived compounds (*enH*$_2$)$NiF_4 \cdot 2(H_2O)$ (**8**) and (*1,4-DAB*)NiF_2 (**9**), which will be introduced in this section.

3-5-1 Synthesis and PXRD Analysis of 8 and 9

Compound **8** was also synthesised by hydrothermal reaction, by mixing 0.485 g (5.0 mmol) ground NiF_2, 2.7 mL (40.5 mmol) *en*, 3 mL (83.3 mmol) HF (48-51 % wt. in water) and 2.5 mL H_2O. This mixture was sealed in a 23 mL Teflon-lined stainless-steel autoclave which was placed in a 190 °C oven and maintained for 72 hours. The product was a clear green solution after cooling the autoclave to room temperature. Single crystals of **8** and a small amount of $NiF_2(H_2O)_2$ (~3.3 % w.t.) crystals were obtained after transferring the solution into a capped beaker and evaporating overnight at room temperature.

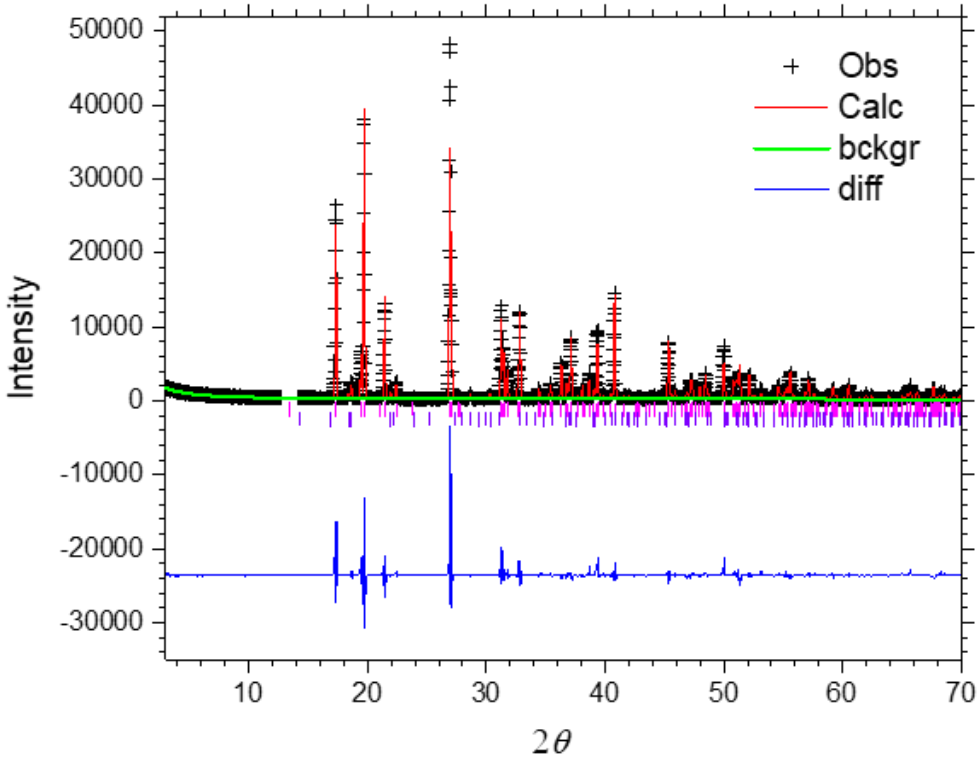

Fig. 3-33 Rietveld plot (PXRD, CuKα1) for **8**. The (10-1) reflection has been excluded. The peaks of the $NiF_2(H_2O)_2$ impurity (~3.3 %) are highlighted by violet tick marks.

PXRD (CuKα1) data were collected from a well ground crystalline sample which was loaded into a steel disc. The Rietveld refinement was based on the same conditions as the previous samples, with a result of wRp = 0.1956, Rp = 0.1427 and χ^2 = 41.11. The fixed crystallographic models were used, based on a CIF file from the single crystal refinement at 173 K, with only profile and lattice parameters being refined. The (h0l) reflections exhibited artificially high intensity, and the peak (10-1) was consequently excluded from the refinement. The fraction of $NiF_2(H_2O)_2$ impurity was calculated to be 3.3 (1) % by weight (Fig. 3-33).

Compound **9** was synthesised from 0.097 g (1.0 mmol) ground NiF_2, 0.6 mL (6.0 mmol) *1,4-DAB*, 0.45 mL (12.5 mmol) HF (48-51 % wt. in water) and 1 mL ethylene glycol (EG). Reagents were mixed and sealed in a 23 mL Teflon-lined stainless-steel autoclave and then

placed in a 160 °C oven for 48 hours. The product, green plate single crystals with ~8.5% w.t. amorphous NiF_2 (broad peaks) was generated after cooling to room temperature and washed with ethanol (EtOH).

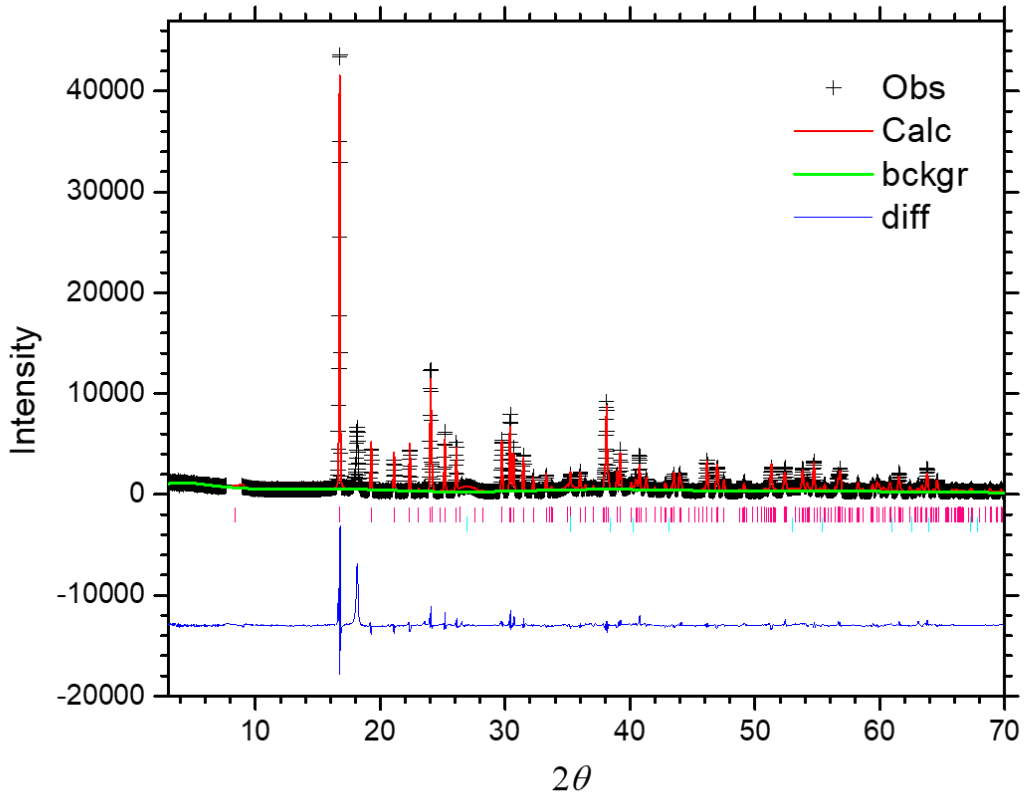

Fig. 3-34 Rietveld plot (PXRD, CuKα1) for **9**. The (100) reflection has been excluded. The peak near $2\theta \sim 18°$ is due to the Teflon sample holder (see Fig. 3-3).

The crystalline sample of **9** was well ground and loaded into a steel disc with a Teflon liner. PXRD (CuKα1) data collection and Rietveld refinement were based on the same conditions as previous samples, with a result of wRp = 0.1977, Rp = 0.1272 and χ^2 = 32.08 for **9**. The fixed crystallographic models were used, based on the CIF file from the single crystal refinement at 298 K, with only profile and lattice parameters being refined. The (h00) reflections exhibiting artificially high intensity, and the (100) peak was excluded from the

refinement. The fraction of amorphous NiF_2 impurity was calculated to be 8.4 (6) % by weight (Fig. 3-34).

3-5-2 Single Crystal Data and Analysis of 8 and 9

Table 3-12 Crystallographic data and refinement details of **8**.

Compound (*T*)	**8** (173 K)
Formula	$(C_2H_{10}N_2)NiF_4\cdot(H_2O)_2$
Formula weight	232.84
Density (g cm^{-3})	2.068
Crystal system	Monoclinic
Space group	$P2_1/n$
a/Å	8.1963(7)
b/Å	5.5023(5)
c/Å	8.5663(8)
β/°	104.590(14)
V/$Å^3$	373.87(6)
Z	2
Measured ref	2834
Independent ref	650
	[*R*(int) = 0.121]
GOOF	0.962
Final *R* indices ($I > 2\sigma(I)$)	*R*1 = 0.0382,
	*wR*2 = 0.0919

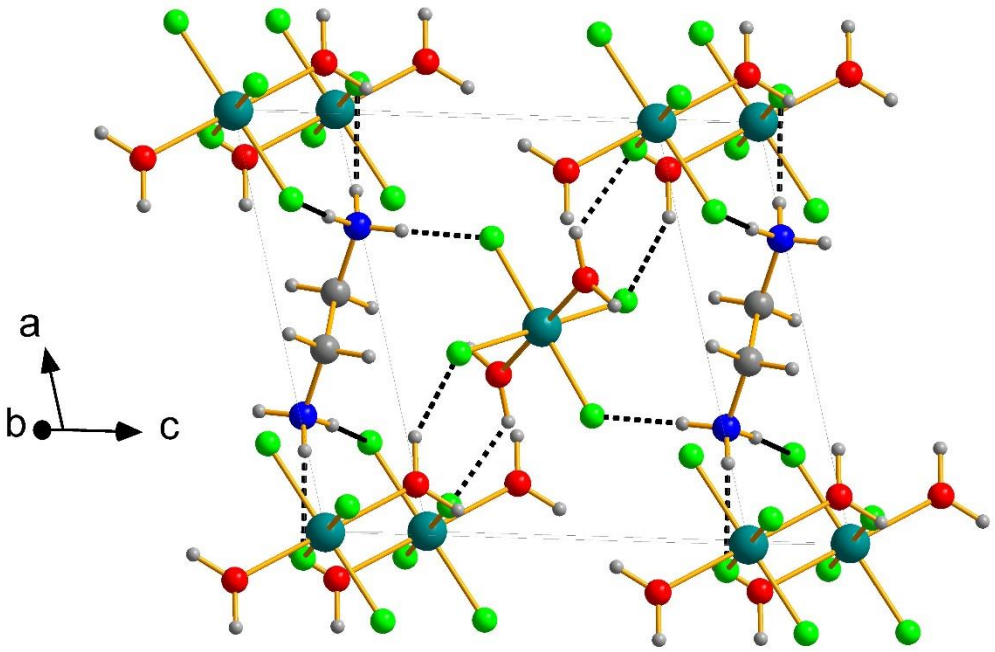

Fig. 3-35 Crystal structure of **8** (hydrogen bonds are depicted black dashes).

Table 3-13 Selected bond lengths (Å) and bond angles (°) of **8** (173 K).

	8 (173 K)
Ni-F1	2.009(2)
Ni-F2	2.0199(19)
Ni-O1	2.064(2)
N1-(H)---F1	2.681(1)
N1-(H)---F1	2.715(3)
N1-(H)---F2	2.912(3)
O1-(H)---F2	2.662(3)
N1-H-F1 angle	175.7
N1-H-F1 angle	163.7
N1-H-F2 angle	151.4
O1-H-F2 angle	172.1

Single crystal data of **8,** collected at 173 K, shows it is crystallised in space group $P2_1/n$ with a = 8.1963(7) Å, b = 5.5023(5) Å, c = 8.5663(8) Å and β = 104.590(14) ° (Table 3-12). The Ni^{2+} cation is situated on an inversion centre, and is 6-coordinated by two water molecules and four F^- ions, forming a $Ni(H_2O)_2F_4$ octahedral monomer. Bond lengths and other geometrical parameters are given in Table 3-13. Each octahedral monomer connects with neighbouring octahedra via H-bonds (O1-(H)---F2). Protonated enH_2 cations are positioned between the octahedra, which connect the octahedra also through three H-bonds (N1-(H)---F) (Fig. 3-35). This reaction was intended to target the Ni analogue of **1.** However, it can be seen, even though the starting materials and methods of synthesis are similar, that the layered perovskite structure has not been produced in this case.

Table 3-14 Crystallographic data and refinement details of **9** at 173 K and 298 K.

Compound (*T*)	**9** (173 K)	**9** (298 K)
Formula	$(C_2H_6N)NiF_2$	$(C_2H_6N)NiF_2$
Formula weight	140.77	140.77
Density (g cm^{-3})	2.299	2.289
Crystal system	Monoclinic	Monoclinic
Space group	$P2_1/c$	$P2_1/c$
a/Å	10.6818(7)	10.6838(8)
b/Å	5.1371(3)	5.1409(4)
c/Å	7.4334(5)	7.4586(5)
β/°	94.379(8)	94.505(8)
V/$Å^3$	406.71(5)	408.39(5)
Z	4	4
Measured ref	3231	3248
Independent ref	507	566
	[R(int) = 0.0804]	[R(int) = 0.0363]
GOOF	0.897	1.017
Final R indices ($I > 2\sigma(I)$)	$R1$ = 0.0293,	$R1$ = 0.0212,
	$wR2$ = 0.0654	$wR2$ = 0.0538

Table 3-15 Selected bond lengths (Å) and bond angles (°) of **9** at 173 K and 298 K.

	9 (173 K)	**9** (298 K)
Ni-F1	1.991(2)	1.9900(14)
Ni-F1	2.031(2)	2.0322(14)
Ni-F2	2.039(2)	2.0428(14)
Ni-F2	2.040(2)	2.0459(13)
Ni-N1	2.042(3)	2.047(2)
Ni-F2	2.076(2)	2.0810(14)
Ni-F2-Ni angle	128.05(10)	127.95(7)
Ni-F2-Ni angle	129.18(10)	129.29(7)

The single crystal data of **9** were collected at 173 K and 298 K from one single crystal, with no evidence of structural phase transition but only small changes of bond lengths and bond angles between the two temperatures. It is crystallised in the monoclinic space group $P2_1/c$ (Table 3-14). Although this is the same space groups as compounds **6** and **7**, the structure of **9** is very different. In **9**, each Ni^{2+} is 6-coordinated, with five F^- ions and one N (-NH_2 group from *1,4-DAB*), thus forming $NiNF_5$ octahedra. Each octahedron is edge sharing (edge F1---F1 and edge F2---F2) with neighbouring octahedra (Fig. 3-36 (a)) forming octahedral chains along the *b*-axis. Additionally, corner (F1) sharing with neighbouring octahedra along the *c*-axis leads to an unusual layered architecture in the *bc*-plane (Fig. 3-36 (b)). The layers are linked by covalently bonded neutral *1,4-DAB* molecules and stacked along the *a*-axis (Fig. 3-36 (c)). This is unusual under the synthetic conditions applied, since it might be anticipated that the DAB molecule would be protonated, and act as a layer separator, rather than a ligand, as it does in the layered perovskites.

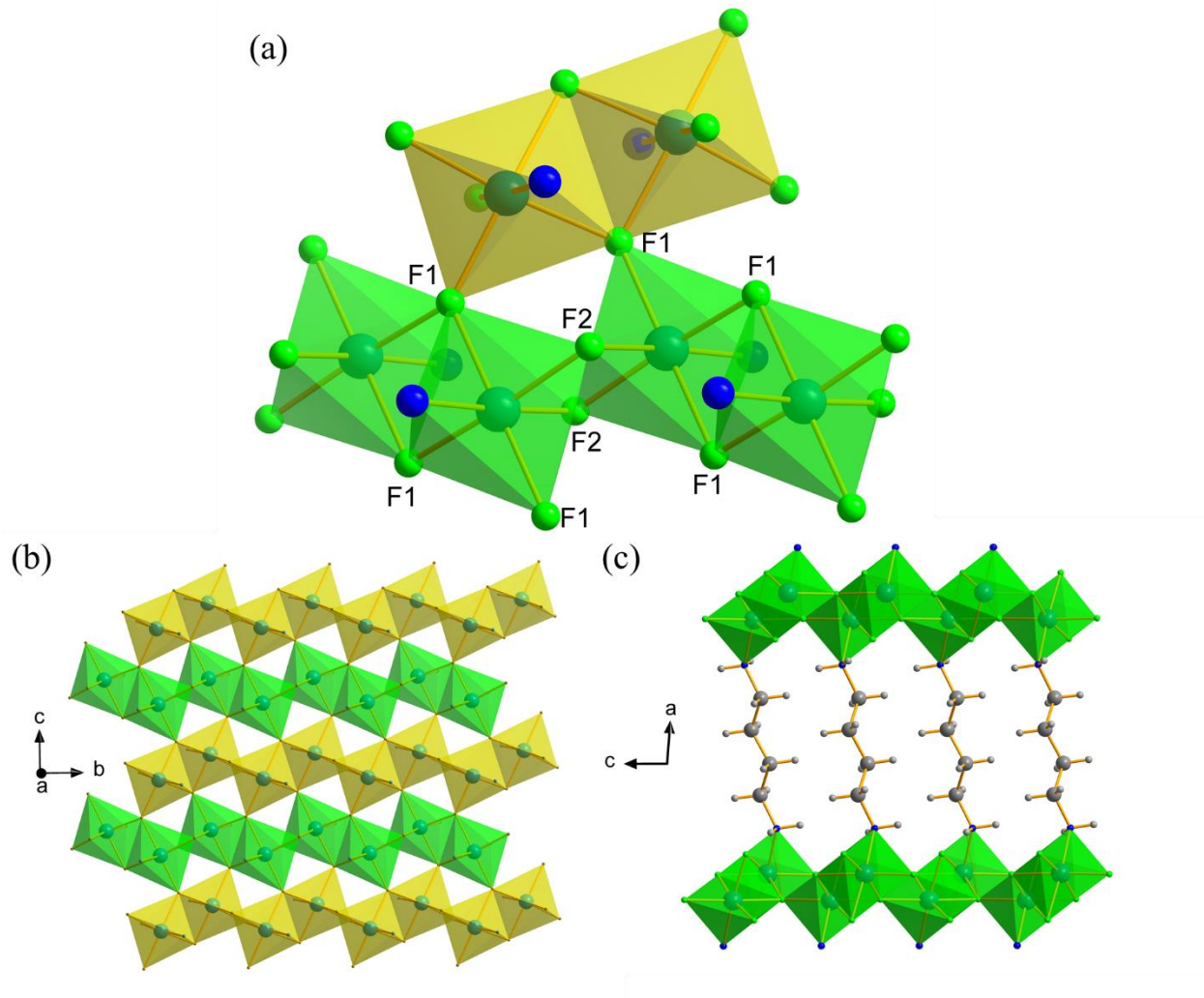

Fig. 3-36 Crystal structure of **9**: (a) Detailed connections of octahedra in the *bc*-plane. (b) extended layer structure of **9** in the *bc*-plane (the yellow and green colours represent different octahedral chains along the *b*-axis) and (c) layer stacking perpendicular to the *a*-axis.

3-6 Discussion and Conclusion

In this chapter we have introduced the synthesis, crystal structures, and magnetic properties of seven hybrid fluoride layered perovskites and two derived compounds. In this part, we will summarise and discuss this series of compounds through these aspects.

3-6-1 Synthesis

All compounds were synthesised from hydro/solvothermal reactions, however the products and impurities were influenced by many factors, for example, starting materials, temperature, and solutions are all playing important roles on this, which will be presented and discussed in the following part.

In all the starting materials, metal-fluoride (MF_2, M = Mn, Co, Ni) is the only source of metals and also the main impurities in products, even though excess diamines were applied in all the reactions (the molar ratio of diamines are normally 6~8 times of MF_2). Due to the poor solubility of MF_2 in H_2O and EG, thorough grinding before the synthesis is an effective way to reduce the remaining MF_2 impurities in the products. Apart from MF_2 impurities, the molar ratio between diamines and HF also draws our attention. Ideally, the molar masses of HF should be double that of diamines in order to protonate all the diamines in reactions. However in some cases, the molar mass of HF is less, for example, 11.1 mmol HF and 8.0 mmol *en* in the synthesis of **1**, 55.6 mmol HF and 40.0 mmol *en* in the synthesis of **2**. In contrast, in the synthesis of compound **9**, even though the molar mass of HF (12.5 mmol) is more than two times of *1,4-DAB* (6.0 mmol), the diamine has still not been protonated. That suggests all the products are the preferred results for the synthesis, and pH has limited effect in the formation of products.

Apart from the starting materials, temperature is also an essential factor to influence the products. As mentioned before, (*en*H_2)MF_4 could be synthesised at 120 °C, 160 °C, and 190 °C and higher temperature results in less MF_2 impurities. However, (*1,3-DAP*) and (*1,4-DAB*) will decompose and large amounts of NH_4MF_3 were found to form in products when the reaction temperature is higher than 160 °C. That is the reason why the reaction temperature for (*1,3-DAP*H_2)MF_4 and (*1,4-DAB*H_2)MF_4 are no more than 130 °C, and more MF_2 impurities were found in the products.

The last factor is the solvent: water is more suitable for the Mn series of compounds, however, $NiF_2(H_2O)_4$, $CoF_2(H_2O)_4$ and $(enH_2)NiF_4{\cdot}2(H_2O)$ (**8**) single crystals will form as products when water is the solvent for the Co and Ni series synthesis. That is the reason why EG became the solvent for the Co and Ni related synthesis. Other organic solvents such as MeOH, EtOH, DMSO were found to produce the products of MF_2 and $(diamine){\cdot}(HF)_2$.

3-6-2 Crystal Structures

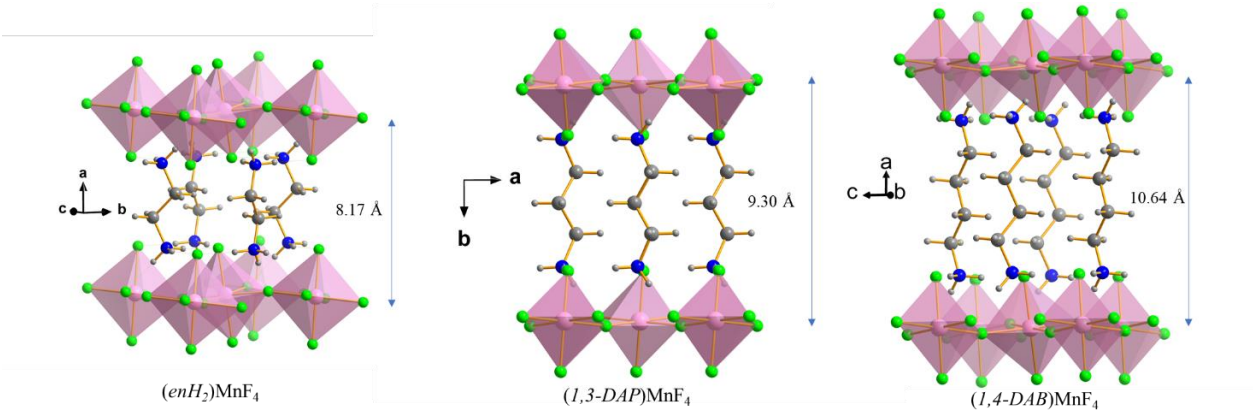

Fig. 3-37 Comparison of the distances between the perovskite layers for C2, C3 and C4 diamine chains.

Based on single crystal and powder crystal data, all the hybrid layered perovskites we investigated here have no phase transitions from 173 K to 300 K. Among these compounds, all the perovskite layers have similar parameters (perovskite axes $a \sim b \sim 6$ Å), but the distances between the perovskite layers are determined by the diamines; the diamines with longer chains will naturally build larger spacings as long as they occur in a 'stretched' conformation (Fig. 3-37). In addition, C2 and C4 series (**1**-**3**, **6** and **7**) crystallise in the same space group, and the *a*-axis (*c*-direction in perovskite structure) is correspondingly not 'doubled' in these cases. In contrast, the C3 analogues (**4**,**5**) have a different space group and a doubled unit cell along the layer direction (*b*-axis, *c* direction in the perovskite convention). Such a difference is caused by the different octahedral tilt systems, whereby alternating layers exhibit tilts of 'same sense'

for even Cn (a^-a^-c) but opposite sense for odd Cn ($a^-a^-c^-$). This phenomenon has also been observed in the chloride analogues.[7-9] Apart from that, the powder samples of all the compounds in this system have strong preferred orientation, even derived compounds, **8** and **9** are also included. In addition, the compounds in the monoclinic crystal system are often crystallised as twins due to their pseudo-tetragonal nature. Previous research about related hybrid perovskites with heavier halogens have also reported this.[7]

3-6-3 Magnetic Properties

The magnetic interactions were constructed through M-F-M bridges and form a 2D magnetic layer in every perovskite octahedral layer. Due to the long distance between the perovskite layers (the shortest is 8.17 Å of (enH_2)MF_4) and lack of magnetic connection medium, it is not likely to form interplane magnetic coupling, which means all the magnetic properties should be similar for the same metal (M) regardless of the length of the diamine chain. Unfortunately, the magnetic properties for some samples are inaccurate because of relatively high amount of M^{2+} impurities, so meaningful quantitative comparisons across the full family of compounds cannot be made. Nevertheless, there are still some common characteristics that can be found, for example, the overall magnetic interactions are antiferromagnetic at high temperature and a canted antiferromagnetic ordering can be observed at low temperature; impurities didn't appear to affect T_N for the Co based compounds. The net ordered magnetic moment of high-spin octahedron appears smaller for Mn (S = 5/2) than for Co (S = 3/2). The reason is that for high-spin Co^{2+} octahedron complexes, the orbital angular momentum is not quenched in their degenerated ground states, so there is always a significant orbital contribution for them. However, in corresponding Mn^{2+} complexes, the ground states are non-degenerate, which do not have a contribution from orbital, and the magnetic moment values are close to the spin only state.

In summary, we have prepared and explored the first examples of layered hybrid fluoride perovskites, some of which show evidence for net switchable magnetisation at low temperature, which could have potential applications as magnetic materials. Further work is necessary to prepare phase-pure samples for more serious magnetic characterisation, including more neutron diffraction studies of the magnetic ordering. The unexpected layered structure of **9** is also very interesting, and preparation of a phase-pure sample to study its magnetic properties should also be a target for further studies.

3-7 References

1. T. Li, R. Clulow, A. J. Bradford, S. L. Lee, A. M. Z. Slawin and P. Lightfoot, *Dalton Trans*., 2019, **48**, 4784–4787.
2. A.C. Larson and R.B. Von Dreele, *General Structure Analysis System (GSAS)*, Los Alamos National Laboratory Report LAUR 86-748, 2000.
3. B. H. Toby, *J. Appl. Cryst*., 2001, **34**, 210-213.
4. (a) A. L. Spek, *J. Appl. Cryst*. 2003, **36**, 7-13; (b) A. L. Spek, *Acta Crystallogr., Sect. D*, 2009, **65**, 148-155; (c) A. L. Spek, *Inorg. Chim. Acta*, 2018, **470**, 232-237; (d) A. L. Spek, *Acta Crystallogr., Sect. E*., 2020, **76**, 1-11.
5. N. F. Stephens, A. M. Z. Slawin and P. Lightfoot, *Chem.Commun*., 2004, 614-615.
6. R. D. Shannon, *Acta Crystallogr. Sect. A: Found. Adv.*, 1976, **32**, 751-767.
7. K. Tichý, J. Beneš, W. Hälg and H. Arend, *Acta Crystallogr., Sect. B: Struct. Crystallogr. Cryst. Chem*., 1978, **34**, 2970-2981.
8. H. Arend, H. Von Känel and P. Wachter, *Phys. Status Solidi B*, 1976, **74**, 151-157.
9. R. Kind, S. Plesko, P. Günter, J. Roos and J. Fousek, *Phys. Rev. B: Condens. Matter Mater. Phys*., 1981, **23**, 5301-5315.
10. A. M. Glazer, *Acta Crystallogr., Sect. B: Struct. Crystallogr. Cryst. Chem*., 1972, **28**, 3384-3392.
11. C. J. Howard and H. T. Stokes, *Acta Crystallogr., Sect. B: Struct. Sci*., 1998, **54**, 782-789.
12. R. Deblieck, G. V. Tendeloo, J. V. Landuyt and S. Amelinckx, *Acta Crystallogr., Sect. B: Struct. Sci*., 1985, **41**, 319-329.
13. C. Brosset, *Z. Anorg. Allg. Chem*., 1937, **235**, 139-147.
14. J. Nouet, J. Pannetier and J. L. Fourquet, *Acta Crystallogr., Sect. B: Struct. Crystallogr. Cryst. Chem*., 1981, **37**, 32-34.

15. G. Knoke and D. Babel, *Z. Naturforsch*., 1979, **34**, 934-938.
16. A. S. Krylov, M. S. Molokeev, S. V. Misyul, S. N. Krylova, A. S. Oreshonkov, A. A. Ivanenko, V. A. Zykova, Y. N. Ivanov, A. A. Sukhovsky, V. N. Voronov, I. N. Safonov and A. N. Vtyurin, *CrystEngComm*, 2016, **18**, 8472-8486.
17. S. C. Abrahams and J. L. Bernstein, *Mater. Res. Bull*., 1972, **7**, 715-720.
18. A. N. Bogdanov, A. V. Zhuravlev and U. K. Rößler, *Phys. Rev. B: Condens. Matter Mater. Phys*., 2007, **75**, 094425 (1–13).
19. V. Petrícek, M. Dušek and L. Palatinus, *Zeitschrift fur Krist*., 2014, **229(5)**, 345-352.
20. (a) H. T. Stokes, D. M. Hatch, and B. J. Campbell, *ISODISTORT, ISOTROPY Software Suite*, iso.byu.edu. (b) B. J. Campbell, H. T. Stokes, D. E. Tanner, and D. M. Hatch, *J. Appl. Cryst*., 2006, **39**, 607-614.
21. K. C. Turberfield, A. Okazaki and R. W. H. Stevenson, *Proc. Phys. Soc*., 1965, **85**, 743–758.
22. R. S. Cowley and K. Carneiro, *J. Phys. C Solid State Phys*., 1980, **13**, 3281–3291.

Chapter 4 Single Crystal Structures and Properties Study of Oxalate Fluoride Coordination Polymers

4-1 Introduction

The oxalate ligand has been widely used in constructing coordination polymers (CPs), especially for special magnetic property research. Our group has recently synthesised and investigated the crystal structures and physical properties of several oxalate CPs, such as $Na_2Fe(C_2O_4)F_2$[1], $KFe(C_2O_4)F$[2,3] and $KTiC_2O_4 \cdot xH_2O$[4]. All those compounds contain magnetic metal-oxalate $[M(C_2O_4)]_\infty^{n+}$ structures in the form of 1D chains, 2D networks or even 3D frameworks. The charges are balanced by inorganic metal cations (Na^+ and K^+). However, there is no previous report about using organic cations to balance the metal-oxalate-fluoride frameworks.

Several examples of metal-oxalate CPs with organic ligands have been investigated in previous work of our group.[5-7] Based on that work, two organic amines draw our attention, ethylenediamine (*en*) and pipzazine (*pipz*). Their size is compatible with metal-oxalate frameworks and can construct versatile connection styles, which provide more possibility to add F^- in the system.

In this chapter, the synthesis and crystal structures of several oxalate fluoride coordination polymers and some by-products based on the two organic cations will be presented and discussed. The facilities and relevant software for single crystal XRD and PXRD characterisations are the same as those used in chapter 3. All the PXRD data were collected at room temperature and most single crystal XRD data were collected at 173 K. In addition, the magnetic properties of some compounds were measured by SQUID magnetometry and the discussions of the results will be presented.

4-2 *en* Based Oxalate Fluoride CPs

In this section, the synthesis and crystal structures of two isostructural *en* based oxalate fluoride CPs (*en*H_2)[$FeF(C_2O_4)]_2$ **(10)** and (*en*H_2)[$MnF(C_2O_4)]_2$ **(11)** will be presented, following by the discussion about the magnetic properties of **10**.

4-2-1 Synthesis

4-2-1-1 (*en*H_2)[$Fe(C_2O_4)F]_2$ (10)

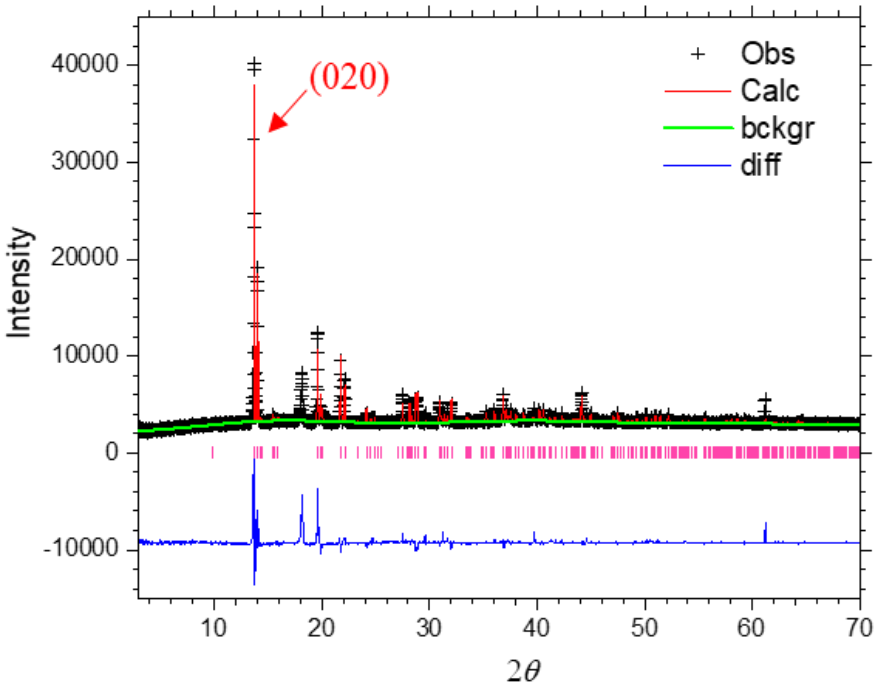

Fig. 4-1 Rietveld plot (PXRD, CuKα1) for **10**. The peak near $2\theta \sim 18°$ is due to the Teflon sample holder (see Fig. 3-3). The (020) peak is shown by the red arrow.

0.180 g (1 mmol) iron oxalate dihydrate ($FeC_2O_4 \cdot 2H_2O$), 0.135 mL (2 mmol) *en*, and 0.2 mL (5.6 mmol) HF (48-51 % wt. in water) were dissolved in 1 mL H_2O and 1 mL EG mixed solvent at room temperature. Then, the homogeneous mixture was sealed in a 30 mL

Teflon-lined stainless-steel autoclave and placed in a 120 °C oven, maintained for 72 hours. After the autoclave was cooled to room temperature, pure yellow block single crystals of **10** were obtained by filtration with washing by EG and then the purity of the sample was confirmed by PXRD (Fig. 4-1).

Rietveld refinements were applied for the PXRD data. A preferred orientation was observed, with (0k0) reflections exhibiting artificially high intensity, which was corrected by the March-Dollase preferential orientation model where the ratio of (010) was 0.8355. The crystallographic models were used, based on the CIF file from the single crystal refinement at 173 K with a space group of *Pnnm*. The refined lattice parameters are a = 12.7433(8) Å, b = 13.0320(7) Å and c = 7.1117(5) Å with wRp = 0.0743, Rp = 0.0344 and χ^2 = 18.39. The refined unit cell parameters are similar with the CIF data measured at 173 K, which shows there is probably no crystallographic phase transition from 173 K to room temperature (see 4-2-2, single crystal part).

4-2-1-2 (*en*H_2)[Mn(C_2O_4)F]$_2$ (11)

0.179 g (1 mmol) manganese oxalate dihydrate ($MnC_2O_4 \cdot 2H_2O$), 0.135 mL (2 mmol) *en*, and 0.2 mL (5.6 mmol) HF (48-51 % wt. in water) were dissolved in 2 mL H_2O at room temperature. Then, the homogeneous mixture was also sealed in a 30 mL Teflon-lined stainless-steel autoclave and then placed in a 120 °C oven, maintained for 72 hours. After the autoclave was cooled to room temperature, pure colourless block single crystals of **11** were obtained by filtration with washing by deionised water and then the purity was also confirmed by PXRD (Fig. 4-2).

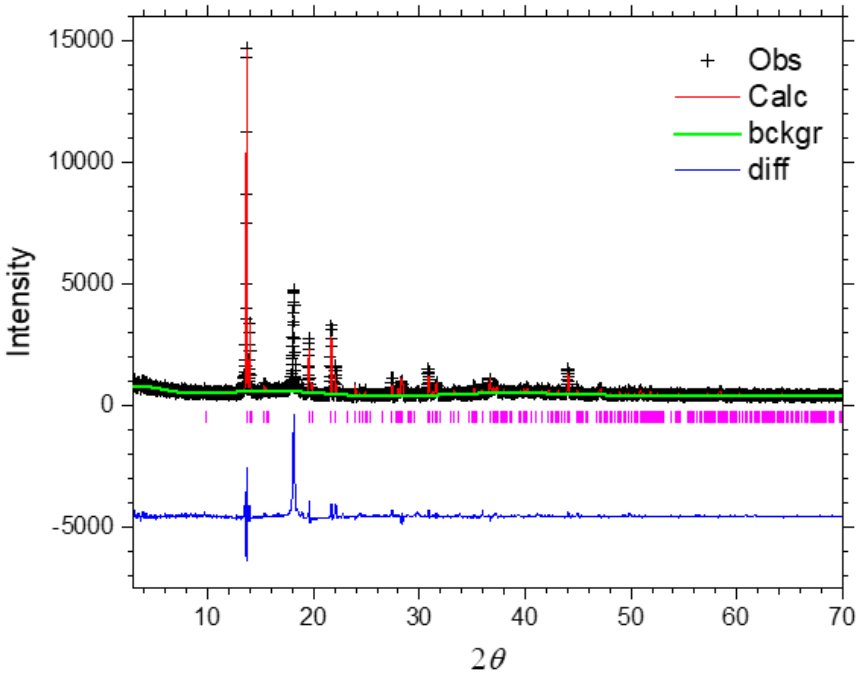

Fig. 4-2 Rietveld plot (PXRD, CuKα1) for **11**. The peak near $2\theta \sim 18°$ is due to the Teflon sample holder (see Fig. 3-3).

Rietveld refinements were also applied for the PXRD data. The (0k0) preferred orientation was also observed, which was also corrected by March-Dollase preferential orientation model with the ratio of (010) being 0.7094. The crystallographic models were used, also based on the CIF file from the single crystal refinement at 173 K. The refined lattice parameters are a = 12.757(1) Å, b = 13.045(1) Å and c = 7.246(1) Å with wRp = 0.1649, Rp = 0.0906 and χ^2 = 14.80. This also confirms no crystallographic phase transition from 173 K to room temperature.

4-2-2 Single Crystal Data and Analysis

Table 4-1 Crystallographic data and refinement details of compounds **10** and **11**.

Compound (*T*)	**10** (173 K)	**11** (173 K)
Formula	$(C_2H_{10}N_2)[Fe(C_2O_4)F]_2$	$(C_2H_{10}N_2)[Mn(C_2O_4)F]_2$
Formula weight	775.72	772.08
Density (g cm^{-3})	2.189	2.141
Crystal system	Orthorhombic	Orthorhombic
Space group	*Pnnm*	*Pnnm*
a/Å	12.7141(7)	12.7422(14)
b/Å	13.0196(12)	13.0123(14)
c/Å	7.1111(6)	7.2234(8)
V/$Å^3$	1177.12(16)	1197.7(2)
Z	2	2
Measured ref	11687	9738
Independent ref	1462	1149
	[*R*(int) = 0.0495]	[*R*(int) = 0.1497]
GOOF	0.980	0.958
Final *R* indices	*R*1 = 0.0305,	*R*1 = 0.0428,
($I > 2\sigma(I)$)	*wR*2 = 0.0783	*wR*2 = 0.1018

Table 4-2 Selected bond lengths (Å) and bond valences for **10** (left) and **11** (right).

	Bond lengths	S_{ij}		**Bond lengths**	S_{ij}
Fe1-F1	2.033(1)	0.355	Mn1-F1	2.088(2)	0.352
Fe1-F2	2.020(1)	0.369	Mn1-F2	2.084(2)	0.349
Fe1-O1	2.147(2)	0.328	Mn1-O1	2.188(4)	0.341
Fe1-O2	2.130(2)	0.343	Mn1-O2	2.163(4)	0.365
Fe1-O3	2.129(2)	0.344	Mn1-O3	2.166(3)	0.362
Fe1-O4	2.138(2)	0.336	Mn1-O4	2.178(4)	0.350
	$\sum Fe1 = 2.075$			$\sum Mn1 = 2.119$	

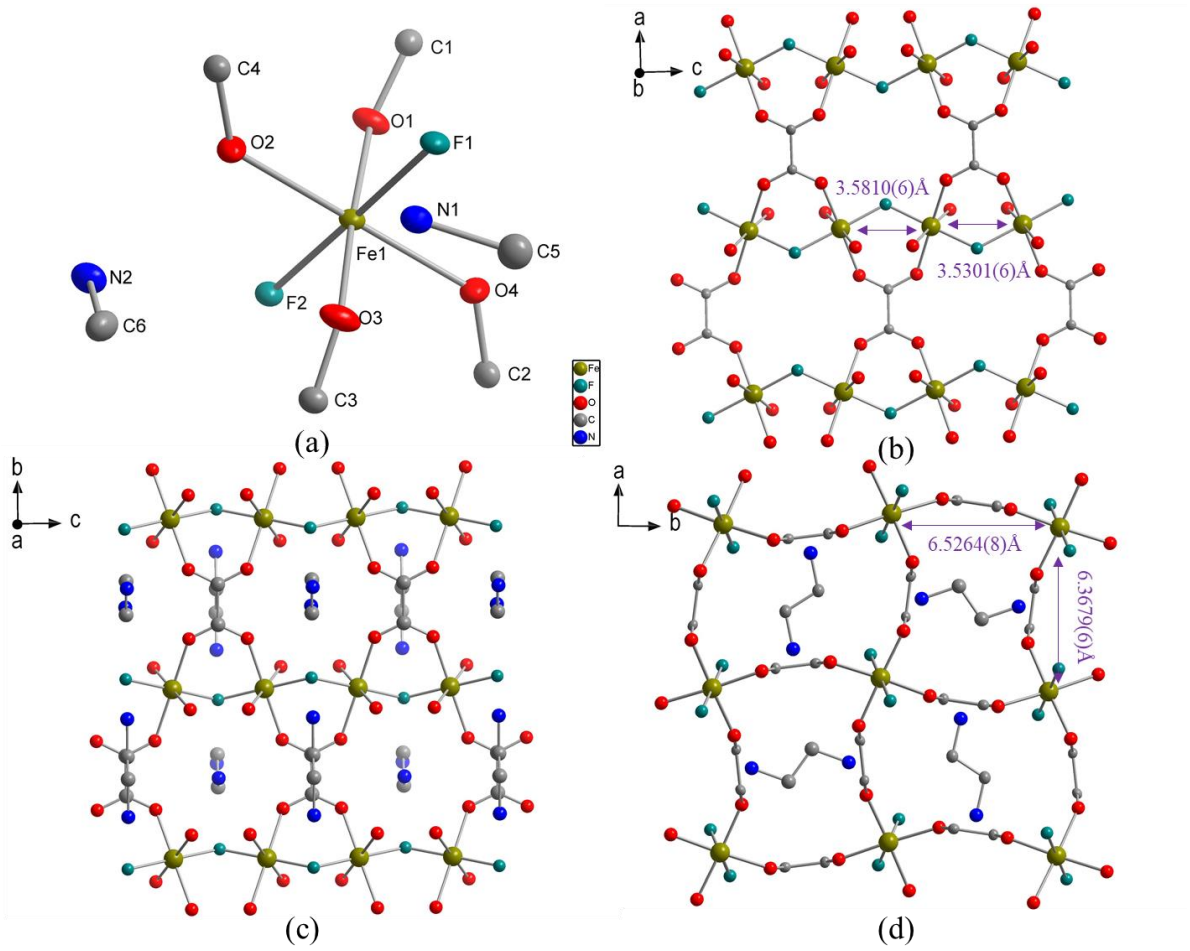

Fig. 4-3 (a) Asymmetric unit in ellipsoid plot of **10**, ellipsoids are represented at 50 %; (b) Polymeric structure of **10** in the *ac*-plane (amines were excluded); (c) Polymeric structure in the *bc*-plane; (d) Polymeric structure in the *ab*-plane. (hydrogen atoms are omitted for clarity.)

The refinements of 173 K single crystal data show the two isostructural compounds, which crystallise in orthorhombic system with space group *Pnnm* (Table 4-1). In the single crystal data, all the cell parameters for **10** are smaller than **11**, which is probably due to the effective atom radius decreasing with the metal atomic number increasing.[8] Iron and manganese are all in the 2+ oxidation state, as confirmed by the bond valence sum calculation ($\sum \mathrm{Fe1} = 2.075$ and $\sum \mathrm{Mn1} = 2.119$) (Table 4-2), which are also confirmed by the charge balanced chemical formulae.

Due to **10** and **11** being isostructural, compound **10** will be taken as the example to discuss the crystal structure in more detail. In **10**, the iron atom (Fe1) is 6-coordinated, with four oxygen atoms (O1, O2, O3 and O4) and two fluorine atoms (F1 and F2) forming *trans*-[FeO_4F_2] octahedron (Fig. 4-3 (a)). The Fe-O bond lengths are between 2.128(2)-2.147(2) Å, while the two Fe-F bond lengths are 2.019(2) and 2.033(2) Å (Table 4-2). Along the *c*-axis, iron atoms are connected by fluoride atoms and form -Fe1-F1-Fe1-F2-Fe1- magnetic chains with two similar distances between neighbour iron atoms being 3.5810(6) Å (Fe1-F1-Fe1) and 3.5301(6) Å (Fe1-F2-Fe1) (Fig. 4-3 (b) and (c)). The corresponding two Fe-F-Fe angles are 123.450(14)˚ (Fe1-F1-Fe1) and 121.905(14)˚ (Fe1-F2-Fe1), which normally meditate a potential antiferromagnetic exchange between iron atoms.[2,3] Along the *a*-axis and *b*-axis, Fe atoms are connected by *cis* bridging oxalate ligands *via* O-C-C-O bridges, with the distances between two neighbour iron atoms being 6.3679(6) and 6.5264(8) Å, respectively (Fig. 4-3 (d)); such a connection style and metal distances may cause a very weak magnetic exchange between the iron atoms along the two oxalate bridges.

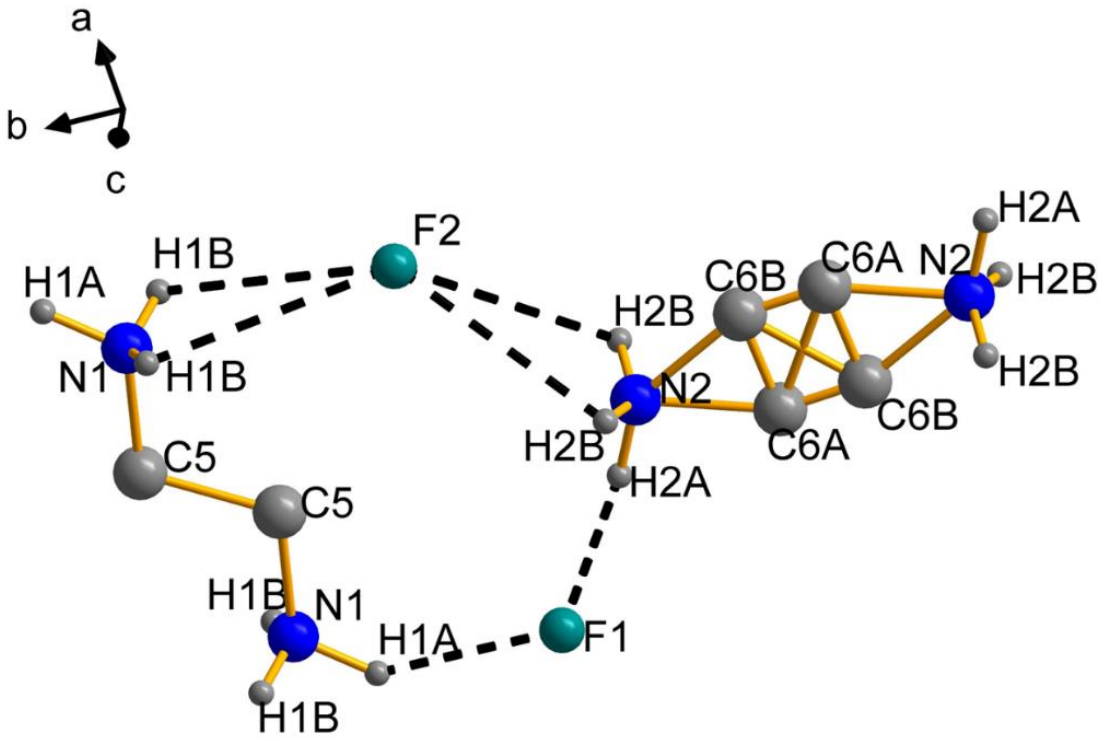

Fig. 4-4 Illustration of ordered (left) *en*H_2^{2+} cations and disordered (right) with the hydrogen bonds (dotted lines). (Some hydrogens are omitted for clarity.)

Table 4-3 The hydrogen bond lengths (Å) and bond angles (°) of **10**.

Bond	**Bond length**	**Bond angle**
N1-(H1A)---F1	2.819(3)	138.7(1)
N1-(H1B)---F2	3.004(3)	96.7(4)
N2-(H2A)---F1	2.872(4)	172.9(2)
N2-(H2B)---F2	2.927(4)	90.8(3)

The (*en*H)$^{2+}$ cations are located within channels of the iron oxalate framework and balance the negative charge of the framework. The cations interact with the framework by hydrogen bonds (N-H---F) (Fig. 4-4). The bond lengths and bond angles are shown in Table 4-

3. In addition, one C atom (C6) is disordered over two positions and the configurations of the order/disorder enH_2^{2+} cations are illustrated in Fig. 4-4.

4-2-3 Magnetic Data and Analysis of 10

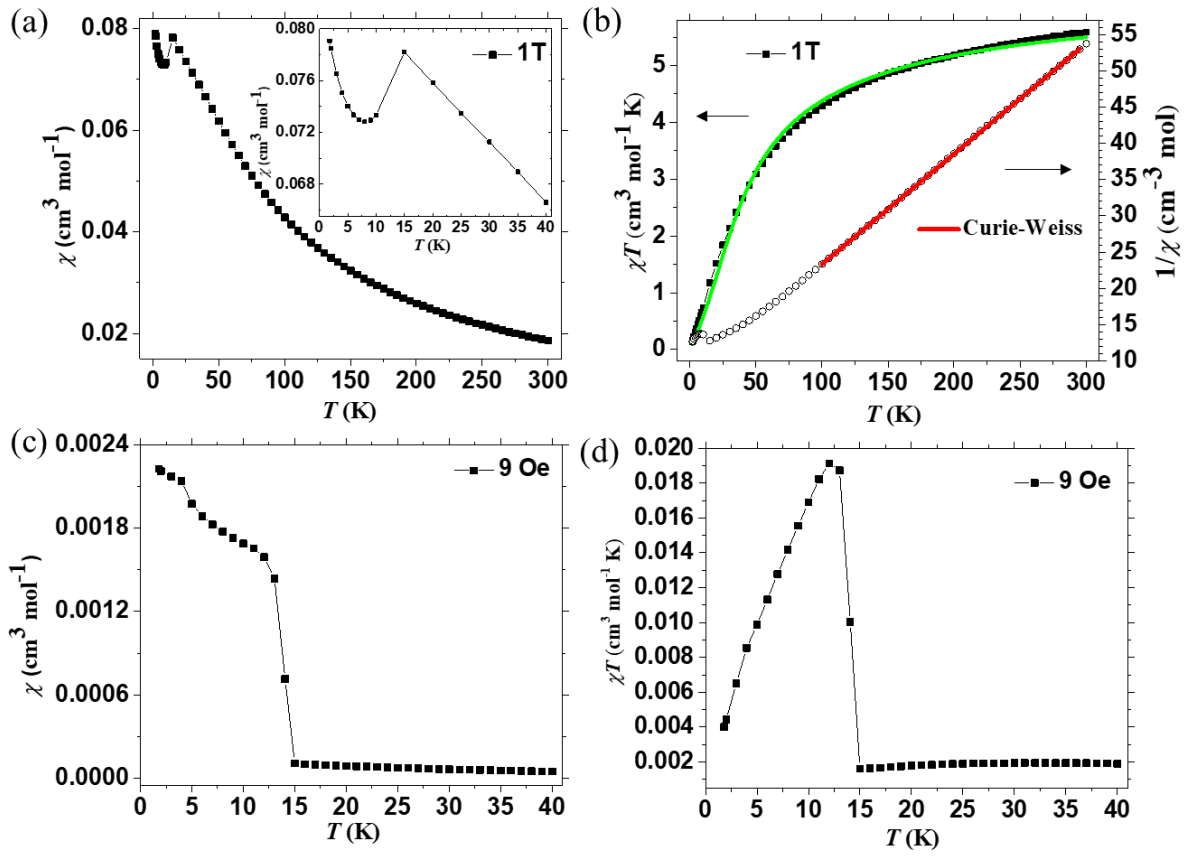

Fig. 4-5 The magnetic data of **10**: (a) χ vs. T plot measured at H = 1 T (The inset shows details in the range 2-40 K); (b) χT vs. T plot measured at H = 1 T (left) with 1D Heisenberg chain model fitting (solid green line) and $1/\chi$ versus T (right) with the Curie-Weiss fitting (solid red line); (c) χ vs. T plot measured at H = 9 Oe; (d) χT vs. T plot measured at H = 9 Oe.

Fig. 4-5 shows the magnetic properties of **10** measured under two DC magnetic fields, 1T (10,000 Oe) and 9 Oe. The χ versus T plot in the range of 2 K $\leq T \leq$ 300 K at 1 T is depicted in Fig. 4-5 (a). χ monotonically increases during cooling, reaching a maximum at 15 K, then monotonically decreases with cooling, which is indicating a magnetic phase transition around

that temperature. However, with further cooling a Curie tail was observed, which may be due to the effect of a small amount of ferromagnetic Fe^{2+} or Fe^{3+} impurities.

The Curie constant, C = 6.58 $cm^3\,mol^{-1}$ K and Weiss constant, θ = −53.47 K were deduced from the T >100 K part of the $1/\chi$ versus T plot, indicating an overall antiferromagnetic exchange interaction. Calculating from C, the Landé factor, g = 2.09 and effective moment, μ_{eff} = 5.13 μ_B per Fe^{2+} (S = 2), which is a little higher than spin-only value (4.90 μ_B) due to the orbital contribution.

The shape of χT versus T plot at 1T also shows the antiferromagnetic interaction between the Fe^{2+} ions, but there is no obvious evidence for magnetic phase transition and the critical temperature peak at 15 K. That is probably due to the phase transition being too weak, and the phenomenon is hidden by the strong applied magnetic field (1T). At 300 K, χT is 5.59 $cm^3\,mol^{-1}$ K, obviously lower than C, indicating a strong antiferromagnetic coupling between the Fe^{2+} ions at room temperature (Fig. 4-5 (b)). The data were fitted by 1D Heisenberg chain model, which is described by equation (4−1):

$$\chi_M = \frac{Ng^2\mu_B{}^2}{kT}\left[\frac{A + Bx^2}{1 + Cx + Dx^3}\right] \qquad (4-1)$$

where N is Avogadro's number, g is the Landé factor, μ_B is Bohr magneton, k is Boltzmann's constant and $x = |J|/(kT)$. A, B, C and D are constant numbers and variable with the changing of spin states of the metal.[9] In this compound, the metal is Fe^{2+} in high spin (S = 2), so the constant numbers are A = 2.0000, B = 71.938, C = 10.482, and D = 955.56.[10] The χT versus T plot is well described by the Heisenberg 1D spin chain model, with the calculated intrachain coupling constant J = −4.39(6) K and Landé factor g = 2.05 (Fig. 4-5 (b)). It also indicates that the main magnetic exchange pathway is the Fe-F-Fe bridge.

The χ versus T plot in the temperature range of 2 K-40 K at 9 Oe also shows a phase transition starting at 15 K but also having a different Curie tail at lower temperature (Fig. 4-5 (c)). The χT versus T plot at 9 Oe indicates the magnetic transition temperature, $T_N \approx 12$ K, lower than the T_N (15 K) in 1T field (Fig. 4-5 (d)). In the absence of magnetisation measurements or field cooled and zero field cooled susceptibility measurements, the spin alignment of **10** is purely antiferromagnetic or has some spin canting cannot be determined. The shifting of critical temperature is probably caused by Fe^{2+} or Fe^{3+} impurities. Otherwise the higher applied field introduces extra magnetic ordering. The frustration index, $f = |\theta|/ T_N \approx 4.5 < 5$ clear shows no significant frustration.

One chemically similar example is $KFe(C_2O_4)F$, a compound which presents frustrated antiferromagnetic ordering below T_N (~ 18.5 K)[1,2] (also see Chapter1 1-3-1-2). In that compound, the 2 D $[Fe(C_2O_4)]^{\infty}$ layers construct a Fe^{2+} triangular network of frustration *via* two Fe-O-C-O-Fe *syn-anti* (5.489(2) and 5.932(2) Å) pathways and one Fe-O-C-C-O-Fe (6.680(1) Å) *cis* bridge. In compound **10**, the $[Fe(C_2O_4)]^{\infty}$ layers construct a rectangular network only *via* two similar but shorter *cis* oxalate bridges Fe-O-C-C-O-Fe (6.3679(6) and 6.5264(8)) Å than $KFe(C_2O_4)F$, which probably also constructs weaker magnetic pathways between the Fe^{2+} ions. Besides, PND and μSR analysis show the antiferromagnetism of $KFe(C_2O_4)F$ is mainly mediated by the Fe-F-Fe chains. Thus, the antiferromagnetism of **10** is also probably mainly mediated by the Fe-F-Fe chains, which also corresponds with the result of 1D Heisenberg fitting. Further magnetic characterisation is needed to investigate the details.

4-3 *pipz* Based Oxalate Fluoride CPs

Comparing with *en*, *pipz* can construct CPs with greater structural variety due to the two nitrogens of *pipz* can coordinate with metal centre. In this section, the synthesis and crystal structure of five *pipz* based oxalate CPs will be presented, including: (*pipz*H_2)$Fe(C_2O_4)F_2$ (**12**), (*pipz*H_2)$Fe(C_2O_4)_2$ (**13**), (*pipz*H_2)$Fe_2(C_2O_4)_2F_2(H_2O)_2$ (**14**), (*pipz*H_2)$Co_2(C_2O_4)_2F_2(H_2O)_2$ (**15**)

and (*pipz*H)Fe(C_2O_4)F·(H_2O) **(16)**. Except for the isostructural compounds **14** and **15**, all the compounds have different crystal structures. In these compounds, all the metal ions are 6-coordinated in octahedral style and connected by oxalate ligands. The *pipz* ligand plays a role as amine to adjust the structures. The magnetic data of compounds **14**-**16** have also been investigated and will be presented here.

4-3-1 Synthesis

4-3-1-1 (*pipz*H_2)Fe(C_2O_4)F_2 (12)

0.90 g (5 mmol) iron oxalate dihydrate ($FeC_2O_4·2H_2O$), 0.86 g (10 mmol) *pipz*, and 0.5 mL (14 mmol) HF (48-51 % wt. in water) were dissolved in 10 mL EG solvent at room temperature. The overall molar ratio of reactants is Fe^{2+}: $C_2O_4^{2-}$: *pipz*: F^- = 1: 1: 2: 2.8. Then, the homogeneous mixture was sealed in a 50 mL Teflon-lined stainless-steel autoclave and placed in a 120 °C oven, maintained for 72 hours. After the autoclave was cooled to room temperature, crystallised product was obtained by filtration with washing by EtOH. There are two kinds of single crystals in the product, yellow chip single crystals of **12** (main phase) and small colourless single crystals (by-product). The single crystals of **12** were collected and characterised by PXRD at room temperature and single crystal structure data were collected at 173 K.

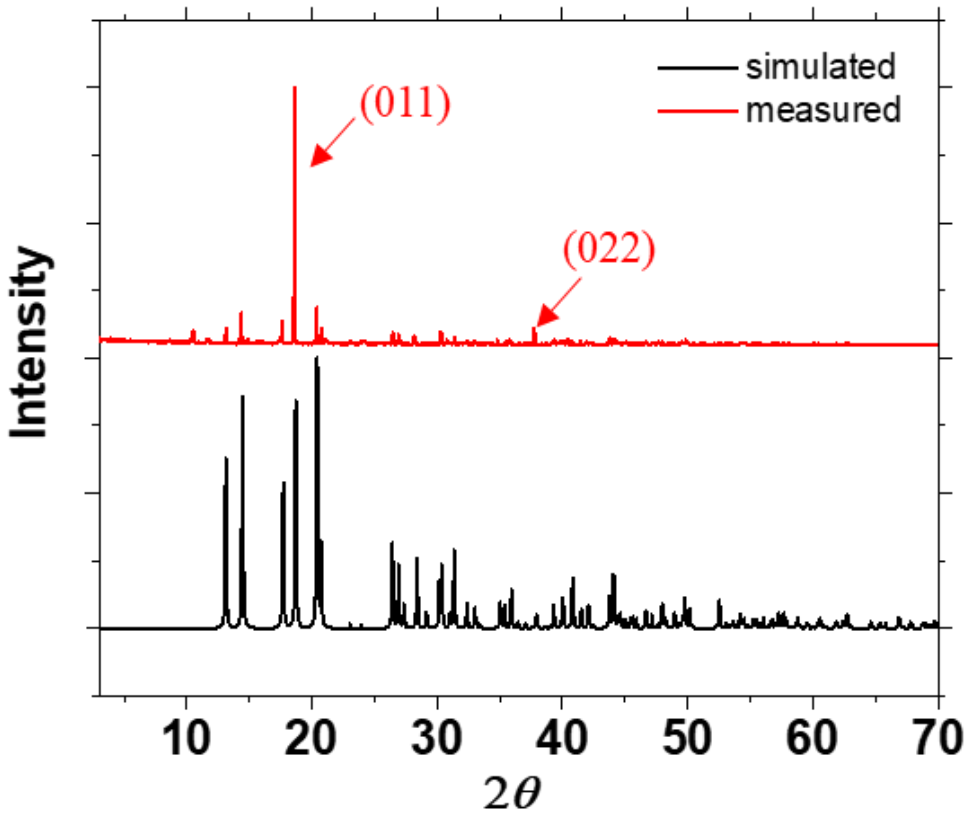

Fig. 4-6 Measured (top) and simulated (bottom) PXRD (CuKα1) pattern of **12**. The measured PXRD data shows the preferred orientation effect (011 and 022 reflections) for the sample.

In measured PXRD data, a distinct preferred orientation was observed, with (011) and (022) reflections exhibiting artificially high intensity (Fig. 4-6). Rietveld refinements were applied for the PXRD data (Fig. 4-7). The preferred orientation peaks (011) and (022) were excluded from the refinement. The crystallographic models were used, based on the CIF file from the single crystal refinement at 173 K with a space group of *P*-1. The refined lattice parameters are a = 5.5959(3) Å, b = 6.8080(4) Å, c = 6.8435(4) Å, α = 81.569(4)˚, β = 80.965(5)˚, and γ = 65.352(3)˚ with wRp = 0.0424, Rp = 0.0252 and χ^2 = 8.937. The cell parameters are also similar with CIF data measured at 173 K, which shows there is probably no crystallographic phase transition during 173 K to room temperature (see 4-3-2-1, single crystal part). In addition, some unmatched peaks at low angle indicate some unidentified

impurity phases were included in the sample, which prohibit the sample for magnetic characterisation. Further research is needed to confirm the impurities in the future.

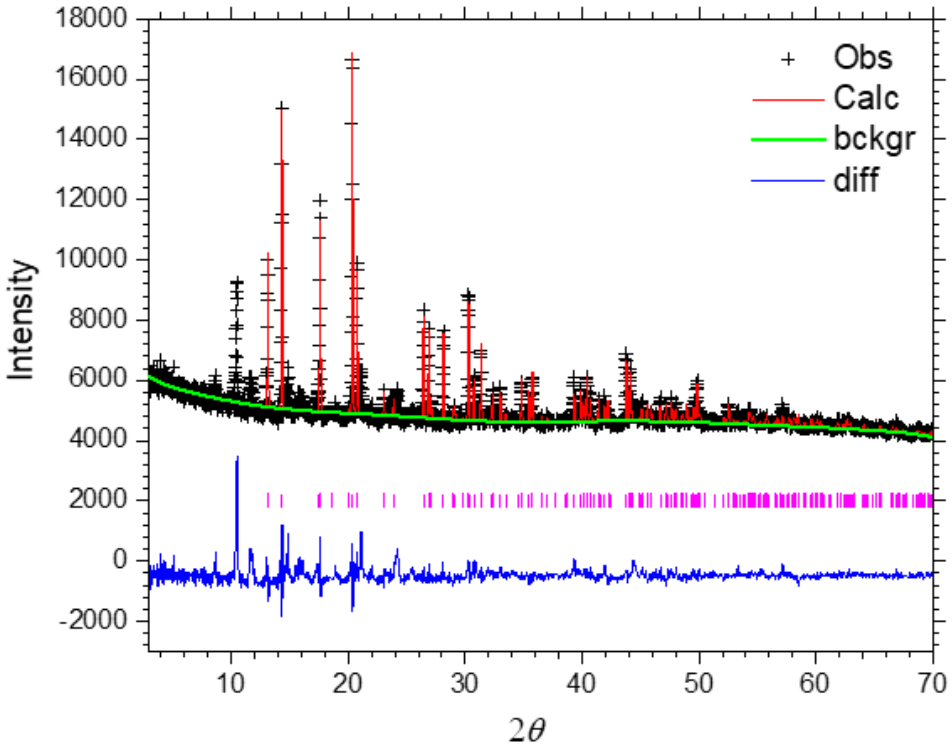

Fig. 4-7 Rietveld plot (PXRD, CuKα1) for **12**. The 011 and 022 reflections have been excluded.

4-3-1-2 (*pipz*H$_2$)Fe(C$_2$O$_4$)$_2$ (13)

Compound **13** was firstly synthesised in a FeF_2, *pipz* and HF reagent system, which product contained a large amount of impurity phase. The synthesis presented here is optimised with no HF in the reaction.

0.540 g (3 mmol) iron oxalate dihydrate ($FeC_2O_4{\cdot}2H_2O$), 0.43 g (5 mmol) *pipz*, and 0.45 g (5 mmol) oxalic acid were dissolved in 3 mL EG and 3 mL H_2O mixed solvent at room temperature. The overall molar ratio of reactants is Fe^{2+}: $C_2O_4^{2-}$: *pipz* = 1: 1.67: 1.67. Then, the homogeneous mixture was sealed in a 30 mL Teflon-lined stainless-steel autoclave and placed

in a 120 °C oven, maintained for 96 hours. After the autoclave was cooled to room temperature, crystallised product was obtained by filtration with washing by EtOH. There are also two crystallised phases in the product, yellow block single crystals of **13** (main phase) and small amount of large colourless single crystals (by-product). The single crystals of **13** were collected and characterised by PXRD at room temperature and single crystal structure data were collected at 173 K.

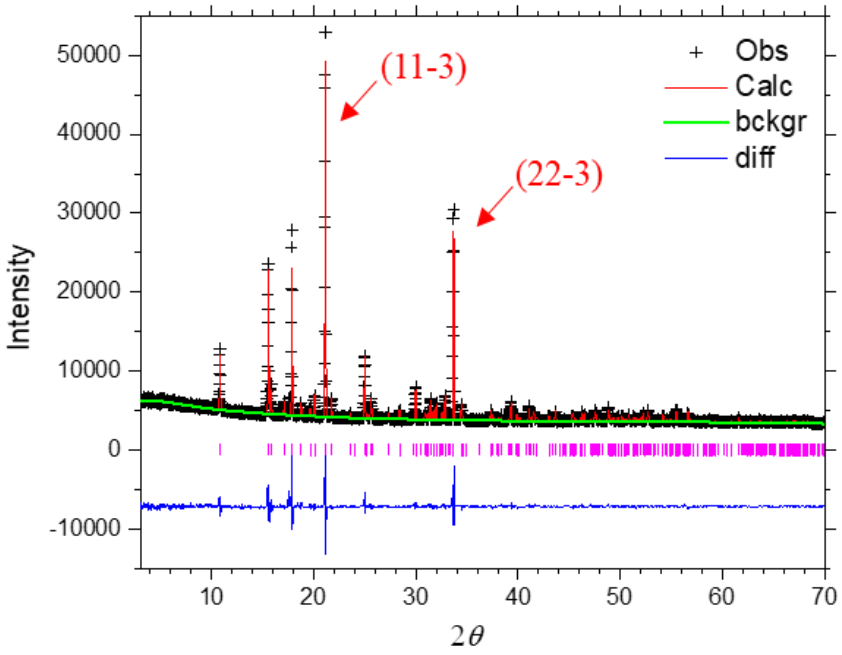

Fig. 4-8 Rietveld plot (PXRD, CuKα1) for **13**. The (11-3) and (22-3) peaks are shown by red arrows.

Rietveld refinements were applied for the PXRD data (Fig. 4-8). A preferred orientation was observed, with (11-3) and (22-3) reflections exhibiting extremely high intensities, which were corrected by the March-Dollase preferential orientation model, where the ratio of (11-3) was 0.7491. The crystallographic models were used, based on the CIF file from the single crystal refinement at 173 K, with a space group of *C*2/*c*. The refined lattice parameters are *a* =

9.6608(5) Å, b = 7.1168(3) Å, c = 16.6915(6) Å and β = 101.809(3)˚ with wRp = 0.0481, Rp = 0.0268 and χ^2 = 10.35. The result also shows no crystallographic phase transition between 173 K and room temperature (see 4-3-2-2, single crystal part).

4-3-1-3 (*pipz*H_2)$Fe_2(C_2O_4)_2F_2(H_2O)_2$ (14)

0.540 g (3 mmol) iron oxalate dihydrate ($FeC_2O_4 \cdot 2H_2O$), 0.43 g (5 mmol) *pipz*, and 0.8 mL (22.4 mmol) HF (48-51 % wt. in water) were dissolved in 3 mL EG and 3 mL EtOH mixed solvent at room temperature. The overall molar ratio of reactants is Fe^{2+}: $C_2O_4^{2-}$: *pipz*: F^- = 1: 1: 1.67: 7.47. Then, the homogeneous mixture was sealed in a 50 mL Teflon-lined stainless-steel autoclave and placed in a 120 °C oven, maintained for 72 hours. After the autoclave was cooled to room temperature, crystallised product was obtained by filtration with washing by EtOH. There are also two crystallised phases in the product, orange prism single crystals of **14** (main phase) and a small amount of large colourless single crystals (by-product). The single crystal products of **14** were picked out manually and collected for magnetic analysis. The single crystal structure data were collected at 173 K and room temperature.

4-3-1-4 (*pipz*H_2)$Co_2(C_2O_4)_2F_2(H_2O)_2$ (15)

0.370 g (2.5 mmol) cobalt oxalate (CoC_2O_4), 0.43 g (5 mmol) *pipz*, and 0.5 mL (14 mmol) HF (48-51 % wt. in water) were dissolved in 2.5 mL EG and 2.5 mL EtOH mixed solvent at room temperature. The overall molar ratio of reactants is Co^{2+}: $C_2O_4^{2-}$: *pipz*: F^- = 1: 1: 2: 5.6. Then, the homogeneous mixture was sealed in a 50 mL Teflon-lined stainless-steel autoclave and placed in a 120 °C oven, maintained for 120 hours. After the autoclave was cooled to room temperature, purple chip single crystals of **15** were obtained by filtration with washing by EtOH. The single crystal products of **15** were collected for magnetic analysis, and single crystal structure data were collected at 173 K. The PXRD data were also measured at room temperature.

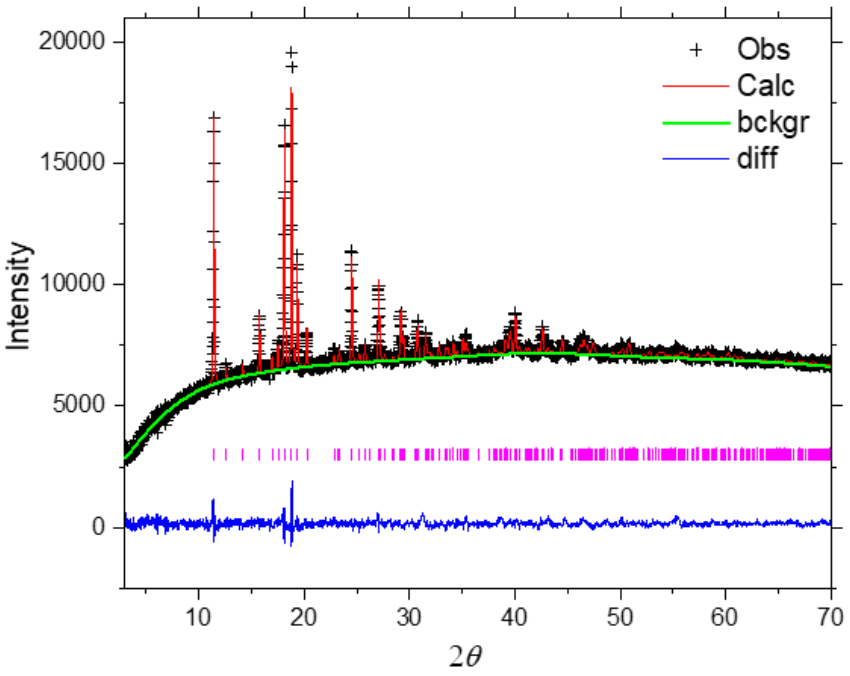

Fig. 4-9 Rietveld plot (PXRD, CuKα1) for **15**.

Fig. 4-9 shows the Rietveld refinement for the PXRD data of **15**. The crystallographic models were used, based on the CIF file from the single crystal refinement at 173 K, with a triclinic space group of *P*-1. The refined lattice parameters are a = 6.4530(5) Å, b = 7.2763(4) Å, c = 7.9963(7) Å, α = 80.646(3)˚, β = 80.937(4)˚, and γ = 80.415(5)˚ with wRp = 0.0187, Rp = 0.0131 and χ^2 = 2.416. The result also shows no crystallographic phase transition between 173 K to room temperature (see 4-3-2-3, single crystal part).

4-3-1-5 (*pipz*H)Fe(C_2O_4)$_2$·(H_2O) (16)

0.180 g (1 mmol) iron oxalate dihydrate ($FeC_2O_4·2H_2O$), 0.340 g (4 mmol) *pipz*, and 0.1 mL (2.8 mmol) HF (48-51 % wt. in water) were dissolved in 1 mL EG and 1 mL EtOH mixed solvent at room temperature. The overall molar ratio of reactants is Fe^{2+}: $C_2O_4^{2-}$: *pipz*: F^- = 1: 1: 4: 2.8. Then, the homogeneous mixture was sealed in a 15 mL Teflon-lined stainless-steel autoclave and placed in a 120 °C oven, maintained for 72 hours. After the autoclave was

cooled to room temperature, the product was obtained by filtration with washing by EtOH. There are three phases in the product: large red block single crystals of **16** (main phase) and small amounts of two impurity phases, colourless stripe single crystals (compound **23**, 5-3-5) and light-yellow powder. The single crystal products of **16** were picked manually and collected for magnetic analysis. The purity of picked sample was confirmed by PXRD at room temperature and the single crystal structure data were collected at 173 K.

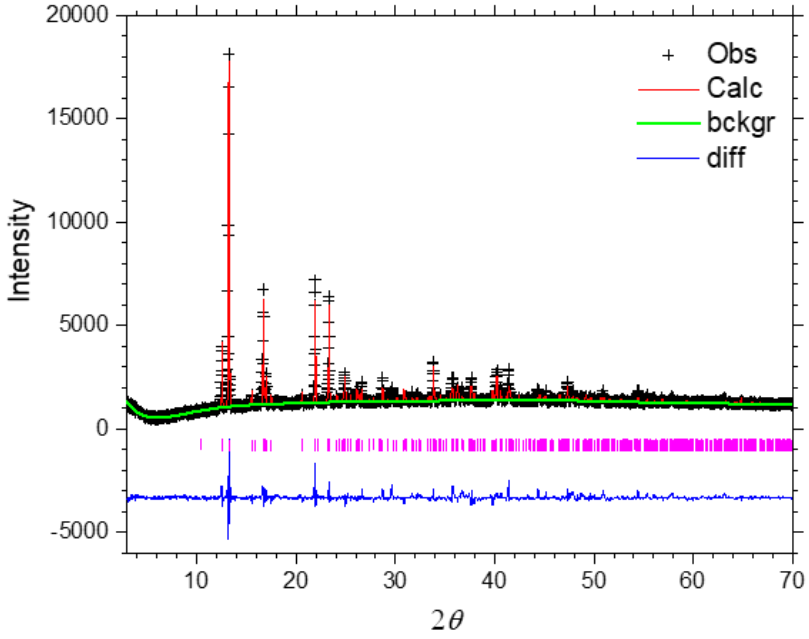

Fig. 4-10 Rietveld plot (PXRD, CuKα1) for **16**.

Rietveld refinements were applied for the PXRD data (Fig. 4-10). The crystallographic models were used, based on the CIF file from the single crystal refinement at 173 K, with a space group of *P*-1. The refined lattice parameters are a = 7.7341(5) Å, b = 8.1466(5) Å, c = 8.7888(7) Å, α = 92.528(5)˚, β = 93.759(5)˚, and γ = 117.294(2)˚ with wRp = 0.0711, Rp = 0.0478 and χ^2 = 6.823. The cell parameters are similar with CIF data measured at 173 K, which shows there is probably no crystallographic phase transition from 173 K to room temperature (see single crystal part, 4-3-2-4).

4-3-2 Single Crystal Data and Magnetic Properties of 12-16.

4-3-2-1 Single Crystal Structure and Analysis for 12

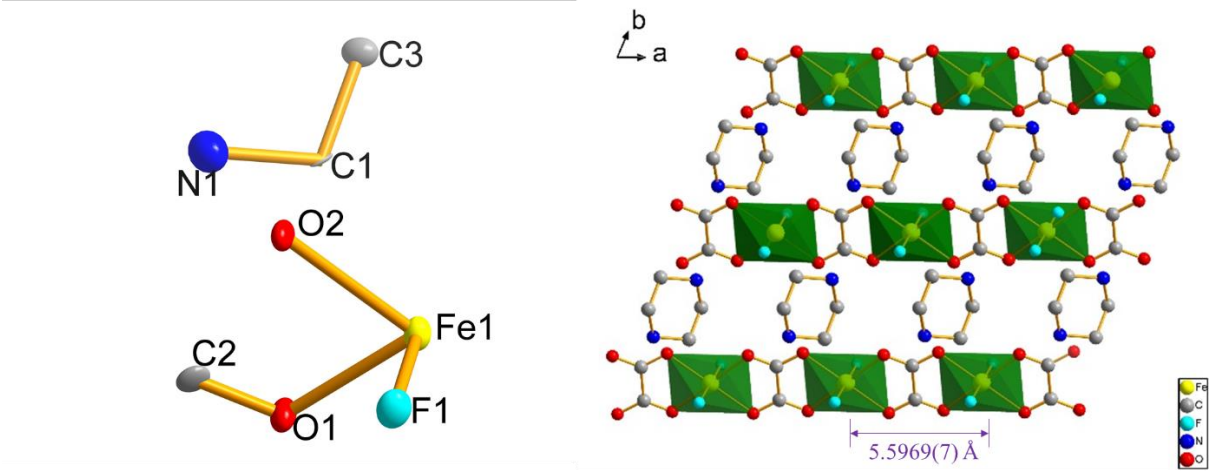

Fig. 4-11 Asymmetric unit in ellipsoid plot (left) with ellipsoids are represented at 50 % and Polymeric structure (right) of **12**. (Hydrogen atoms are eliminated for clarity.)

Table 4-4 Crystallographic data and refinement details of **12**.

Compound (*T*)	**12** (173 K)
Formula	$(C_4H_{12}N_2)Fe(C_2O_4)F_2$
Formula weight	270.03
Density (g cm^{-3})	1.934
Crystal system	Triclinic
Space group	*P*-1
a/Å	5.5969(7)
b/Å	6.7463(8)
c/Å	6.8529(8)
α/°	81.769(16)
β/°	80.921(16)
γ/°	65.625(13)
V/Å^3	231.86(5)
Z	1
Measured ref	1988
Independent ref	819
	[*R*(int) = 0.0476]
GOOF	1.094
Final *R* indices ($I > 2\sigma(I)$)	*R*1 = 0.0554,
	*wR*2 = 0.1484

Table 4-5 Selected bond lengths (Å) and bond valences for **12**.

	Bond lengths	S_{ij}
Fe1-F1	2.012(3)	0.375
Fe1-F1	2.012(3)	0.375
Fe1-O1	2.165(5)	0.311
Fe1-O1	2.165(5)	0.311
Fe1-O2	2.156(3)	0.321
Fe1-O2	2.156(3)	0.321
		$\sum \mathrm{Fe1} = 2.014$

The single crystal data of **12** were measured at 173 K and the refined crystal structure is depicted in Fig. 4-11. The iron atom (Fe1) is in a centrosymmetric position, which is 6-coordinated, with four oxygen atoms (O1 and O2) and two fluorine atoms (F1) forming an octahedron (Fig. 4-11 (left)). The iron cation is calculated in 2+ state ($\sum \mathrm{Fe1} = 2.014$), with the Fe-O bond lengths of 2.156(3) and 2.165(5) Å, while the two equivalent Fe-F bond lengths are 2.012(3) Å (Table 4-5).

The Fe^{2+} cations are connected by the carboxylate groups of bis-bidentate oxalate ligands through *anti-anti-*μ^2*-*η^1*:*η^1 Fe-O-C-O-Fe bridges and form nearly straight one-dimensional magnetic chains with the Fe-Fe distance being 5.5969(7) Å (*a*-axis length, Fig. 4-11 (right)). This structural feature is similar with the synthesis reaction reagent, humboldtine ($FeC_2O_4 \cdot 2H_2O$)[11,12] with the H_2O molecules being substituted by F^- ions. The intrachain magnetic connection between Fe^{2+} cations in **12** should therefore be similar with $FeC_2O_4 \cdot 2H_2O$, being an antiferromagnetic interaction.[13] The distances of interchain neighbouring Fe^{2+} cations are 6.7463(8) Å (*b*-axis length) and 6.8529(8) Å (*c*-axis length). Since there is no effective magnetic bridge, the interchain magnetic interactions should be very weak. So, a magnetic characterisation is needed to reveal the real magnetic properties of **12**.

The protonated pipzazine cation acts as a compensating species to balance the charge. Besides, it also attaches to the octahedra by hydrogen bonds and links the $(FeC_2O_4F_2)^{2-}$ chains to form a 3D structure (Fig. 4-12).

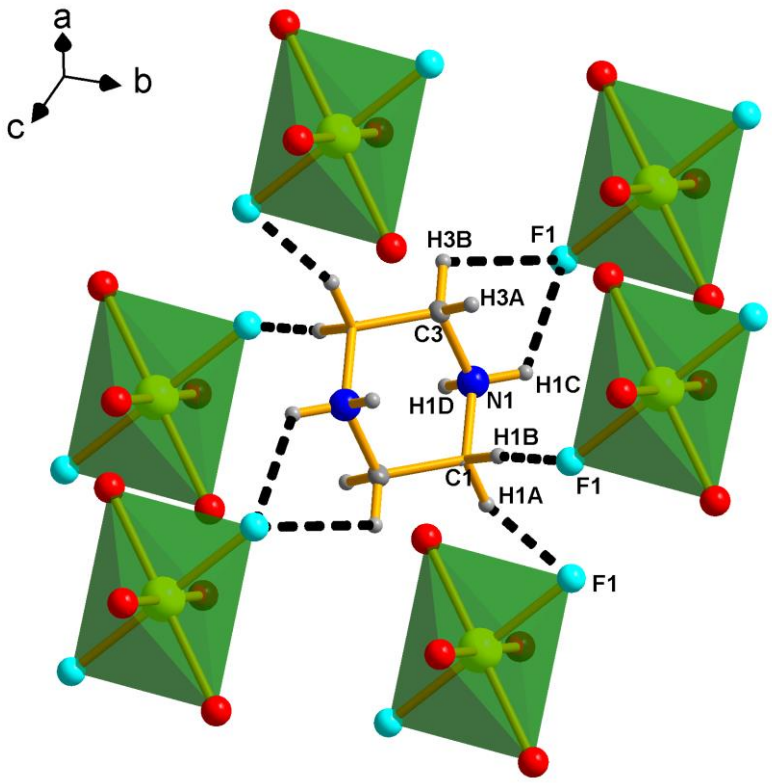

Fig. 4-12 Illustration of the hydrogen bonds (dotted lines) of **12**.

4-3-2-2 Single Crystal Structure and Analysis for 13

Table 4-6 Crystallographic data and refinement details of **13**.

Compound (*T*)	**13** (173 K)
Formula	$(C_4H_{12}N_2)Fe(C_2O_4)_2$
Formula weight	320.05
Density (g cm^{-3})	1.909
Crystal system	Monoclinic
Space group	*C*2/*c*
a/Å	9.6889(6)
b/Å	7.0652(4)
c/Å	16.6338(11)
β/°	101.996(6)
V/Å^3	1113.78(12)
Z	4
Measured ref	4533
Independent ref	980
	[*R*(int) = 0.0302]
GOOF	1.026
Final *R* indices ($I > 2\sigma(I)$)	*R*1 = 0.0209,
	*wR*2 = 0.0526

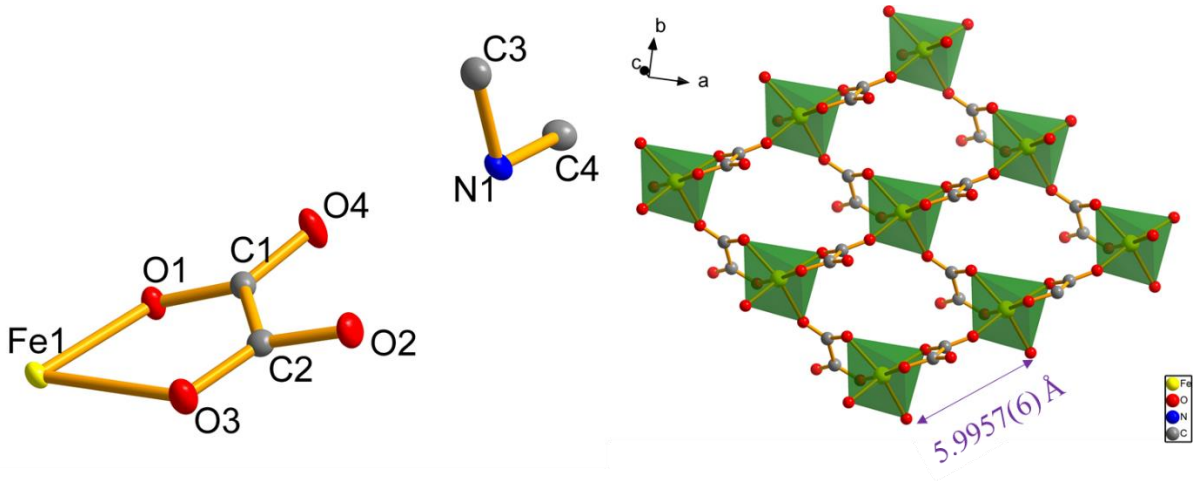

Fig. 4-13 Asymmetric unit in ellipsoid plot (left) with ellipsoids are represented at 50 % and iron-oxalate layer (right) of **13**. (Hydrogen atoms are eliminated for clarity.)

Table 4-7 Selected bond lengths (Å) and bond valences for **13**.

	Bond lengths	S_{ij}
Fe1-O1	2.065(1)	0.409
Fe1-O1	2.065(1)	0.409
Fe1-O2	2.163(1)	0.314
Fe1-O2	2.163(1)	0.314
Fe1-O3	2.208(1)	0.278
Fe1-O3	2.208(1)	0.278
		$\sum \mathrm{Fe1} = 2.002$

Single crystal data of **13** were measured at 173 K (Table 4-6). The refinement shows the compound crystallises as monoclinic with space group *C*2/*c*. The iron atom (Fe1) is in a centrosymmetric position and 6-coordinating with six oxygen atoms (O1, O2 and O3). The shortest Fe-O bond length is 2.065(1) while the longest is 2.208(1) Å (Table 4-7) through which a FeO_6 pseudo-octahedon is formed (Fig. 4-13 (left)). The iron cation is also in 2+ state, which is confirmed by the BVS calculation ($\sum \mathrm{Fe1} = 2.002$).

The Fe pseudo-octahedra are connected by the oxalate ligands through *syn-anti*-μ^2-η^1:η^1 Fe-O-C-O-Fe bridges, to form 2D rhombus-like $[Fe(C_2O_4)_2^{2-}]_\infty$ magnetic layers with all the Fe-Fe distances equal to 5.8857(6) Å (Fig. 4-13 (right)). Normally, the *syn-anti* carboxylate bridge can mediate ferromagnetic interactions.[14, 15] However, we have not found any similar oxalate example in such a connection style yet. However, due to the instrument's issue, the magnetic properties of **13** have not been investigated. In the future, further measurements are needed to reveal the magnetic properties of **13**.

The protonated piperazine cation acts as a compensating group to balance the charge. In addition, it also connects with the 2D layers by two hydrogen bonds (N1-(H1A)---O4 and N1-(H1B)---O1) and binds the 2D layers into a 3D structure (Fig. 4-14). The nearest Fe-Fe interlayer distance is 8.4470(6) Å, which is not likely to build significant magnetic interactions, especially with no direct magnetic pathway. Thus, the magnetic behaviour of **13** is more likely to approach a 2D structure.

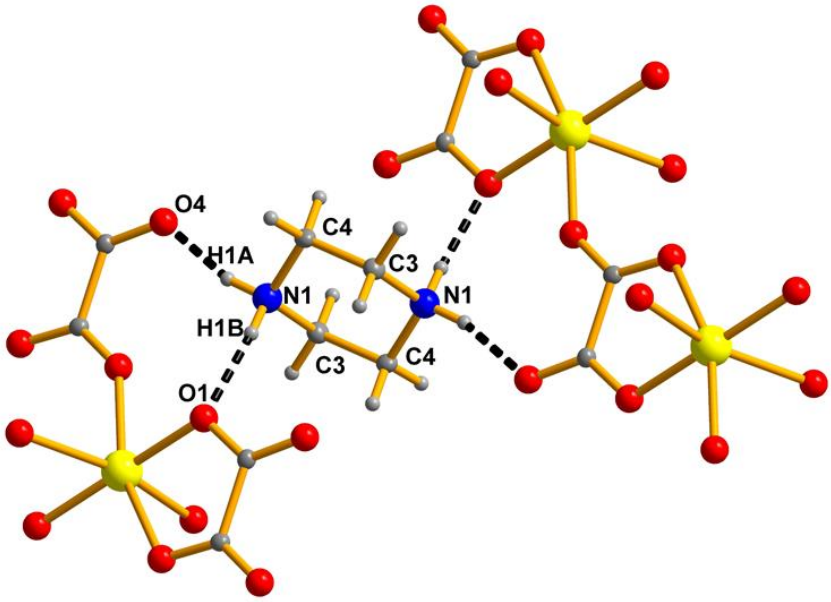

Fig. 4-14 Illustration of the hydrogen bonds (dotted lines) of **13**.

Table 4-8 Crystallographic data and refinement details of **14** and **15**.

Compound (*T*)	**14** (173 K)	**14** (298 K)	**15** (173 K)
Formula	$(C_4H_{12}N_2)_{0.5}Fe(C_2O_4)F(H_2O)$	$(C_4H_{12}N_2)_{0.5}Fe(C_2O_4)F(H_2O)$	$(C_4H_{12}N_2)_{0.5}Co(C_2O_4)F(H_2O)$
Formula weight	224.96	224.96	228.04
Density (g cm^{-3})	2.041	2.028	2.103
Crystal system	Triclinic	Triclinic	Triclinic
Space group	*P*-1	*P*-1	*P*-1
a/Å	6.4775(5)	6.4959(5)	6.4240(11)
b/Å	7.2789(5)	7.3073(5)	7.2742(11)
c/Å	8.0073(6)	8.0117(6)	8.0048(14)
α/°	81.626(8)	81.565(9)	80.46(3)
β/°	81.557(8)	81.386(8)	80.81(3)
γ/°	81.135(9)	81.072(9)	80.20(3)
V/$Å^3$	366.05(5)	368.47(5)	360.16(11)
Z	2	2	2
Measured ref	3139	3175	2575
Independent ref	1289	1298	1274
	[*R*(int) = 0.0252]	[*R*(int) = 0.0270]	[*R*(int) = 0.1092]
GOOF	1.048	1.055	0.947
Final *R* indices ($I > 2\sigma(I)$)	*R*1 = 0.0289,	*R*1 = 0.0327,	*R*1 = 0.0664,
	*wR*2 = 0.0724	*wR*2 = 0.0800	*wR*2 = 0.1479

4-3-2-3 Single Crystal Structure, Magnetic Properties, and Analysis for 14 and 15

Single crystal data of **14** were collected at 173 K and 298 K with the same single crystal. No evidence of any structural phase transition was observed, but only small changes of bond lengths and angles within the temperature range. Higher temperature corresponds with larger *a*, *b*, *c* lengths and unit cell volume. As **14** and **15** are isostructural and no phase transition was observed for **14**, only one single crystal dataset of **15** was collected, at 173 K. The result of refinements shows the compounds crystallised in triclinic with the space group *P*-1. (Table 4-8)

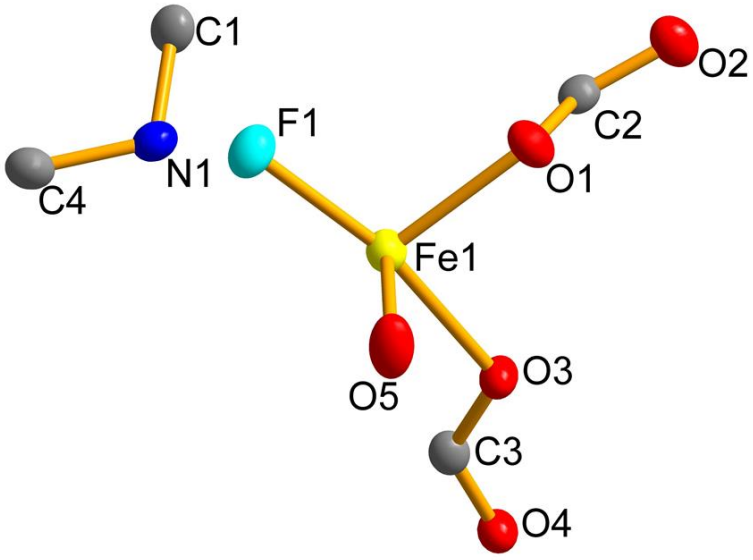

Fig. 4-15 The asymmetric unit structure of **14** (298 K) in ellipsoid plot with ellipsoids are represented at 50 %. (Hydrogen atoms are eliminated for clarity.)

The description of the crystal structure of the compounds is depicted based on the CIF file of **14** (298 K). The asymmetric structure shows Fe1 is 6-coordinated, with five oxygen atoms (O1, O2, O3 and O4 from two oxalate ligands and O5 from H_2O molecule) and one fluorine atom (F1) forming a pseudo-octahedron (Fig. 4-15). The Fe-O bond lengths are between 2.128(3)-2.177(3) Å, while the only Fe-F bond length is 1.990(3) Å (Table 4-9). Iron

and cobalt are both in the 2+ oxidation state, as confirmed by the bond valence sum calculation ($\sum \mathrm{Fe1} = 2.045$ (173 K) and 2.031 (298 K), $\sum \mathrm{Co1} = 2.008$) (Table 4-9, 4-10), which are in agreement with the charge balanced chemical formulae.

Table 4-9 Selected bond lengths (Å) and bond valences for **14** at 173 K (left) and 298 K (right).

	Bond lengths	S_{ij}	**Bond lengths**	S_{ij}
Fe1-F1	1.991(2)	0.398	1.990(3)	0.399
Fe1-O1	2.139(2)	0.335	2.138(3)	0.336
Fe1-O2	2.163(2)	0.314	2.169(3)	0.309
Fe1-O3	2.126(2)	0.347	2.133(3)	0.340
Fe1-O4	2.175(2)	0.304	2.177(3)	0.302
Fe1-O5	2.126(2)	0.347	2.128(3)	0.345
		$\sum \mathrm{Fe1} = 2.045$		$\sum \mathrm{Fe1} = 2.031$

Table 4-10 Selected bond lengths (Å) and bond valences for **15** (173 K).

	Bond lengths	S_{ij}
Co1-F1	1.999(5)	0.379
Co1-O1	2.096(5)	0.336
Co1-O2	2.128(6)	0.308
Co1-O3	2.118(5)	0.316
Co1-O4	2.112(5)	0.321
Co1-O5	2.083(6)	0.348
		$\sum \mathrm{Co1} = 2.008$

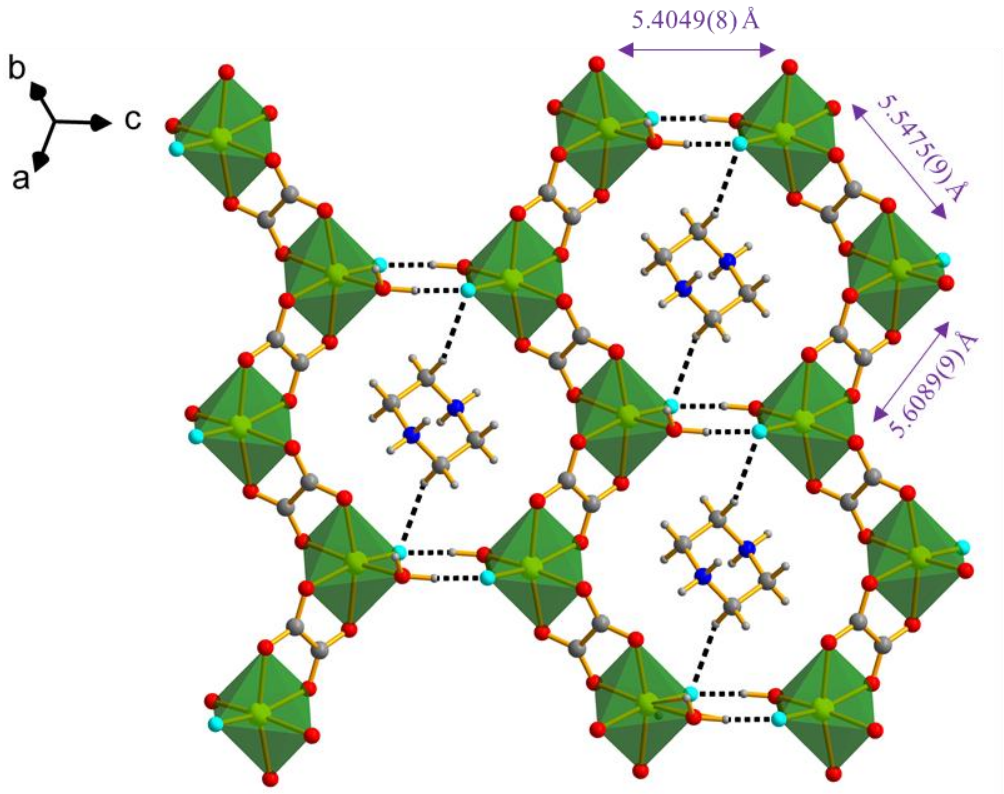

Fig. 4-16 Illustration of the iron-oxalate chains connection of **14** (298 K). (Hydrogen bonds are shown as dotted lines.)

The Fe pseudo-octahedra are connected by the carboxylate groups of bis-bidentate oxalate ligands through *anti-anti-*μ^2*-*η^1*:*η^1 Fe-O-C-O-Fe bridges and form 1D magnetic chains with Fe-Fe distances of 5.5475(9) and 5.6089(9) Å (Fig. 4-16). Similar metal-oxalate chain structures have been reported, for which the magnetic properties also been investigated.[16-18] Besides the metal-oxalate magnetic exchange pathways, neighbouring magnetic chains are linked through Fe-O-H---F-Fe (5.4049(8) Å), which can also be considered as a potential magnetic interaction pathway.[19] Thus, the entire $[Fe(C_2O_4)F(H_2O)^-]_\infty$ part can be regarded as a nearly flat 2D *quasi*-honeycomb magnetic spin-frustrated system. The shortest Fe-Fe interlayer distance is 5.0948(9) Å which is even shorter than the intralayer connections (Fig. 4-17). However, it is hard to construct effective magnetic interactions through that route since no effective magnetic exchange pathway was observed. The isostructural compound **15** has

analogous magnetic exchange pathways, but the corresponding distances for Fe are longer than Co (5.3629(23) Å and 5.4637(25) Å for *anti-anti-*μ^2*-*η^1*:*η^1 Co-O-C-O-Co and 5.5068(25) Å for Co-O-H---F-Co), which will theoretically construct stronger magnetic interactions.

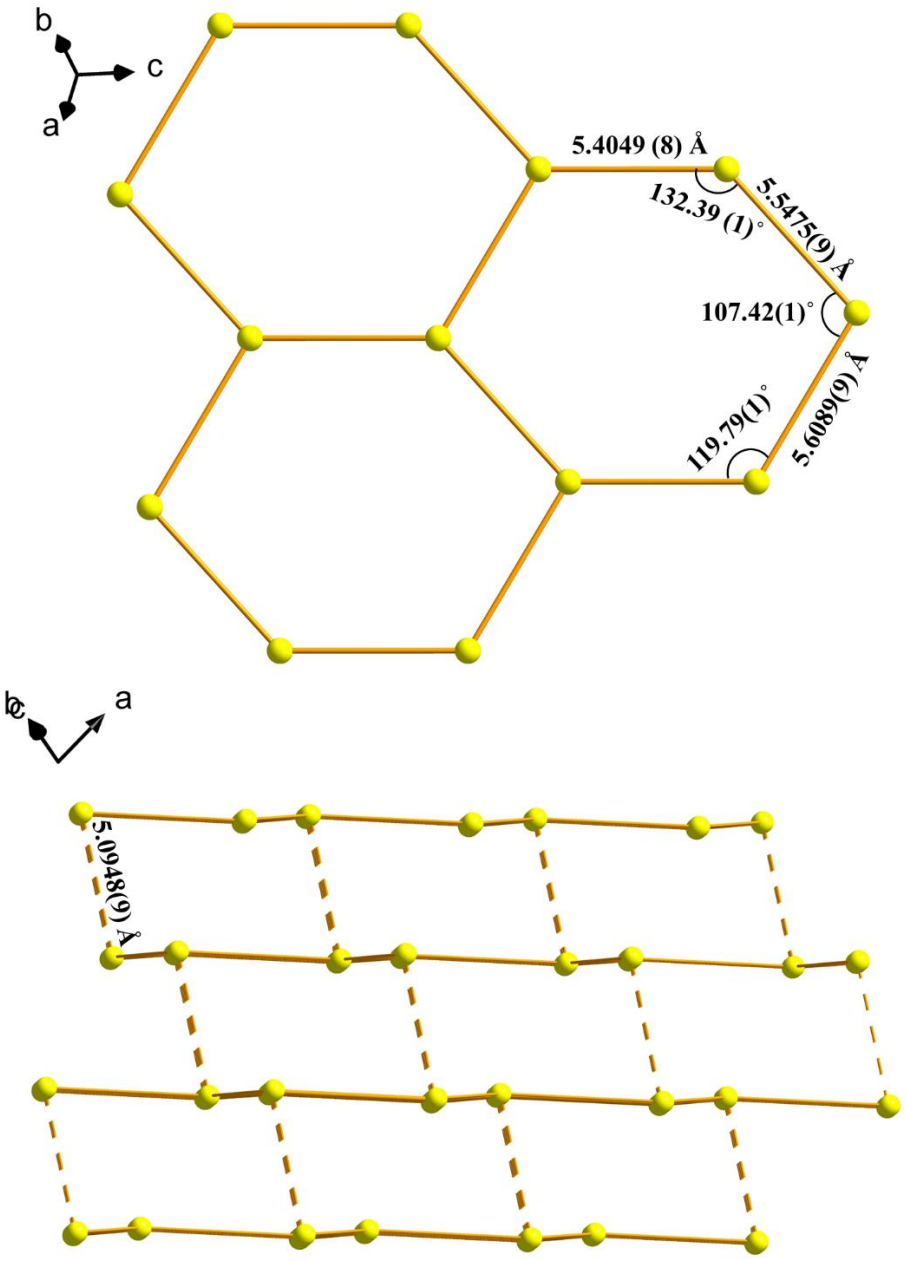

Fig. 4-17 Illustration of the honeycomb structure with Fe network in top view (top) and side view (bottom) of **14** (298 K). Dotted lines mean there is no interlayer magnetic interaction.

The protonated piperazine cation locates in the cavity of the “honeycomb” and balances the charge (Fig. 4-16). It attaches with the skeleton structure through a C4-(H4B)---F1 hydrogen bond. Besides, the piperazine also connects two neighbouring layers of the located honeycomb through a N1-(H1B)---F1 hydrogen bond (Fig. 4-18).

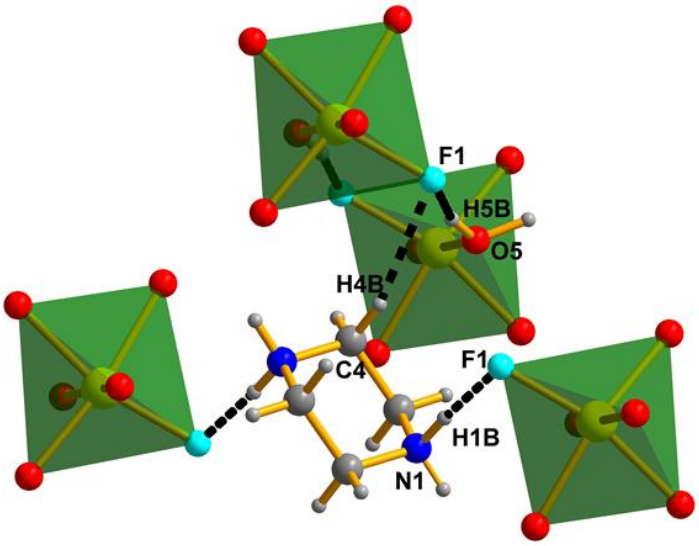

Fig. 4-18 Illustration of the hydrogen bonds (dotted lines) of **14**.

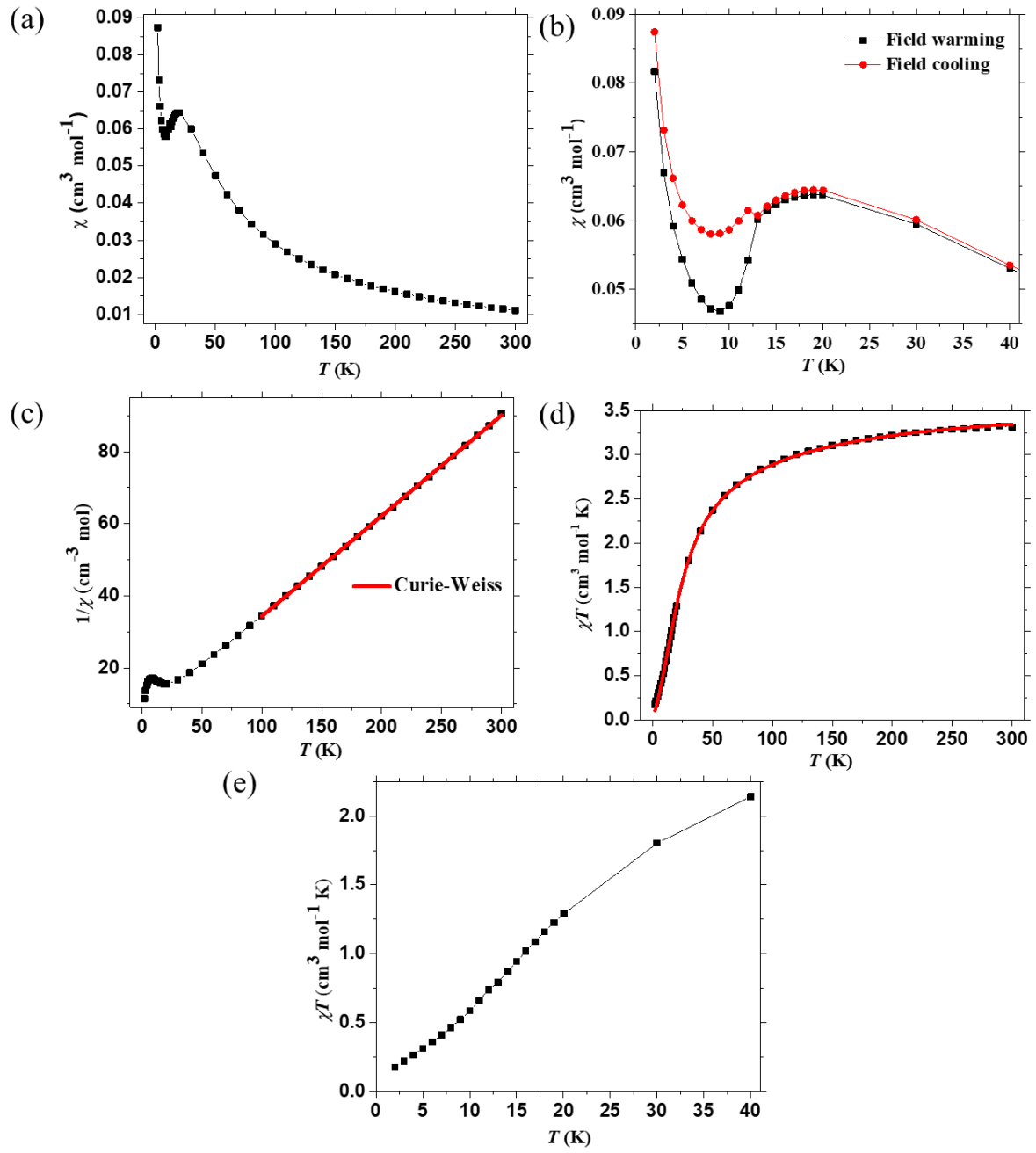

Fig. 4-19 The magnetic data of **14** measured at 100 Oe: (a) field cooling χ vs. T plot in the range 2K- 300 K; (b) detailed field cooling (red) and field warming (black) χ vs. T plot: 2-40 K; (c) $1/\chi$ versus T with the Curie-Weiss fit (solid red line) to $1/\chi$; (d) χT vs. T plot in the range 2K- 300 K with 1D Heisenberg chain model fitting (solid red line) and (e) detailed χT vs. T plot: 2-40 K.

The magnetic data of **14** measured at 100 Oe are shown in Fig. 4-19. In the field cooling χ versus T plot (Fig. 4-19 (a)), χ monotonically increases during cooling, until 20 K, then monotonically decreases and forms a peak, which indicates a low-dimensional antiferromagnetic ordering. Upon further cooling, another tiny sharp peak is observed around 12 K (Fig. 4-19 (b)). This may be caused by a small amount of magnetic Fe^{2+} or Fe^{3+} impurities, or perhaps by interchain spin interactions changing or by instrument error. In the field warming process, the small peak has disappeared, which shows it is probably not caused by impurities.

The Curie constant, C = 3.59 $cm^3\,mol^{-1}$ K and Weiss constant, θ = −23.01 K were deduced from the T >100 K part of the $1/\chi$ versus T plot, corresponding to the antiferromagnetic exchange interaction (Fig. 4-19 (c)). Based on the data, the derived Landé factor, g = 2.17 and effective moment, μ_{eff} = 5.36 μ_B per Fe^{2+}, which is somewhat higher than spin-only value (4.90 μ_B), probably due to an orbital contribution.

At high temperature (270 K−300 K), χT is saturated around 3.3 $cm^3\,mol^{-1}$ K, nearly in a paramagnetic state (Fig. 4-19 (d)). The shape the χT versus T plot clearly shows an antiferromagnetic interaction between the Fe^{2+} ions, which is well described by an S = 2 1D Heisenberg chain model fitting, with the intrachain coupling constant J = −2.64(2) K and g = 2.21. Such a small coupling constant indicates the magnetic connections between Fe centres are weak. The magnetic ordering peak which should be appear at $T_N \approx$ 20 K is also missing (Fig. 4-19 (e)). All the evidence shows the magnetic connection is weak in this compound; further measurements in a lower applied field would probably show more details. The frustration index, $f = |\theta|/ T_N \approx 1.15$ indicates no frustration. Thus, the main magnetic exchange pathway of **14** is likely to be the 1D *anti-anti* carboxylate bridge.

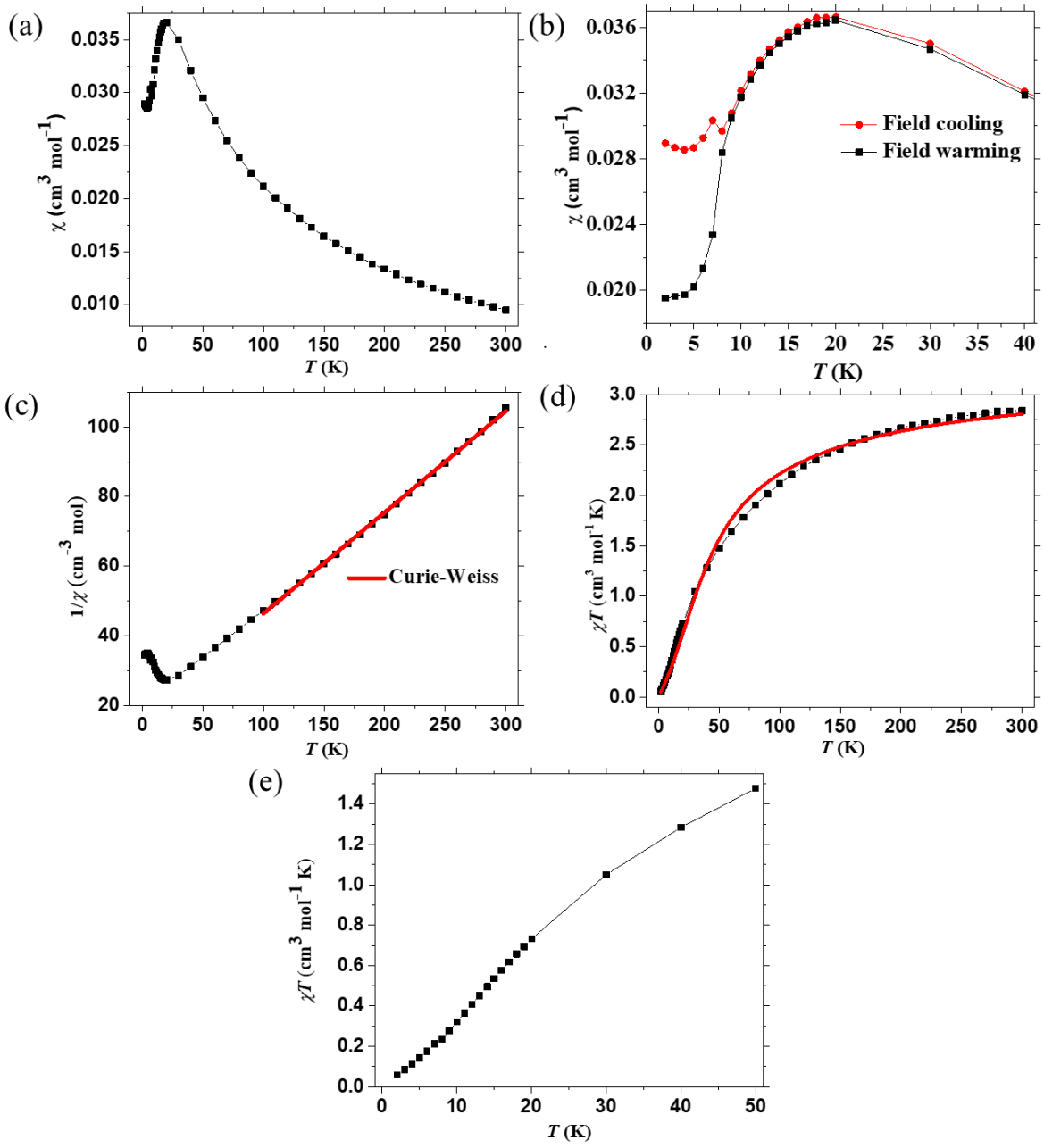

Fig. 4-20 The magnetic data of **15** measured at 100 Oe: (a) field cooling χ vs. T plot in the range 2K- 300 K; (b) detailed field cooling (red) and field warming (black) χ vs. T plot: 2-40 K; (c) $1/\chi$ versus T with the Curie-Weiss fit (solid red line) to $1/\chi$; (d) χT vs. T plot in the range 2K- 300 K with 1D Heisenberg chain model fitting (solid red line) and (e) detailed χT vs. T plot: 2-40 K.

The magnetic data of **15** were also measured at 100 Oe, are shown in Fig. 4-20, which show similar features to **14**, with only numerical differences. The field cooling χ versus T plot follows the same trend as **14** with a similar critical temperature, T_N = 20 K (Fig. 4-20 (a)). Like in **14**, a small peak was also present in the field cooling process at 7 K (Fig. 4-20 (b)). The peak also disappeared in field warming measurement, which phenomenon is similar in **14**.

The Curie constant, C = 3.44 $cm^3\ mol^{-1}$ K and Weiss constant, θ = −59.30 K were deduced from the T >100 K part of the $1/\chi$ versus T plot, indicating a stronger antiferromagnetic exchange interaction than **14** (Fig. 4-20 (c)). The Landé factor, g = 2.71 and effective moment, μ_{eff} = 5.25 μ_B per Co^{2+} (S = 3/2), which is slightly higher than the spin-only value (4.90 μ_B), due to a strong orbital contribution.

At 300 K, χT is 2.84 $cm^3\ mol^{-1}$ K, lower than C, indicating an antiferromagnetic interaction at room temperature (Fig. 4-20 (d)). The χT vs. T plot is also fitted by a 1D Heisenberg chain model based on equation (4−1) with different constant setting (A = 1.2500, B = 17.041, C = 6.7360, and D = 238.47)[9] for a S = 3/2 system. The result shows the intrachain coupling constant J = −7.1(2) K and g = 2.63. The fitting plot also shows a little bias, which is probably caused by the spin-orbital coupling effect. Similar with **14**, there is still no magnetic ordering peak at 20 K in the χT vs. T plot (Fig. 4-20 (e)). The frustration index, $f = |\theta|/ T_N \approx 3$, higher than **14**, but still showing no significant frustration behaviour.

4-3-2-4 Single Crystal Structure, Magnetic Properties, and Analysis for 16

Single crystal data of **16** were collected at 173 K. The structural refinement shows the compound crystallised as triclinic with space group *P*-1 (Table 4-11). The asymmetric unit shows Fe1 is 6-coordinated, with four oxygen atoms from the oxalate ligand (O1, O2, O3 and O4), one terminal fluorine atom (F1) and one nitrogen from *pipz*H^+ (N2), thus forming a pseudo-octahedron (Fig. 4-21 (left)). The Fe-O bond lengths are in the range 2.127(2)-2.191(2) Å (Table 4-12), Fe-F is 1.948(2) and Fe-N, 2.186(2) Å. Bond valence sum calculation confirms the iron cation is in the 2+ state ($\sum \mathrm{Fe1} = 2.008$), which is in agreement with the chemical formula.

Table 4-11 Crystallographic data and refinement details of **16**.

Compound (*T*)	**16** (173 K)
Formula	$(C_4H_{11}N_2)Fe(C_2O_4)F\cdot(H_2O)$
Formula weight	268.03
Density (g cm^{-3})	1.842
Crystal system	Triclinic
Space group	*P*-1
a/Å	7.7113(5)
b/Å	8.1746(5)
c/Å	8.6739(6)
α/°	92.49(1)
β/°	93.301(1)
γ/°	117.393(8)
V/$Å^3$	483.15(7)
Z	2
Measured ref	4062
Independent ref	1684
	[*R*(int) = 0.0785]
GOOF	1.003
Final *R* indices ($I > 2\sigma(I)$)	*R*1 = 0.0415,
	*wR*2 = 0.1014

Table 4-12 Selected bond lengths (Å) and bond valences for **16**.

	Bond lengths	S_{ij}
Fe1-F1	1.948(2)	0.447
Fe1-O1	2.176(2)	0.303
Fe1-O2	2.183(2)	0.297
Fe1-O3	2.127(2)	0.346
Fe1-O4	2.191(2)	0.291
Fe1-N2	2.186(2)	0.324
		$\sum Fe1 = 2.008$

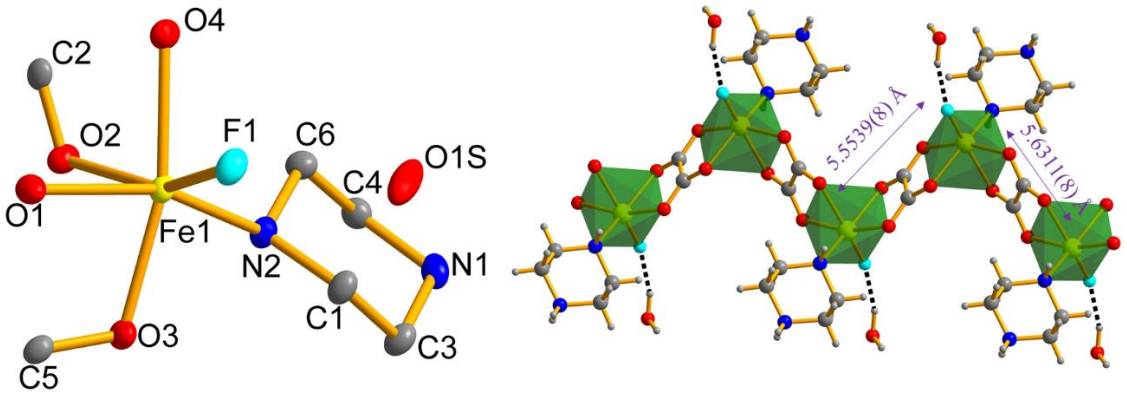

Fig. 4-21 Asymmetric unit in ellipsoid plot (left) with ellipsoids are represented at 50 % (Hydrogens are omitted for clarity) and iron-oxalate chain structure (right) of **16**.

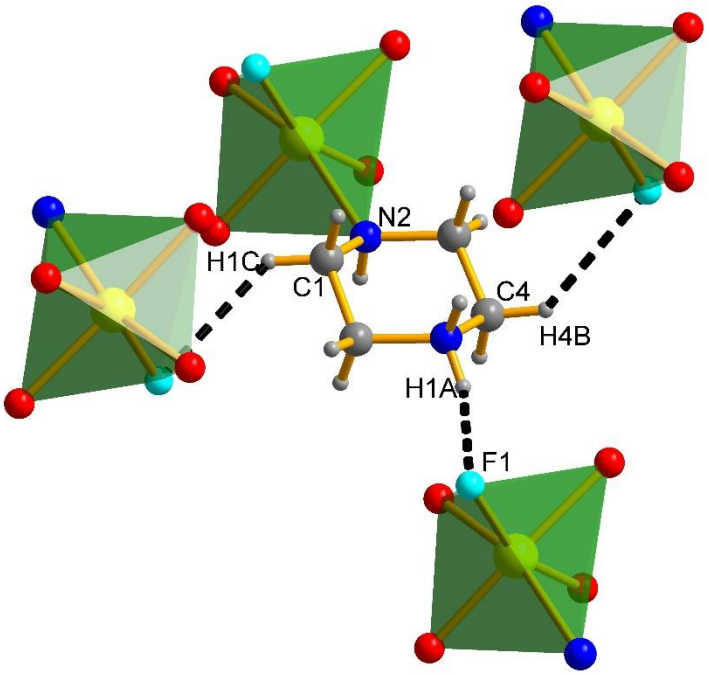

Fig. 4-22 Illustration of the hydrogen bonds (dotted lines) of **16**.

Similar with compounds **14** and **15**, the Fe pseudo-octahedra of **16** are also connected by two carboxylate groups of bis-bidentate oxalate ligands through *anti-anti-*μ^2*-*η^1*:*η^1 Fe-O-C-O-Fe bridges and form 1D magnetic chains where the Fe-Fe distances are 5.5539(8) and 5.6311(8) Å (Fig. 4-21 (right)). One interesting thing is that only one nitrogen of the piperazine is protonated and *pipz*H^+ coordinates with Fe^{2+} as a terminal ligand group. This is probably caused by the low ratio of HF in the starting materials in synthesis process. The channel water molecule combines with the structure by the O1S-H1S---F1, O1S-H1R---O3 and N2-H2C---O1S hydrogen bonds. In addition, there are no direct interchain connections, which theoretically would suggest an intrinsically 1D magnetic chain structure. The 3D structure is contributed by the piperazine cations, which connect the isolated magnetic chains by hydrogen bonds (Fig. 4-22).

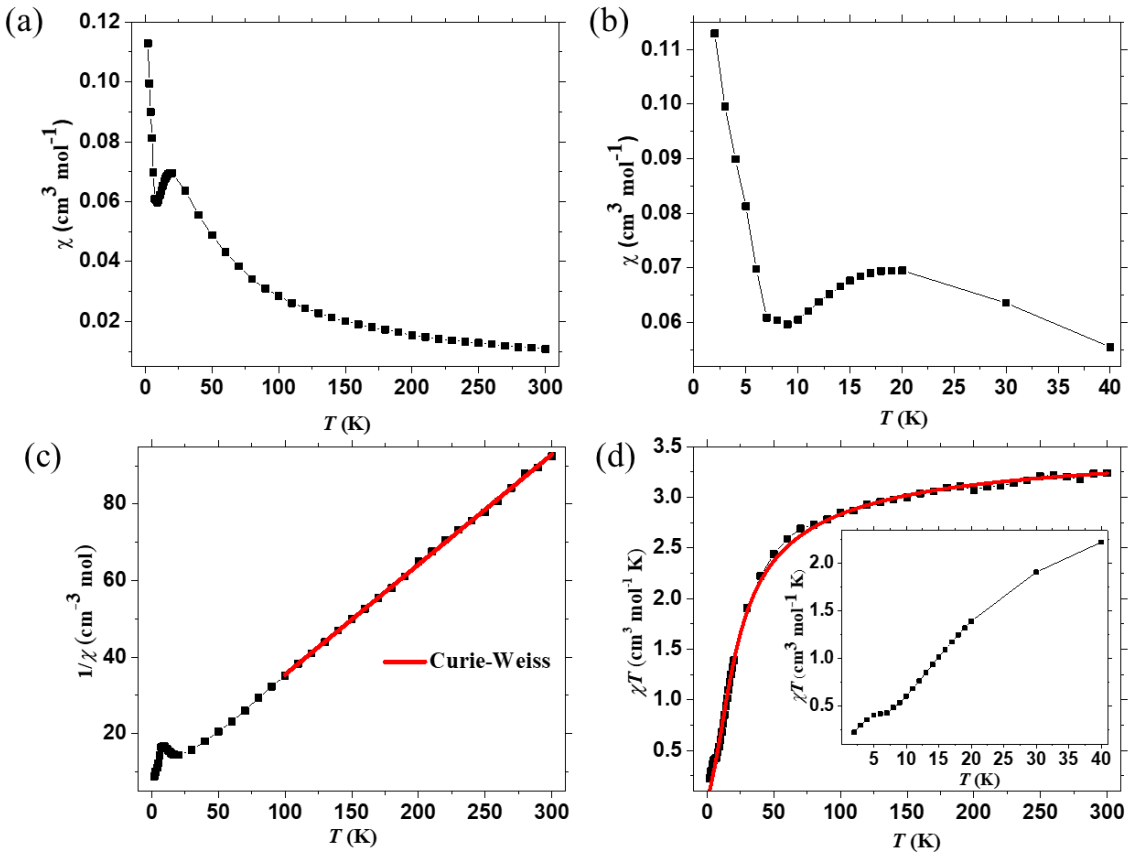

Fig. 4-23 The magnetic data of **16** at 100 Oe: (a) χ vs. T plot (2 K-300 K); (b) χ vs. T (2 K-40 K); (c) $1/\chi$ versus T with the Curie-Weiss fit to $1/\chi$ and (d) χT vs. T plot (The inset shows details in the range 2-40 K) with a 1D Heisenberg chain model fit.

Magnetic data of **16** were measured in a 100 Oe magnetic field. The magnetic properties of **16** are roughly similar with **14** and **15** but have some differences in detail. The χ versus T plot (Fig. 4-23 (a)) shows a low-dimensional antiferromagnetic ordering with the critical temperature ~19 K (Fig. 4-23 (b)).

Calculating from the T >100 K part of the $1/\chi$ versus T plot, the Curie constant, C = 3.48 $cm^3\ mol^{-1}$ K and Weiss constant, θ = −23.24 K, corresponding to an antiferromagnetic exchange interaction (Fig. 4-22 (c)). Deduced from the Curie-Weiss law, the Landé factor, g = 2.15 and effective moment, μ_{eff} = 5.28 μ_B per Fe^{2+}, which is higher than spin-only value (4.90 μ_B) due to the orbital contribution. The χT is 3.24 $cm^3\ mol^{-1}$ K at 300 K, which is nearly

saturated, indicating a paramagnetic state at room temperature (Fig. 4-23 (d)). The χT versus T plot is also well fitted by an S = 2 1D Heisenberg chain model (equation (4−1)) with the intrachain coupling constant J = −2.35(3) K and g = 2.16. The result shows a weak antiferromagnetic interaction through the *anti-anti* 1D oxalate chain.

4-4 Oxalated CPs with EG Capping

In the previous section, ethylene glycol (EG) is a solvent in the synthesis. However, surprisingly, it can coordinate with metal cations and build oxalate CPs as a neutral ligand. Here, the synthesis and crystal structure of two isostructural compounds (EG)Fe(C_2O_4) (**17**) and (EG)Co(C_2O_4) (**18**) will be presented.

4-4-1 Synthesis

4-4-1-1 (EG)Fe(C_2O_4) (17)

0.180 g (1 mmol) iron oxalate dihydrate ($FeC_2O_4{\cdot}2H_2O$), 0.14 ml (~2 mmol) dimethylamine (DMA), and 0.2 mL (5.6 mmol) HF (48-51 % wt. in water) were dissolved in 2 mL EG solvent at room temperature. Then, the homogeneous mixture was sealed in a 15 mL Teflon-lined stainless-steel autoclave and placed in a 120 °C oven, maintained for 72 hours. After the autoclave was cooled to room temperature, the crystallised product was obtained by filtration with washing by deionised water. The product contains two crystallised phases, large orange block single crystals of **17** (main phase) and large colourless single crystals (by-product). The single crystal products of **17** were picked out and the crystal structure data were collected at 173 K.

4-4-1-2 (EG)Co(C_2O_4) (18)

0.150 g (~1 mmol) cobalt oxalate (CoC_2O_4), 0.14 ml (~2 mmol) dimethylamine (DMA), and 0.2 mL (5.6 mmol) HF (48-51 % wt. in water) were dissolved in 2 mL EG solvent at room temperature. Then, the homogeneous mixture was sealed in a 15 mL Teflon-lined stainless-

steel autoclave and placed in a 120 °C oven, maintained for 72 hours. After the autoclave was cooled to room temperature, pure red block single crystals of **18** were obtained by filtration with washing by deionised water. The purity was confirmed by PXRD at room temperature and single crystal structure data were collected at 173 K.

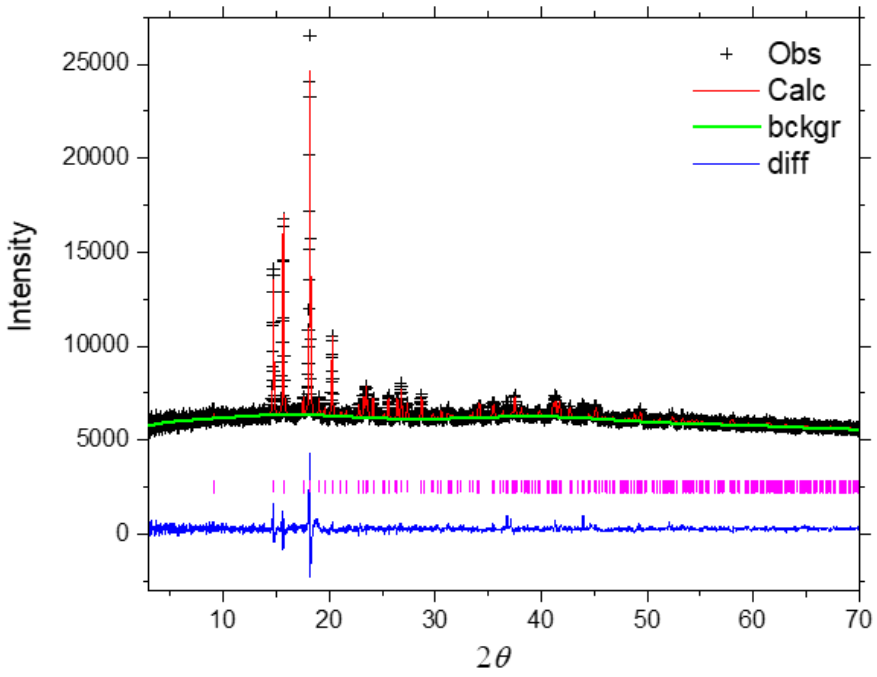

Fig. 4-24 Rietveld plot (PXRD, CuKα1) for **18**.

Fig. 4-24 shows the Rietveld refinement for the PXRD data of **18**. The refined parameters include background, scale factor, CW profile functions (GU, GV, GW and LX), cell parameters, the atomic positions for non-hydrogen atoms and Uiso for Co. The crystallographic models were used, based on the CIF file from the single crystal refinement at 173 K with a space group of *Pbca*. The refined lattice parameters are a = 7.6596(8) Å, b = 9.3432(10) Å, and c = 19.573(2) Å with wRp = 0.0233, Rp = 0.0144 and χ^2 = 3.416.

4-4-2 Single Crystal Structure and Analysis for 17 and 18

Table 4-13 Crystallographic data and refinement details of **17** and **18**.

Compound (*T*)	**17** (173 K)	**18** (173 K)
Formula	$(C_2H_6O_2)Fe(C_2O_4)$	$(C_2H_6O_2)Co(C_2O_4)$
Formula weight	205.94	209.02
Density (g cm^{-3})	1.911	1.999
Crystal system	Orthorhombic	Orthorhombic
Space group	*Pbca*	*Pbca*
a/Å	7.8045(8)	7.6346(5)
b/Å	9.3911(10)	9.2913(7)
c/Å	19.529(2)	19.5793(14)
V/Å^3	1431.3(3)	1388.86(17)
Z	8	8
Measured ref	10158	10516
Independent ref	1260	1220
	[*R*(int) = 0.1647]	[*R*(int) = 0.1015]
GOOF	0.978	1.045
Final *R* indices ($I > 2\sigma(I)$)	*R*1 = 0.0724,	*R*1 = 0.0370,
	*wR*2 = 0.1924	*wR*2 = 0.0919

Single crystal data of **17** and **18** were both collected at 173 K. The structural refinement shows the compounds crystallise in the orthorhombic system with space group *Pbca* (Table 4-13). Comparing the cell parameters refined from single crystal data and PXRD data, there is no phase transition from 173 K to room temperature. Bond valence sum calculation confirms the metal centres in both samples are in the 2+ state ($\sum \mathrm{Fe1} = 2.116$ and $\sum \mathrm{Co1} = 2.047$), which corresponds with the chemical formulae (Table 4-14).

Table 4-14 Selected bond lengths (Å) and bond valences for **17** (left) and **18** (right).

	Bond lengths	S_{ij}		**Bond lengths**	S_{ij}
Fe1-O1	2.097(5)	0.374	Co1-O1	2.084(3)	0.347
Fe1-O2	2.161(5)	0.317	Co1-O2	2.107(3)	0.326
Fe1-O3	2.096(5)	0.376	Co1-O3	2.081(3)	0.349
Fe1-O4	2.112(5)	0.361	Co1-O4	2.107(3)	0.326
Fe1-O5	2.157(5)	0.318	Co1-O5	2.093(3)	0.338
Fe1-O6	2.102(5)	0.370	Co1-O6	2.069(3)	0.361
		$\sum$Fe1 = 2.116			$\sum$Co1 = 2.047

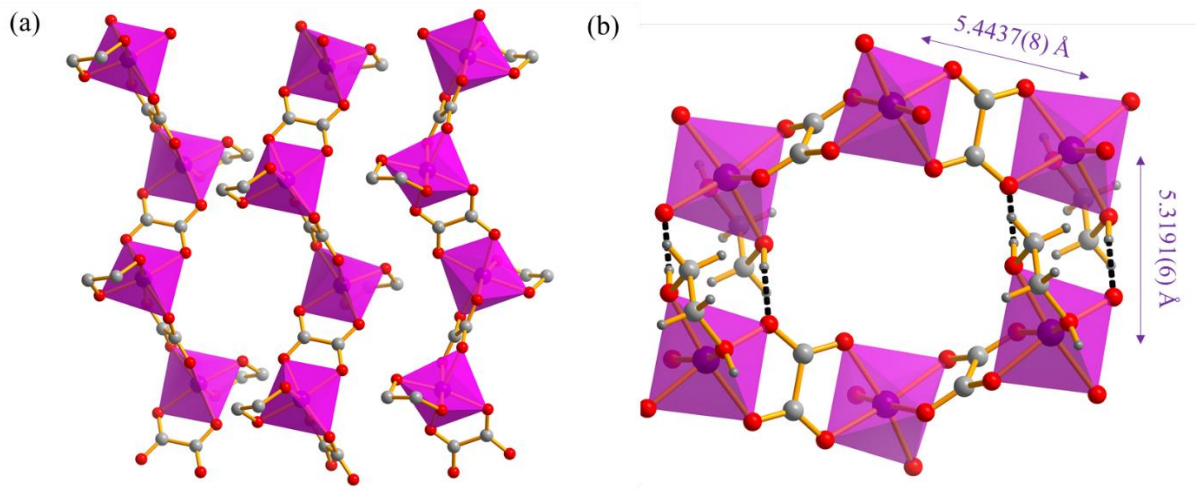

Fig. 4-25 (a) iron-oxalate chain structure of **18** (H atoms of EG not shown) and (b) illustration of H-bonding connections in **18**.

The crystal structure of the compounds is depicted in Fig. 4-25, based on the refined CIF file of **18** as an example. The Co is 6-coordinated, with oxygen atoms from two oxalate ligands and two hydroxyl groups of EG, forming a fairly regular octahedron (Fig. 4-25 (a)). The Co-O bond lengths are in the range 2.069(3)-2.107(3) Å (Table 4-14). The Co octahedra are connected by the carboxylate groups of bis-bidentate oxalate ligands through *anti-anti*-μ^2-η^1:η^1 Co-O-C-O-Co bridges, forming 1D magnetic chains with the intrachain Co-Co distance equal to 5.4437(8) Å (Fig. 4-25 (b)). The EG molecules act as bidentate terminal ligands of the

1D chains and also act as the connectors of neighbouring chains through Co1-O5-H5---O1-Co1 (5.3191(6) Å) and through Co1-O6-H6---O2-Co1 (6.0110(6) Å). If the shorter Co1---Co1 through H-bond is considered as a potential weak magnetic interaction pathway, the compound could be regarded as a *quasi*-honeycomb spin-frustrated system like **14** and **15**. However, the Co network structure here is not a flat honeycomb. It is more like a cyclohexane chair conformation structure, which theoretically would build different magnetic pathway than **14** and **15** (Fig. 4-26)**.** Further magnetic characterisation is needed to reveal the real magnetic properties of **17** and **18**.

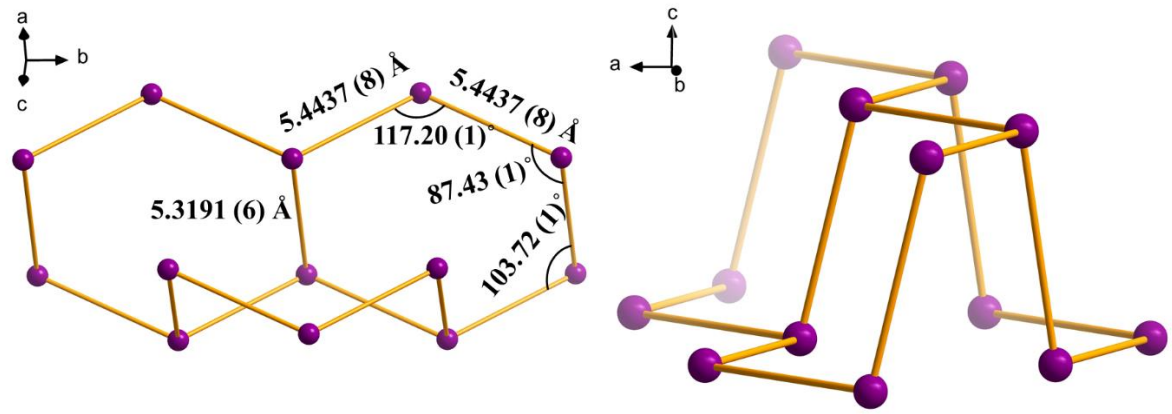

Fig. 4-26 Illustration of the honeycomb structure with Co network in top view (left) and side view (right).

4-5 Discussion and Conclusion

In this chapter, the syntheses and crystal structures of nine oxalate-based CPs were investigated, with six of them being amine-templated oxalate fluoride CPs. The magnetic properties of those compounds that could be obtained in a sufficiently pure state have also been revealed. Among those samples, we find some interesting similarities and differences, comparing with reported known compounds.

Firstly, in the synthesis process, all the compounds were prepared through solvothermal reactions at 120 ℃. After the synthesis, we found nearly all the compounds were synthesised accompanied with by-products, which evidence the diversity and complexity of the systems and the difficulties to synthesise pure products. In addition, reaction time is an important factor to the size and quality of crystals but unfortunately appears to have little influence in eliminating the by-products.

Table 4-15 The relationship between reagent and compound structure in the *pipz* systems.

Product	**M^{2+}: $C_2O_4^{2-}$: *pipz*: F^-**	**solution**	**Formula**
12	1: 1: 2: 2.8	EG	(*pipz*H_2)Fe(C_2O_4)F_2
13	1: 1.67: 1.67: 0	EG: H_2O = 1: 1	(*pipz*H_2)Fe(C_2O_4)$_2$
14	1: 1: 1.67: 7.47	EG: EtOH = 1: 1	(*pipz*H_2)Fe_2(C_2O_4)$_2F_2$(H_2O)$_2$
15	1: 1: 2: 5.6	EG: EtOH = 1: 1	(*pipz*H_2)Co_2(C_2O_4)$_2F_2$(H_2O)$_2$
16	1: 1: 4: 2.8	EG: EtOH = 1: 1	(*pipz*H)Fe(C_2O_4)F·(H_2O)

In the *pipz* series structures, the syntheses are summarised in Table 4-15. All the compounds were synthesised in EG or mixed EG with other solvents. The ratio of $M^{2+}/C_2O_4^{2-}$ in reagents is probably an important factor to influence the resulting products. Compound **13** is the only example with M^{2+}: $C_2O_4^{2-}$ = 1: 2, and also the only example containing a 2D M-oxalate layered structure. The ratio of reagents is also the only example of $M^{2+}/C_2O_4^{2-} > 1$. Thus, we could construct more interesting M-oxalate structures in versatile dimensions by adjusting the ratio of $M^{2+}/C_2O_4^{2}$ in the future.

Compound **16** is a special example, in the sense that it was synthesised under the environment where the amount of *pipz* is higher than HF. In this case, *pipz* acts as a ligand rather than just a charge-balancing template. However, the *pipz* is still half protonated even

when HF is lacking, and the iron cations remain in the +2 state in the product. Thus, we probably can introduce more coordinated *pipz* by reacting with higher *pipz*/F ratio.

The compounds containing F^- are all in the structure form of M-oxalate chain style, which is probably due to F^- normally acting as a terminal ligand in these systems. Besides, the Fe-F bond is shorter than Fe-O, which may help to build distorted octahedra and form many interesting intra- or interchain connections. All the Fe cations in these compounds are in the +2 valence state, which is probably due to the acid reaction environment.

The analysis of magnetic data shows this series of compounds typically construct 1D magnetic chains. Hence, the most suitable magnetic model in the amine oxalate fluoride CPs system is the 1D Heisenberg chain model. This also indicates that the major magnetic exchange pathway is the metal-oxalate intrachain connection and most of these examples, based on Co^{2+}/Fe^{2+}, exhibit weak antiferromagnetic interactions. The magnetic behaviours at low temperature are more complicated, where some variations in detail are probably raised by the secondary interchain correlations, especially for the compounds which contain magnetic pathways through interchain H bonds.

The work discussed in this chapter was intended to be of a very exploratory nature. With hindsight, it can be seen that these systems are rich in a variety of new compounds that in themselves are worthy of further investigation. Moreover, it is clear that further variations in reaction conditions are highly likely to expand the range of materials prepared, thus allowing more detailed understanding of the chemistry-composition-structure relationships and, ultimately, the opportunity to target more specific functional properties.

4-6 References

1. W. Yao, M. T. Sougrati, K. Hoang, J. Hui, P. Lightfoot and A. R. Armstrong, *Chem. Mater*., 2017, **29**, 2167–2172.
2. W. Yao, L. Clark, M. Xia, T. Li, S. L. Lee and P. Lightfoot, *Chem. Mater*., 2017, **29**, 6616–6620.
3. K. Tustain, L. Farrar, W. Yao, P. Lightfoot, I. Da Silva, M. T. F. Telling and L. Clark, *Inorg. Chem*., 2019, **58**, 11971–11977.
4. A. H. Abdeldaim, T. Li, L. Farrar, A. A. Tsirlin, A. S. Gibbs, P. Manuel, P. Lightfoot, G. J. Nilsen and L. Clark, *Phys. Rev. Mater*., 2020, **4**, 104414.
5. Z. A. D. Lethbridge, A. D. Hillier, R. Cywinski and P. Lightfoot, *Dalt. Trans*., 2000, **4**, 1595–1599.
6. Z. A. D. Lethbridge, S. K. Tiwary, A. Harrison and P. Lightfoot, *Dalt. Trans*., 2001, **2**, 1904–1910.
7. Z. A. D. Lethbridge, A. F. Congreve, E. Esslemont, A. M. Z. Slawin and P. Lightfoot, *J. Solid State Chem*., 2003, **172**, 212–218.
8. R. D. Shannon, *Acta Crystallogr. Sect. A: Found. Adv*., 1976, **32**, 751-767.
9. W. Hiller, J. Strähle, A. Datz, M. Hanack, W. E. Hatfield, L. W. ter Haar and P. Gütlich, *J. Am. Chem. Soc*., 1984, **106**, 329–335.
10. Y. Matsushita and Y. Ueda, *Inorg. Chem*., 2003, **42**, 7830–7838.
11. T. Echigo and M. Kimata, *Phys. Chem. Miner*., 2008, **35**, 467-475.
12. T. Echigo and M. Kimata, *Can. Mineral*., 2010, **48**, 1329–1358.
13. S. De, S. Barros and S. A. Friedberg, *Phys. Rev*., 1966, **141**, 637–640.
14. C.N.R. Rao, S. Natarajan, R. Vaidhyanathan, *Angew. Chem. Int. Ed*., 2004, **43**, 1466-1496.
15. Y. Z. Zheng, Z. Zheng and X. M. Chen, *Coord. Chem. Rev*., 2014, **258**–**259**, 1–15.

16. E. Coronado, M. C. Gimenez, C. J. Gomez-Garcia and F. M. Romero, *Polyhedron*, 2003, **22**, 3115–3122.
17. E. Coronado, J. R. Galán-Mascarós and C. Martí-Gastaldo, *J. Am. Chem. Soc*., 2008, **130**, 14987–14989.
18. B. Sieklucka, R. Podgajny, D. Pinkowicz, B. Nowicka, T. Korzeniak, M. Bałanda, T. Wasiutyński, R. Pełka, M. Makarewicz, M. Czapla, M. Rams, B. Gaweł and W. Łasocha, *CrystEngComm*., 2009, **11**, 2032–2039.
19. S. C. Abrahams and E. Prince, *J. Chem. Phys*., 1962, **36**, 50–55.

Chapter 5 Synthesis and Crystal Structure studies of Metal(III)-Fluorides

5-1 Introduction

In chapter 4, many crystallised impurities have been found during the synthesis of metal-oxalate-fluoride compounds, especially in the synthesis of Fe^{2+} compounds. The crystal structures of most impurities were found, by single crystal XRD analysis, to be Fe(III)-fluorides with protonated amines acting as templates. Furthermore, some of our other reactions in oxalate-containing systems (including Cr^{3+}) produced bulk products that were predominantly metal fluorides.

The organically-templated fluorides and oxyfluorides are well-known for their interesting crystal structures and physical properties, especially for the vanadium series compounds.[1-4] However, only a few examples of solvothermally synthesised iron(III)-fluorides with organic template have been reported so far.[5-10] Thus, this chapter describes our exploration of some of these systems and the discovery of some novel compounds. This sheds further light on the relationships between ferrous-oxalate-fluorides and iron-fluorides in solvothermal synthesis.

The M(III)-F compounds presented in this chapter are classified in three types: Cr(III) based fluorides (**19**, **20**), *en*H_2-Fe(III) fluorides (**21**, **22**), and *pipz*H_2-Fe(III) fluorides (**23-25**). The facilities and relevant software for single crystal XRD analysis are the same as used in chapters 3 and 4.

5-2 Synthesis

5-2-1 The Synthesis of $K_2CrF_5(H_2O)$ (19)

0.0275 g (0.25 mmol) chromium fluoride (CrF_3), 0.0315 g (0.25 mmol) oxalic acid dihydrate ($C_2H_2O_4 \cdot 2H_2O$), 0.0093 g (0.25 mmol) ammonium fluoride (NH_4F) and 0.0581 g (1 mmol) potassium fluoride (KF) were dissolved in 6 mL H_2O and 8 mL EtOH mixed solvent at room temperature. Then, the homogeneous mixture was sealed in a 50 mL Teflon-lined stainless-steel autoclave and placed in a 190 °C oven, maintained for 72 hours. After the autoclave was cooled to room temperature, the crystallised product was obtained by filtration with washing by deionised H_2O. The product contains green block crystals of **19** and large amount of green powder impurities. A small amount of single crystals of **19** were picked out manually. The PXRD data were collected on a STOE STADIP with Cu X-ray primary beam monochromator (CuKα1) with the ground picked single crystals sample sealed in a glass capillary (Fig. 5-1). Due to the strong background (fluorescence), the data were not processed by Rietveld refinement. The single crystal structure data were collected at 173 K and a simulated PXRD pattern was obtained from the refined result.

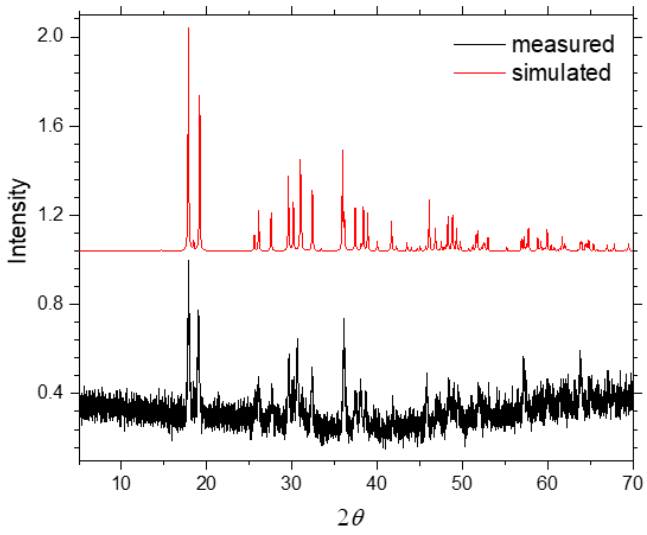

Fig. 5-1 Simulated (top) and measured (bottom) PXRD diffraction patterns of **19**.

5-2-2 The Synthesis of $K_3Cr(C_2O_4)F_4 \cdot H_2O$ (20)

Compound **20** was synthesised by the layered solution method. All the reagents are the same as those used in the synthesis of **19**, which were separated and dissolved in two solutions: 0.0275 g (0.25 mmol) chromium fluoride (CrF_3), 0.0093 g (0.25 mmol) ammonium fluoride (NH_4F), and 0.0581 g (1 mmol) potassium fluoride (KF) were dissolved in 6mL deionised H_2O. Meanwhile, 0.0315 g (0.25 mmol) oxalic acid dihydrate ($C_2H_2O_4 \cdot 2H_2O$) was dissolved in 8 mL EtOH. Then the water solution was transferred into a test tube and slowly layered with the ethanol solution. 22 days later, green prism crystals were formed at the interface between the solutions. The single crystal structure data were collected at 173 K. Because of the low yield, PXRD data were not collected for this compound.

5-2-3 The Synthesis of $(enH_2)FeF_5(H_2O)$ (21)

Compound **21** was synthesised by the combination of hydrothermal reaction and layered solution method. The hydrothermal reaction was achieved by dissolving 0.08 g (0.5 mmol) iron oxide (Fe_2O_3), 0.126 g (1 mmol) oxalic acid dihydrate ($C_2H_2O_4 \cdot 2H_2O$), 0.25 mL (7 mmol) HF (48-51 % wt. in water), and 0.135 mL (2 mmol) *en* in 20 mL H_2O at room temperature. Then, the homogeneous mixture was sealed in a 50 mL Teflon-lined stainless-steel autoclave and placed in a 100 °C oven, maintained for 120 hours. After the autoclave was cooled to room temperature, a clear light-yellow solution was obtained. 5 mL of the solution was transferred to a test tube and layered with 5 mL ethanol solution. After 16 days, colourless block single crystals of **21** were obtained at the interface between the solutions and some yellow powder impurities were obtained at the bottom. The single crystal structure data were collected at 173 K. PXRD data were also not collected for **21** due to the low yield of the sample.

5-2-4 The Synthesis of (*en*H_2)FeF_5 (22)

Compound **22** were originally discovered as impurity phases in the synthesis of **10** (see 4-2) and it has been previous synthesised in a FeF_3, *en*, HF and 1-butyl-3-methylimidazolium bromide ionothermal synthesis system.[11] The synthesis presented here is improved and oxalate ligand is involved in the reaction.

0.180 g (1 mmol) iron oxalate dihydrate ($FeC_2O_4 \cdot 2H_2O$), 0.067 mL (1 mmol) *en*, and 0.5 mL (14 mmol) HF (48-51 % wt. in water) were dissolved in 1 mL H_2O and 1 mL EG mixed solvent at room temperature. Then, the homogeneous mixture was sealed in a 30 mL Teflon-lined stainless-steel autoclave and placed in a 120 ℃ oven, maintained for 96 hours. After the autoclave was cooled to room temperature, the crystallised product was obtained by filtration with washing by EtOH. There are two kinds of single crystals in the product, colourless chip single crystals of **22** and yellow block single crystals of **10**. The single crystal structure data of **22** were collected at 173 K. PXRD data were not collected due to insufficient sample.

5-2-5 The Synthesis of (*pipz*H_2)$FeF_5 \cdot (H_2O)$ (23)

0.056 g (0.5 mmol) ferric fluoride (FeF_3), 0.172 g (2 mmol) *pipz*, and 0.8 mL (22.4 mmol) HF (48-51 % wt. in water) were dissolved in 1 mL EG at room temperature. Then, the homogeneous mixture was sealed in a 15 mL Teflon-lined stainless-steel autoclave and placed in a 120 ℃ oven, maintained for 120 hours. After the autoclave was cooled to room temperature, pure colourless rod single crystals of **23** were obtained by filtration with washing by deionised water. The PXRD data were collected on a PANalytical Empyrean with Cu X-ray primary beam monochromator (CuKα1) with the sample placed in a rotatable Teflon disc sample holder. The PXRD data were refined by Rietveld method. The single crystal structure data were collected at 173 K.

Fig. 5-2 shows the Rietveld refinement for the PXRD data of **23**. The crystallographic models were used, based on the CIF file from the single crystal refinement at 173 K, with a monoclinic space group, $P2_1/n$. The refined lattice parameters are a = 11.5017(5) Å, b = 5.8831(2) Å, c = 13.6393(9) Å and β = 91.306(3)˚ with wRp = 0.0407, Rp = 0.0282 and χ^2 = 3.657. The result shows no crystallographic phase transition between 173 K and room temperature (see 4-3-2-3, single crystal part).

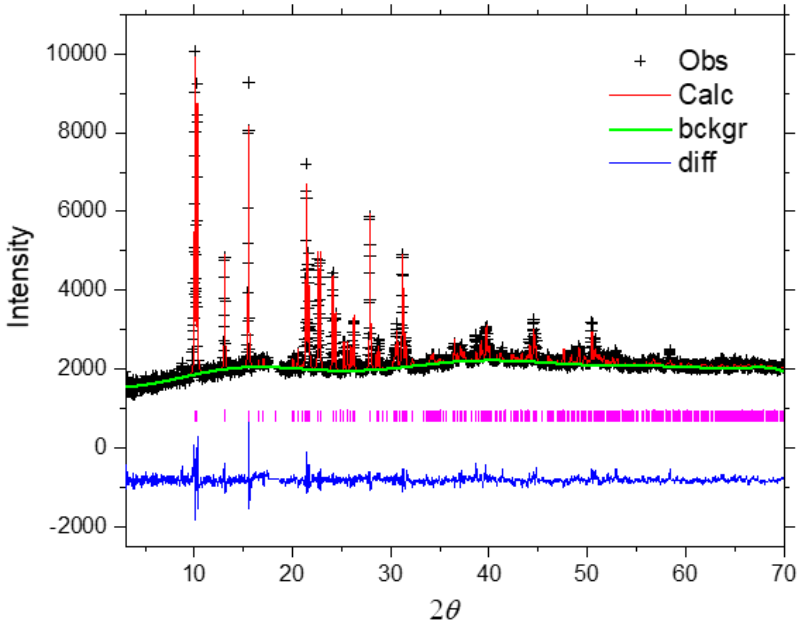

Fig. 5-2 Rietveld plot (PXRD, CuKα1) for **23**. The Teflon peak near $2\theta \sim 18°$ (see Fig. 3-3) has been excluded from the refinement.

5-2-6 The Synthesis of (*pipz*H$_2$)$_3$Fe$_4$F$_{18}$·2(H$_2$O) (24)

0.056 g (0.5 mmol) ferric fluoride (FeF_3), 0.086 g (1 mmol) *pipz*, and 0.8 mL (22.4 mmol) HF (48-51 % wt. in water) were dissolved in 15 mL EG at room temperature. Then, the homogeneous mixture was sealed in a 30 mL Teflon-lined stainless-steel autoclave and placed in a 120 ℃ oven, maintained for 120 hours. After the autoclave was cooled to room

temperature, the product was obtained by filtration with washing by EtOH. There are also three crystallised phases in the product, yellow powder (main phase), large colourless rod single crystals of compound **23** and small colourless chip single crystals of **24**. The single crystal products of **24** were picked out manually and the single crystal structure data were collected at 173 K. The PXRD data were not collected due to the low yield of the sample.

5-2-7 The Synthesis of (*pipz*H_2)$_2$$Fe_3F_{13}$·($H_2O$) (25)

0.094 g (1 mmol) iron fluoride (FeF_2), 0.086 g (1 mmol) *pipz*, and 0.252 g (2 mmol) oxalic acid dihydrate ($C_2H_2O_4$·$2H_2O$) were dissolved in 2 mL EG at room temperature. Then, the homogeneous mixture was sealed in a 50 mL Teflon-lined stainless-steel autoclave and placed in a 120 °C oven, maintained for 96 hours. After the autoclave was cooled to room temperature, the product was obtained by filtration with washing by EtOH. There are three phases in the product, yellow powder (main phase), large rod single crystals of **23** and a small amount of chip colourless single crystals of **25**. The single crystal products of **25** were picked out manually and the single crystal structure data were collected at room temperature. The PXRD data were not collected due to the low yield of the sample.

5-3 Single Crystal Data and Analysis

5-3-1 $K_2CrF_5(H_2O)$ (19)

Table 5-1 Crystallographic data and refinement details of compounds **19** and **20**.

Compound (*T*)	**19**	**20**
Formula	$K_2CrF_5(H_2O)$	$K_3Cr(C_2O_4)F_4(H_2O)$
Formula weight	243.22	351.34
Density (g cm^{-3})	2.735	2.496
Crystal system	Monoclinic	Monoclinic
Space group	*C*2/*c*	$P2_1$
a/Å	9.6750(7)	8.2481(7)
b/Å	7.7565(5)	6.4408(5)
c/Å	7.9239(5)	8.8110(7)
β/°	96.695(3)	92.7080(10)
V/$Å^3$	590.59(7)	467.56(7)
Z	4	2
Measured ref	2858	3015
Independent ref	661	1629
	[*R*(int) = 0.0195]	[*R*(int) = 0.0225]
GOOF	1.071	1.052
Final *R* indices (*I* > 2*σ*(*I*))	*R*1 = 0.0144, *wR*2 = 0.0419	*R*1 = 0.0261, *wR*2 = 0.0657

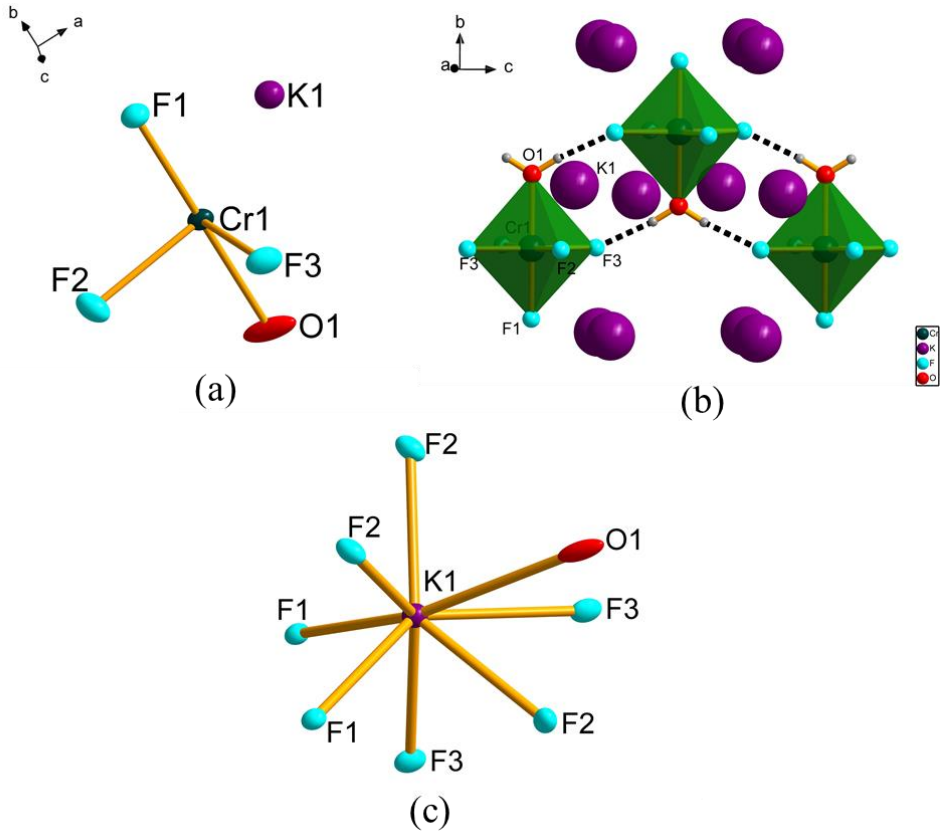

Fig. 5-3 (a) The asymmetric unit in ellipsoid plot with ellipsoids are represented at 50 % (hydrogen atoms are omitted) and (b) Polymeric structure constructed by hydrogen bonds (dotted lines) of **19**; (c) Coordination polyhedron of K1 in ellipsoid plot with ellipsoids are represented at 50 % (hydrogen atoms are omitted).

Single crystal data of **19** were measured at 173 K (Table 5-1). The refinement shows the compound crystallises in the monoclinic system with space group *C*2/*c*. The chromium atom (Cr1) is on a 2-fold axis and 6-coordinating with five fluorine atoms (F1, F2 and F3) and one oxygen atom (O1) of H_2O molecule (Fig. 5-3 (a)). The Cr-F bond lengths are in the range of 1.8957(11)-1.9083(3) Å while the Cr-O bond is 2.0010(15) Å (Table 5-2) through which a slightly distorted $CrF_5(H_2O)$ octahedron is formed. The Cr octahedral monomers are connected by the hydrogen bonds O1-(H1)---F3 with the O---F distance is 2.5382 (11) Å and form a zig-zag 1D chain (Fig. 5-3 (b)).

The potassium atoms (K1) connect the monomers into a 3D structure through coordination bonds, which are eight-coordinated (Fig. 5-3 (c)) by seven F atoms with bond lengths 2.6617(9)-2.8057(4) Å and one O atom with bond length 3.2250(4) Å (H-bonds are not included and the coordination distance limit of K is set to 3.3 Å). The chromium cation is in the 3+ state, and potassium cation is in 1+ state, which are confirmed by the BVS calculation ($\sum \mathrm{Cr1} = 3.158, \sum \mathrm{K1} = 0.994$) (Table 5-2).

Table 5-2 Selected bond lengths (Å) and bond valences for **19**.

	Bond lengths	S_{ij}		**Bond lengths**	S_{ij}
Cr1-F1	1.8957(11)	0.543	K1-F1	2.7866(4)	0.117
Cr1-F2	1.8973(9)	0.541	K1-F1	2.8057(4)	0.111
Cr1-F2	1.8973(9)	0.541	K1-F2	2.6779(9)	0.157
Cr1-F3	1.9083(8)	0.526	K1-F2	2.6839(10)	0.154
Cr1-F3	1.9083(8)	0.526	K1-F2	2.7877(9)	0.116
Cr1-O1	2.0010(15)	0.481	K1-F3	2.6617(9)	0.164
	$\sum \mathrm{Fe1} = 3.158$		K1-F3	2.7670(9)	0.123
			K1-O1	3.2250(4)	0.052
				$\sum \mathrm{K1} = 0.994$	

5-3-2 $K_3Cr(C_2O_4)F_4 \cdot H_2O$ (20)

The refinement of the single crystal data shows compound **20** crystallises in the monoclinic system with space group *C*2/*c* (Table 5-1). The chromium atom (Cr1) is 6-coordinating with four fluorine atoms (F1, F2, F3 and F4) and two oxygen atoms (O1 and O4) from the bidentate oxalate ligand (Fig. 5-4 (a)). The Cr-F bond lengths are in the range of 1.892(3)-1.916(3) Å while the two Cr-O bonds are 1.974(4) and 1.998(3) Å (Table 5-3), through which a distorted octahedral monomer is formed. The channel water molecule interacts with the octahedron through O5-H---F2 hydrogen bond with the O---F distance 2.744 (6) Å

(Fig. 5-4 (b)). Due to the enlarged thermal motion of the channel water molecule, positions of the two H atoms cannot be determined from Q peaks or riding model during the refinement.

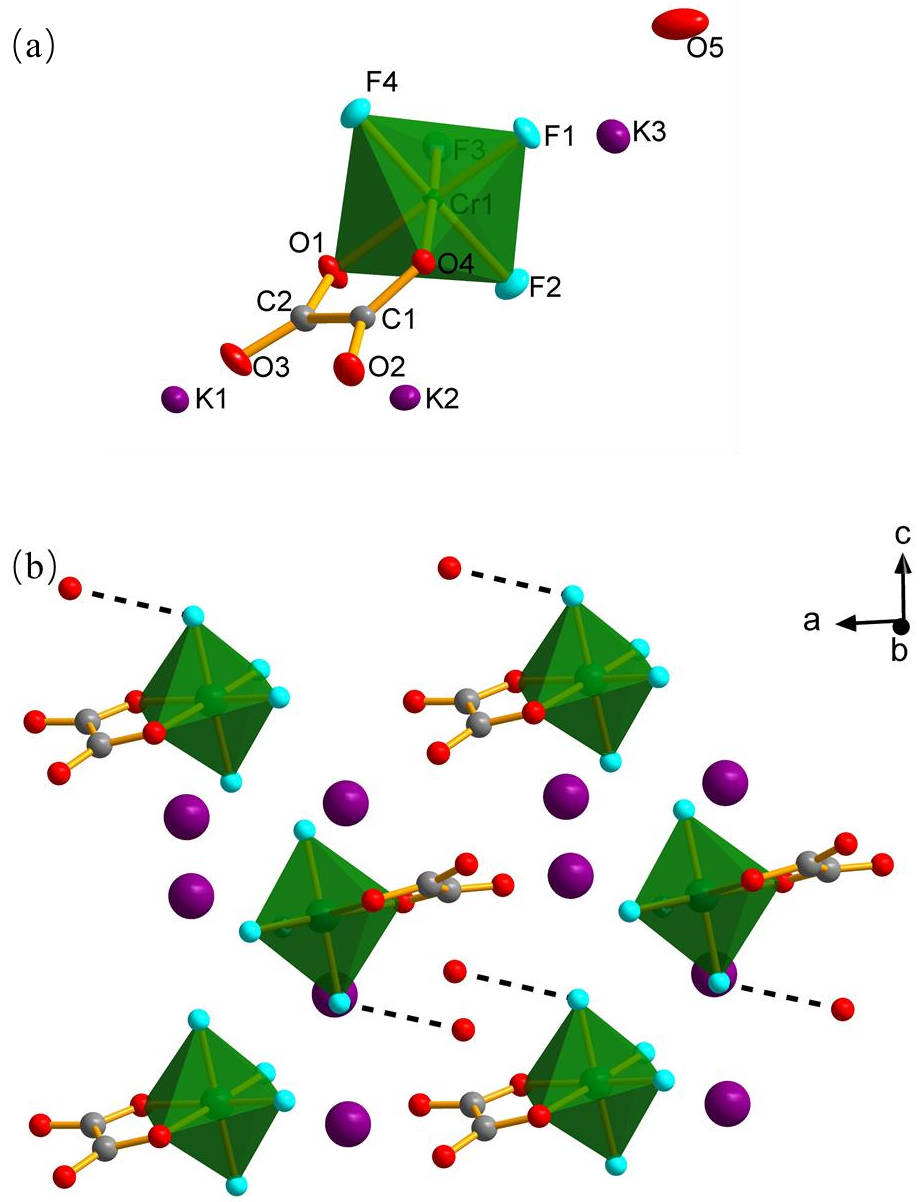

Fig. 5-4 (a) The asymmetric unit without hydrogen atoms in ellipsoid plot with ellipsoids are represented at 50 % and (b) polymeric structure with hydrogen bonds (dotted lines) of **20**.

The potassium atoms (K1, K2 and K3) connect the octahedral monomer into a 3D structure through coordination bonds and H bonds. K1 is eight-coordinated by four F atoms with bond lengths 2.640(3)-3.124(2) Å and four O atoms with bond lengths 2.753(4)-3.124(3)

Å; K2 is seven-coordinated by four F atoms with bond lengths 2.619(3)-2.691(2) Å and three O atoms with bond lengths 2.625(4)-3.269(5) Å, and K3 is nine-coordinated by six F atoms with bond lengths 2.732(4)-3.141(4) Å and three O atoms with bond length 2.726(5)-3.276(4) Å (Fig. 5-5). Similar with **19**, H-bonds are not included and the coordination distance limit of K is set to 3.3 Å. BVS calculation shows the chromium cation is in 3+ state, and all three potassium cations are in 1+ state ($\sum \mathrm{Cr1} = 3.141,\ \sum \mathrm{K1} = 1.124,\ \sum \mathrm{K2} = 1.180$ and $\sum \mathrm{K3} = 1.197$) (Table 5-3).

Table 5-3 Selected bond lengths (Å) and bond valences for **20**.

	Bond lengths	S_{ij}		**Bond lengths**	S_{ij}
Cr1-F1	1.899(3)	0.539	K2-F1	2.619(3)	0.184
Cr1-F2	1.916(3)	0.514	K2-F2	2.691(3)	0.151
Cr1-F3	1.900(3)	0.537	K2-F3	2.660(3)	0.164
Cr1-F4	1.892(3)	0.549	K2-F4	2.625(3)	0.181
Cr1-O1	1.974(4)	0.517	K2-O2	2.747(4)	0.190
Cr1-O4	1.998(3)	0.485	K2-O3	2.625(4)	0.264
	$\sum \mathrm{Fe1} = 3.141$		K2-O5	3.269(5)	0.046
				$\sum \mathrm{K2} = 1.180$	
K1-F1	3.124(3)	0.047	K3-F1	2.732(3)	0.135
K1-F3	2.877(3)	0.091	K3-F1	2.828(3)	0.104
K1-F4	2.640(3)	0.174	K3-F2	2.732(4)	0.135
K1-F4	2.660(3)	0.164	K3-F2	3.013(3)	0.063
K1-O1	2.753(4)	0.187	K3-F3	2.741(3)	0.132
K1-O2	2.772(4)	0.177	K3-F3	3.141(4)	0.045
K1-O3	2.863(4)	0.139	K3-O1	3.276(4)	0.045
K1-O4	2.933(4)	0.115	K3-O2	3.110(5)	0.071
	$\sum \mathrm{K1} = 1.094$		K3-O5	2.726(5)	0.201
				$\sum \mathrm{K3} = 0.931$	

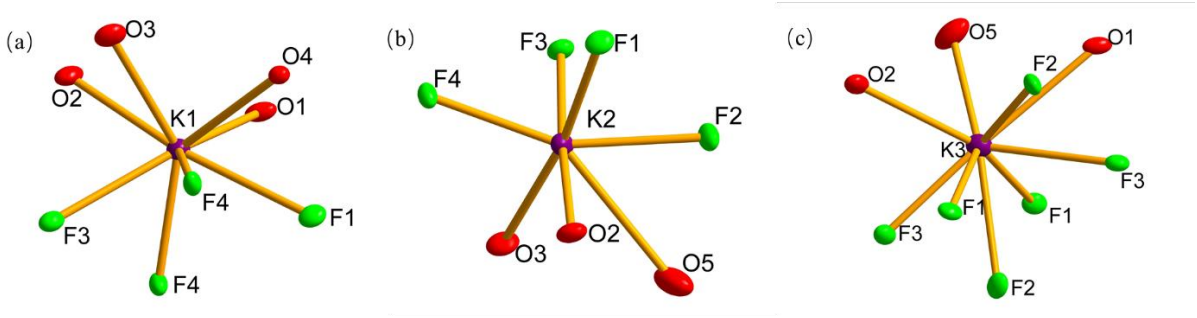

Fig. 5-5 The coordination polyhedra in ellipsoid plot with ellipsoids are represented at 50 % of (a) K1, (b) K2 and (c) K3 in **20**.

5-3-3 (*en*H$_2$)FeF$_5$(H$_2$O) (21)

Table 5-4 Crystallographic data and refinement details of compounds **21** and **22**.

Compound (*T*)	**21**	**22**
Formula	$(C_2H_{10}N_2)FeF_5(H_2O)$	$(C_2H_{10}N_2)FeF_5$
Formula weight	230.99	212.97
Density (g cm^{-3})	1.948	2.158
Crystal system	Monoclinic	Tetragonal
Space group	$P2_1$	$P4/ncc$
a/Å	6.2477(5)	12.8670(10)
b/Å	7.4793(8)	12.8670(10)
c/Å	8.7812(9)	7.9173(5)
β/°	106.358(3)	90
V/Å^3	393.72(7)	1310.8(2)
Z	2	8
Measured ref	3358	9804
Independent ref	1385	581
	[R(int) = 0.0257]	[R(int) = 0.0584]
GOOF	1.007	1.072
Final R indices (I > 2σ(I))	R1 = 0.0209, wR2 = 0.0547	R1 = 0.0309, wR2 = 0.0747

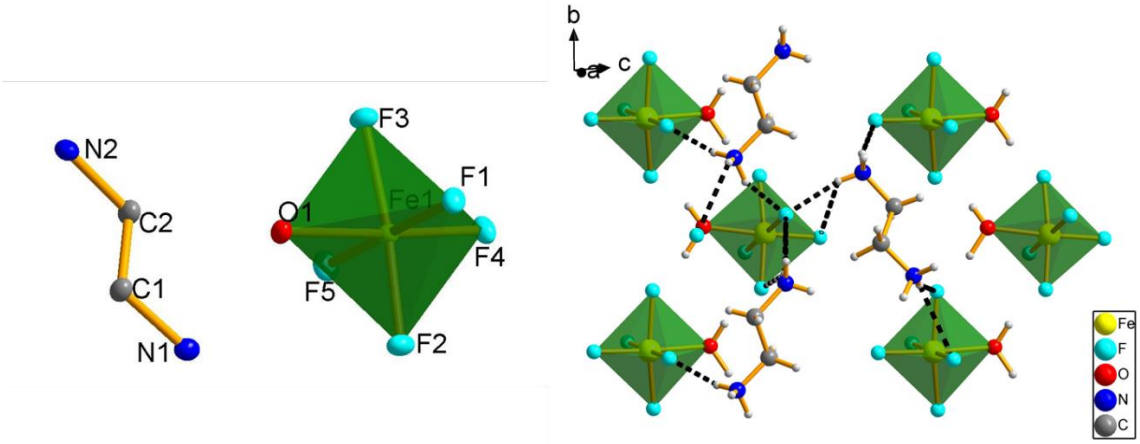

Fig. 5-6 Asymmetric unit without hydrogen atoms in ellipsoid plot with ellipsoids are represented at 50 % (left) and polyhedral view (right) of **21** (hydrogen bonds are shown in dotted lines).

The compound **21** crystallises in the monoclinic system with a polar space group $P2_1$ (Table 5-4). The iron atom (Fe1) is 6-coordinating with five fluorine atoms (F1, F2, F3 F4 and F5) and one oxygen atom (O1) of the H_2O molecule (Fig. 5-6 (left)). The Fe-F bond lengths are in the range of 1.889(2)-1.933(2) Å while the Fe-O bond is 2.083(2) Å, through which a distorted octahedral monomer is formed. The BVS calculation supports iron cation being in the 3+ state ($\sum$Fe1 = 2.844) (Table 5-5).

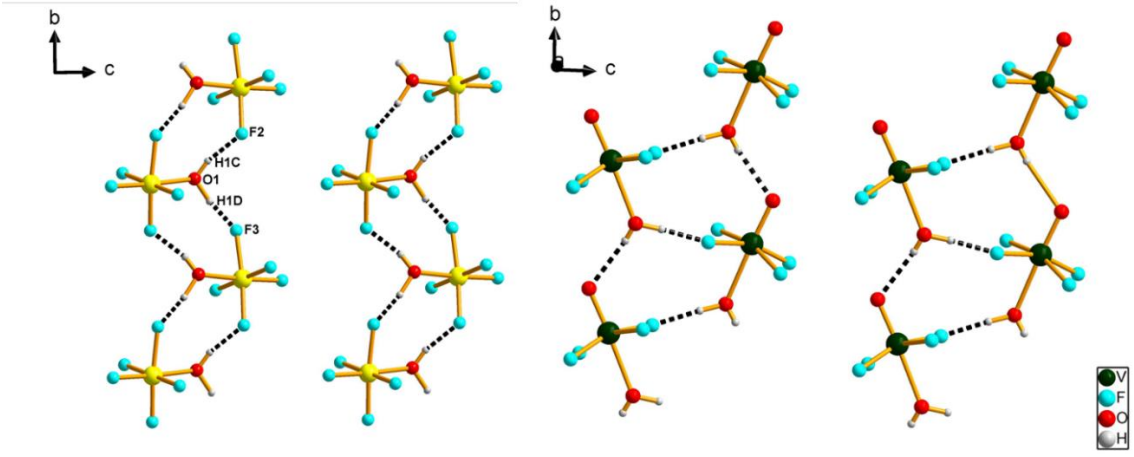

Fig. 5-7 Illustration of hydrogen bonding chains (dotted lines) of **21** (left) and $(enH_2)[VOF_4(H_2O)]$[3].

The neighbouring octahedra are connected through O1-(H1C)---F2 and O1-(H1D) ---F3 hydrogen bonds with O---F distances 2.612(4) Å and 2.621(4) Å (Fig. 5-7 (left)). A similar compound with the same space group (*en*H_2)[$VOF_4(H_2O)$] has been investigated in our group (Fig. 5-7 (right)).[3] The short V=O bond in that compound makes a stronger distortion of the octahedron, which builds a different H bonding connection between the octahedra through O-H---F and O-H---O=V. Another similar structure (*en*H_2)[$AlF_5(H_2O)$][12] has the same hydrogen bond connection mode as **21** because of the similar octahedral distortion for both samples.

The octahedral chains are further connected by the *en*H_2^{2+} cations though the N-H---F2 hydrogen bonds and form the 3D structure.

Table 5-5 Selected bond lengths (Å) and bond valences for **21**.

	Bond lengths	S_{ij}
Fe1-F1	1.933(2)	0.465
Fe1-F2	1.914(2)	0.490
Fe1-F3	1.937(2)	0.460
Fe1-F4	1.889(2)	0.524
Fe1-F5	1.895(2)	0.516
Fe1-O1	2.083(2)	0.389
		$\sum \mathrm{Fe1} = 2.844$

5-3-4 (*en*H_2)FeF_5 (22)

The compound **22** crystallises in the tetragonal system with a space group *P*4/*ncc* (Table 5-4). In **22**, there are two iron atoms (Fe1 and Fe2) which are both 6-coordinating with fluorine atoms (Fig. 5-8 (a)). Fe1 is coordinated by four coplanar terminal F atoms (F1) with equal distance (1.9138(17) Å) and two *trans*, bridging F atoms (F2) with the bond lengths 1.957(3) and 2.001(3) Å, forming a distorted octahedron (Table 5-6). The [FeF_4F_2] octahedra are connected by F2 and form staggered 1D chains in corner sharing style. Fe2 is coordinated by four coplanar terminal F atoms (F3) with equal distance (1.9070(17) Å) and two *trans*, bridging

F atoms (F4) with equal bond lengths 1.97933(13) Å, forming a fairly regular octahedron. The [FeF_4F_2] octahedra interact in corner sharing style through F4 and form eclipsed 1D chains (Fig. 5-8 (b) and (c)). Three structures with similar octahedron arrangement, (*en*H_2)ScF_5[13], (*en*H_2)VF_5[14] and (*en*H_2)$TiOF_4$[15] have been reported. The *en*H_2^{2+} cation in **22** acts as a compensating group to balance the charge. It also connects with the octahedra by N1-(H1C)---F3, N1-(H1D)---F1, and N1-(H1E)---F1 hydrogen bonds with N---F distances 2.6517(29) Å, 2.7381(30) Å and 2.7850(29) Å and binds the 1D chains into a 3D structure (Fig. 5-8 (b) and (c)). The valence states for both Fe are confirmed to be 3+ by BVS calculation ($\sum Fe1 = 2.783$ and ($\sum Fe2 = 2.818$) (Table 5-6).

Table 5-6 Selected bond lengths (Å) and bond valences for **22**

	Bond lengths	S_{ij}		**Bond lengths**	S_{ij}
Fe1-F1	1.9138(17)	0.490	Fe2-F3	1.9070(17)	0.499
Fe1-F1	1.9138(17)	0.490	Fe2-F3	1.9070(17)	0.499
Fe1-F1	1.9138(17)	0.490	Fe2-F3	1.9070(17)	0.499
Fe1-F1	1.9138(17)	0.490	Fe2-F3	1.9070(17)	0.499
Fe1-F2	1.957(3)	0.436	Fe2-F4	1.97933(13)	0.411
Fe1-F2	2.001(3)	0.387	Fe2-F4	1.97933(13)	0.411
	$\sum Fe1 = 2.783$			$\sum Fe2 = 2.818$	

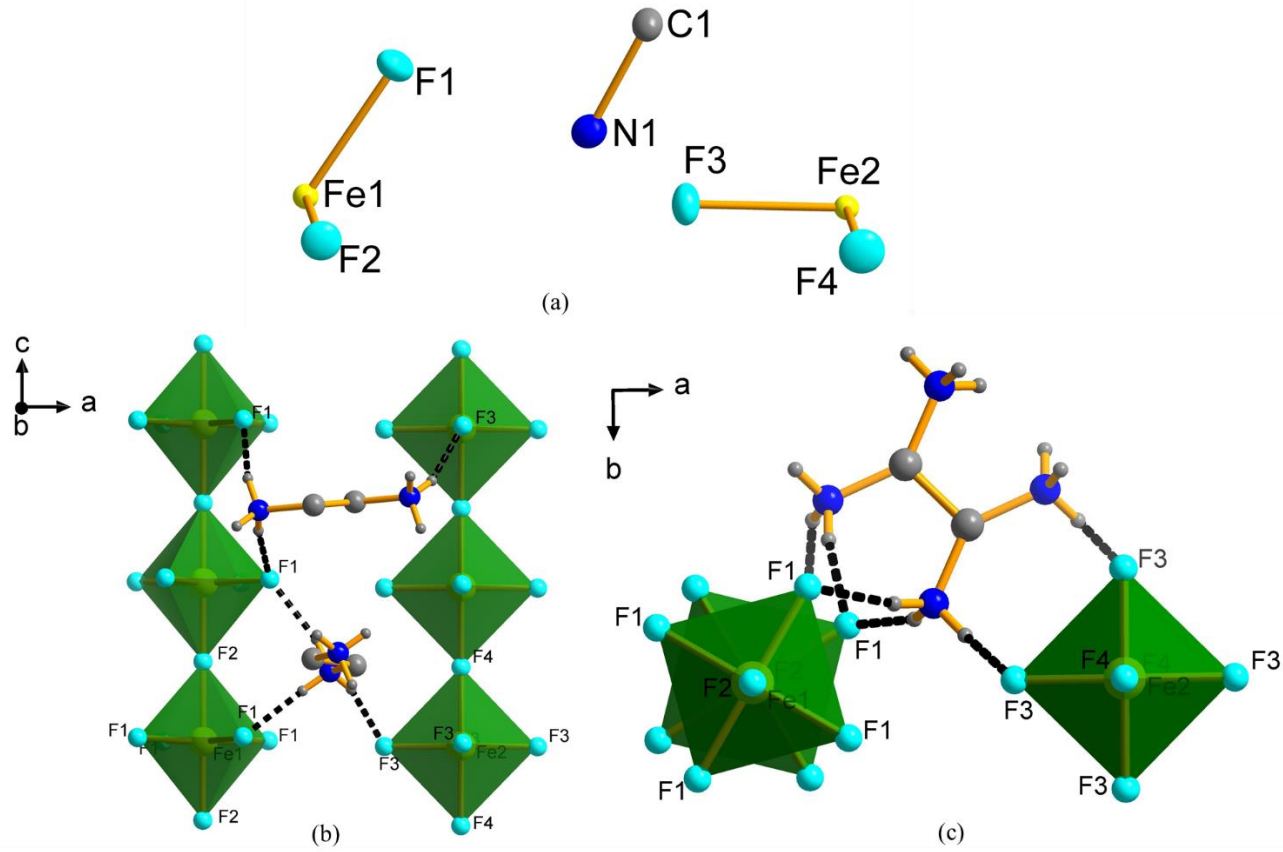

Fig. 5-8 Asymmetric unit without hydrogen atoms in ellipsoid plot with ellipsoids are represented at 50 % (a) and polyhedral structure viewed along the *b*-axis (b) and *c*-axis (c) of **22**. (Carbon-bound hydrogens have been omitted and selected hydrogen bonds are depicted by dotted lines).

Table 5-7 Crystallographic data and refinement details of compounds **23**-**25**.

Compound (*T*)	**23**	**24**	**25**
Formula	$(C_4H_{12}N_2)FeF_5\cdot(H_2O)$	$(C_4H_{12}N_2)_3Fe_4F_{18}\cdot 2(H_2O)$	$(C_4H_{12}N_2)_2Fe_3F_{13}\cdot(H_2O)$
Formula weight	257.02	865.90	608.88
Density (g cm^{-3})	1.862	2.046	2.145
Crystal system	Monoclinic	Monoclinic	Monoclinic
Space group	$P2_1/n$	$P2/c$	$C2/c$
a/Å	11.4695(8)	16.9178(13)	20.5365(14)
b/Å	5.8774(4)	13.6023(10)	13.5405(9)
c/Å	13.6090(10)	12.8848(10)	13.5727(9)
β/°	91.553(6)	108.530(3)	92.588(4)
V/Å^3	917.06(11)	2811.4(4)	3770.4(4)
Z	4	4	8
Measured ref	7243	23474	15772
Independent ref	1588	4952	3321
	[*R*(int) = 0.0403]	[*R*(int) = 0.0627]	[*R*(int) = 0.1532]
GOOF	1.045	1.006	1.014
Final *R* indices ($I > 2\sigma(I)$)	*R*1 = 0.0250, *wR*2 = 0.0756	*R*1 = 0.0331, *wR*2 = 0.0843	*R*1 = 0.0608, *wR*2 = 0.1364

5-3-5 (*pipz*H$_2$)FeF$_5$·(H$_2$O) (23)

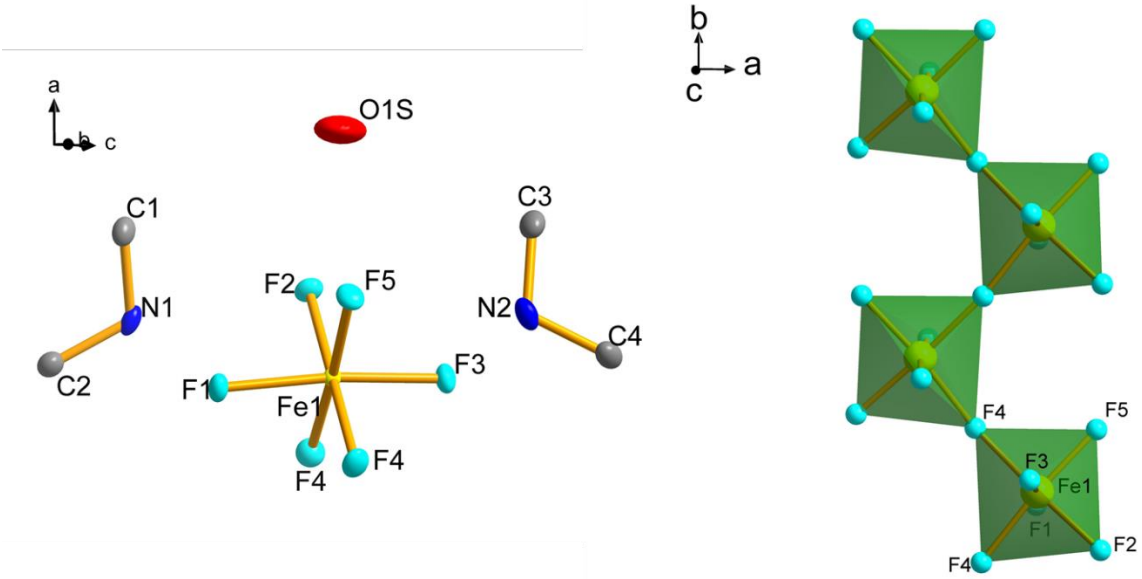

Fig. 5-9 The building unit in ellipsoid plot with ellipsoids are represented at 50 % (left) and zigzag octahedral chain along the *b*-axis (right) of **23**. (Hydrogen atoms are eliminated for clarity.)

Table 5-8 Selected bond lengths (Å) and bond valences for **23**.

	Bond lengths	S_{ij}
Fe1-F1	1.9098(11)	0.495
Fe1-F2	1.9182(11)	0.485
Fe1-F3	1.9020(11)	0.506
Fe1-F4	1.9833(11)	0.407
Fe1-F4	1.9967(11)	0.391
Fe1-F5	1.9052(11)	0.502
		$\sum \mathrm{Fe1} = 2.786$

Single crystal data of **23** were collected at 173 K. The structural refinement shows the compound crystallises in the monoclinic system with space group $P2_1/n$ (Table 5-7). A similar compound (*pipz*H$_2$)VF$_5$·(H$_2$O)[14] has been investigated previously by our group. The building unit of **23** shows Fe1 is 6-coordinated by four coplanar F atoms (F4 for bridging, F2 and F5 for

terminal) with distances 1.9052(11)-1.9967(11) Å and two *trans*, terminal F atoms (F1 and F3) with the bond lengths 1.9098(11) and 1.9020(11) Å respectively, forming an octahedron (Fig. 5-9 (left) and Table 5-8). The [FeF_4F_2] octahedra interact in corner sharing style through F4 and form zigzag 1D chains with the intrachain Fe-Fe distance 3.9292 (3) Å (Fig. 5-9 (right)).

The protonated *pipz*H_2 cation acts as a compensating group to balance the charge. In addition, it also connects with the 1D chains by N-H---F hydrogen bonds and binds the 1D chains into a 3D structure (Fig. 5-10). The channel water molecule interacts with the chain structure through the O-H---F hydrogen bond with an O---F distance of 2.761(3) Å. Due to the enlarged thermal motion of the channel water molecule, positions of the two H atoms cannot be determined from Q peaks or riding model during the refinement. The iron cation in **23** is also in 3+ state, which is confirmed by the BVS calculation ($\sum Fe1 = 2.786$).

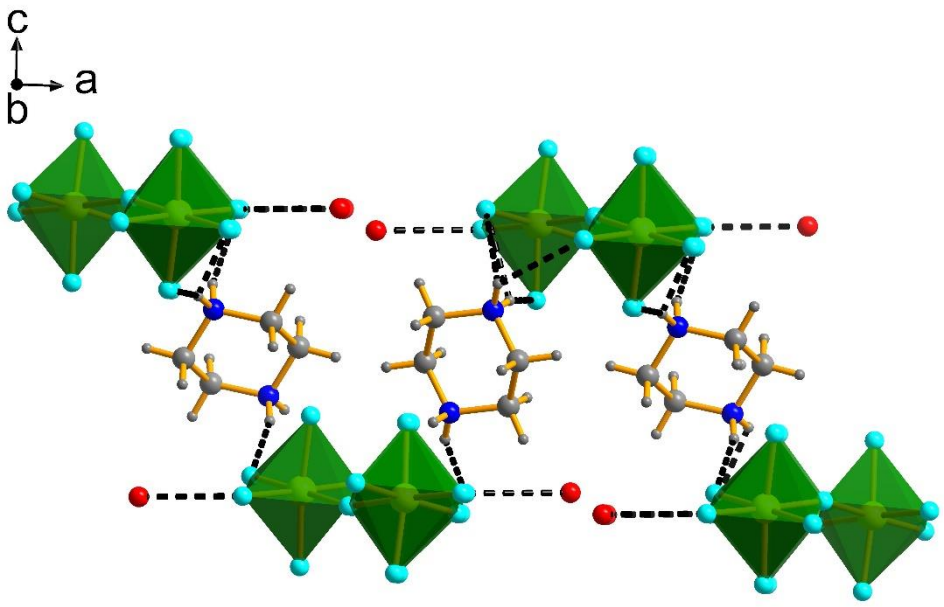

Fig. 5-10 polyhedral structure of **23** viewed along the *b*-axis. (Hydrogen bonds are depicted by dotted lines)

5-3-6 (*pipz*H$_2$)$_3$Fe$_4$F$_{18}$·2(H$_2$O) (24)

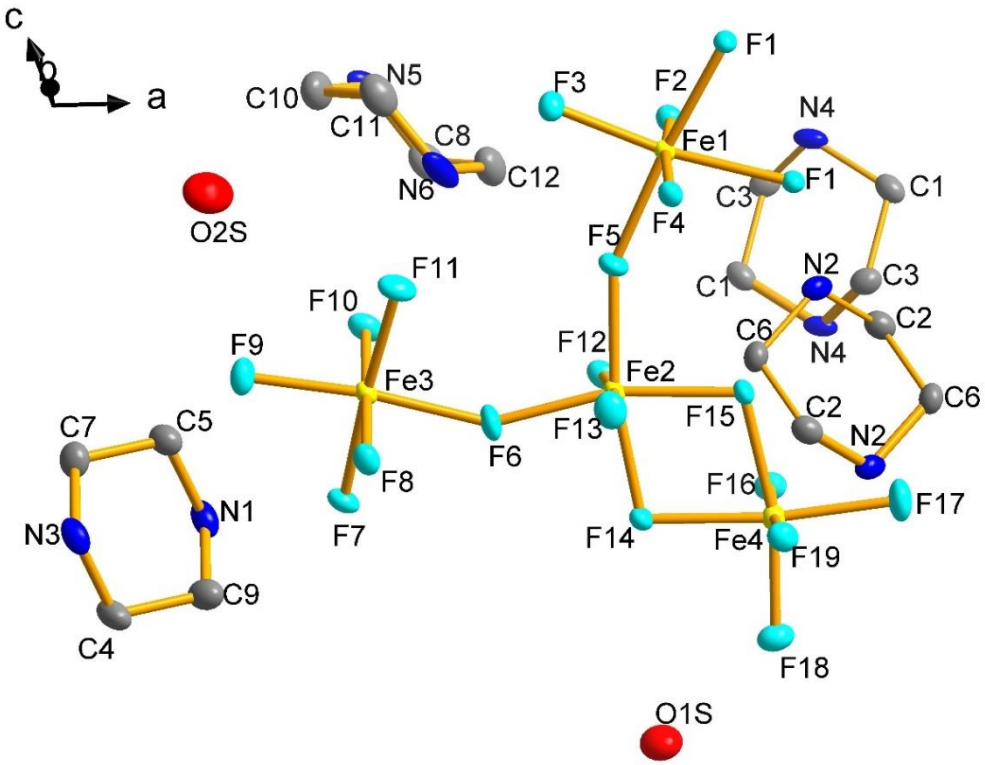

Fig. 5-11 The building unit of **24** in ellipsoid plot with ellipsoids are represented at 50 %. (Hydrogen atoms are eliminated for clarity)

The refinement of single crystal data of **24** at 173 K shows the compound crystallised the monoclinic system with space group $P2_1/c$ (Table 5-7). A similar compound with mixed valence state vanadium atoms (*pipz*H$_2$)$_3$V$^{III}_3$V^{IV}F$_{17}$O·1.5(H$_2$O)[15] has been reported. The building unit of **24** is depicted in Fig. 5-11, which shows there are in total four Fe cations which are all 6-coordinated by fluorine atoms and form octahedra. Fe1 is surrounded by four coplanar bridging F atoms (F1, F3 and F5) with distances 1.9052(11)-2.018(2) Å and two *trans*, terminal F atoms (F2 and F4) with the bond lengths 1.872(2) and 1.910(2) Å, respectively; Fe2 is coordinated by four coplanar bridging F atoms (F5, F6, F14 and F15) with distances 1.945(2)-2.016(2) Å and two *trans*, terminal F atoms (F12 and F13) with the bond lengths 1.884(2) and 1.846(2) Å, respectively; the Fe3 octahedron is formed by four coplanar bridging F atoms (F6,

F8, F9 and F10) with distances 1.911(2)-1.971(2) Å and two *trans*, terminal F atoms (F7 and F11) with the bond lengths 1.9839(8) and 1.909(2) Å, respectively; while Fe4 is surrounded by four coplanar bridging F atoms (F14, F15, F17 and F18) with distances 1.874(2)-2.024(2) Å and two *trans*, terminal F atoms (F16 and F19) with the bond lengths 1.879(2) and 1.898(2) Å, respectively.

In one building unit, the Fe2 octahedron connects with Fe1 and Fe3 octahedra through corner sharing F atoms and connects with F4 octahedra in edge sharing style to form a "Y" shaped tetrameric secondary building unit (SBU). The "Y" shaped tetrameric groups are connected through further alternate corner- and edge-sharing pathways to form a 2D flat layer with [Fe_{18}] rings (Fig. 5-12(a)). The 2D layers are stacked in staggered style along the *b*-axis (Fig. 5-12(b)).

Table 5-9 Selected bond lengths (Å) and bond valences for **24**.

	Bond lengths	S_{ij}		**Bond lengths**	S_{ij}
Fe1-F1	1.999(2)	0.389	Fe2-F5	1.945(2)	0.451
Fe1-F1	2.018(2)	0.370	Fe2-F6	1.947(2)	0.448
Fe1-F2	1.872(2)	0.549	Fe2-F12	1.884(2)	0.531
Fe1-F3	1.876(2)	0.543	Fe2-F13	1.846(2)	0.589
Fe1-F4	1.910(2)	0.497	Fe2-F14	2.016(2)	0.372
Fe1-F5	1.972(2)	0.419	Fe2-F15	1.970(2)	0.421
	$\sum Fe1 = 2.767$			$\sum Fe2 = 2.812$	
Fe3-F6	1.971(2)	0.420	Fe4-F14	2.024(2)	0.364
Fe3-F7	1.9839(8)	0.405	Fe4-F15	2.007(2)	0.381
Fe3-F8	1.914(2)	0.491	Fe4-F16	1.879(2)	0.539
Fe3-F9	1.911(2)	0.494	Fe4-F17	1.9466(5)	0.448
Fe3-F10	1.911(2)	0.494	Fe4-F18	1.874(2)	0.546
Fe3-F11	1.909(2)	0.497	Fe4-F19	1.898(2)	0.512
	$\sum Fe3 = 2.801$			$\sum Fe4 = 2.790$	

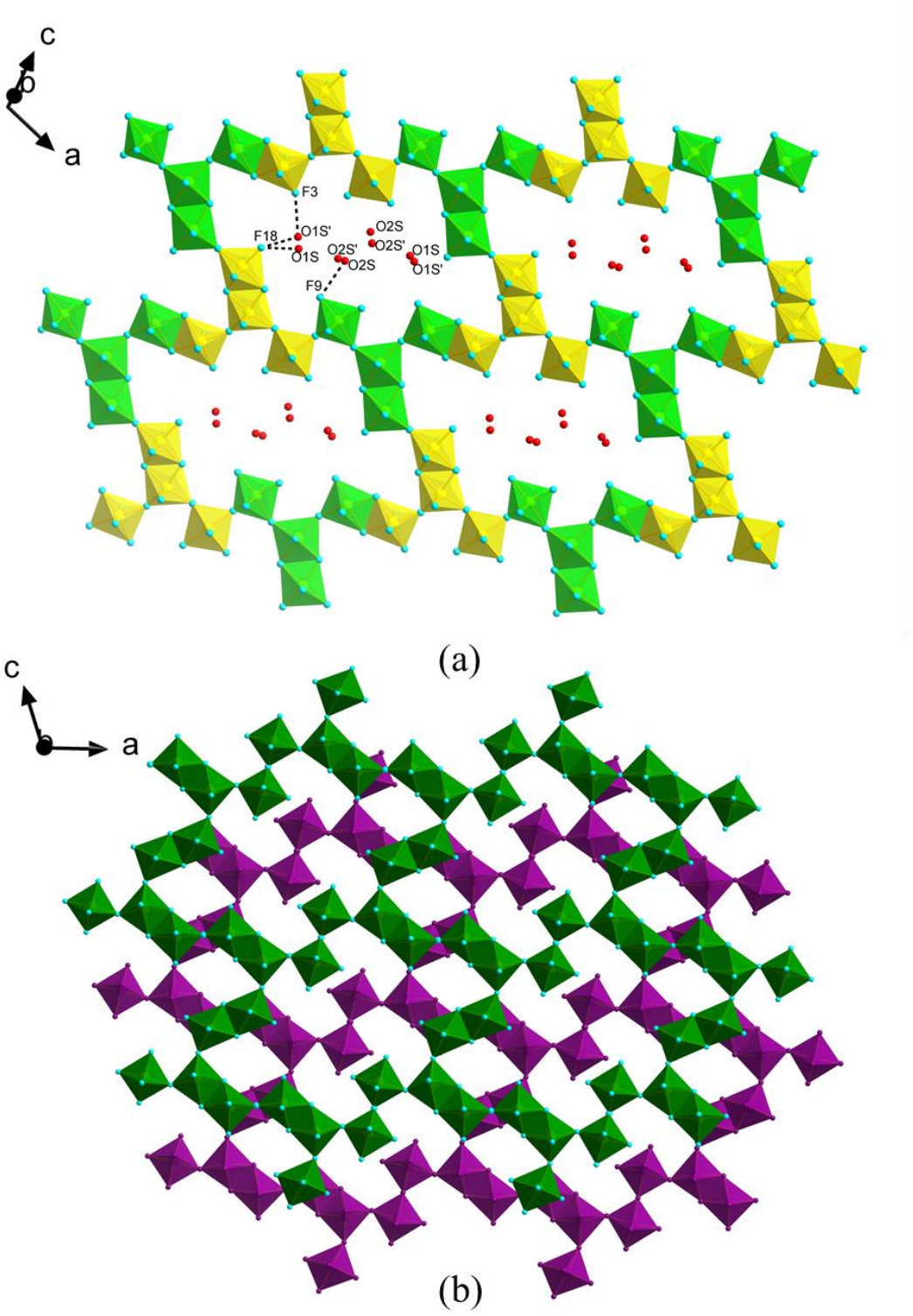

Fig. 5-12 (a) The 2D layers with channel water molecules of **24**. The octahedra with different colours show how the "Y" shaped Fe-F building units are connected. (Selected hydrogen bonds were depicted by dotted lines); (b) Plan view of the layer stacking, with different layers shown in different colours. (*pipz*H_2 and water molecules are eliminated for clarity)

The channel H_2O molecules are located in the cavity of the [Fe_{18}] rings and connect the layer structure through O1s-H---F18, O1s'-H---F18, O1s'-H---F3 and O2s-H---F19 with the O---F distances 2.418(7), 2.485(10), 2.856(13) and 2.846(7) Å, respectively. Due to the high disorder of the channel water molecules, positions of the two H atoms cannot be determined from Q peaks or riding model during the refinement. More accurate channel water number will be determined through TGA in the future. The *pipz*H_2^{2+} cations locate in the interlayer positions and link the neighbouring [Fe_{18}] rings through hydrogen bonds thus forming the 3D structure (Fig. 5-13). All the four iron cations in **24** are in the 3+ state, which is confirmed by the BVS calculation ($\sum$Fe1 = 2.767, $\sum$Fe2 = 2.812, $\sum$Fe3 = 2.801 and $\sum$Fe4 = 2.790).

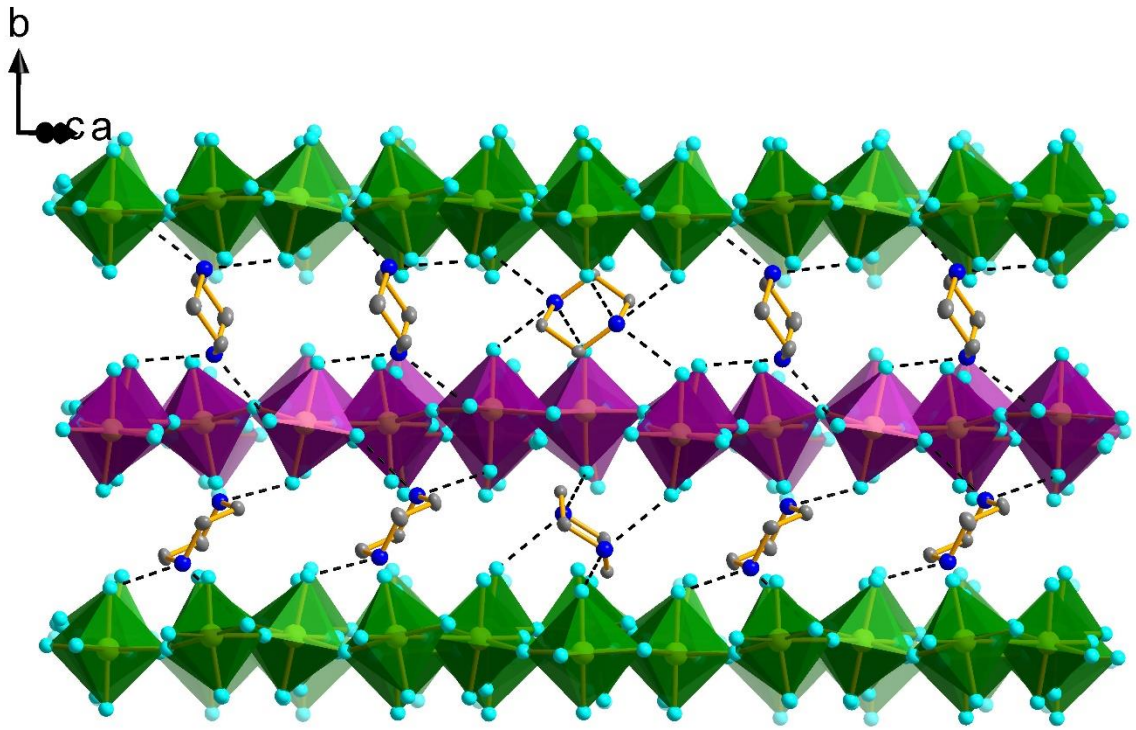

Fig. 5-13 The stacking of the layers with *pipz*H_2 along the *b*-axis of **24**. (Selected hydrogen atoms are eliminated for clarity but hydrogen bonds were depicted by dotted lines.)

5-3-7 (*pipz*H$_2$)$_2$Fe$_3$F$_{13}$·(H$_2$O) (25)

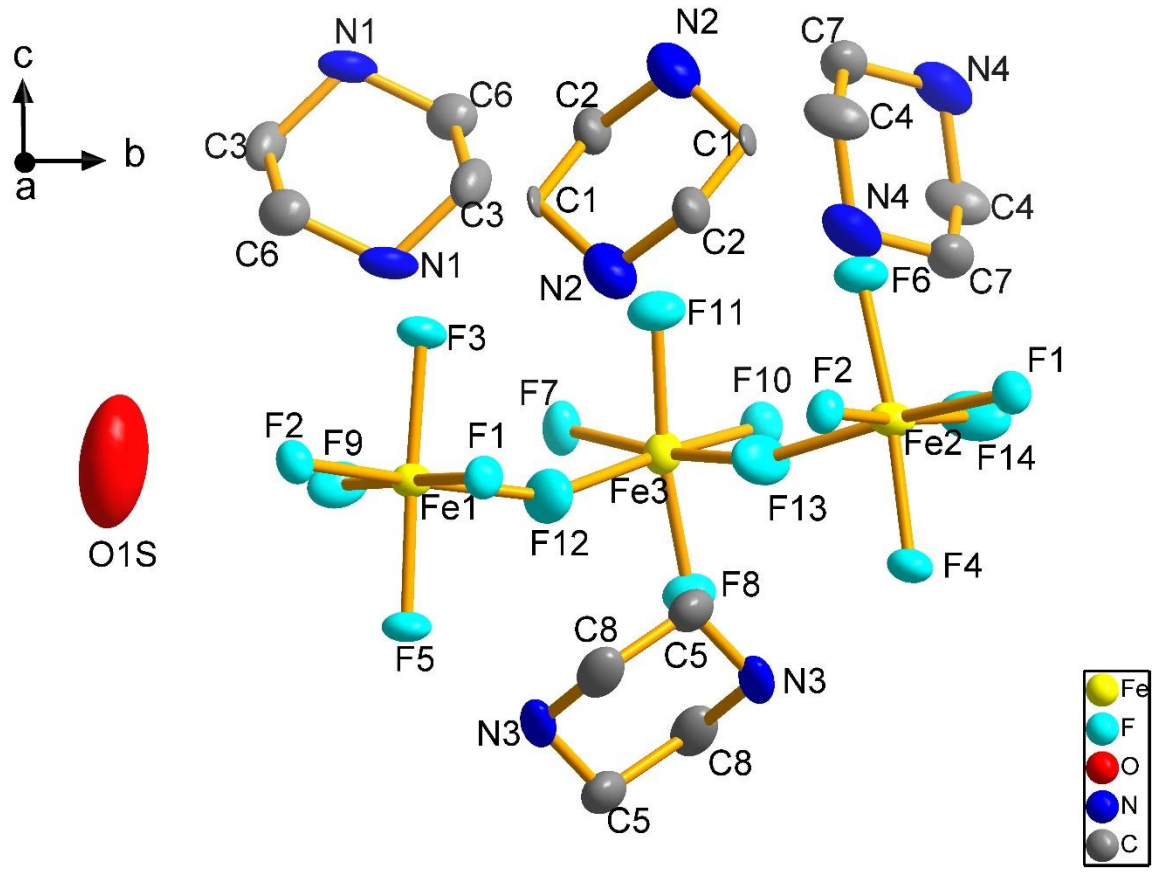

Fig. 5-14 The building unit of **25** in ellipsoid plot with ellipsoids are represented at 50 %. (Hydrogen atoms are eliminated for clarity)

The compound **25** was crystallised in the monoclinic system with space group *C*2/*c* based on the result of the single crystal data refinement (Table 5-7). Fig. 5-14 shows the building unit of **25**, in which three Fe cations are all 6-coordinated by fluorine atoms and form octahedra. Each Fe cation is surrounded by four coplanar bridging F atoms with distances 1.859(6)-2.027(5) Å and two *trans*, terminal F atoms with the bond lengths 1.849(5)-1.905(5) Å, respectively.

In one building unit, the Fe3 octahedron connects with Fe1 and Fe2 octahedra through corner sharing F atoms (F12 and F13, respectively) forming a “V” shaped trimeric octahedral building unit. The “V” building units are connected through the edge-sharing pathways and

form a 2D flat layer with [Fe_{14}] rings (Fig. 5-15(a)). The 2D layers are stacked in staggered style along the *c*-axis (Fig. 5-15(b)). The channel H_2O molecules are in the cavity of the [Fe_{14}] rings and interact with single layers through hydrogen bonds, with O1s-H---F9 and O1s-H---F14 with distances of 2.895(17) and 2.770(17) Å.

Table 5-10 Selected bond lengths (Å) and bond valences for **25**.

	Bond lengths	S_{ij}		**Bond lengths**	S_{ij}
Fe1-F1	2.008(5)	0.380	Fe2-F1	1.984(5)	0.405
Fe1-F2	1.968(5)	0.423	Fe2-F2	2.027(5)	0.361
Fe1-F3	1.905(5)	0.502	Fe2-F4	1.900(5)	0.509
Fe1-F5	1.883(5)	0.534	Fe2-F6	1.905(5)	0.502
Fe1-F9	1.875(5)	0.544	Fe2-F13	1.939(6)	0.458
Fe1-F12	1.932(6)	0.465	Fe2-F14	1.859(6)	0.568
	$\sum Fe1 = 2.848$			$\sum Fe2 = 2.803$	
Fe3-F7	1.992(5)	0.396			
Fe3-F8	1.875(5)	0.546			
Fe3-F10	2.020(5)	0.367			
Fe3-F11	1.849(5)	0.584			
Fe3-F12	1.924(6)	0.477			
Fe3-F13	1.932(6)	0.465			
	$\sum Fe3 = 2.835$				

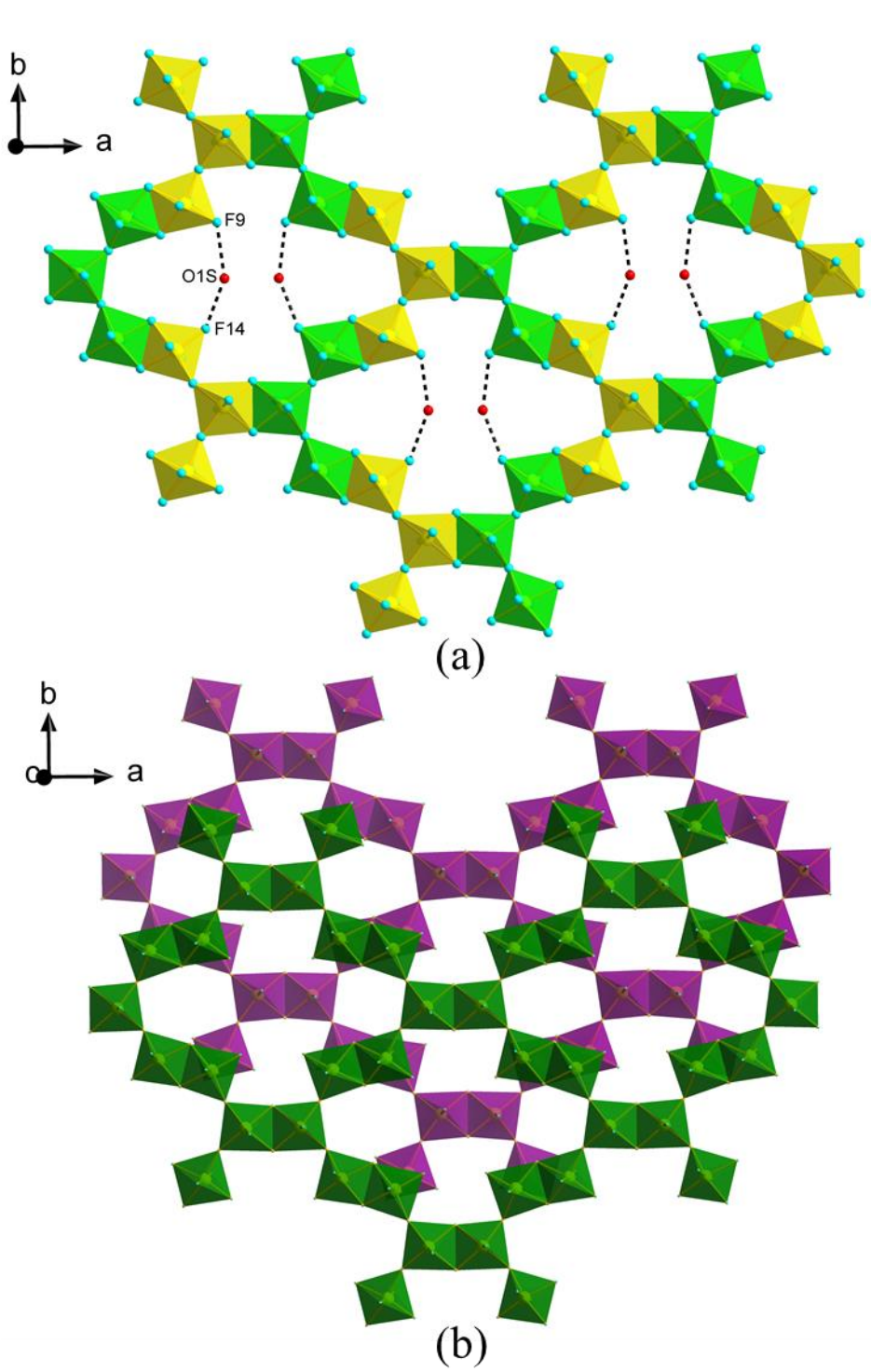

Fig. 5-15 (a) The 2D layers with channel water molecules of **25**. The octahedra with different colours show how the "V" shaped Fe-F building units are connected. (Hydrogen bonds were depicted by dotted lines); (b) Plan view of the layer stacking with different layers are shown in different colours. (*pipz*H_2 and water molecules are eliminated for clarity)

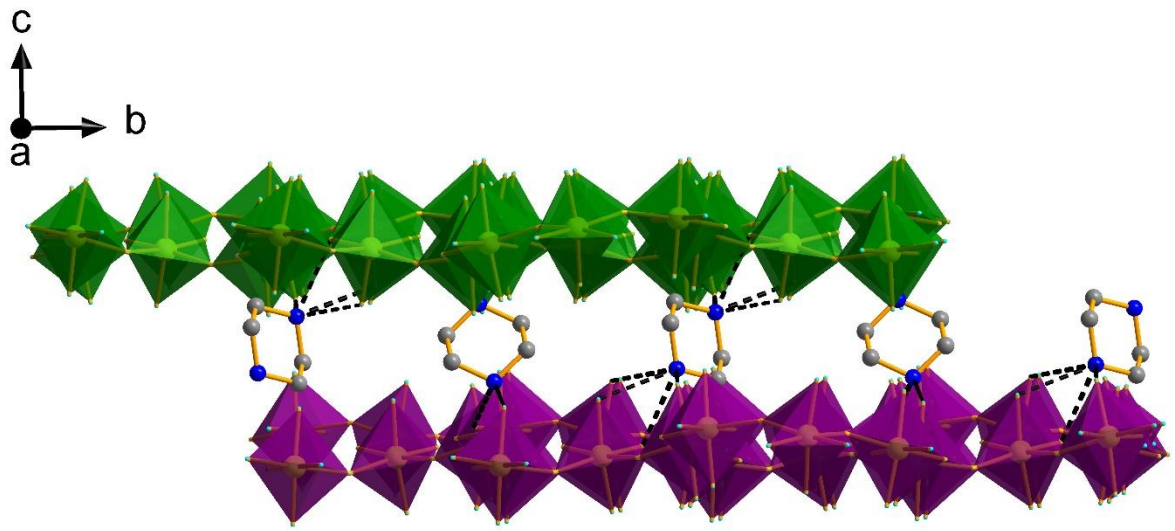

Fig. 5-16 The stacking of the layers with *pipz*H_2 along the *c*-axis of **25**. (Selected hydrogen atoms are eliminated for clarity but hydrogen bonds were depicted by dotted lines.)

Like **24**, the channel water molecule in **25** is also with an enlarged thermal motion and the positions of corresponding H atoms cannot be determined from Q peaks or riding model during the refinement. Ideally, a TGA measurement is also needed to determine the accurate number of water molecules in the structure. The *pipz*H_2^{2+} cations also locate in the interlayer positions and link the neighbouring [Fe_{14}] rings through hydrogen bonds, forming the 3D structure (Fig. 5-16). All the three iron cations in **25** are in the 3+ state, which is confirmed by the BVS calculation ($\sum Fe1 = 2.848, \sum Fe2 = 2.803$ and $\sum Fe3 = 2.835$).

5-4 Discussion and Conclusion.

In summary, the crystal structures of seven Cr(III)- and Fe(III)-fluorides were presented here. However, the low yield stopped further characterisation for most of the samples. Synthetic modifications are necessary in the future in order to promote the purity and yield of the products, so that further characterisation and property measurements might be carried out.

In the Cr(III)-fluoride system, many attempts to introduce organic amines as cation by solvothermal reactions failed. Apart from compounds **19** and **20**, all the other products are in a green "jelly" amorphous state, and no single example else of the products has been successfully recrystallised. Even many hydro/solvothermally prepared Cr(III)-fluoride compounds have been reported,[7,16-21] however, there is no previous report about Cr(III)-oxalate-fluorides before **20**. Except for oxalate, many other organic acid ligands (malonic acid, succinic acid, fumaric acid and pimelic acid, etc.) have also been tried in syntheses, but no Cr-containing crystalline product has been obtained so far. All these results prove the single crystal structures based on Cr in the system are not easily obtained under these conditions, presumably due to the kinetic inertness of Cr^{3+} (d^3).

The only two examples, compounds **19** and **20** are Cr monomers. The syntheses process of them are interesting. In general, proper higher pressure and higher temperature may induce more complicated, higher dimensionality structures. In any case, the two compounds seem to be an exception in this system. The starting materials of **19** and **20** are all the same. Compound **19** is an inorganic compound which is obtained by solvothermal reaction at 190 ˚C, while **20** contains an oxalate ligand, which is achieved by the layered solution method at room temperature. Interestingly, many reported Cr(III)-fluoride compounds containing monomer or dimer units were synthesised by solvothermal reactions with temperatures higher than 150 ˚C.[7,16,17] However, some Cr(III)-fluoride or Cr(III)-oxalate compounds with higher dimensionalities were synthesised at low temperature[18-21]. Thus, maybe milder synthetic

conditions, such as layered solution reactions are more suitable for synthesising Cr based structures with higher dimensionality in this system, which is worth trying to achieve more structures in the future.

The Fe(III)-fluoride system is more complicated. Even though many similar structures have been reported based on other metals (e.g. V, Al, Sc, etc.), the syntheses are not as easy as these. Most of the compounds were firstly obtained as the impurities in the synthesis of Fe(II)-oxalate-fluoride compounds. Unlike the yellow colour of Fe(II)-oxalate-fluorides, all Fe(III)-fluorides are colourless, which is easy to distinguish in the products. Many syntheses without oxalate ligands have been tried. However, none of them can improve the yields much. The synthesis methods listed in this chapter are the best so far. Maybe more attempts are needed to reach higher yields of the compounds.

In the *en*H_2 system, compound **21** and **22** have only one H_2O molecule difference in the formula, but the structures are very different. This is probably caused by different synthesis methods. As a contrast of the Cr system in this chapter, this is a good example of higher pressure and higher temperature producing higher dimensionality structures, as was shown previously in the similar vanadium oxyfluoride system[4].

In the *pipz*H_2 system, compound **23** is always the main phase in all the syntheses, and it is also the main impurity in the *pipz*-Fe(II)-oxalate-fluoride system, even though the syntheses were in lower acidity and higher temperature. Compounds **24** and **25** are in a kind of homologous series, both have [Fe_x] ring layer structures and are stacking in the same style. Based on the order, a homologous composition (*pipz*H_2)$_n$Fe$_{(n+1)}$F$_{(5n+3)}$·x(H_2O) (n = 1, 2, 3…) series with (*pipz*H_2)FeF_5·x(H_2O) as the differential moiety can be predicted. For example, when n = 1, the formula is (*pipz*H_2)Fe_2F_8·x(H_2O). There are various possibilities for the connectivity of the iron fluoride layer. One possibility can be considered as a perovskite-like

layer and forming a [Fe_4] ring structure with the octahedra connection in corner-shared style only, like the layered perovskite structures described in chapter 3. An inorganic compound example with such a Fe_2F_8 layer has been reported previously.[22] Except for the [Fe_4] ring layer, there are also many other Fe_2F_8 layers which could form by the corner-sharing, edge-sharing or mixed sharing of octahedra. Perhaps, only the experimental results will tell the answer.

5-5 References

1. P. DeBurgomaster, W. Ouellette, H. Liu, C. J. O'Connor, G. T. Yee and J. Zubieta, *J. Inorg. Chim. Acta*, 2010, **363**, 1102–1113.
2. J. F. Scott and R. Blinc, *J. Phys. Condens. Matter*, 2011, **23**, 113202.
3. N. F. Stephens, M. Buck and P. Lightfoot, *J. Mater. Chem.*, 2005, **15**, 4298–4300.
4. D. W. Aldous, N. F. Stephens and P. Lightfoot, *Dalton. Trans*., 2007, 4207–4213.
5. U. Bentrup, M. Feist and E. Kemnitz, *Prog. Solid State Chem*., 1999, **27**, 75–129.
6. M. R. Silva, A. M. Beja, B. F. O. Costa, J. A. Paixão and L. A. Da Veiga, *J. Fluor. Chem*., 2000, **106**, 77–81.
7. A. Ben Ali, M. Trang Dang, J. M. Grenèche, A. Hémon-Ribaud, M. Leblanc and V. Maisonneuve, *J. Solid State Chem*., 2007, **180**, 1911–1917.
8. K. Adil, M. A. Saada, A. Ben Ali, M. Body, M. T. Dang, A. Hémon-Ribaud, M. Leblanc and V. Maisonneuve, *J. Fluor. Chem*., 2007, **128**, 404–412.
9. A. Ben Ali, J. M. Grenèche, M. Leblanc and V. Maisonneuve, *Solid State Sci*., 2009, **11**, 1631–1638.
10. A. Zouaghi, A. Benali, V. Maisonneuve and M. Leblanc, *Acta Crystallogr. Sect. E*, 2010, E**66**, m702-m703.
11. F. H. Aidoudi, PhD thesis, University of St Andrews, 2011.
12. U. Bentrup, A. Ahmadi, H.-C. Kang and W. Massa, *Z. Anorg. Allg. Chem*., 1998, **624**, 1465-1470.
13. N. F. Stephens and P. Lightfoot, *Solid State Sci*., 2006, **8**, 197–202.
14. D. W. Aldous, N. F. Stephens and P. Lightfoot, *Inorg. Chem*., 2007, **46**, 3996–4001.
15. J. Lhoste, R. Gervier, V. Maisonneuve, M. Leblanc and K. Adil, *Solid State Sci*., 2009, **11**, 1582–1586.

16. K. W. Krämer, R. Schenker, J. Hauser, H. Weihe, H. U. Güdel and H. B. Bürgi, *Z. Anorg. Allg. Chem*. 2001, **627**, 2511-2516.
17. S. G. Thoma, F. Bonhomme, M. Nyman, M. A. Rodriguez and T. M. Nenoff, *J. Fluor. Chem*., 2001, **108**, 73–77.
18. F. K. Larsen, J. Overgaard, S. Parsons, E. Rentschler, A. A. Smith, G. A. Timco and R. E. P. Winpenny, *Angew. Chem. Int. Ed*., 2003, **42**, 5978–5981.
19. E. Coronado, M. C. Gimenez, C. J. Gomez-Garcia and F. M. Romero, *Polyhedron*, 2003, **22**, 3115–3122.
20. M. Jurić, P. Planinić, N. Brničević, D. Milić, D. Matković-Čalogović, D. Pajić and K. Zadro, *Eur. J. Inorg. Chem*., 2006, 2701-2710.
21. J. Vallejo, I. Castro, M. Déniz, C. Ruiz-Pérez, F. Lloret, M. Julve, R. Ruiz-García and J. Cano, *Polyhedron*, 2013, **52**, 1246–1255.
22. M. Leblanc and G. Ferey, *Acta Crystallogr. Sect. C Cryst. Struct. Commun*., 1990, **46**, 13–15.

Chapter 6 Summary, Conclusions and Future Work

6-1 Summary and Conclusions

The main purpose of the work described in this thesis is to synthesise new organic-inorganic hybrid CPs through hydro/solvothermal reactions and to investigate the crystal structures and physical properties of them.

Chapter 3 introduces the first examples of organic-inorganic hybrid fluoride layered perovskites of the general formula AMF_4. The organic components are linear chain diamines with different numbers of carbon (C2, C3 and C4), the metals are Mn, Co and Ni in the +2 valence state. The single crystal XRD data show that the C2 and C4 compounds are crystallised in monoclinic with space group $P2_1/c$ and the C3 compounds are crystallised in orthorhombic, *Pnma* at room temperature (300 K). All the compounds have no phase transition from 173 K to 300 K. The synchrotron XRD and powder neutron diffraction data show no phase transition from 20 K to 300 K for the C2 series compounds. Only small changes in cell parameters are observed. This series compounds can be considered as derived structures from the aristotype $TlAlF_4$, a DJ phase perovskite structure with $n = 1$. In this series of compounds, the perovskite layers in all the compounds with the same metal are identical in topology, which are formed by corner-shared octahedra. The layers are separated by protonated diamines along the *c*-axis. The octahedral tilting in the C2 and C4 series is a^-a^-c, in Glazer-like notation, while in the C3 series it is $a^-a^-c^-$, which causes a doubled *c*-axis in the case of the odd C analogues.

In the perovskite layers, the intralayer magnetic exchange pathway for all the compounds is the 2D M-F-M bridge, with M-M distances around 4.2 Å. However, there is probably no long-range interplane magnetic coupling due to the lack of a significant magnetic connection medium and the long distance between the perovskite layers. The magnetic properties for the C2-C4 compounds based on Mn^{2+} and Co^{2+} metals were measured by SQUID

magnetometry. All the compounds present overall antiferromagnetic interactions at high temperature, which are corresponding with the 2D M-F-M magnetic connection model. Even though the magnetic exchange pathway is the same, the magnetic signals for Co^{2+} (S = 3/2) are much stronger than Mn^{2+} (S = 5/2), leading to a higher critical temperature (T_N). When the temperature is lower than the critical temperature, all the compounds show canted antiferromagnetic ordering. Powder neutron diffraction experiments were carried out for (enH$_2$)CoF$_4$ (**2**), which confirm that the T_N for the compound is ~ 83 K. The most satisfactory magnetic space group for the compound is $P2_1'/c'$, and there is no magnetic phase transition between 20 K and 83 K, with the magnetic moments (Mx0, My0, Mz0) = (3.53, 0, 0.53) and (1.65, 0, 0.13), respectively.

Chapter 4 describes the crystal structures and magnetic properties of nine metal-oxalate frameworks. Due to the variety of connection modes of the oxalate ligand, many compounds with different structures can be synthesised by simply adjusting the ratio of reagents. In this section, the valence state of metals in all the compounds is +2 and two organic compounds (*en* and *pipz*) are applied as templates. For *en* template, two isostructural (enH$_2$)[M(C$_2$O$_4$)F]$_2$ (**10** and **11**) compounds were obtained, in which the oxalate ligands and fluorine interact with the metal centre to form a magnetic 3D framework and the templates are located in the cavities of the framework. Magnetic measurement shows the Fe^{2+} compound **10** exhibits antiferromagnetic interactions. Even though two competing magnetic pathways, i.e. *cis* oxalate ligand and F exist in the compounds, the magnetic data analysis shows that the M-F-M bridge is the main magnetic pathway for the Fe^{2+}, which has also been identified by fitting a 1D Heisenberg model.

For the *pipz* template, seven compounds are obtained, of which six display *anti-anti* metal-oxalate 1D magnetic chain structures and one adopts a 2D layer structure with metals connected by the *syn-anti* mode of the oxalate ligands. The magnetic data analysis of compound

(*pipz*H)Fe(C_2O_4)$_2$·(H_2O) (**16**) shows the magnetic interaction through the 1D *anti-anti* oxalate bridge is weakly antiferromagnetic, which is also confirmed by the 1D Heisenberg model fitting. In compounds (*pipz*H_2)$Fe_2(C_2O_4)_2F_2(H_2O)_2$ (**14**) and (*pipz*H_2)$Co_2(C_2O_4)_2F_2(H_2O)_2$ (**15**), in addition to the *anti-anti* oxalate connection, an extra magnetic pathway is possible through weak O-H---F linkages, which builds a honeycomb-like magnetic connection through both bridges. However, the magnetic data of the two compounds are also best fitted by the 1D Heisenberg model. Thus, comparing with 1D *anti-anti* oxalate bridge, the connections through O-H---F bridge are perhaps too weak to be counted.

Chapter 5 discusses the synthesis and crystal structures of seven metal(III)-fluorides. Two are based on Cr (green colour) and five are based on Fe, which are colourless. Three of them are metal fluoride monomers, which are linked by the coordination bonds of potassium ($K_2CrF_5(H_2O)$ (**19**) and $K_3Cr(C_2O_4)F_4·H_2O$ (**20**)) or the hydrogen bonds of protonated ethylenediamines ((*en*H_2)$FeF_5(H_2O)$ (**21**)). Compounds (*en*H_2)FeF_5 (**22**) and (*pipz*H_2)FeF_5·(H_2O) (**23**) both contain metal fluoride octahedral corner-shared 1D chains, which are linked by the hydrogen bonds of (*en*H_2) or (*pipz*H_2), respectively. Compounds (*pipz*H_2)$_3Fe_4F_{18}$·2(H_2O) (**24**) and (*pipz*H_2)$_2Fe_3F_{13}$·(H_2O) (**25**) are two apparently homologous structures with (*pipz*H_2)FeF_5·x(H_2O) as the differential moiety. The two compounds contain magnetic 2D rings structures, which are worthy for further research in the future.

6-2 Future Work

There are three parts in the future work corresponding to the three sections in the thesis. The first part is to explore more of the organic-inorganic hybrid fluoride layered perovskites, including more compositions, structures and physical property modifications. Firstly, the structures can be modified by changing metals in similar sizes or involving extra metals, to build bi-metal or tri-metal structures. In addition, the magnetic properties of the compounds could be enhanced by increasing the density of metals, for example, stacking more perovskite

layers ("*n* >> 1") of the DJ phase. Finally, other diamines can be introduced in this system, including chiral ones, to introduce ferroelectricity and accomplish multiferroic perovskite materials.

For the oxalate fluoride CPs, the first step is to synthesise and isolate enough pure samples of **12**, **13**, **17** and **18**, and characterise their magnetic properties. Neutron diffraction can be applied to determine the specific spin interactions at low temperature for compounds **14** and **15**. In addition, the system can be further explored by changing the ratio of reactants: for example, by decreasing the ratio of $M^{2+}/C_2O_4^-$ in synthesising *pipz* based compounds would probably build higher dimensionality $C_2O_4^-$ networks.

For the M(III)-fluorides system, the priority is to find effective synthesis methods to create sufficient pure samples for further physical characterisations. For Cr-F based compounds, more syntheses should be tried at mild conditions to obtain the Cr-oxalate-F CPs. The syntheses and physical properties of homologues of **24** and **25** could also be investigated to explore this unusual series of compounds.

Appendix A

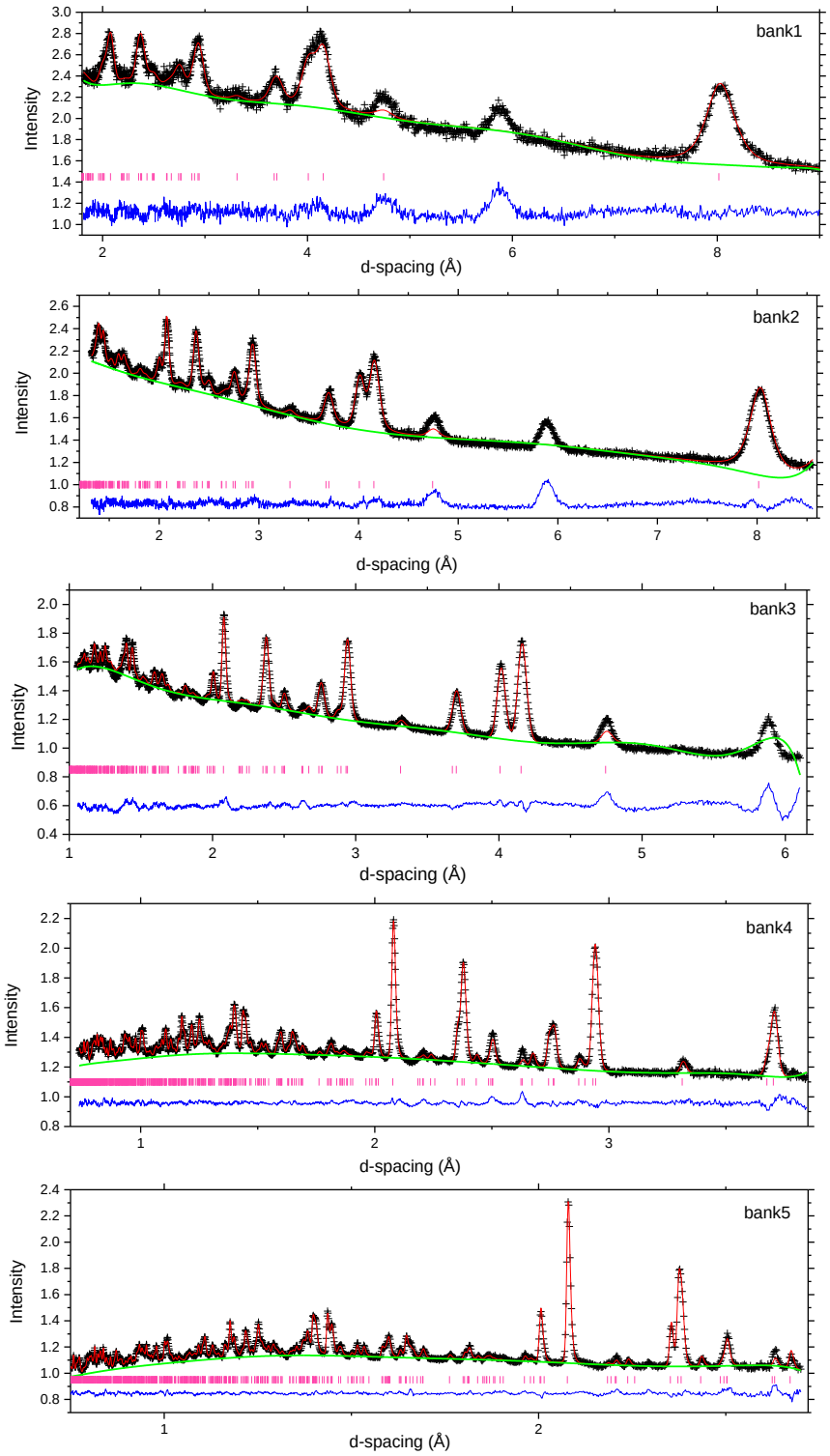

Fig. A-1 Rietveld plots of GEM neutron diffraction experiment data from bank1 to bank5 for **2** at 20 K.

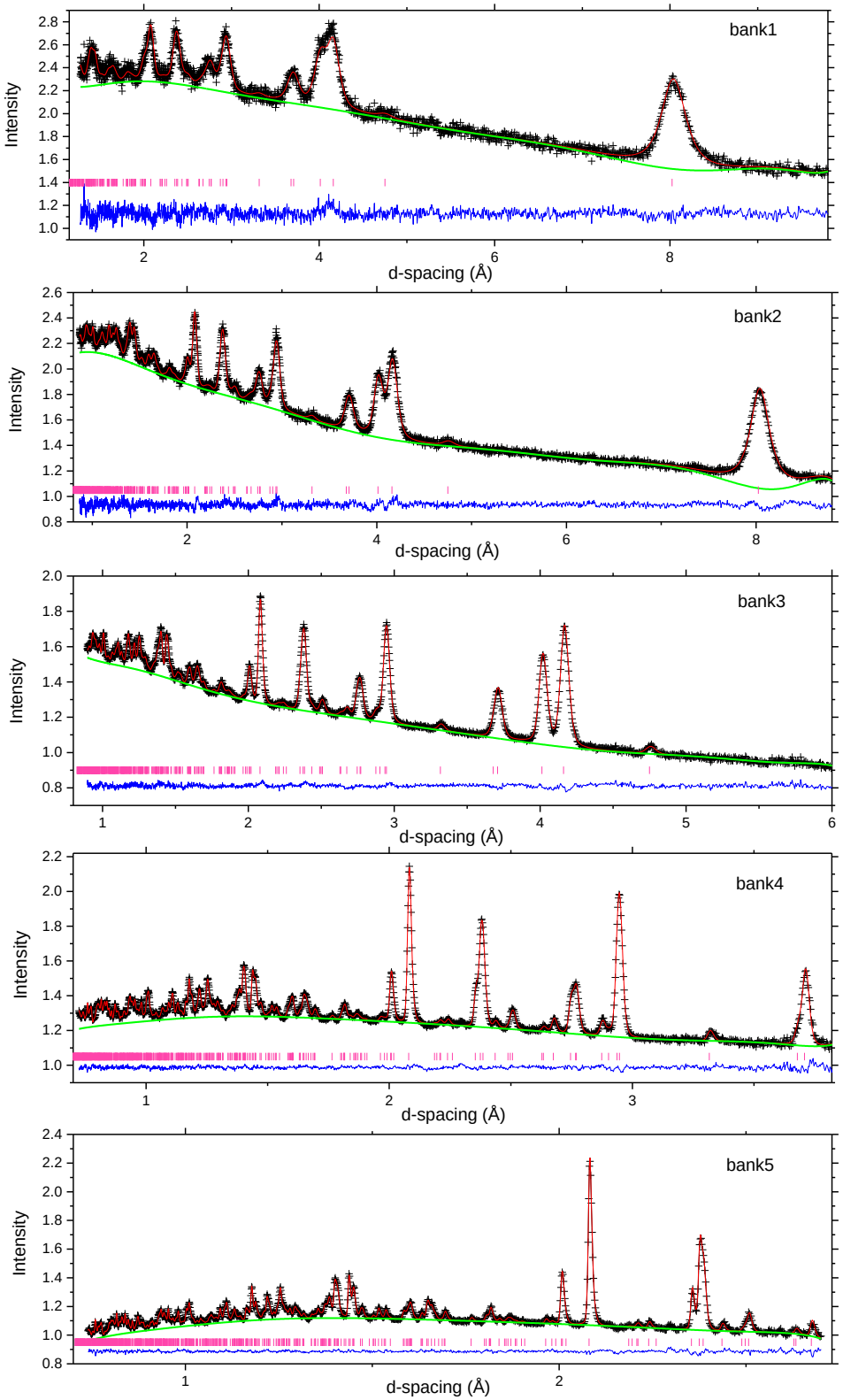

Fig. A-2 Rietveld plots of GEM neutron diffraction experiment data from bank1 to bank5 for **2** at 180 K.

Appendix B

List of publications:

1. A. H. Abdeldaim, **T. Li**, L. Farrar, A. A. Tsirlin, A. S. Gibbs, P. Manuel, P. Lightfoot, G. J. Nilsen and L. Clark, Realising square and diamond lattice *S* = 1/2 Heisenberg antiferromagnet models in the *α* and *β* phases of the hybrid coordination framework , $KTi(C_2O_4)_2 \cdot xH_2O$. *Phys. Rev. Mater*., 2020, 4, 104414.

2. Y-Y. Guo, L-J. Yang, S. Biberger, J. A. Mcnulty, **T. Li**, K. Schötz, F. Panzer, and P. Lightfoot, Structural diversity in layered hybrid perovskites, A_2PbBr_4 or $AA'PbBr_4$, templated by small disc-shaped amines. *Inorg. Chem*., 2020, 59, 12858-12866.

3. **T. Li**, R. Clulow, A. J. Bradford, S. L. Lee, A. M. Z. Slawin and P. Lightfoot, A hybrid fluoride layered perovskite, (*en*H_2)MnF_4. *Dalt. Trans*., 2019, 48, 4784–4787.

4. W. Yao, L. Clark, M. Xia, **T. Li**, S. L. Lee and P. Lightfoot, Diverse Family of Layered Frustrated Magnets with Tailorable Interlayer Interactions. *Chem. Mater*., 2017, 29, 6616–6620.